A numerical study of ocean circulation and ice-ocean interaction, beneath the Amery Ice Shelf, Antarctica.

by

Michael J. M. Williams
BSc(hons) MSc(Otago)

(Michael John Mostyn)

Submitted in fulfilment of the
requirements
for the degree of
Doctor of Philosphy
University of Tasmania

September 1999

Declaration

This thesis contains no material which has been accepted for a degree or diploma by the University of Tasmania or any other institution, except by way of background information which is duly acknowledged. To the best of my knowledge and belief this thesis contains no material previously published or written by another person, except where due acknowledgement is made in the text.

Michael J. M. Williams
23 September 1999

Authority of access

This thesis may be made available for loan and limited copying in accordance with the Copyright Act 1968.

Michael J. M. Williams
23 September 1999

Abstract

Simulations of the ocean dynamics in the cavity under the Amery Ice Shelf, East Antarctica, were carried out using a three-dimensional numerical ocean model. The aims were as follows: first, to describe the ocean circulation, the temperature and salinity distributions, and the interaction of the ocean with the base of the ice shelf; second, to investigate the strength of the influence of the external circulation in Prydz Bay on the circulation in the ocean cavity; third, to investigate the impact of any change in climate on the dynamics of the ocean cavity and the basal mass balance of the Amery Ice Shelf.

The simulations show that the circulation in the ocean cavity is predominantly horizontal and approximately follows the contours of water column thickness. It is driven by the density gradient in the cavity, which is strongly influenced by the heat and salt fluxes from melting and freezing processes at the ice-ocean interface and by the horizontal exchange of heat and salt across the open ocean boundary at the ice front. This horizontal exchange is strongly influenced by the velocity field at the ice front.

Estimates of the basal component of the mass loss of the Amery Ice Shelf were found from model runs with different ice front boundary conditions. The computed loss varied between 10.6 Gta^{-1} and 20.2 Gta^{-1}, depending on which boundary condition was applied at the ice front. The bulk of the melting occurred near the southern grounding line of the ice shelf, although substantial melting also occurred in areas where heat transport by the horizontal circulation was large. Accretion was restricted to areas where water, from upstream melting, was supercooled as it ascended the ice shelf base.

In further studies the model domain was expanded to the north to encompass the adjacent ocean in Prydz Bay. The aim was to allow flow across the ice front to evolve freely. To ensure realistic circulation and water mass distribution in Prydz Bay, temperature and salinity observations were assimilated into the Prydz Bay portion of the domain. This eliminated the need for complicated sea ice models and the arbitrary specification of water mass characteristics. This was only partially successful. The model circulation in Prydz Bay was consistent with observations, but the temperature and salinity were not. This inconsistency raises doubts about the corresponding temperature and salinity distribution in the ocean cavity, and about the fluxes between the ocean and the ice shelf.

The impact of possible ocean climate change to the north of the Amery Ice Shelf was investigated using the smaller domain model. First, two cooler ocean scenarios appropriate to glacial climates or reduced sea ice growth were applied. Second, temperature increases in the range of 0.1°C to 3.0°C were applied at the ice front boundary. For some of these scenarios changes in salinity were considered. The circulation in the ocean cavity, in particular the strength and structure of some gyres close to the ice front, was affected by the changes. In addition, heat flux from warmer water increased the mean melt rate and the net rate of mass loss from the ice shelf. These rates increased approximately linearly with temperature (at $\sim$0.45 $ma^{-1}°C^{-1}$ and $\sim$22.0 $Gta^{-1}°C^{-1}$), suggesting substantial modification of the ice shelf would occur in a warmer climate.

Acknowledgements

The completion of this thesis would not have been possible without the help of many people. In particular, I would like to acknowledge the guidance and encouragement of my supervisors Bill Budd and Roland Warner. Their assistance has been more than any student could wish for.

I am greatly indebted to Klaus Grosfeld, Rüdiger Gerdes, and Jürgen Determann, of the Alfred-Wegener-Insitut für Polar- und Meeresforschung, Bremerhaven, Germany, for providing the code for the numerical models used in this thesis, for their guidance during my stay at AWI, and for their helpful comments on sections of this thesis.

Two publications have arisen out of the work. The first [Williams et al., 1998a] was co-authored with Adrian Jenkins, of the British Antarctic Survey, and Jürgen Determann. This paper is a parallel review of the material presented in Chapter 3. I would like to thank my co-authors for their assistance in developing my understanding of subice shelf oceanography. The second publication [Williams et al., 1998b], was co-authored with my supervisors, and presented preliminary results from this thesis.

I would like to thank the anonymous reviewers of these two papers. Their responses to these publications provided guidance for presenting and interpreting the results in this thesis.

I would also like to acknowledge the following people for providing data, Ian Allison (Antarctic CRC and Australian Antarctic Division) for the radio echo-sounding data from the Amery Ice Shelf region; Andrew Forbes (CSIRO Division of Marine Research) for the FISHOG CTD data; and Phil O'Brien (Australian Geological Survey Organisation) for the bathymetric soundings in Prydz Bay.

Finally, I would like to thank Karen Skeggs for her continuous support throughout.

Contents

Chapter 1

Introduction

Ice Shelves are regions of thick floating ice, which fringe approximately 40% of the coast of Antarctica (Figure 1.1). Ice shelves around Antarctica form an important part of the global climate system. They provide a direct connection between the Antarctic Ice Sheet and the world's oceans, as the majority of the ice which forms Antarctica's ice shelves originates from the Antarctic Ice Sheet. Melting from the base of the ice shelves could account for approximately 20% of the ice lost from the Antarctic Ice Sheet [Jacobs et al., 1992].

The small scale features of the interaction between ice shelves and the ocean underneath are well understood, however, the overall details of individual ice shelves are poorly known. Observing the ocean cavity is physically difficult because the thickness of the ice shelf, generally between 1200 m near the grounding line and 250 m near the ice front, restricts access to the ocean. Some observations in ocean cavities have been made, but they are sparse and generally cover short time spans [e.g., Jacobs et al., 1979; Nicholls et al., 1991; Nicholls et al., 1997]. Due to these restrictions, numerical ocean modelling is an essential tool for understanding this environment.

Ocean modelling under ice shelves is a problem which has unique aspects. In contrast to the remainder of the world's oceans where the surface layers are heavily influenced by atmosphere-ocean exchange, the ice shelf insulates the ocean from the affects of the atmosphere.

The interaction between the ice shelves and the ocean is largely thermodynamic, with heat and salt fluxes occurring between the ice shelf and the underlying ocean. The local nature of these fluxes is largely understood and can be easily characterised. This characterisation is, however, highly dependent on the properties of the ocean beneath the ice shelf. Thus to determine these fluxes the ocean needs to be well described.

Water cooled below the surface freezing temperature is generated by interaction with the ice shelf. This water mass, known as Ice Shelf Water (ISW), only forms under ice shelves. ISW may have a significant impact on the waters of the continental shelf. It is believed to provide a suitably cold source of water to help in the formation of Antarctic Bottom Water (AABW) [Foldvik and Gammelsrød, 1988]. AABW is the dominant water mass at the bottom of most of the world's ocean basins and it has a key role in driving the deep global ocean circulation.

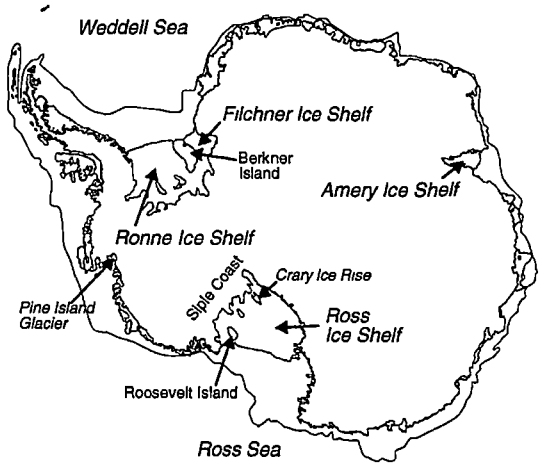

Figure 1.1: Map of Antarctica showing the ice shelves (shaded) and the 1000 m isobath.

Various modelling strategies have been used to simulate the ocean circulation under ice shelves and quantify the impact of the circulation on the ice shelf basal processes. Of the different strategies tried, three-dimensional numerical ocean models have generally been the most successful. To date, three-dimensional numerical models have been applied to cavities under several theoretical ice shelves [Determann and Gerdes, 1994; Grosfeld et al., 1997], the Filchner-Ronne Ice Shelf [Determann et al., 1994], and the Filchner Ice Shelf [Grosfeld and Gerdes, 1998]. Given the success of the three-dimensional model in representing the circulation under the Filchner-Ronne Ice Shelf, it is timely to apply the model to cavities under other ice shelves.

Even though the detailed cavity geometry under the Amery Ice Shelf is not well known, applying a three-dimensional model to the cavity will improve the general understanding of the processes involved in modelling ocean cavities under ice shelves. In addition, answers are needed for the following questions related to the Amery Ice Shelf and the adjacent seas. First, what role does the Prydz Bay Gyre, which lies to the north of the Amery Ice Shelf, play in the circulation and distribution of temperature and salinity under the ice shelf? Second, what affect does the ocean cavity under the Amery Ice Shelf have on the mass balance of the ice shelf? Third, how do possible climate variations change the mass balance of the ice shelf?

The Amery Ice Shelf is the third largest embayed ice shelf in Antarctica and constitutes the outflow from the Lambert Basin, East Antarctica. There are uncertainties in the components of the mass balance calculation for the Lambert Basin, including the net basal melting from the Amery Ice Shelf. Knowledge of the amount of ice lost by basal melting from the Amery Ice Shelf will assist in improving the assessment of the mass balance of the Lambert Basin.

The scale of the interaction between the cavity under the Amery Ice Shelf and the Prydz Bay Gyre is unknown. Oceanographic observations have been made in Prydz Bay, and from these, estimates of flow between the bay and the cavity under the ice shelf have been proposed, including suggestions that the

gyre is driving the inflow waters [e.g., Wong 1994; Wong et al. 1998]. Outflow from under the Amery Ice Shelf also appears important within Prydz Bay, as it is linked to the formation of dense bottom like waters.

This study attempts to answer these questions, along with characterising the oceanography of the cavity under the Amery Ice Shelf, and the interaction between the ice shelf and the ocean cavity.

In Chapters 2 to 4 background material for the overall study is presented. Chapter 2 contains a review of the developments in ocean modelling under ice shelves. This discusses the strategies which have been used to study the ocean circulation and the processes at the ice shelf-ocean interface over the past 10 to 15 years. This includes a summary of the previous numerical study of the ocean cavity under the Amery Ice Shelf [Hellmer and Jacobs, 1992]. In Chapter 3 short summaries of the oceanography of Prydz Bay and the glaciology of the Amery Ice Shelf relevant to this thesis are presented. This is followed in Chapter 4 by a detailed description of the governing equations of the numerical ocean model utilised in the study, along with the boundary conditions on the model domain. Details on the formation of the model data fields for the water column thickness, ice shelf draft, and the temperature and salinity conditions along the ice front boundary of the model are also included.

In the chapters which follow the background material the results from several modelling studies are presented. In Chapter 5, the different boundary conditions which can be applied along the ice front and the effect these have are examined. Using the results from several simulations, estimates are derived for comparison with more direct analysis of observations. These include marine ice layer thicknesses and estimates of the basal component of mass balance for the ice shelf.

In Chapter 6 the impact of different climate change scenarios on the processes in the cavity are examined. The climate change experiments were implemented by modifying the ocean temperature, and in some cases the salinity along the ice front while retaining the cavity geometry. The main aspect examined was the effect of changes on the basal component of the ice shelf mass balance. Changes in the ocean circulation and the water column structure are also discussed. These are generally related to the change in the heat and salt fluxes at the model boundaries.

The model domain is extended in Chapter 7 to include Prydz Bay. This extension moves the boundary away from the ice front, removing the need to prescribe flow across the ice front. This is done because the results of Chapter 5 indicate there is some difficulty in realistically prescribing the boundary conditions at the ice front. In an attempt to ensure that the temperature and salinity in Prydz Bay are realistically reproduced, temperature and salinity observations are assimilated into the Prydz Bay part of the ocean domain. It was expected the assimilation of these observations into the model domain would also ensure a realistic circulation developed in the model domain, and this would lead to water masses with appropriate temperature and salinity flowing under the ice shelf.

In Chapter 8 the results from the previous chapters are drawn together,

and general conclusions are made. These include the implications from the thesis regarding future field observations, which the results suggest are needed to provide a more accurate understanding of the ocean circulation and mass exchange under the ice shelf.

Chapter 2

Review of modelling ocean cavities under ice shelves

The lack of an extensive observational database in cavities under ice shelves, places a great reliance on the use of mathematical models to describe the oceanography under ice shelves. In this chapter a review of previous and current modelling efforts is presented. In the first section the boundary conditions at the ice shelf-ocean interface are discussed. These are a distinctive component of ocean cavity models. In the sections which follow the individual models are discussed.

A variety of different modelling approaches have been used. Numerical models of ocean circulation under ice shelves can be easily grouped into three categories. These are: tidal models, tidally driven models, and thermohaline circulation models. Of these, the tidally driven and thermohaline circulation models focus on the circulation and water mass properties in the ocean cavity. Little work has been done on tidally driven models, as the thermohaline circulation appears to be the dominant process. The tidal models generally focus on determining the tidal constituents in the ocean cavity and the tidal response of the ice shelf, and are not considered in this review.

A recent study [Williams et al., 1998a] reviews a similar range of material to that presented in this chapter.

2.1 Boundary processes at the ice shelf-ocean interface

The description of processes occurring at the boundary between the ice shelf and the ocean cavity are important in all models of circulation in ocean cavities under ice shelves. The ice shelf is a solid boundary with negligible horizontal motion ($< 10^{-4}$ ms^{-1}), so its dynamic influence is to exert a drag on the motion of the water, much like that exerted by the sea bed. A free-slip condition or a quadratic drag law are the commonly used parameterisations. In free surface models the ice shelf is assumed to have no flexural rigidity, so it rises and falls passively with the tides. Only within a few kilometres of the grounding line is this thought to be a poor assumption [MacAyeal, 1984b].

The thermodynamic influence of the ice shelf-ocean interface is more complex, because it is a boundary between two phases of the same material. Given sufficient time to adjust, a mixture of ice and water will always be at the in situ freezing temperature. An input of heat to the system will cause ice to melt, while loss of heat causes freezing. The salinity of the water affects the situation by changing the temperature of the freezing point [Loewe, 1961; Doake, 1976].

The models generally assume that the process of adjustment at the ice shelf-ocean interface is sufficiently rapid that the interface is always at the in situ freezing temperature. The heat flux out of the ocean is dependent on the contrast between the in situ freezing temperature and the ocean temperature. This is balanced by the heat loss (or gain) from melting (or freezing) and the heat flux through the ice shelf.

The salt flux at the boundary has a similar relationship to the heat flux, although there is no flux of salt into the ice shelf. This is based on observations of marine ice beneath the Filchner-Ronne Ice Shelf [Oerter et al., 1992], where low salinities were found, suggesting little salt is removed from the water column at the ice shelf-ocean interface.

Three equations are typically used to describe these boundary processes:

$$T_b = aS_b + b + cP \tag{2.1}$$

$$\gamma_T(T - T_b) = \frac{mL}{C_w} + \frac{Q_{IS}}{C_w} \tag{2.2}$$

$$\gamma_S(S - S_b) = mS_b \tag{2.3}$$

where T and S are water temperature and salinity respectively, with the subscript b indicating conditions at the boundary, P is the pressure at the base of the ice shelf, m is the melt rate (negative for freezing), L is the latent heat of fusion, C_w is the specific heat capacity of sea water, Q_{IS} is the heat flux through the ice shelf, γ_T and γ_S are transfer coefficients for heat and salt and a, b and c are constants parameterising the in situ freezing temperature.

The heat flux through the ice shelf, Q_{IS}, is difficult to calculate as the temperature gradients within the ice shelf are largely unknown. In studies where the heat flux through the ice shelf is included it is usually estimated by assuming a linear temperature gradient through the ice shelf. This gives an equation of the form,

$$Q_{IS} = -K_I \frac{\Delta T}{\Delta z}, \tag{2.4}$$

where K_I is the thermal conductivity of ice, ΔT is the temperature difference between the top and bottom of the ice shelf and Δz is the thickness of the ice shelf. This generally gives an estimate of the heat flux through the ice shelf which is about two orders of magnitude smaller than the other heat flux components [Determann and Gerdes, 1994] and because of this some studies have chosen to ignore the heat flux through the ice shelf in their parameterisation of ice-ocean boundary conditions.

The transfer coefficients, γ_T and γ_S, are used to subsume much of the small scale physics occurring at the boundary. The transfer coefficients are known to vary with velocity, boundary layer thickness and a number of other parameters,

yet it is unclear how these processes can be accurately parameterised. Several studies [e.g., Jenkins, 1991; Jenkins and Bombosch, 1995; Hellmer et al., 1998] have included complex parameterisations of the transfer coefficients, while other studies [e.g., Hellmer and Olbers, 1989; Determann et al., 1994] assume both coefficients are constant.

The role of the salt flux in the boundary conditions varies depending on the magnitude of the two transfer coefficients. If the difference between the two transfer coefficients is small, then the salt flux plays a lesser role in the boundary conditions. Because of this some models do not include the salt flux in their boundary condition parameterisation.

The final term in the freezing point relationship (Equation 2.1) is of fundamental importance. At atmospheric pressure, 90% of ocean waters freeze at temperatures between -1.87°C and -1.92°C, however at a depth of 1500 m, the corresponding range is -3.01°C to -3.06°C. Even if sea water has been cooled to the surface freezing point by interaction with the polar atmosphere, it still has the potential to melt ice at depth. Melting ice at depth may then cool the ocean to temperatures below the surface freezing point, generating buoyant Ice Shelf Water (ISW). Foldvik and Kvinge [1974] noted that, should such 'potentially supercooled' water be raised to the surface, in situ supercooling would result and frazil ice could form. Doake [1976] and Robin [1979] discussed the significance of buoyant supercooled water for driving freezing beneath ice shelves. They both used the concept of a layer of water adjacent to the ice shelf base being maintained at the freezing point by phase changes. Should the slope of the ice shelf base and prevailing ocean currents be such as to the drive the layer to greater depth, melting would result. Conversely, a current ascending along an upwards sloping base could cause freezing. Robin [1979] suggested the possibility of melting beneath the thick ice near an ice shelf grounding line and refreezing beneath the thinner ice near the ice front, a process referred to as an 'ice pump' by Lewis and Perkin [1986].

2.2 Tidally driven models

2.2.1 Early work

The first numerical studies of ocean circulation under ice shelves were carried out by MacAyeal [1984b; 1985a]. In these two studies, the tidal simulations from MacAyeal [1984a] were used to describe two possible ocean circulations under the Ross Ice Shelf, and the consequent patterns of melting and freezing at the base of the ice shelf. The ocean circulation described by MacAyeal [1984a] assumed that tidally induced vertical mixing was dominant in driving the ocean circulation. In MacAyeal [1985a] this assumption was changed, and it was assumed tidal rectification drove the ocean circulation.

MacAyeal [1984b] compared the calculated tidal dissipation rates with the rate at which energy would be consumed if melt water produced at the ice shelf base were mixed throughout the water column. Although he did not know the actual basal melt rates, he was able to estimate the amount of melting necessary

to maintain a stratified water column. By assuming an upper limit on the melt rate of 0.05 ma^{-1}, he suggested that all regions requiring a melt rate higher than this to maintain a stratified water column would be well mixed, and that the location of the 0.05 ma^{-1} melt rate contour would be the approximate position of the tidal front within the ocean cavity. This analysis implied that widespread areas with a well-mixed water column should exist along the Siple Coast (Figure 1.1).

In the latter work, MacAyeal [1985a] was able to calculate the flow of a series of lagrangian tracers in the ocean cavity. From the tracer paths MacAyeal showed that tidal rectification generated steady currents along the sides of several topographic features, and induced large currents near the ice front. However, flow crossing the ice front tended to turn back because few isobaths originating at the ice front extended very far into the ocean shelf cavity. He concluded that tidal rectification could play an important role in driving water into the cavity, and that it may be the cause of the high melt rates observed close to the ice front, but tidal rectification appeared to be an inefficient means of ventilating the greater portion of the ocean cavity under the Ross Ice Shelf.

2.2.2 One-dimensional mixed layer model

Scheduikat and Olbers [1990] developed two one-dimensional vertical layer models, to model flow under the Ross Ice Shelf. The results of the two models were compared to the conditions observed at the drill site known as J9 (82.37°S, 168.62°W), on the Ross Ice Shelf. The models were also used to calculate the ablation rates in the southeastern portion of the ice shelf, which is the expected origin of so called Deep ISW. The models were forced by a barotropic tidal current and coupled to the ice shelf by setting the ice-water interface to the freezing point. The first model had two layers: a horizontally homogeneous mixed layer, over a bottom layer in which the temperature and salinity were specified and the barotropic tidal forcing was applied.

In the second model a third layer was introduced between the mixed layer and the bottom layer. Other changes were the addition of advective transport for heat and salt, and changing the bottom layer from a passive layer to a turbulent boundary layer. These modifications enabled a better estimate of the entrainment fluxes at the base of the mixed layer.

In the two layer model, Scheduikat and Olbers found the melt rate had a strong dependence on the shape of the tidal ellipse, which described the barotropic tidal current providing the forcing. This led to the classification of the model results into ablation and accumulation regimes. If the tidal current forcing was isotropic, i.e., constant in time, the system assumed a steady state which was independent of the strength of the current. However the mixed layer depth varied with the current strength. During the formation of the mixed layer, warm salty water was entrained from below, this warmed the mixed layer and drove melting at the ice shelf. This in turn thinned the mixed layer.

When the two layer model was driven with anisotropic tidal currents, the model operated in a cyclic state, with alternating entrainment conditions where the mixed layer thickened, and detrainment conditions where the mixed layer

thinned. When the model was entraining it behaved in a similar manner to the isotropic case.

After a 30° rotation in the tidal ellipse the model moved into a detrainment state. Here the net production rate of turbulent kinetic energy, due to the shear of the tidal current at the ice shelf base, was no longer sufficient to balance the buoyancy effects. Thus the mixed layer became thermodynamically decoupled from the lower layer, with only the heat and salt fluxes at the ice shelf-ocean boundary affecting the mixed layer. This cooled and freshened the mixed layer close to the freezing point during detrainment. After the tidal ellipse passed through its minimum, the model switched back to entraining. However, the amount of entrainment was weak until the tidal forcing neared its maximum, from where the cycle was repeated.

Increasing the time variability of the tidal currents increased the alternating rates of entrainment and detrainment. Consequently, there was an increased melt rate and a decrease in the mean thickness of the mixed layer. However, the model state was not generally determined by the strength of the tidal current or the production of turbulent kinetic energy (which controls the entrainment velocity between the top and bottom layers), but instead by the temporal variability of the turbulent kinetic energy.

In general the ablation rates from the two layer model were unrealistic. This was most likely due to the character of the laminar bottom layer, which overestimated the entrainment flux at the lower boundary of the mixed layer. This motivated Scheduikat and Olbers to develop the three layer model.

Scheduikat and Olbers found with isotropic tidal forcing the results from the three layer model were equivalent to the isotropic two layer model results. This was because interaction between the intermediate layer and the bottom layer shut down. The lack of interaction between the bottom layer and the intermediate layer meant that the intermediate layer behaved similarly to the bottom layer in the two layer model, and little occurred in the bottom layer.

As in the two layer model, if anisotropic forcing was used, the three layer model was characterised by alternating entrainment and detrainment stages. The cyclic stages were similar to those of the two layer model, but the overall rate of ablation was considerably reduced. This was because of the change of behaviour in the bottom layer, which showed only weak fluctuations, in contrast to the top mixed layer which was characterised by high variability.

Detrainment into both the top and bottom layers from the intermediate layer arose in the system when tidal forcing was nearly at a minimum. The choice of entrainment zone thickness (a scale parameter introduced with the intermediate layer) modified the resulting melt rate, as well as the structure of the temperature and salinity profiles in the intermediate layer. A higher entrainment zone thickness resulted in higher entrainment fluxes at the base of the mixed layer and a correspondingly higher melt rate.

The most realistic model results were found by using a tidal ellipse fitted to observations at the J9 drill site. From this Scheduikat and Olbers believed High Salinity Shelf Water (HSSW) did not mix with overlying layers on its way south under the ice shelf until it reached regions where the water column thickness

was less than 300 m. This is also consistent with the findings of MacAyeal [1984b, 1985a]. Variation in the thickness of the bottom layer and mixed layer were also in good agreement.

The melt-freeze rates at several locations in the southeast part of the Ross Ice Shelf were calculated using the K_1 tidal component ellipses of MacAyeal [1984a] for forcing. Ablation rates greater than 0.4 ma^{-1} were obtained, especially southeast of the Crary Ice Rise where the ablation rates were highest. In the far south near the grounding line the tide is approximately isotropic, this led to accumulation taking place at the ice shelf base.

Scheduikat and Olbers concluded the occurrence of melting or freezing depended strongly on the character of the tidal energy necessary to elevate the dense water of the bottom layer. They found the velocity and length scale only affected the melt rate if the tidal current showed distinct anisotropy. However, the melt rates did show a strong correlation to the thickness of the water column.

Scheduikat and Olbers concluded by suggesting that the melt rates observed from the three layer model should be considered as maximum possible melt rates under the Ross Ice Shelf, and would be expected if only vertical processes were being considered. In general, they believed that if improved sets of observations were available the model would be an effective tool for predicting local ablation and accumulation rates beneath ice shelves. The neglect of internal wave energy as a dissipative source in the calculations of turbulent kinetic energy, and therefore on the entrainment velocity, was highlighted as a possible problem in the model design.

2.3 Thermohaline models of circulation under ice shelves

2.3.1 Analytical model

Nøst and Foldvik [1994] presented a two-layer analytic model which assumed melting occurred close to the grounding line, and that some of the melt-water froze at some distance from the grounding line. Nøst and Foldvik presented two different versions of their model, the first was without heat exchange with the ice shelf, while the second included heat exchange. In both models the lower layer was regarded as an infinite source of mass, heat, and energy.

In the first model the salinity and temperature of the upper layer were found to satisfy the relationship

$$S = S_W \left(1 - \frac{C_w(\theta_W - \theta)}{L}\right) \tag{2.5}$$

where θ and S are the temperature and salinity of the upper layer, θ_W and S_W are the temperature and salinity of the underlying water mass, C_w is the specific heat capacity of water, and L is the latent heat of fusion for ice. Nøst and Foldvik then use separate arguments in zones of melting and freezing to

set the temperature in the upper layer equal to the in situ freezing point. This generates a system where the salinity and temperature are a known function of the depth of the ice shelf-ocean interface and the lower layer temperature and salinity. They are also independent of the entrainment rate of water from the lower layer into the upper layer.

For the second model where heat exchange with the ice shelf is incorporated, different arguments are again used in melting and freezing zones. In the melting zones the relationship between salinity and temperature is

$$S_W\left(1-\frac{C_w(\theta_W-\theta)}{L}\right)<S<S_W\left(1-\frac{C_w(\theta_W-\theta)}{L'}\right) \tag{2.6}$$

where L' includes the additional heat conduction from the ice shelf and is taken to be independent of the depth of the ice shelf-ocean interface. The possible variation in the salinity occurs because with the inclusion of heat exchange the temperature-salinity relationship becomes dependent on the entrainment rate between the two layers. At typical values, $\theta_W = -1.9°\text{C}$ and $S_W = 34.70$ PSU, the salinity range was within 0.04 PSU.

Similarly in the freezing zone the temperature salinity relationship is dependent on the entrainment rate of water from below. The salinity varies over the range,

$$S_W\left(1-\frac{C_w(\theta_W-\theta)}{L}\right)<S<S_W\left(1-\frac{C_w(\theta_f(H_0)-\theta)}{L}-\frac{C_w(\theta_W-\theta_f(H_0))}{L'}\right) \tag{2.7}$$

where $\theta_f(H_0)$ is the in situ freezing temperature at the beginning of the freezing zone.

In general with this model (in both melting and freezing regions of an ice shelf), the temperature of the ISW layer will be controlled by the difference between the heat fluxes at the ice-ocean interface, and the fluxes from entrainment between the layers. The salinity range can then be calculated from the relevant equation. Despite the importance of the fluxes between the layers, the selected entrainment rate had little influence on the result.

2.3.2 Plume Model

The Plume Model evolved from a stream-tube model used to simulate the drainage of shelf water off polar continental shelves into the abyssal ocean [Killworth, 1977; Melling and Lewis, 1982]. Here, the term stream-tube refers to fluid with uniform properties flowing within an idealised conduit of streamlines that separate the plume from its surroundings. It was initially adapted for buoyant melt-water plumes in ocean cavities under ice shelves by MacAyeal [1985b].

It followed from earlier work [MacAyeal, 1984b] where he had proposed an ocean cavity circulation under the Ross Ice Shelf in which HSSW, with a salinity of 34.75 and a temperature at the surface freezing point, filled the deeper sections of the ocean cavity. Melting caused by vertical mixing along the Siple Coast could then drive a thermohaline circulation with a buoyant layer flowing

along the ice shelf base with a return flow of HSSW below. By assuming a balance between the work done against friction and the release of gravitational potential energy, MacAyeal [1984b] was able to estimate the likely strength of the circulation and showed that it could ventilate the cavity in about five years, a time scale consistent with results of tracer studies of water from the ocean cavity [Michel et al., 1979].

MacAyeal [1985b] applied the model to an idealised ice shelf, representative of the Ross Ice Shelf. The ice shelf had a constant basal slope of 10^{-3}, over a distance of 1000 km. MacAyeal hypothesised a double plume mechanism under the ice shelf to generate the two types of ISW observed in the Ross Sea. The deeper plume from which Deep ISW would form was fed by HSSW, while the shallower plume which generated the Shallow ISW was fed by water with the characteristics of a warm core of water observed off the ice front.

The criterion used by MacAyeal [1985b] to stop the evolution of the plume was when the plume broke free of the ice shelf base and began to interweave with the stratified ambient water column. This criterion was taken to be the point at which the plume buoyancy was so low that the equations for the velocity and flow direction were no longer valid, because the inertial terms, which were ignored in the model evolution equations, become comparable to buoyancy terms.

The model was highly dependent on the choice of values for the entrainment of water from outside the plume and the friction parameter at the ice shelf-ocean interface. Because of this MacAyeal [1985b] chose to explore the range of parameter space rather than attempting to tune the model parameters to the available observations. This was also done with the aim of identifying a set of qualitative rules governing the evolution of the plumes in the ocean cavity. The other aims of the model were to identify where the Deep ISW and Shallow ISW plumes broke free, and to examine how the Earth's rotation effects the plume evolution.

MacAyeal found the effects of the Earth's rotation were counter balanced by the effects associated with the coasts, by inverted channels in the base of the ice shelf or by baroclinic instabilities. These are all effects of either a high entrainment or friction parameter. Plume entrainment rates were found to reduce when Coriolis, rather than friction, was balancing the buoyancy force within the plume.

MacAyeal also found that basal melting near the ice front was not likely to be caused by sustained entrainment of heat from the HSSW, suggesting other features of the ocean circulation needed to be examined.

In Jenkins [1991] a model similar in concept to MacAyeal's [1985b] was presented. Here it was assumed that the circulation and mixing beneath ice shelves was driven entirely by thermohaline processes. The ocean beneath the ice shelf was treated as a two layer system, with the ambient fluid filling most of the cavity having the characteristics of HSSW. Importantly, this lower layer was assumed to be passive with negligible fluid motion. The upper layer, i.e., the plume, consisted of positively buoyant ISW which was driven upwards along the ice shelf base.

Jenkins' [1991] Plume Model was also based, with some changes, on the equations presented by Killworth [1977]. The major changes from MacAyeal's [1985b] model were restricting the plume to one dimension, and neglecting the influence of the Earth's rotation. Jenkins improved on MacAyeal's model by including additional equations to account for melting and freezing at the upper boundary, and the resulting freshwater flux.

The four equations used to govern the system were :

$$\frac{d(UD)}{dx} = e + m \tag{2.8}$$

$$\frac{d(U^2D)}{dx} = -D\Delta\rho g \sin\alpha - KU^2 \tag{2.9}$$

$$\frac{d(TUD)}{dx} = T_{sw}e + Tm + (T_0 - T)\gamma_T \tag{2.10}$$

$$\frac{d(SUD)}{dx} = S_{sw}e + Sm + (S_0 - S)\gamma_S \tag{2.11}$$

where x is the distance along the plume, D the plume thickness, U the plume velocity, e the entrainment velocity, m the melt-water production rate, g the acceleration due to gravity, α the ice shelf basal gradient, K the drag coefficient, γ_T and γ_S are the heat and salt exchange coefficients, T, T_{sw} and T_0 the temperature of ISW, HSSW and the ice shelf interface respectively, and similarly S, S_{sw}, and S_0 are the respective salinities. The density contrast between ISW and HSSW,

$$\Delta\rho = 7.86 \times 10^{-4}(S - S_{sw}) - 3.87 \times 10^{-5}(T - T_{sw}), \tag{2.12}$$

was derived from a linear equation of state for sea water.

The heat and salt fluxes at the ice shelf-ocean boundary were governed by equations similar to those presented in Section 2.1. The heat and salt transfer coefficients (γ_T and γ_S) were velocity dependent and were of a form derived by Kader and Yaglom [1972, 1977] for a smooth boundary. In balancing the heat flux equation Jenkins included the heat flux through the ice shelf in his model by assuming the temperature gradient through the ice shelf was linear with a temperature of -20°C at the top of the ice shelf.

As with MacAyeal's [1985b] model, Jenkins' Plume Model terminated when the plume was deemed to no longer be in contact with the ice shelf. This was determined when either the density gradient between the plume and lower layer became zero, or the ice front was reached.

This Plume Model was first applied to an ice shelf flowline of the Ronne Ice Shelf [Jenkins, 1991]. This flowline was chosen so a comparison could be made with the glaciological steady state melting and freezing rates previously calculated by Jenkins and Doake [1991] .

The simulated basal melting and freezing rates are shown in Figure 2.1, along with the results of Jenkins and Doake [1991]. Agreement was in general good, although large discrepancies were found over the first 150 km from the grounding line and in the last 50 km to 80 km before the ice edge. Jenkins [1991] argued that the discrepancies in the first 150 km were caused, either by

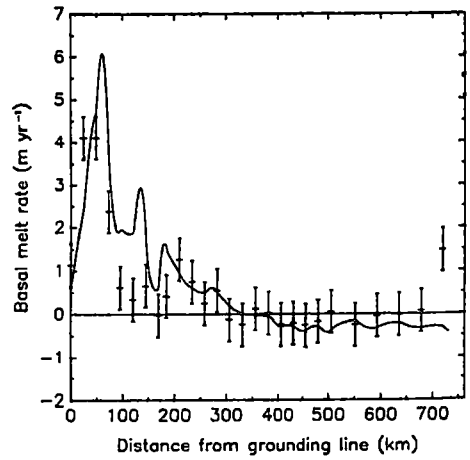

Figure 2.1: Steady state basal melt rates calculated by Jenkins and Doake [1991] for a flowline on Ronne Ice Shelf (crosses with approximate one standard deviation error bars) and melt rates derived from the Plume Model (solid line). Melting/freezing rates are expressed as a water equivalent thickness per unit time. [Figure 3, Jenkins, 1991]

excluding the effects of vigorous tidal mixing, or by lateral variations in the ice thickness, reducing the accuracy of Jenkins and Doake's [1991] measurements. Over the last 50 to 80 km, it was suggested the discrepancy was most likely the result of warmer waters near the surface being driven beneath the ice shelf by tidal rectification near the ice front [MacAyeal, 1985b].

The effects of changes in the initial conditions and in the values of several key physical parameters on the principal results, and their sensitivity to these changes, were also studied. It was found the basic form of the mass balance curve, shown in Figure 2.1, remained unaltered, as any change which increased the melt rate also increased the freezing rate, so the final melt-water fraction remained almost unaltered. From this Jenkins concluded that the location of the melting and freezing zones was controlled principally by depth. The transition from ablation of the ice shelf to accumulation was found to occur where the sensible heat supply was no longer sufficient to prevent ISW becoming supercooled. The sensible heat supply was effected by the change in the plume temperature, which in turn was controlled by the dependence of the in situ freezing point on pressure.

The variability observed by Jenkins and Doake [1991] in the melt-freeze rate over the first 300 km of the Ronne Ice Shelf flowline was explained by Jenkins [1991], as the influence of the ice shelf basal slope on the entrainment process. In particular, a steeper basal gradient implies more efficient entrainment and a greater melt rate. Increasing the basal slope not only increased the gravitational component driving the flow, but it also decreased the component controlling the stability of the stratification.

Jenkins was also interested in the sensitivity of the model to changes in the temperature of the underlying water mass. Using the Plume Model, only the immediate effects of a rapid change could realistically be modelled, as the ice

shelf basal topography would be expected to change with a slow warming of the underlying water mass, and changing topography was not included in the plume model.

Modified Weddell Deep Water, which is 0.59°C warmer than HSSW, was chosen as the replacement water mass as it forms the warmest water currently encroaching under the Ronne Ice Shelf. An increase in the melt rate was found, with the mean melt rate increasing from 0.6 ma^{-1} to 2.6 ma^{-1}. More importantly, the melt-water plume did not attain neutral buoyancy allowing the plume to reach the ice front and almost eliminating basal freezing.

Nicholls and Jenkins [1993] presented some modifications to the Plume Model of Jenkins [1991]. These included making the velocity dependence on the heat and salt transfer coefficients explicit, improving the conservation of heat and salinity, and slightly modifying the heat and salt balance calculations at the ice shelf-ocean interface. The improved model was applied to a glaciological flowline that extended from the grounding line of the Rutford Ice Stream across the Ronne Ice Shelf to the ice front. The orientation of the flowline was directed so that it met a drill site providing access to the ocean cavity and was very similar to the flowline modelled in Jenkins [1991]. Nicholls and Jenkins comment that a buoyant plume in the water column underlying an ice shelf does not in general follow a glaciological flowline. However, neglecting the effect of the Coriolis force, as the Plume Model does, the likely path of a buoyant plume originating at the grounding line and passing through the drill site location will be along lines of steepest ascent, which for this area are approximately parallel to flowlines from the coast to the ice front.

Nicholls and Jenkins used additional observations, not available to Jenkins [1991], for comparison purposes. These observations included salinity and temperature measurements collected at the drill site along the plume path and salinity and temperature measurements collected in a shore lead near where the flowline arrived at the ice front.

It was assumed that the conductivity, temperature, and depth (CTD) measurements made in the shore lead at the ice front were typical of the characteristics of the emerging plume. They indicate a salinity of between 34.56 PSU and 34.63 PSU and a minimum temperature of -2.09°C. At the point where the model plume detaches from the ice shelf base the plume's salinity and temperature are 34.60 PSU and -2.25°C. The salinities agree well, but the model temperature is 0.25°C lower. Two suggestions were made by Nicholls and Jenkins to explain the temperature difference. The first was that additional water could be entrained into the plume as it travelled the 50 km between detaching from the ice shelf base and the ice shelf front. The second was that additional latent heat may have been added by the formation of frazil ice in the plume, although they estimated this would raise the salinity of the plume by 0.06 PSU.

At the drill site, which was 460 km along the flowline from the grounding line, direct comparison between the model and observations were possible as the plume had not yet detached from the ice shelf. The observations suggested a 360 m deep water column was present, consisting of an approximately 200 m thick layer of ISW, over a 100 m thick layer of modified Weddell Sea Water

(WSW). These layers were separated by a weak 50 m pycnocline. This approximates the two layer structure assumed by the model, although the thickness of the layers was reversed in the model, with the plume being smaller than the lower layer with a thickness of 60 m. Nicholls and Jenkins suggest the discrepancy in the layer thicknesses may have been from the effects of sporadic breaking of internal waves. Although Nicholls and Jenkins did find evidence of internal wave activity in the oceanographic observations taken at the drill site, it seems unlikely that breaking of internal waves would provide sufficient mixing to explain the difference in plume thicknesses between the model and observations. For the oceanographic parameters of temperature, salinity, and deuterium good agreement was found between the model results and the observations.

The modelled thickness of the accumulated ice at the drill site was determined by integrating the accumulation rate from the point where freezing started, then allowing the strain of the whole ice shelf to thin the basal layer. This was then compared with the measured thickness of the marine ice layer through the drill hole, where excellent agreement between the observed marine ice layer thickness of 46 ± 5 m, and the modelled thickness of 48 m was found.

Nicholls and Jenkins suggested agreement between the model results and the available oceanographic observations was good and thus lent considerable support to the theory that large scale circulation beneath the Ronne Ice shelf is driven primarily by interaction between the sea and the ice shelf base.

Lane-Serff [1995] made no major changes to the Plume Model as developed by Jenkins [1991] and improved by Nicholls and Jenkins [1993] when applying the model to a theoretical ice shelf with a simple geometry. This allowed a broader insight into the general features of plume flow. Lane-Serff introduced two useful concepts for characterising the flow in Plume Models. These are the 'equilibrium' values of temperature and salinity towards which the properties of the plume tend, and the 'ambient freezing point' which indicates the depth of transition between the melting and freezing stages of the plume.

Using initial conditions similar to those of Jenkins [1991], Lane-Serff argued the flow can be divided into two regions: the first where melting is important and the buoyancy flux increases with the addition of melt water, and the second where melting is less important (with possible refreezing) and the buoyancy flux decreases with height until the plume detaches from the ice shelf. The division between these two regions is indicated by whether the buoyancy flux is increasing or decreasing.

In the first region, Lane-Serff solved for equilibrium values of temperature and salinity, after assuming the ambient conditions in the lower layer were constant with distance from the grounding line (x). That is conditions were sought where,

$$\frac{dT}{dx} = 0 \quad \text{and} \quad \frac{dS}{dx} = 0 \tag{2.13}$$

held, making it possible to solve for the 'equilibrium' temperature and salinity. After solving the equations numerically for the 'equilibrium' temperature and salinity, it was found the plume tended rapidly towards these values and followed them closely at first. However as the depth decreased the values in the plume

drifted away from the local equilibrium temperature and salinities. In effect the 'inertia' of the system increased until the restoring tendencies of the system were overwhelmed. This moved the plume into the second phase.

After a number of model runs with basal slopes between 10^{-4} and 5×10^{-3}, and various values for the ambient temperature and salinity, Lane-Serff was able to estimate an upper bound on the length of the first phase of the plume. The change in depth from the origin of the plume to the 'ambient freezing point' provided a useful length scale, as it was dependent on the pressure freezing relationship and the salinity and temperature of the ambient sea water. For the range of basal slopes modelled and for salinity in the range of 30 to 40 and temperature in the range of freezing to 0°C, the following expression was found:

$$z_{m/f} = z_0 + (0.6 \pm 0.1)(z_{amb} - z_0), \tag{2.14}$$

where $z_{m/f}$ was the depth of the melt freeze transition, z_0 the depth of the source water and z_{amb} the ambient freezing point, which is the vertical depth at which ambient sea water would freeze.

In the second phase of the flow Lane-Serff found the effects of melting and freezing were of only minor importance to the plume. By ignoring their effects the equations could be reduced to those of a turbulent, entraining gravity current flowing on a slope surrounded by a stratified ambient fluid. Using results from previous work [Lane-Serff, 1993], Lane-Serff estimated the point where the current left the slope as

$$z_2 = 1.5 F^{1/3} N^{-1} E_0^{-1/2} (K/\sin\theta)^{1/6}, \tag{2.15}$$

where F is the buoyancy flux at the origin of the second phase, N the ambient buoyancy frequency, E_0 is a constant dimensionless parameter (equalling 0.036), K is a drag coefficient, and θ is the slope of the base of the ice shelf.

Removing the melting and freezing allowed a difference in the buoyancy flux, which Lane-Serff suggested could change the zero buoyancy depth by up to 100 m. This appears significant if the depth of zero buoyancy is only 265 m, and in turn raises doubts about the validity of ignoring the effects of melting and freezing.

Lane-Serff concluded that the geometry of the flow depended mainly on the ambient temperature and salinity conditions and only weakly on the values of parameters describing the flow, such as the basal slope or the entrainment velocity.

2.3.3 Plume Model with frazil ice

Studies of the marine ice formation on the base of ice shelves have suggested that this layer consists of an unconsolidated mixture of ice crystals and water [Engelhardt and Determann, 1987; Nicholls et al., 1991]. This supports a suggestion by Robin [1979] that most of the basal accumulation beneath ice shelves would result from ice crystals growing in the supercooled water column and subsequent deposition of these crystals onto the ice shelf base.

Motivated by this Jenkins and Bombosch [1995] extended the Plume Model used by Jenkins [1991] and Nicholls and Jenkins [1993] to include the dynamics of frazil ice. The plume of ISW was treated as a turbulent, particle-laden gravity current ascending a reactive boundary and containing a suspended load which evolved in response to the supercooling of the water and the inverted sedimentation of the crystals.

To simplify the inclusion of frazil ice into the model the frazil ice crystals were assumed to be disc shaped and uniform in size, with each experiencing the mean water temperature and salinity. Heat and salt transfer leading to crystal increase or decrease was assumed to occur on the edge of each disc. The ice crystals initially formed around seed crystals, which were only introduced into the plume when it was supercooled.

The frazil ice concentration (C) was always expected to be small, so the Boussinesq approximation was applied to the ice-water mixture. This led to modifications to the main equations governing the evolution of the plume. The new equations governing the plume were:

$$\frac{\partial}{\partial s}(DU) = e + m + p \tag{2.16}$$

$$\frac{\partial}{\partial s}(DU^2) = -\frac{(\rho_m - \rho_a^D)}{\rho_0} Dg \sin\alpha - KU^2 \tag{2.17}$$

$$\frac{\partial}{\partial s}(DUC)) = \frac{\rho_0}{\rho_i}(p - f) \tag{2.18}$$

$$\begin{aligned}\frac{\partial}{\partial s}((1-C)DUT) &= eT_a + mT_b - (1-C)\gamma_T^b(T - T_b) \\ &\quad -(1-C)D\gamma_T^c(T - T_c^D)A_c + \int_{-D}^{0} w'T_c dn\end{aligned} \tag{2.19}$$

$$\begin{aligned}\frac{\partial}{\partial s}((1-C)DUS) &= eS_a + mS_b - (1-C)\gamma_S^b(S - S_b) \\ &\quad -(1-C)D\gamma_S^c(S - S_c^D)A_c + \int_{-D}^{0} w'S_c dn\end{aligned} \tag{2.20}$$

In the above equations n and s are the spatial coordinates normal and parallel to the ice shelf base, p is the precipitation rate of frazil ice (positive when mass is gained by the plume), $\frac{\rho_0}{\rho_i}$ is the ratio of sea water density to ice density, f is the total volume of fluid at reference density melted from the frazil ice per unit area of the plume per unit time, T_a and S_a are the temperature and salinity of the ambient water, T_b and S_b are the temperature and salinity of the ice shelf base, T_c and S_c are the temperature and salinity of the frazil ice crystals, T_c^D and S_c^D are the temperature and salinity at the edge of the frazil ice crystals, w' is the melt rate of frazil ice per unit volume, γ_T^b and γ_S^b are the heat and salt transfer coefficients at the ice shelf base, γ_T^c and γ_S^c are the heat and salt transfer coefficients for the frazil ice crystals, and A_c is the total surface area of the disc edges. If the ice concentration C is set to zero, these equations are similar to those of Section 2.3.2.

The boundary conditions at the ice shelf-ocean interface used in the Plume Model with Frazil Ice are similar to those used by Jenkins [1991], with slight modifications to account for the effects of frazil ice in the plume.

Two other important processes are also involved in coupling the frazil ice dynamics to the plume. These are the transfer of heat and salt between the ice crystals and the plume, and the deposition of the ice crystals onto the ice shelf base from being in turbulent suspension. The heat and salt balances for each ice crystal are analogous to the balances at the ice shelf-ocean interface. Once integrated over the plume thickness, the balance equations become :

$$(1-C)\gamma_T^c(T-T_c^D)D\frac{2C}{r} = \frac{L}{C_w}f \tag{2.21}$$

$$(1-C)\gamma_S^c(S-S_c^D)D\frac{2C}{r} = fS_c^D, \tag{2.22}$$

where r is the radius of the frazil ice disc. The ice crystal deposition was treated as an inverted sedimentation process. Jenkins and Bombosch then followed the reasoning of a sedimentation scheme described by McCave and Swift [1976] to derive the following expression,

$$\rho_0 p = -\rho_i C W_d \cos\alpha(1-\frac{U^2}{U_C^2})He(1-\frac{U^2}{U_C^2}), \tag{2.23}$$

where W_d is the buoyant drift velocity, U_C is the critical plume velocity for frazil ice deposition, and $He(x)$ is the Heaviside function.

Jenkins and Bombosch [1995] applied the model to a simplified ice shelf configuration, which they considered to be representative of the base of a large Antarctic ice shelf. The ice shelf had a constant slope over 600 km, with the grounding line at 1400 m and the ice edge front at 285 m in depth. The ambient water mass was assumed to be HSSW with a linear gradient in salinity and temperature through the water column. The model was run with five different frazil ice crystal sizes, all with an initial concentration volume fraction of 5×10^{-9}.

Different results were found for different size crystals. The smaller crystals were found to stay in suspension longer, with the smallest size used (0.5 mm diameter) staying in suspension for the length of the plume. In contrast the largest size crystal (4.5 mm diameter) precipitated out of the plume very rapidly. In general, it was found there was a delay before concentrations of the frazil ice crystals increased significantly, during which time the temperature difference between the crystal surface and the plume water rose. This approximately equalled the degree of supercooling found in the previous applications of the Plume Model. Here the degree of supercooling was dependent on the ease of heat transfer between the water and the crystals. Larger crystals required larger amounts of supercooling to drive crystal growth, as the total mass of crystals had proportionally less edge surface area than the same mass of smaller crystals. This feature of the system also tended to make the concentration of frazil ice crystals oscillate with distance along the plume, with the amount of oscillation dependent on the size of the crystal.

The precipitation rate tended to differ more than the concentration, as it was driven by the dynamics of the plume. For larger crystals the peak precipitation rates coincided with concentration maxima, whereas for smaller crystals

peak precipitation was delayed until the concentration started to fall. This was because of the ease with which the crystals were held in suspension, so the smaller crystals were only able to precipitate out when the plume velocity fell and the plume approached neutral buoyancy.

Three basic modes of behaviour were found for the model. Below a certain crystal size all the crystals were held in suspension and the plume remained buoyant for the length of the ice shelf. If crystals were larger than a second critical size they precipitated out rapidly, leaving no seed crystals in the plume. Both critical sizes were found to be dependent on the parameters chosen for the thermal response and the gravitational response of the crystals in the plume. Any crystals in the range between the two critical values gave a broadly similar picture of basal accumulation although rates did vary. Increasing either the radius or the thickness produced similar results: a slowing of the thermal response and an increase in the drift velocity, which consequently led to an increase in the amplitude of the oscillations in ice crystal concentration.

Jenkins and Bombosch concluded that the addition of frazil ice to the ISW plume had two effects, one thermodynamic and the second dynamic. The suspended ice crystals provided a much greater surface on which freezing could take place, so supercooled water in the plume was converted to ice more efficiently. This resulted in lower levels of supercooling than in the model without frazil ice, making direct freezing to the ice shelf of minor importance. They also suggested that the levels of supercooling at the ice shelf-ocean interface were still overestimated in this model. This was because in using a depth integrated plume the heat fluxes were calculated from a water temperature in the middle of the plume and not adjacent to the ice shelf. The amount by which the level of supercooling was overestimated was equivalent to the change in the in situ freezing temperature over the half depth of the plume.

The dynamic effect was from the ice crystals in suspension giving the plume extra buoyancy. This provided positive feedback between the plume and the ice concentration. If the concentration grew the deposition of crystals became less likely as the plume gained momentum. However, once precipitation commenced the loss of buoyancy caused the plume to decelerate, increasing the rate of deposition. Also possible density inversions appeared in the water column. By the time the ice front was reached the water was 0.04 PSU more saline and 0.17°C colder than the underlying water, but stability was maintained by the presence of the suspended ice crystals.

Other important points which Jenkins and Bombosch mentioned were the use of a single size of ice crystals leading to oscillations in the crystal concentration, and the use of a possibly overly simplified crystal deposition scheme. They finally concluded that including frazil ice in the plume offers an attractive solution to the problem of how the thick layer of marine ice found on the base of some Antarctic ice shelves may have formed. This occurs because of the positive feedback mechanism, where the plume velocity slowed because of loss of buoyancy due to precipitation, causing an increase in the rate of deposition. This then continued till the ice crystal concentration drops and the velocity was able to increase.

Bombosch and Jenkins [1995] highlighted this phenomenon of the model when they applied the model to twelve plume paths beneath the Filchner-Ronne Ice Shelf, with the aim of showing the localised intensive freezing. Three model runs were done for each of the paths with the frazil ice crystal size being varied (2 mm, 2.5 mm and 3 mm) between the runs.

For example, in the central Filchner-Ronne Ice Shelf four plume paths were modelled, one from the area of inflow of the Foundation Ice Stream, and three through the Doake Ice Rumples. From the flowline along the Foundation Ice Stream it was observed that the varying slope of the ice shelf base influenced the behaviour of the ISW plume, through the plume velocity in two ways. The upward component of the plume velocity determined how rapidly the ice concentration grew, while the forward component of the plume velocity determined where ice deposition was most intense.

Bombosch and Jenkins concluded that the model accounted for the location of thick deposits of marine ice on the base of the Filchner-Ronne Ice Shelf. Four regions of high basal accumulation were identified: near Cape Zumberge, near the Fowler Peninsula, downstream of the Henry Ice Rise, and on the eastern flank of Berkner Island. The first three of these are at the upstream end of the main bodies of marine ice identified beneath the Filchner-Ronne Ice Shelf by glaciological observations. Based on observations a zone of accumulation was also anticipated downstream of the Doake Ice Rumples, but this was not found by the model.

Direct freezing onto the ice shelf base was also observed in the model where glaciological evidence suggests it does not occur. It may, however, have previously been missed, as it is predicted to be only a thin layer on the base of the ice shelf. The most important conclusion of Bombosch and Jenkins [1995] is that the physics of frazil ice growth within a turbulent plume and deposition from the turbulent plume naturally leads to localised regions of intense accumulation.

2.3.4 Two-dimensional vertical overturning model

This model was first described by Hellmer and Olbers [1989], when it was used to model the ocean cavity under the Filchner Ice Shelf. The model was subsequently further developed and was used to describe channel flow beneath the Filchner-Ronne Ice Shelf south of Berkner Island [Hellmer and Olbers, 1991], flow under the Amery Ice Shelf [Hellmer and Jacobs, 1992], flow around Roosevelt Island in the Ross Ice Shelf [Hellmer and Jacobs, 1995], and most recently flow under Pine Island Glacier [Hellmer et al., 1998].

In the model [Hellmer and Olbers, 1989], henceforth labelled the HO Model, the large scale motion of an incompressible ocean under an ice shelf was described using Boussinesq and hydrostatic approximations to the momentum balance and the continuity equation. Then following Robin [1979], it was assumed the thermohaline circulation under the ice shelf was predominantly two-dimensional, with velocities parallel to the ice front less than the velocities perpendicular to the ice front. Hence the effects of Coriolis and across ice shelf gradients are ignored. Hellmer and Olbers were able to describe the dynamics

in terms of the vorticity equation :

$$\Psi_{zzt} + (v\Psi_{zz})_y + (w\Psi_{zz})_z = g\rho_y + A_H\Psi_{zzyy} + A_V\Psi_{zzzz} \tag{2.24}$$

where g is the acceleration due to gravity, ρ is the density, A_H and A_V are the horizontal and vertical diffusion coefficients. The horizontal and vertical velocities, v and w are related to the streamfunction (Ψ) by

$$v = \Psi_z \quad \text{and} \quad w = -\Psi_y. \tag{2.25}$$

In both these equations the subscripts represent the relevant partial derivatives.

The coupling to the thermohaline processes is via the density torque $g\rho_y$, where the density is calculated using a full equation of state for sea water. The thermohaline balances are described by the conservation equation:

$$X_t + (vX)_y + (wX)_z = K_H X_{yy} + K_V X_{zz} \tag{2.26}$$

where X represents either potential temperature, salinity or the passive tracers, and K_H and K_V are the horizontal and vertical diffusion coefficients. Convective adjustment is also applied to remove any static instabilities in the water column.

Boundary conditions were chosen for the vorticity equation, so that on solid boundaries the perpendicular and parallel velocities vanished, and at the open boundary the inflow and outflow was normal to the boundary. The boundary conditions for the thermohaline processes are assumed to be entirely advective at the open ice front boundary.

Hellmer and Olbers included the heat flux through the ice shelf in their heat balance equations at the ice shelf-ocean interface (Equation 2.2). This was done by assuming a linear temperature gradient through the ice shelf, and a temperature of -20°C at the ice shelf surface. The transfer coefficients were assumed to be constant in both the heat and salt flux balance equations.

At the ice front hydrographic observations collected from near the ice front were used to prescribe inflow temperatures and salinities.

Filchner Ice Shelf

In Hellmer and Olbers [1989] a transect under the Filchner Ice Shelf was modelled. The HO Model was configured with a 1100 m deep, flat sea floor below a constant slope ice shelf which had a draft ranging from 300 m to 900 m, over 620 km. The model was spun up over a period of ten model years, and it was found after running for 500 days that the model settled to a quasi-periodic state with a period of approximately 300 days.

The ocean circulation was dominated by a single circulation cell, which was generated by the different gradients in the potential density field. The cell transported water masses from the ice shelf edge toward the grounding line near the sea floor, where the new inflow first made contact with the ice shelf. The water then rose along the ice shelf base, where the strong gradients in the streamfunction indicated relatively high velocities. The high velocities then disappeared after the streamlines detached from the base at mid-range

depths, and the streamlines tended horizontally toward the open boundary. The detachment led to the evolution of a pair of counter rotating cells in the upper part of the water column. These dominated the circulation at shallower depths.

Interaction between the ice shelf and ocean was evident from the distribution of melting and freezing along the ice shelf base. Strong melting occurred near the grounding line at a rate of $\sim$1.5 ma^{-1}. Accretion from freezing did not occur until approximately 490 km from the grounding line. Melting occurred again close to the front.

Qualitative agreement was available by comparing the outflow from the model with observations, this was generally found to be good. Comparison of the melt and accumulation rates from the model, with ice shelf mass balance calculations and results from other numerical models were also made. As many of the observational mass balance calculations were not from the Filchner Ice Shelf, only basic comparisons were made, however nearly all the model rates fitted within the range of the mass balance calculations.

To test the sensitivity of the model, several independent changes were made to the boundary conditions. The first was to introduce seasonal variation in the temperature and salinity profiles at the open boundary. This produced no change in the upper circulation, however, below 750 m several circulation cells developed. The second change was to vary the temperature and salinity by increasing and decreasing them by 0.02°C and 0.02 PSU, respectively. With an increase in temperature and salinity the circulation was dominated by three cells with different orientations, whereas if the temperature and salinity were decreased, the circulation consisted of a single cell. These variations were generated by the different temperatures of water interacting with the ice shelf near the grounding line. The third change was to introduce a sloping bottom to the topography that ran parallel to the ice shelf. Here the circulation was also dominated by a single cell. With the small separation between the fresh and salty water in the channel regime, the density gradient steepened and increased the strength of the circulation when compared with the standard model.

Hellmer and Olbers concluded that the model illustrated the importance of processes at the ice shelf-ocean boundary. At the ice front the model reproduced the two minimum temperature layers which have been observed in the Filchner Depression. It also illustrated that the production of ISW could change by as much as 40% due to moderate variations in the characteristics of WSW, indicating the sensitivity of the subice shelf ocean to climate change.

Filchner-Ronne Ice Shelf

In Hellmer and Olbers [1991] the model of the Filchner Ice Shelf was extended to include communication with the Ronne Ice Shelf, via a channel south of Berkner Island. To achieve this Hellmer and Olbers modified the model, so it represented a channel under the ice shelf and had an open boundary at each end. The streamfunction at the bottom of the cavity was fixed at zero, and at the ice shelf-ocean interface a time varying function was used. The time varying function represented the flow through the channel and was solved at each time

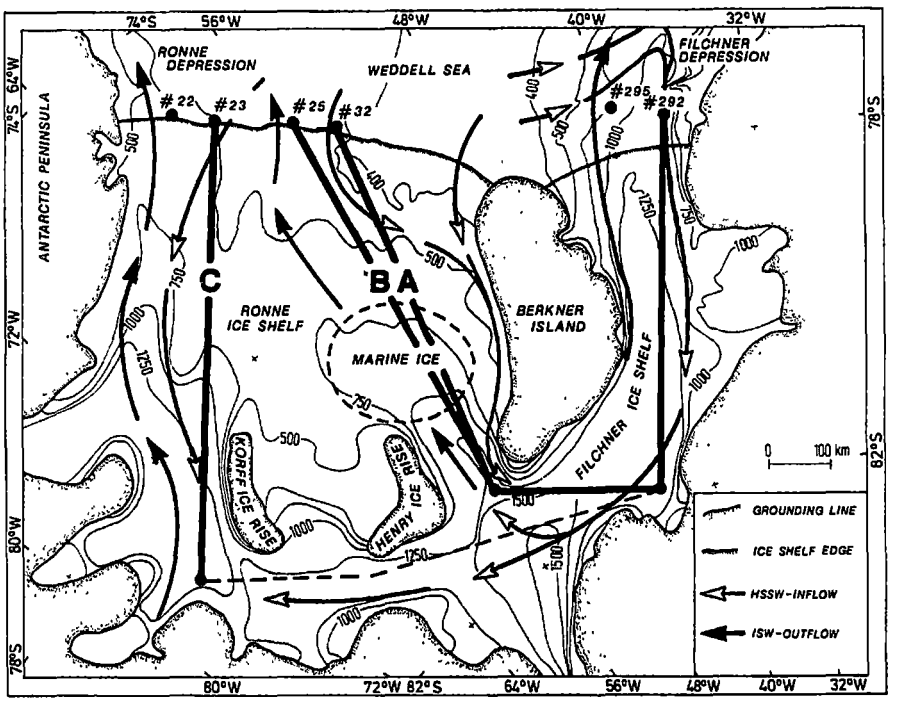

Figure 2.2: Map of bottom topography beneath Filchner-Ronne Ice Shelf in metres below sea level, after Pozdeyev and Kurinin [1987], including possible paths of HSSW and ISW, the area of accumulated marine ice, and the sections labelled with A, B, and C supplying the boundary conditions [Figure 1, Hellmer and Olbers, 1991].

step. The solution of the top boundary condition is similar to the problem of solving barotropic flow in a three-dimensional primitive equation model. The use of such a time varying equation allowed for the possibility of flow through the channel.

Hellmer and Olbers ran the model along three vertical sections (see Figure 2.2). In all three sections the topography under the Filchner Ice Shelf was the same as used in Hellmer and Olbers [1989]. Under the Ronne Ice Shelf the ice shelf draft was the same for all three sections. However, the bottom topography under the Ronne Ice Shelf was varied depending on which path was being modelled.

On Path A, the circulation under the Filchner Ice Shelf was dominated by a single circulation cell similar to that observed in Hellmer and Olbers [1989]. The cell transported relatively warm, salty water near the bottom into the ocean cavity. This flow diverged where the ice shelf reached maximum draft. Approximately a quarter of the flow penetrated under the Ronne Ice Shelf to support circulation there. The remainder of the flow turned back, and ascended close to the ice shelf, similar in behaviour to that modelled in Hellmer and Olbers [1989].

Under the Ronne Ice Shelf inflow of shelf water at the ice front was absent,

so outflow of melt-water occupied the entire water column at the ice front. The source of the water was flow from the ocean cavity under the Filchner Ice Shelf. Hellmer and Olbers [1991] recorded closed streamlines which indicated possible recirculation of water parcels in the cavity. The Ronne Ice Shelf cavity circulation cell formed an 'ice pump' mechanism. This makes the Ronne Ice Shelf cavity colder, with less melting (maximum rate $\sim$1.5 ma^{-1}). However, comparison of the melt-water plumes leaving the two cavities showed the Ronne Ice Shelf plume was comparatively warmer than the plume from the Filchner Ice Shelf. The difference being caused by the different depths of separation of the plumes from the ice shelves.

The circulation patterns along Path B were generally similar to those of Path A. The inflow into the Filchner Ice Shelf and the outflow from the Ronne Ice Shelf both increased by approximately 30% compared with Path A, additionally the circulation cell under the Ronne Ice Shelf was weaker than in the Path A experiment.

To avoid the elongation of the model domain along Path C, Hellmer and Olbers assumed ice shelf-ocean interaction only occurred along the solid lines shown in Figure 2.2, and that the water masses were unmodified along the dotted section of the path. With the deeper shelf at the Ronne Ice Shelf edge, and an initially more saline cavity, changes in the circulation pattern beneath the ice shelves occurred. Both the Ronne and Filchner Ice Shelf cavities had circulation cells similar to those along the other paths, but with the strength in the Filchner Ice Shelf cell reduced, and the Ronne Ice Shelf circulation increased by a factor of four. The Ronne Ice Shelf cell then transported HSSW into the lower part of the cavity, which became warmer and saltier than along the other paths resulting in a higher melt rate ($\sim$4 ma^{-1}).

From Hellmer and Olbers [1989] it was clear the circulation was dependent on the density profile at the open boundary. In Hellmer and Olbers [1991] the salinity profile was changed at the inflow of the Ronne Ice Shelf to generate changes in the density profile. For Path C it was found an inflow salinity of 34.67 was critical. If the salinity was below this the bottom flow would reverse, with water from the Filchner Ice Shelf entering the Ronne Ice Shelf cavity. Any shelf water flowing under the Ronne Ice Shelf ascended toward the ice shelf base before the deepest part was reached, this led to a decrease in the melt rate. The circulation pattern under the Filchner Ice Shelf remained constant and was independent of the salinity of the inflow to the Ronne Ice Shelf cavity.

Hellmer and Olbers [1991] concluded the model results emphasised the importance of the area south of Berkner Island. Here the direction of the flow was dependent on the salinity profiles at the ice shelf boundaries, and the topography of the model domain under the Ronne Ice Shelf. The major differences in the results between the models presented in Hellmer and Olbers [1989] and Hellmer and Olbers [1991], was the increased circulation and the higher ablation rates beneath the Filchner Ice Shelf. As with the earlier version of the HO Model, the circulation was driven by the density in the cavity, which was dependent on the inflow of salty shelf water, but dominated by the heat and salt fluxes at the ice shelf-ocean interface.

For Paths A and B the development of the closed cell circulation under the Ronne Ice Shelf was dependent on the depth at the ice front, and not on the salinity of HSSW. In contrast the circulation along Path C was mainly influenced by the salinity of the inflow water, as a deeper continental shelf existed at the Ronne Ice Shelf edge on Path C.

The important improvement identified by Hellmer and Olbers [1991] was the enhanced ventilation of the ice shelf cavities under the Filchner-Ronne Ice Shelf by considering the flow south of Berkner Island.

Amery Ice Shelf

Hellmer and Jacobs [1992] applied the HO Model to several different cavity configurations representing the Amery Ice Shelf. Starting with ice thickness data from Budd et al. [1982], and a flat bottomed ocean. The affects of a gentle (0.1%) and a steep (0.2%) basal slope near the grounding line were considered on the circulation in the cavity. One objective of Hellmer and Jacobs was to model the formation of a 158 m thick marine ice layer observed by Morgan [1972] on the bottom of the ice shelf at the drill hole site known as G1 (see Section 3.2 for more detail).

With a gentle basal slope, a flow towards the grounding line of relatively warm shelf water near the sea floor was seen in the model. In the area where the water column was less than 100 m thick, the inflow water was cooled to less than the surface freezing temperature. This transformation from shelf water to ISW, without contact with the ice shelf occurred because of melting at the ice shelf-ocean interface which in the shallow part of the cavity was able to cool the whole water column.

The ISW then stayed in contact with the ice shelf all the way to the ice front, because melting at the grounding line ($\sim$1 ma^{-1}) increased the buoyancy of the ISW. With this configuration of the model no marine ice layer was observed at G1, as the transition from melting to freezing occurred between G1 and the ice front.

With a steep basal slope near the grounding line, the model results showed greater melt in the 60 km nearest the grounding line, however, this was offset by less melting near the centre of the ice shelf. A slight shift in the position and lengthening of the accumulation zone were also noticed. Overall there was only a small variation in the net ice mass balance compared with the scenario of a gentle basal slope near the grounding line. No change was noticed in the circulation of the ocean cavity as the density gradient remained largely unchanged. Hellmer and Jacobs concluded that the basal slope was of importance to the regional rate of accumulation, but tended to have no net impact on the larger scale circulation.

By introducing a discontinuous ice thickness, Hellmer and Jacobs attempted to evaluate the effects of upwelling through a sudden change in the pressure along the ice shelf-ocean interface. They found that abrupt thickness discontinuities caused little or no change in melt rates near the grounding line or the ice front, but the freezing zone shifted towards the grounding zone when steep steps were placed in these areas. As varying the ice shelf thickness caused little

effect, Hellmer and Jacobs then considered the effects of various ocean floor topographies. They first considered a concave ocean floor with depths of 800 m near the front, 850 m at the grounding line, and 1000 m in between. Here the streamfunction showed that the concave topography created a partially closed circulation which intensified the exchange of inflow and outflow characteristics, especially near the mouth of the ocean cavity. Overall comparable results were found between the concave and flat ocean floors, for both gentle and steep ice shelf draft slopes near the grounding line.

The introduction of a variable depth sill at different locations in the sea floor had the effect of reducing the circulation strength as sill height increased. However, if the blocking by the bottom topography was sufficiently strong a separate circulation cell developed between the grounding line and the sill. This had the effect of cooling the cavity between the grounding line and sill towards the in situ freezing point at the top of the sill. This occurred because the only sensible heat remaining for melting was from the freezing point pressure dependence. This was sufficient to allow only a small melt-water flux into the upper layer. The maximum amount of melting occurred near the crest of the sill, where the inflow of shelf water was closest to the ice. It appeared the sill acted as a thermodynamic barrier with a density gradient between the crest and ice front driving circulation near the cavity mouth. The strength of the overall circulation was reduced by 80% compared with the concave ocean floor scenario, but accumulation did not change. Hellmer and Jacobs suggested these simulations showed the overall thermohaline circulation was sensitive to variations in the ocean floor topography.

In an attempt to portray the three-dimensional flow under the Amery Ice Shelf, Hellmer and Jacobs [1992] followed the channel flow model presented by Hellmer and Olbers [1991]. The channel was configured with steep sloping basal ice in two cavities, joined by a 120 km section which traversed the grounding line of the Amery Ice Shelf. One cavity had a flat ocean floor and the other a gently sloping ocean floor. For convenience these will respectively be called Cavities A and B. At each end of the cavity the model was forced by different hydrographic casts.

Hellmer and Jacobs found more than half of Cavity A was occupied by shelf water with a temperature greater than -1.9°C, whereas the temperature of most of the water in Cavity B was less than -2.0°C. The thickness of the warmer water decreased as it flowed toward the grounding line, where melt of up to 2.7 ma^{-1} initiated two buoyant plumes with different characteristics. In Cavity A heat derived from mixing caused higher melt rates, and a plume which left the cavity at between 220 m and 480 m depth (the ice shelf was 220 m thick at the front of both cavities). Less melting was found in Cavity B, as it was completely filled by supercooled water, and the accumulation zone began $\sim$100 km from the ice front, where a cooler plume covered the upper 300 m of the water column (The ISW plume was also apparent in hydrographic stations taken near the front of the Amery Ice Shelf between 1965 and 1987 [Hellmer and Jacobs, 1992]).

There was a strong correlation between the temperature fields and the melt rates in the two cavities. The amount of ice melted was high in both cavities,

with an increase of ~50% for Cavity A over the previous flat bottomed simulations. This was probably caused by increased ventilation of the cavity. The results of the channel simulation were very dependent on grounding line depth and unrestrained flow in that region.

The temperature and salinity characteristics of the water in both cavities tended to fall along single mixing lines between the source shelf waters and the water mass formed at the grounding line. Temperature and salinity values common to both cavities only occurred near the grounding line. In the remainder of the domain, Cavity A was warmer than Cavity B.

Hellmer and Jacobs [1992] concluded ice shelf mass loss could be accounted for by any flat sea floor or channel flow model. None of the model simulations reproduced the marine ice layer observed at G1, the highest net accumulation was ~10 m from the channel flow simulations. Given the high sensitivity of the thermohaline circulation to the cavity shape, Hellmer and Jacobs may have been able to select a cavity configuration which could have given better agreement with the observations. It is also possible the reproduction of the marine ice layer at G1, may not have been achievable with this model, as the formation of the marine ice may have been caused by subgrid scale local circulation effects. Overall Hellmer and Jacobs concluded the model results were consistent with results from the Filchner-Ronne Ice Shelf, and the model had reasonable agreement with the ocean station data in Prydz Bay.

Ross Ice Shelf

In Hellmer and Jacobs [1995] seasonally varying temperature and salinity boundary conditions were used to force several model domains, which represented the ocean cavity under the eastern part of the Ross Ice Shelf, in the vicinity of Roosevelt Island. The governing equations of the model were modified slightly from the earlier models. The change was to make the heat and salt transfer coefficients, used in calculating heat and salt fluxes at the ice shelf-ocean interface, dependent on the ocean velocity at the interface.

Several paths of different water column thicknesses and lengths were modelled. Cavity lengths of 460 km, 600 km, and 800 km were used, with water column thicknesses of 160 m, 200 m, and 240 m. To minimise the difference between cavity configurations due to pressure effects on the freezing point of water, the water column thicknesses were varied by moving the sea floor and keeping the ice shelf draft constant. Each model was integrated for five years before seasonal forcing was introduced for the remaining five years of the integration.

Hellmer and Jacobs described the results for the 800 km long, 200 m thick cavity in detail, as they indicated this was representative of the behaviour in all the cavities. Here the external density gradient drove a flow through the ocean cavity from west to east. The net drift was accompanied by three intermittent counter flows. One was a melt-water plume rising along the western ice shelf base. In the eastern cavity a deep melt water core occupied different levels of the water column at different times of the year. The annual cycle in the ocean boundary forcing appeared positively correlated with the interior salinities and

velocities, and did not change with water column thickness. However, in thinner cavities the water column was more homogeneous due to stronger mixing between bottom inflow and waters modified by interaction with the ice shelf. This enhanced mixing also lowered the interior temperature of the cavity, with the changes weakening the current through the cavity.

The ocean cavity was modified to investigate the affects of a shallow water column near the Siple Coast grounding line. To achieve this the interior 150 km of the 800 km cavity was reduced to a water column thickness of 80 m. This was done by increasing the ice shelf draft. Major changes occurred in the western cavity, with the appearance of a relatively strong near bottom return flow. This was due to a reversal in the density gradient in the lower water column. The shallower interior was fresher. This occurred partly because the shelf water was diluted at the entrance of the thinner cavity, but also because ice shelf-ocean interaction at the deeper ice shelf base was enhanced by the deepening of the ice shelf draft to thin the water column. At the eastern ice front melt-laden outflow dominated year round, preventing fresher and warmer shelf water from flowing into the cavity as part of a shallow circulation pattern. Hellmer and Jacobs commented that some of the changes observed in the long, narrow cavity may have been artifacts of the cavity configuration where water could be unrealistically forced through the narrow portion of the ocean cavity.

Comparison of the model output with in situ measurements suggested that the modelled outflow reproduced the basic periodicity of the seasonal current flow. The maximum current velocity was best modelled by the shortest and deepest cavity, but the period of the flow was better matched by the longest cavity. Increasing the range of the annual variability of the salinity field improved the estimation of the maximum velocity.

To evaluate the impact of substantially different shelf water characteristics on basal mass fluxes, Hellmer and Jacobs assumed that over a 100 year period Modified Circumpolar Deep Water might gradually replace current shelf water. For the 100 year simulation ice shelf equilibrium was not assumed, 'icy' grid points were converted to 'wet' grid points when an appropriate amount of melting occurred. For Year 100 the average melt rate increased from 0.18 ma^{-1} to 1.38 ma^{-1} with only a temperature increase included in the forcing. This melt rate is similar to that predicted by Jenkins [1991] for a cavity under the Ronne Ice Shelf filled with Modified Weddell Deep Water. With both temperature and salinity increases the melt rate in Year 100 was 0.98 ma^{-1}, mainly due to a 25% reduction in cavity throughflow. While ice shelf advance would replace some portion of melted ice from upstream, negative feedbacks on the density caused by freshening would retard increases in melting due to warmer temperatures.

Hellmer and Jacobs concluded the model results agreed in several respects with time series observations off the Ross Ice Shelf. For most of the simulated cavity configurations, seasonal and interannual shelf water variability increased the average melt rate above the static environment. Long term trends have the potential to change the ocean circulation and basal mass fluxes over longer time scales, but to a lesser extent they also alter the ocean cavity's configuration.

Pine Island Glacier

Recently, the HO Model has also been applied to the Pine Island Glacier by Hellmer et al. [1998]. For a profile of the ice shelf, they used the radio echo sounding profile of Crabtree and Doake [1982]. The sea bed was assumed to be parallel for most of the cavity to the base of Pine Island Glacier with a water column thickness of 980 m. Near the grounding line the water column was reduced to 160 m

In this application of the model the flux calculations at the ice shelf-ocean interface were modified, as the earlier formulations in the two-dimensional model appeared inadequate in the high melt regime found under the Pine Island Glacier. Three modifications were made.

The first was to the transfer coefficients, γ_T and γ_S, these were modified from being constant to follow the parameterisation introduced by Jenkins [1991]. In contrast to Jenkins model the velocity was not used in directly calculating the transfer coefficient, but instead the coefficient was taken to be dependent on a friction velocity which was included in the heat and salt flux balance equations.

The second modification was to the heat flux through the ice shelf. In previous models this was calculated by assuming the temperature gradient through the ice shelf was linear. In this study, Hellmer et al. used an alternative treatment in areas where Pine Island Glacier was melting. This method, based on the work of Wexler [1960], makes the heat flux through the ice shelf proportional to both the melt rate and the temperature difference, i.e.,

$$Q_{IS} = -\rho_i C_i m \Delta T, \tag{2.27}$$

where ρ_i is a typical density for ice, C_i is the heat capacity of ice, m is the melt rate, and ΔT is the temperature difference through the ice shelf. This formulation gives a heat flux into the ice shelf which is an order of magnitude larger than that found by assuming the temperature gradient is linear. In the areas where freezing occurs, if indeed it was found under the Pine Island Glacier, it is unclear how the heat flux into the ice shelf has been parameterised, although it would be expected that there would be little heat flux into the ice shelf in freezing areas.

The third modification was to the heat and salt flux equations into the top ocean model layer. The equations used were:

$$K_v T_z = \frac{Q_T}{\rho_w C_w} - \frac{\rho_i}{\rho_w} m (T_b - T), \tag{2.28}$$

$$K_v S_z = \frac{Q_S}{\rho_w} - \frac{\rho_i}{\rho_w} m (S_b - S), \tag{2.29}$$

where the notation follows that of Equations 2.2 and 2.3, and K_v is the vertical diffusivity, the z subscript denotes the vertical gradient of temperature or salinity in the ocean model, Q_T and Q_S are respectively the heat and salt flux out of the ocean model, and ρ_w is a typical density for water. Except for the final terms on the right hand side of each equation, these are similar to those used in most models for flux out of the top model layer. The extra terms added by

Hellmer et al. represent the effect of mixing the melt-water into the ocean. This extra mixing is significant for the high melt rates found beneath Pine Island Glacier.

Hellmer et al. found Circumpolar Deep Water (CDW) flowed into the cavity, with a velocity of $\sim$2 cms^{-1}, at depths below 820 m. This increased to $\sim$5 cms^{-1} further into the domain. In the outflow the mean velocity was 1 cms^{-1}. Most of the upwelling occurred in a band 15-30 km from the grounding line, while the flow closer to the grounding line was weak.

The outflow temperatures were warmer than the surface freezing temperature indicating that no freezing occurred under the glacier tongue. The mean melt rate was 12.5 ma^{-1}, with the peak melt rate $>$ 25 ma^{-1} at 20-50 km from the grounding line.

In contrast to other studies [e.g., Jenkins, 1991; Hellmer and Jacobs, 1995], the melt rate did not correlate with the basal gradient. In this study the melting extended downstream of the steepest basal gradient. This is caused by the dependence of the heat and salt transfer coefficients on the horizontal, rather than the vertical velocity.

Comparison with hydrographic sections off the ice front showed that the model outflow reproduced a range of observed values, with clusters of observations in θ/S space. The clusters reflected the stepped structure of the temperature and salinity profiles.

Hellmer et al. also conducted a sensitivity study on the affect of the sea bed shape beneath the glacier, particularly near the grounding line. They found the melt rates and ocean circulation did not change significantly when the sea bed was reduced to a depth of 1300 m.

They also examined the affect of increasing the temperature of the inflowing water mass. This induced additional melt, to a level suggested by Hellmer et al. as unreasonable. The inflowing water mass (CDW) was also replaced with low salinity shelf water. This dramatically reduced the amount of melt, however, no freezing was observed.

2.3.5 Three-dimensional model

The most important physics missing from both the Plume Model, as implemented by Jenkins [1991], and HO Models, is the effect of the Earth's rotation on the ocean dynamics. It is also highly desirable to remove the constraint of planar circulation, which generally forces inflow at the bottom of the cavity and outflow at the top of the cavity. To achieve this it is necessary to use a three-dimensional ocean model.

The first use of a three-dimensional model in studying ocean cavities was by Determann and Gerdes [1994], who used a three-dimensional, primitive equation ocean model based on the work of Bryan [1969] and Cox [1984]. This is the model utilised in later chapters of this thesis, and full details of the current model are presented in Chapter 4.

As part of their model development Determann and Gerdes made significant changes to the ice shelf-ocean boundary conditions. They noted the small magnitude of the heat flux through the ice shelf, if a linear temperature gradient

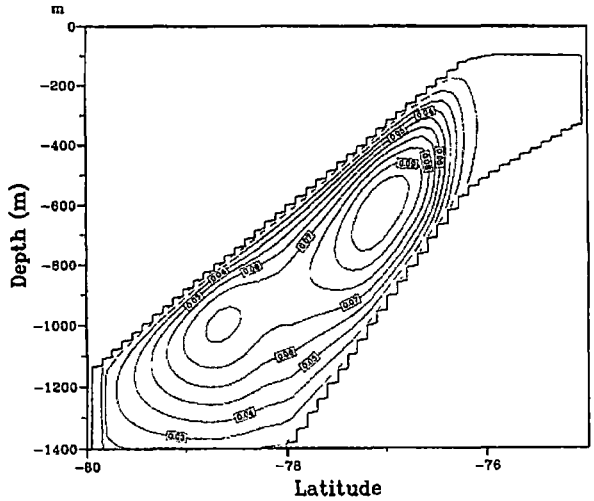

Figure 2.3: Streamfunction of the zonally integrated mass transport for a model domain similar in shape and extent to the Ronne Ice Shelf. Contour Interval 0.2 Sv [Fig. 3b, Determann and Gerdes, 1994]

was assumed. This motivated them to remove the heat flux through the ice shelf from their parameterisation of the boundary conditions.

Their other change was to assume the salinity at the ice-ocean interface was sufficiently similar to their top model layer that the salt flux balance (Equation 2.3) could be ignored. The melt rate at the ice-ocean interface was then found from the heat flux balance alone, using the top model layer salinity to determine the in situ freezing temperature. The heat and freshwater flux into the ocean were then calculated from the melt rate.

The model was modified to allow for the use of a σ-layer system for the vertical coordinate by Gerdes [1993]. The advantage of the σ-layer system is that it allows the precise specification of kinematic boundary conditions at the ice shelf base and the sea bed, as these are both coordinate surfaces. The thermodynamic boundary conditions at the ice shelf-ocean interface were specified in the manner outlined in Section 2.1. Forcing was provided by hydrographic conditions at the ice front, which were characteristic of the Southern Weddell Sea. Here the model had an open boundary which the treatment of the boundary conditions distinguished between inflow and outflow. In the case of inflow, a relaxation with a time scale of 100 days was used to adjust model temperatures and salinities to those specified by the boundary forcing. Outflowing currents could leave the cavity without being reflected at the boundary.

General aspects of the circulation were investigated using an idealised domain which was representative of the central part of the Ronne Ice Shelf, but with ice thickness and sea bed depth which varied only meridionally. The outer portion of the ice shelf had a shallow and gently inclined base, with a steeper basal slope near the grounding line. This mimicked the effect of the large ice draft gradients generally seen in the thicker parts of ice shelves. The sea bed deepened inland, giving a maximum water column thickness under the cen-

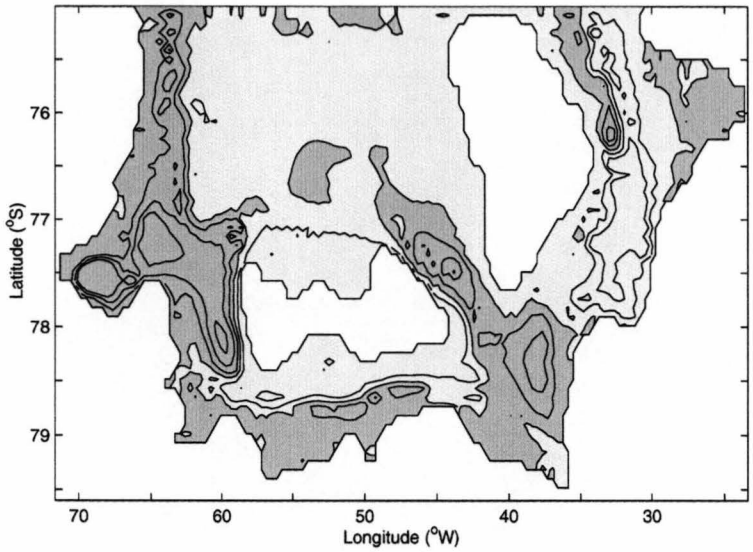

Figure 2.4: Streamfunction of the vertically integrated mass transport predicted for the circulation beneath the Filchner-Ronne Ice Shelf. A barotropic flow of 1 Sv is prescribed across the depression while the same transport is assumed to leave the Filchner depression. This result is representative for all experiments although they use different open-ocean boundary conditions. Robust features of the circulation are cyclonic gyres in basins and depressions (dark grey) and anticyclonic circulation around submarine plateaus and ice rises (light gray). The contour interval is 0.4 Sv and the zero contour is at the boundary of the two colours. After Figure 1, in Determann et al. [1994].

tral ice shelf. As a result of the weakly stratified water column vertical shear was found to be small, so that the general circulation was well described by the streamfunction for the vertically integrated mass transport. This showed a strong cyclonic gyre, centred on the latitude at which the northward gradient of the water column thickness changed sign. The gyre was a manifestation of the conservation of angular momentum, which in the absence of external torques, constrains a steady barotropic flow to follow contours of f/H (f being the Coriolis parameter and H the water column thickness). The strong meridional gradients of surface and bottom topography provided the dominant controls on f/H, so the barotropic flow was almost entirely zonal, except in frictional layers at the meridional boundaries. Meridional overturning as given by the zonally integrated mass transport, which is shown in Figure 2.3, was weak in comparison with that simulated by the two-dimensional model [e.g., Hellmer and Olbers, 1989]. 'Ice pumping' occurred predominantly in the horizontal plane, with melting being generated by the descending currents in the east, and freezing by the ascending currents in the west. The region next to the ice front was very inactive, suggesting a largely internal circulation with little heat exchange across the open boundary.

Determann et al. [1994] applied the model to the actual topography of the Filchner-Ronne Ice Shelf. Along the ice front the model was forced by hydro-

graphic observations collected by Gammelsrød [1994]. Once again, the vertically integrated mass transport evolved in a pattern that was guided by the water column thickness distribution. Cyclonic gyres filled the deeper basins under the ice shelf while anticyclonic flow was found around ice rises. Little flow occurred across the open boundary, unless it was specified as part of the boundary condition. Figure 2.4 shows the results of a simulation in which inflows and outflows of 1 Sv were prescribed in the Ronne and Filchner depressions, with no flow across other parts of the open boundary. In the two depressions the circulation extended further south from the ice front, but there was no direct communication between the two depressions. The circulation around the islands in the southern part of the ice shelf produced strong melting in the west where warmer water was forced down along a deepening ice shelf base, and rapid freezing in the east where colder water ascended a shallowing base. Freezing rates computed at the north-eastern corner of the islands, in the order of 1 ma^{-1} to 3 ma^{-1}, were consistent with those derived by Determann [1991] based on the assumption of a balanced glaciological budget.

2.3.6 Three-dimensional model including the open ocean

Grosfeld et al. [1995, 1997] extended the three-dimensional model discussed above to include part of the open ocean in front of the ice shelf. The domain they chose had an ice shelf cavity similar to the idealised cavity used by Determann and Gerdes [1994]. This was connected to an open ocean which comprised two thirds of the domain and included a continental shelf and the southern part of an abyssal plain. It was designed to approximate the bathymetry of the Weddell Sea. The major modifications involved in this extension of the model are discussed in Chapter 7, where the model is applied to a domain representing the ocean cavity under the Amery Ice Shelf and Prydz Bay. This extension of the domain removed the need for boundary conditions at the ice front. Instead the ice front now forms a sharp step in the water column thickness inside the model domain. In order to avoid the need for steeply sloping σ surfaces at this step, additional coordinate surfaces were introduced into the upper part of the open ocean domain. Beneath the ice shelf, surface boundary conditions were specified as in Determann and Gerdes [1994] while the open ocean was driven by wind stress and thermohaline forcing, the latter being simulated with a one-dimensional, thermodynamic sea ice model. On the northern boundary of the open ocean part of the domain, potential temperature and salinity were restored to hydrographic data.

As with the earlier three-dimensional model results communication across the ice front was very small (Figure 2.5a). Neither the wind driven circulation at the open ocean, nor the thermohaline circulation in the cavity crossed the ice front. The abrupt change in the water column thickness created a boundary layer, characterised by an anticyclonic circulation which allowed only a limited exchange of water masses at a few points along the ice front. Where ISW could leave the cavity, upwelling of this water mass produced extensive surface freezing. In further experiments two submarine depressions were introduced under the ice shelf idealising the Ronne and Filchner depressions (Figure 2.5b).

a)

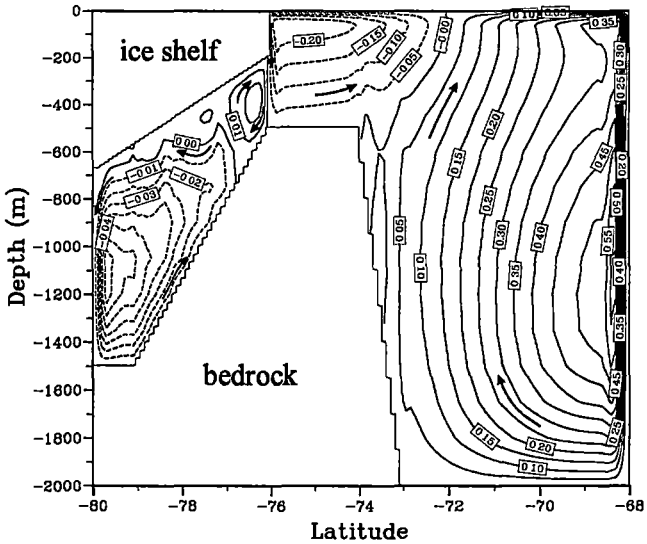

b)

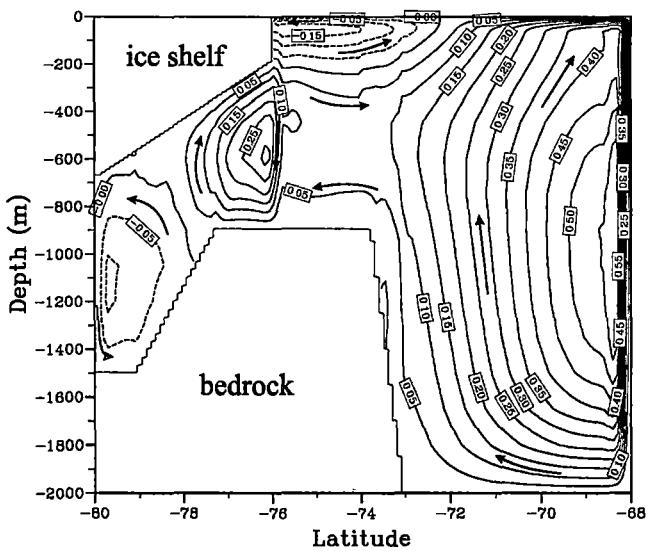

Figure 2.5: Streamfunction of the zonally integrated mass transport for two versions of the extended three-dimensional model: a) contains an open ocean section similar to the southern Weddell Sea, and b) also contains two depressions in the ocean floor which are shown in the figure. Between the two depressions in Figure b the topography is as for Figure a. [Figures 6c and 7d, Grosfeld et al., 1997].

The inclined walls of these depressions had an important affect on the resulting circulation. If they had been vertical, f/H contours would have ended at the ice shelf front, because of the step in water column thickness, and created a barrier to barotropic currents. However, in this case f/H contours crossed the ice front with only a small lateral displacement. The barotropic mode could then follow these contours, leading to higher exchange across the ice front (Figure 2.5).

In addition to the wind driven gyre of the open ocean and to the inner circulation, three extra horizontal circulation cells evolved in the ice front area ($\sim$76°S). Two of the cells transported about 0.3 Sv within each depression and reached about 50 km from the ice front. A third cell of about the same magnitude evolved around the submarine plateau, which was situated between the depressions. Heat, salt and momentum could be exchanged between these gyres by diffusion across the fronts separating them. In this way some heat from the open ocean could be transported to the grounding line, albeit less effectively than if it were advected there by the mean circulation.

In Grosfeld and Gerdes [1998] the model was applied to the area of the Filchner Trough, which lies both under and in front of the Filchner Ice Shelf. The focus of the paper was to explore the impact of two different climate change scenarios: the impact of warmer water accessing the cavity under the ice shelf, and the impact of reduced HSSW formation near the Filchner Ice Shelf.

Both climate impact scenarios were compared with a simulation of the present day. In the present day run, Grosfeld and Gerdes found the circulation system was mainly horizontal, with the ice shelf boundary blocking flow across the ice front. The main gyre which formed in the Filchner Trough to the north of the ice shelf did extend a small way under the ice shelf. The flow across the ice shelf was approximately 0.5 Sv and entered along the Coates Land coast, and had a northward outflow along the east coast of Berkner Island.

To simulate warmer waters in the model domain the water temperature was increased by 0.6°C to represent a change of water mass to Modified Warm Deep Water, a water mass found on the southern Weddell Sea shelf. This change decreased the strength of the main circulation gyre outside the ice shelf, while the circulation under the ice shelf remained the same. However, the deep cavity under the ice shelf was now ventilated with waters 0.05°C warmer than in the present day run. This increased the melt rates under the ice shelf, which led to outflowing ISW being warmer and fresher than in the present day. Grosfeld and Gerdes suggest this change in ISW properties could influence the water masses in the Weddell Sea, in particular, modifying deep and bottom water mass formation.

To study the impact of HSSW on the circulation, Grosfeld and Gerdes stopped the HSSW formation in the model domain after the model had reached a steady state. Again the strength of the main gyre outside the ice shelf decreased and its influence under the ice shelf also decreased. The gyre only penetrated into the shallower parts of the ocean cavity. This in turn reduced the outflow of ISW, and affected the properties of the outflowing ISW. The ISW was colder and fresher, and helped establish a vertical 'ice pump' between the base of the ice shelf and the formation of sea ice in front of the ice shelf.

Table 2.1: Summary of ocean cavity modelling studies by ice shelf.

Ice Shelf	Model	Reference	Page
Amery	HO Model	Hellmer & Jacobs [1992]	26
Filchner	HO Model	Hellmer & Olbers [1989]	22
	3-dimensional	Grosfeld & Gerdes [1998]	36
Filchner-Ronne	HO Model	Hellmer & Olbers [1991]	23
	3-dimensional	Determann et al. [1994]	33
		Gerdes et al. [1998]	33
	Plume with frazil	Bombosch & Jenkins [1995]	21
Pine Island	HO Model	Hellmer et al. [1998]	30
Ronne	Plume	Jenkins [1991]	12
		Nicholls & Jenkins [1993]	15
Ross	Plume	MacAyeal [1985b]	11
	Tidally forced	Scheduikat & Olbers [1990]	8
	HO Model	Hellmer & Jacobs [1995]	28
Theoretical	Analytical	Nøst & Foldvik [1994]	10
or idealised	Plume	Lane-Serff [1995]	16
	Plume with frazil	Jenkins & Bombosch [1995]	19
	3-dimensional	Determann & Gerdes [1994]	32
		Grosfeld et al. [1995]	34
		Grosfeld et al. [1997]	34

Note: The theoretical and idealised ice shelves vary between studies.

Grosfeld and Gerdes concluded the reduction of HSSW formation was the more likely of the two climate change scenarios to occur in the near future. This was mainly because they considered it highly unlikely for CDW or a similarly warm water mass to be able to directly access the ocean cavity under the Filchner Ice Shelf.

2.4 Summary

The range of different models used in studies of the ocean circulation under the ice shelves surrounding Antarctica is broad. Some models have been applied to more than one ice shelf. In Table 2.1 the various studies are summarised by ice shelf. This table includes the page number where the study is discussed in this chapter.

In the majority of the models presented in this chapter, only those which use thermohaline forcing have been considered. This focus has possibly arisen from the conclusions drawn by MacAyeal [1984b, 1985a] that thermohaline circulation plays the dominant role in ventilating the Ross Ice Shelf cavity. Since MacAyeal's studies, only one study of interaction of tidally-driven currents with an ice shelf has been made [Scheduikat and Olbers, 1990]. The restricted dimensions in this model gave no opportunity for the model to represent the large

scale circulation within the ocean cavity. However, the model demonstrated the importance of the kinetic energy budget in driving mixing between the layers in the ocean cavity.

Although the general approach to describing the ice shelf-ocean interaction has been similar in all the models, there has been some variation, particularly in the estimation of heat flux through the ice shelf, and in the role of the salt flux balance at the interface.

Three different approaches have been used for the heat flux through the ice shelf: it has been ignored [e.g., Determann and Gerdes, 1994], given a linear temperature gradient treatment [e.g., Hellmer and Olbers, 1989; Jenkins, 1991], and a complex treatment [Hellmer et al., 1998]. The magnitudes of the heat flux terms were estimated by Determann and Gerdes [1994] and they found that the heat flux into the ice shelf was approximately 1% of the other heat flux terms, if a linear temperature gradient through the ice shelf was assumed. They used this to justify ignoring the heat flux through the ice shelf. However, since the beginning of this current study Hellmer et al. [1998] have presented a new treatment of the flux through the ice shelf, which suggests that in areas of basal melting this heat flux term is larger, at $\sim$10% of the other heat flux terms.

In the early models it was assumed the salt flux balance at the ice-ocean interface was fundamental in determining the rates of melting and freezing. This was because of the small value of the salinity transfer coefficient in comparison to the heat transfer coefficient. This meant the slower salt transfer rate governed the equilibration of temperature and salinity at the ice-ocean interface. Although this does occur in models with constant coefficients [e.g., Hellmer and Olbers, 1989], the salt flux balance appears to plays only a partial role in determining the rates of melting and freezing in models with parameterised transfer coefficients [e.g., Jenkins, 1991]. This reduced role in models with parameterised transfer coefficients is because the parameterised salt transfer coefficient is generally larger, by at least one order of magnitude, than was assumed in the models which use a constant salt transfer coefficient.

If the role of the salt balance is reduced because the heat and salt transfer coefficients are close in magnitude, then the choice of Determann and Gerdes [1994] to ignore the salt balance in their parametrisation of the boundary conditions may be a reasonable assumption to make, if one is attempting to simply the boundary conditions as much as possible.

In all of the models except the Plume Model with Frazil Ice (Section 2.3.3) melting and freezing was only able to occur at the ice shelf-ocean interface. The results from the two studies using the Plume Model with Frazil Ice [Jenkins and Bombosch, 1995; Bombosch and Jenkins, 1995] suggested the formation of frazil ice may be important for the formation of marine ice layers on the base of ice shelves. This conclusion came from the ability of the frazil ice scheme to generate highly localised marine ice deposits, from the precipitation of frazil ice crystals out of the plume. Jenkins and Bombosch [1995] report rates of up to 2 ma^{-1}. However, the generation of highly localised marine ice deposits is not restricted to the Plume Model with Frazil Ice. Determann et al. [1994]

found high rates of freezing near the Doake Ice Rumples in the Ronne Ice Shelf, which would lead to the formation of marine ice layers. This suggests the three-dimensional model is able to achieve high rates of marine ice deposition from direct freezing, and does not necessarily require the use of a frazil ice scheme for the formation of marine ice layers. However, given the success of the Plume Model with Frazil Ice in producing significant freezing, it is not clear that freezing on the base of ice shelves can simply be regarded as the reverse of melting, and that perhaps the boundary conditions currently in use in most models may not accurately represent freezing process.

Despite the contrast in approaches a number of common features emerge from the collection of models that have been used to study the thermohaline circulation beneath ice shelves. Perhaps the most robust feature is that all show a sensitivity to the shape of the ocean cavity. Plume Models contain no reference to the sea bed, but they are responsive to the basal slope of the ice shelf. The circulation simulated by the HO Model reacts to the topography of both the ice shelf base and the sea bed. If these combine to give a maximum water column thickness at the ice front, the result is the open overturning cell assumed by the Plume Models. With a water column thickness that reaches its maximum somewhere between the grounding line and the ice front, the overturning becomes partially or completely closed. In the three-dimensional models the water column thickness appears paramount in determining the pattern of the circulation. Whatever the precise nature of the interaction between the water column thickness and the circulation, the sensitivity of all the models suggests a strong coupling.

The sensitivity of ice shelves to a change in oceanic climate is a subject addressed in some of the studies [Jenkins, 1991; Hellmer and Jacobs, 1995; Hellmer et al., 1998; Grosfeld and Gerdes, 1998], and on this point there is some disagreement. Plume Models suggest that the vigour of the buoyant overturning should be strongly related to the ambient water temperature, because of a positive feedback in which higher melt rates give stronger thermohaline forcing [Jenkins, 1991]. However, the free access of the warmer ambient water mass to the cavity must be taken for granted in those studies. In the HO Model, a warming at the ice front must be drawn into the cavity before it can impact the ice shelf, yet a similar response by the ocean cavity circulation and ice shelf mass balance to that seen in the Plume Models has been reported [Hellmer and Jacobs, 1995].

Given the similarity in the mathematical descriptions of the thermodynamic processes taking place at the ice shelf-ocean interface (Section 2.1), it is unsurprising to find similarities in the distribution of melting and freezing in the different models. This similarity arises from the pressure dependence of the freezing point (Equation 2.1) which means descending currents melt ice and ascending currents freeze ice. However, only the three-dimensional models reproduce the descending currents adjacent to the ice shelf. In the Plume and HO Models the currents are generally ascending the ice shelf draft (the exception is in some configurations of the HO channel flow models where there is net flow through the cavity, e.g., Hellmer and Olbers [1991]). The formation of

the descending currents in the three-dimensional model is due to the dominant barotropic circulation. The ability of the descending currents to melt ice allows for the formation of circulation systems which can melt ice off one side of a gyre and freeze ice on to the ice shelf on the other side, in effect forming a horizontal 'ice pump'. This is a feature also noted in some of the results of Hellmer and Olbers [1991].

The discrepancies between the different models suggest the results of the simpler models should be rejected in favour of three-dimensional models. The main argument for this is the inability of the simpler models to simulate the primarily geostrophic balance of the circulation. However, it could be argued this criterion is unreasonable, as in many cases the horizontal axes of the simpler models have been selected to include the influence of the earths rotation on the flow. Another argument in favour of the simpler models is their skill in reproducing both oceanographic and glaciological observations, although this may be because of the ease with which these models can be tuned. Given the freedom which tuning allows, when such models are used in situations where no observations are available for tuning the output the errors in the dynamics have an unknown impact. In these situations the behaviour of the three-dimensional models should be more credible. It remains difficult to assess which of the models gives us the most authentic representation of reality, because our knowledge of that reality is presently poor.

Chapter 3

Background oceanography and glaciology

In this chapter summaries of research on the oceanography of Prydz Bay, and the glaciology of the Amery Ice Shelf are presented. The summaries are focused on features of the oceanography and glaciology which are relevant to the aims of the overall study.

In the first section the oceanography of Prydz Bay, which in this thesis is considered to be the ocean area south of the shelf break and north of the Amery Ice Shelf, is summarised. This is followed by two sections on the glaciology of the Amery Ice Shelf. The first discusses general features of the ice shelf, and the second the mass balance of the ice shelf.

3.1 Oceanography of Prydz Bay

Several studies of the oceanography of Prydz Bay have been carried out using a combination of historical and recent observations [e.g., Smith et al., 1984; Middleton and Humphries, 1989; Smith and Treguer, 1994; Wong, 1994; Nunes Vaz and Lennon, 1996; Wong et al., 1998]. A consistent picture of the oceanography of Prydz Bay has evolved from the different studies.

The most commonly used data set was that collected by various Australian cruises as part of the Biological Investigation of Marine Antarctic Systems and Stocks (BIOMASS) project. The BIOMASS project involved seven cruises between 1981 and 1987. This data set was often supplemented with data sets from French and Soviet cruises to the area.

Prior to 1992, the oceanography cruises were carried out in Prydz Bay as part of biological surveys, generally as part of the BIOMASS program. The data sets collected were not optimal for determining the physical oceanography of the region. In particular, cruises often had poor horizontal resolution especially in areas of oceanographic interest, e.g., near the Amery Ice Shelf front and over the continental slope. They also tended to lack near-bottom resolution [Wong, 1994]. To improve on this a comprehensive oceanographic survey of Prydz Bay was carried out as part of the Fisheries and Oceanographic Voyage (FISHOG) by the Australian Antarctic Division, in February 1992.

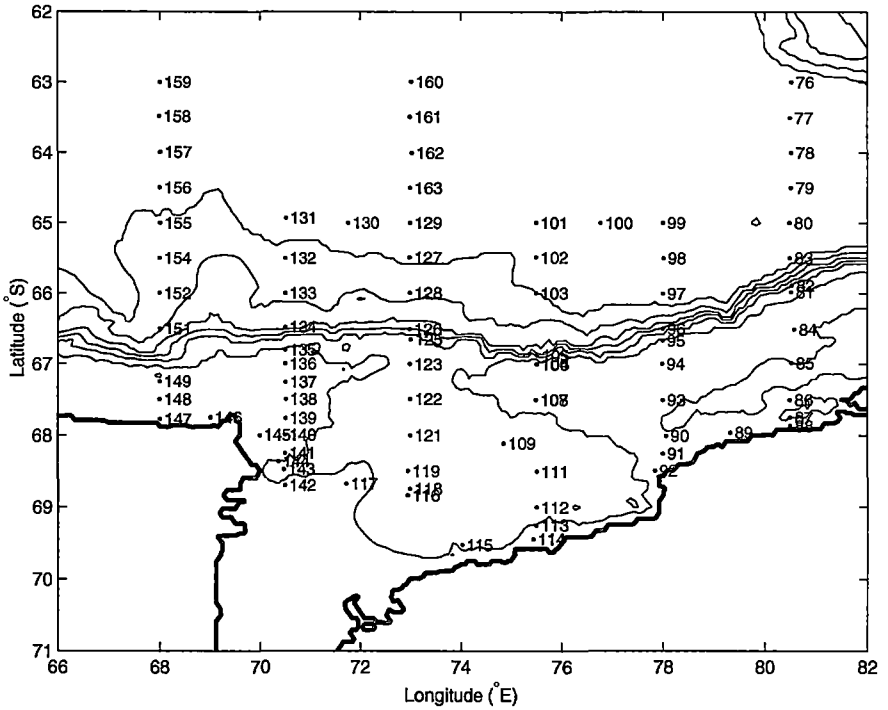

Figure 3.1: The location of CTD stations in the FISHOG data set. The bathymetry is taken from the ETOP05 data set and contoured at 500 m intervals. After Figure 3.1 in Wong [1994].

A summary of the results from the analysis of the FISHOG data set by Wong [1994] and Wong et al. [1998] is presented here. A detailed review of the work prior to FISHOG is given by Wong [1994].

On the FISHOG voyage 88 conductivity-temperature-depth (CTD) profiles were collected and analysed. The location of the CTD stations is shown in Figure 3.1. Because of the comprehensive nature of the survey, Wong [1994] and Wong et al. [1998] were able to present a coherent picture of the oceanography in the Prydz Bay region.

On the shelf the coldest waters ($< -2.0°C$) were found at an average depth of $\sim$200 m in the stations near the Amery Ice Shelf. Warmer saltier water was found at intermediate depths. The shelf waters were generally saltier and warmer in the east than in the west. Off the continental shelf the general structure of the water column in the FISHOG data set had small temperature and salinity gradients in the east-west direction. In the north-south direction the waters on the shelf were fresher and colder than the oceanic waters with particularly sharp salinity gradients being observed near the coast.

In Table 3.1 the definitions in terms of potential temperature and salinity for the seven water masses observed in Prydz Bay during FISHOG are presented. The definitions used are those presented by Wong et al. [1998]. They are slightly different from those originally used by Wong [1994]. The most substantial difference is the change in terminology from High Salinity Shelf Water (HSSW) to Low Salinity Shelf Water (LSSW).

The mostly likely reason for the change in name is that the most saline shelf

Table 3.1: The potential temperature and salinity of water masses identified in Prydz Bay [Table 1, Wong et al., 1998].

Water mass		Temperature (°C)		Salinity	
Summer Surface Water	SSW	-1.8	2.1	30.6	34.2
Winter Water	WW	-1.9	-1.5	34.2	34.5
Low Salinity Shelf Water	LSSW	-2.0	-1.5	34.5	34.6
Ice Shelf Water	ISW	<	-2.0	34.3	34.5
Circumpolar Deep Water	CDW	0.0	2.0	34.67	34.75
Modified CDW	MCDW	-1.5	1.0	34.2	34.67
Antarctic Bottom Water	AABW	<	0.0	34.66	34.71

water found in Prydz Bay was not as saline as similar waters found in the Ross and Weddell Seas [e.g., Jacobs et al., 1970; Foster and Carmack, 1976]. It does form via a similar mechanism; the rejection of brine during winter time sea ice formation. It was found in the deepest part of the shelf (~69°S 74°E), and in the FISHOG data set was confined to Prydz Bay.

The Summer Surface Water (SSW) layer is a highly variable layer whose temperature and salinity are highly dependent on the distribution of sea ice. Below the SSW layer there is a layer of Winter Water (WW) — this is a remnant of surface water formed during winter. The thickness of the WW layer varies between 30 m in the ocean domain and 300 m over the shelf.

In the FISHOG data set Ice Shelf Water (ISW) was found in only a small region just to the north of the western side of the Amery Ice Shelf. This gives a strong indication of interaction between the waters of Prydz Bay and the ocean cavity under the ice shelf.

Further evidence of ISW which has formed under the Amery Ice Shelf being advected into Prydz Bay was found by Penrose et al. [1994]. They found evidence of ice crystals at depth, and suggested the crystals could have formed in a plume of supercooled water coming from under the ice shelf. The ice crystals were found as back scatter in echo soundings near the ice front. CTD profiles were also collected at the same location and thus found local freezing conditions occurring between 40 m to 260 m in depth, while ice was observed in the echo sounding record between 20 m and 75 m.

Modified Circumpolar Deep Water (MCDW) was observed in the majority of the sections on the shelf. It is formed from a mixture of Circumpolar Deep Water (CDW) and shelf waters. It is cooler, fresher, and less dense than the local CDW, which is restricted to the oceanic part of the domain at depths between 300 m and 3000 m. In a previous survey [Middleton and Humphries, 1989] the densest form of MCDW was named Prydz Bay Bottom Water, and was believed to be a mixture of CDW and shelf water in Prydz Bay.

The Antarctic Bottom Water (AABW) observed during FISHOG can be classified into low (< 34.68) and high (> 34.68) salinity varieties. The low salinity variety was generally observed to the east of Prydz Bay, and was most

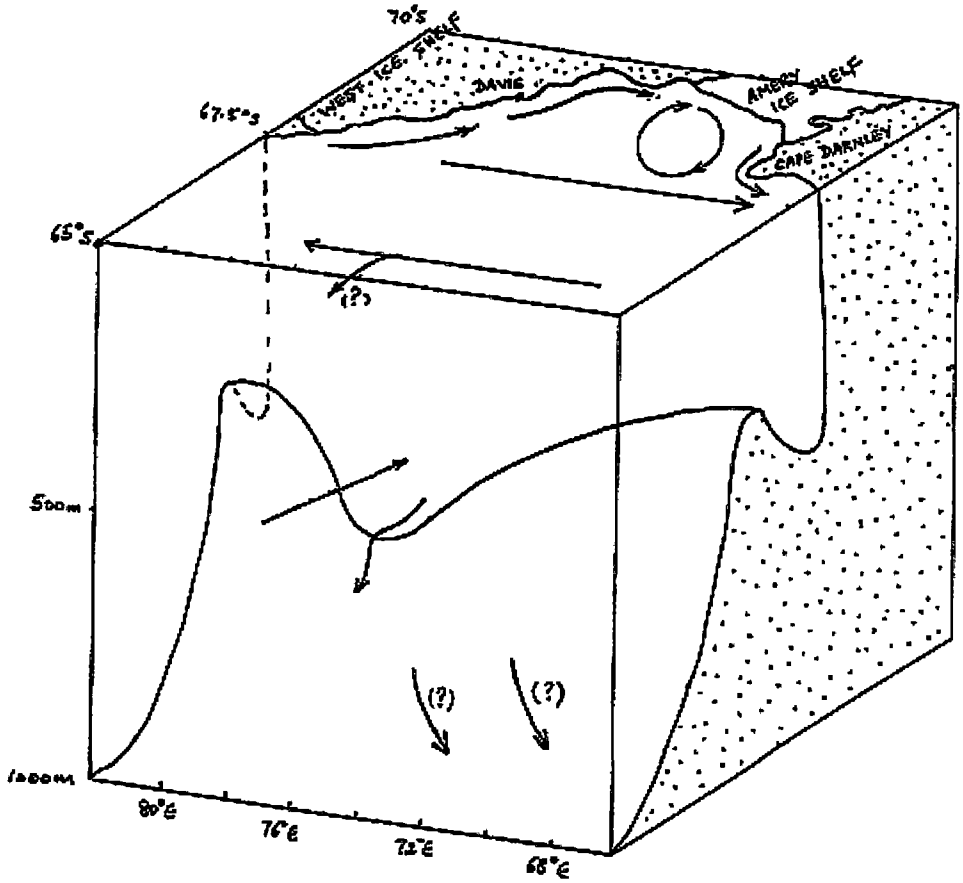

Figure 3.2: A schematic of the geostrophic circulation in the Prydz Bay region [Figure 4.1, Wong, 1994].

likely formed from advection of Weddell Sea Bottom Water or Adelie Land Bottom Water. The high salinity AABW was generally observed in the western transects. Its water mass properties were anomalous and not consistent with the advection of other water masses. Wong et al. [1998] hypothesised that the high salinity AABW was formed locally, but this required shelf waters to reach a salinity in the range of 34.67 to 34.72. This water mass if sufficiently cold would be HSSW, but could only form if there was sufficient local brine rejection.

Utilising the temperature and salinity profiles Wong et al. [1998] calculated the geostrophic circulation in the Prydz Bay region. Four main features were found in the horizontal circulation: an eastward zonal flow between 63°S and 66°S, a narrow westward flowing slope current between 66°S and 67°S, a strong westward flowing coastal current, and a cyclonic gyre in the bay. These features are shown in Figure 3.2 from Wong [1994].

The northernmost feature in the oceanic domain is associated with the Antarctic Circumpolar Current. On the shelf the slope and coastal currents are associated with the East Wind drift, a westward flowing coastal current

driven by the mean easterly winds from the Antarctic Plateau. The slope current was estimated to have a transport ~0.2 Sv. The coastal current transport was generally larger than this.

Inside Prydz Bay the contours of effective geopotential anomaly, calculated by Wong [1994], show a gyre formed about a dynamic low in Prydz Bay (68.5°S 73.0°E) by the presence of LSSW. The gyre is confined to the western half of Prydz Bay. It has the effect of intensifying parts of the coastal current which are in the vicinity of the gyre. The gyre has an average velocity of ~1.5 cms^{-1}, in comparison to the coastal current velocity of (~8 cms^{-1}). The gyre suggests the coastal current could flow under the Amery Ice Shelf with a transport of between ~0.2 Sv and ~1.0 Sv [Wong, 1994], consequently this would introduce LSSW (or HSSW if it forms during winter) to the base of the Amery Ice Shelf at the eastern end of the ice front.

3.2 Glaciology of the Amery Ice Shelf

The glaciology of the Amery Ice Shelf was the subject of several field programs between 1962 and 1971 [Budd, 1966; Budd et al., 1967; Morgan, 1972; Morgan and Budd, 1975; Budd et al., 1982].

In Budd [1966] and Budd et al. [1967] initial assessments from surveys carried out between 1962 and 1965 were presented. It was found the ice shelf surface sloped downwards from the Lambert Glacier to the ice front. As no ice shelf thickness data were available, the thickness was calculated by utilising density profiles from the Ross Ice Shelf. Budd found that the ice shelf showed a rapid increase in the ice shelf velocity and the creep rate near the ice front.

At a location known as G1 (69.48°S 71.73°E) (see Figure 3.3) an ice core was collected during 1968. Morgan [1972] analysed the oxygen isotope ratios and found a sharp change in the isotope values at 270 m depth (from the ice shelf surface) which marked the bottom of the glacier ice. Below this depth isotope values were close to that of sea water and it was assumed the remainder of the core was frozen sea water. The thickness of the ice shelf at G1 was estimated to be 428 m by radar echo-sounding — giving a marine ice layer thickness of 158 m. It has been suggested [Morgan, 1972] that the thick marine ice layer may have been caused from sea water filling an inverted crevasse and then freezing. Recent studies of the Filchner-Ronne Ice Shelf [Thyssen et al., 1993; Grosfeld et al., 1998] have found marine ice layers of similar thickness, suggesting thick marine ice layers are common on large ice shelves.

The major deficiency of the initial survey [Budd, 1966] was the lack of coinciding ice shelf thickness and elevation data. This deficiency was rectified by the collection of radar echo-sounding (RES) data along the central traverse line of the ice shelf. This data was presented by Morgan and Budd [1975].

In Budd et al. [1982] the results of the previous studies combined with the analysis of the subsequent work were presented. By combining the data for surface elevation and thickness with that of the ice shelf geometry, Budd et al. [1982] found that surface slope and the ice shelf width provided the primary driving force for the high velocities near the centre of the ice shelf, which reach

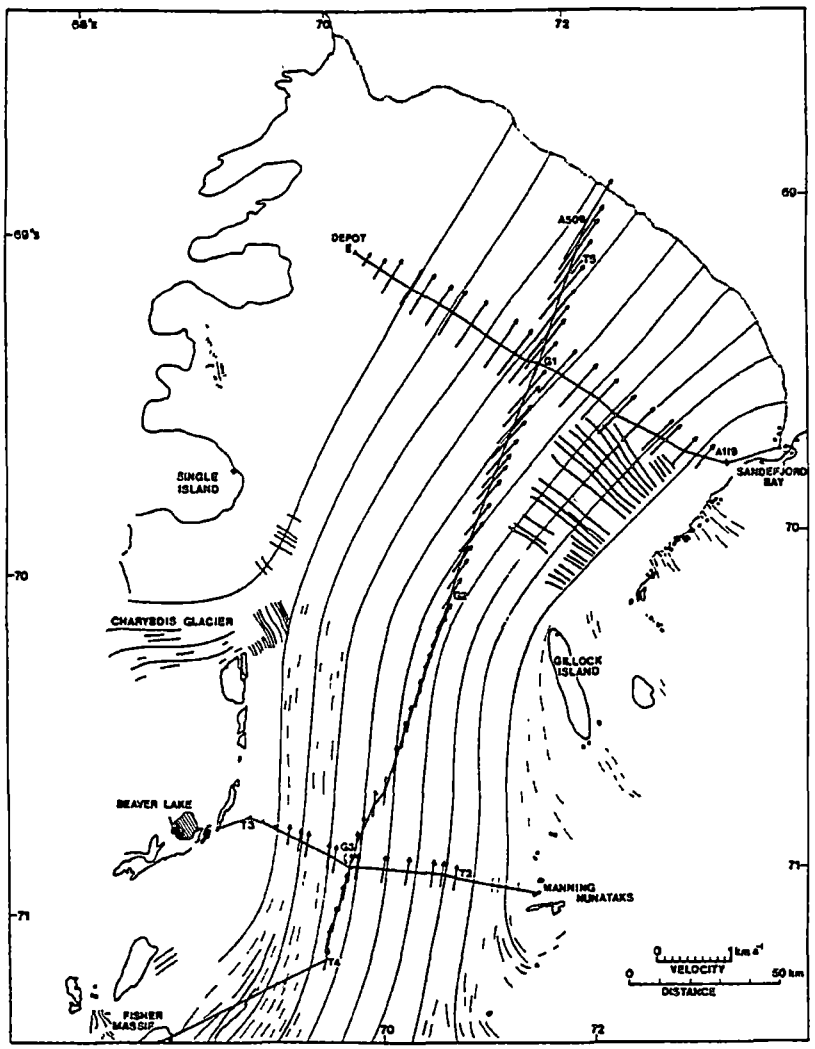

Figure 3.3: Map of the Amery Ice Shelf, showing the results of the Amery Ice Shelf Project, including the traverse velocity vectors and flow-lines derived from satellite image features [Figure 1, Budd et al., 1982].

1.2 kma^{-1} near the ice front. On the scale of 1 km to 5 km high frequency surface and basal fluctuations occur and are apparently related. On larger scales the ice shelf thickness is relatively uniform across the ice shelf. Near the grounding line assumed by Budd et al. [1982] ($\sim$71.2°S, Figure 3.3), the ice shelf appears to thicken before gradually thinning as it nears the ice front.

By modelling the paths of particles in the ice shelf under the observed ice deformation, and how these would change over the length of the ice shelf, Budd et al. [1982] were able to estimate the basal melt or growth rate. They inferred substantial growth of ice occurred to within 70 km of the ice front. In the 70 km near the ice front the rate dropped to almost zero. By calculating how the marine ice layer would accumulate given the inferred growth rate and the ice strain rate, good agreement was found with the marine ice layer estimated by Morgan [1972].

Budd et al. concluded from the survey results that the dynamics of the ice shelf flow can be modelled reasonably to a first approximation from the lateral shear stress and strain rates. The high vertical strain rate ($\sim$1.6 %a^{-1}) rather than melting appeared to be the major limiting factor on the forward growth of the ice shelf from thickness advection. This thinning reduced the ice shelf thickness as it moved northward increasing the likelihood of periodic calving of large icebergs.

3.3 Mass balance of the Amery Ice Shelf

The important aspect of the ice shelf relevant to this study is its mass balance, and in particular the basal component of mass balance. The major components of the Amery Ice Shelf mass balance are the flow across the grounding line, calving of icebergs from the ice front, net snow accumulation on the surface of the ice shelf, and net melting from the base of the ice shelf. Estimates of these components have been made for the Amery Ice Shelf.

The majority of the flow across the grounding line of the Amery Ice Shelf comes from the Lambert Glacier. In a mass balance study of the Lambert Basin Allison [1979] estimated the mass flux upstream of the ice shelf grounding line, near the confluence of the Fisher and Mellor Glaciers, at $\sim$30 Gta^{-1}. Between the confluence and the grounding line he also estimated approximately 7 Gta^{-1} was lost in surface ablation. The two other mass inputs into the ice shelf were estimated by Budd et al. [1967], who estimated the mass flux from glaciers feeding the sides of the ice shelf at 14 Gta^{-1}, and the accumulation of snow on the surface of the ice shelf at 9 Gta^{-1}.

Estimates of the basal mass loss from the Amery Ice Shelf have been given by Jacobs et al. [1992] and Wong et al. [1998]. Jacobs et al. [1992] utilised melt rates from Hellmer and Jacobs [1992] modelling study of the ocean cavity under the Amery Ice Shelf (Section 2.3.4). They assumed a melt rate from the base of the Amery Ice Shelf of 0.65 ma^{-1}over an area of 3.9×10^4 km^2 to give a net melt of 23 Gta^{-1}.

Utilising the CTD profiles near the front of the Amery Ice Shelf Wong et al. [1998] calculated several estimates of the heat and salt flux out of the ocean cavity under the Amery Ice Shelf. The heat fluxes were then converted to an equivalent melt rate for the base of the Amery Ice Shelf by assuming all the heat flux across the ice front was equal to the latent heat flux at the ice shelf base.

Wong et al. [1998] calculated the fluxes from three analyses using different CTD stations in each analysis. Experiment One used stations 115, 116, 117, and 143 (Figure 3.1). Experiment Two used stations 115, 117, 118, and 142. Experiment Three used stations 115, 116, 117, 142, and 143. In each experiment the surface waters down to 100 db or 120 db were excluded. Their results are presented in Table 3.2.

From these various experiments they calculated the average net melt rates from the temperature data at 26.4 ± 8.6 Gta^{-1}, and the average freshwater flux due to melting from the salinity data at 14.7 ± 4.6 Gta^{-1}. It is clear the

Table 3.2: Estimates of melt rates and freshwater flux from under the Amery Ice Shelf [Table 2, Wong et al., 1998]. The reference transport is included to insure mass conservation through the section.

Experiment	Depth range (db)	Ref. Transport (cms^{-1})	Melt Rate (m^3s^{-1})	Melt Rate (Gta^{-1})	Freshwater Flux (m^3s^{-1})	Freshwater Flux (Gta^{-1})
One	100 - bot	0.0936	814	25.6	411	12.9
	120 - bot	0.1005	631	19.9	342	10.7
Two	100 - bot	0.1771	1278	40.3	695	21.9
	120 - bot	0.2178	675	21.3	392	12.3
Three	100 - bot	0.0527	1055	33.2	600	18.9
	120 - bot	0.0861	582	18.3	361	11.4

estimates are very sensitive to the small number of CTD profiles across the face of the ice shelf cavity and to the unknown role seasonality in the temperature and salinity in Prydz Bay might play. They place their best estimate of basal mass loss at between 10.7 Gta^{-1} and 21.9 Gta^{-1}, with a mean of 14.7 Gta^{-1}.

No comprehensive estimate of the mass loss by calving at the front of the Amery Ice Shelf has been made. A tentative estimate can be made by assuming the ice shelf is in a steady state. The total mass input into the ice shelf is approximately 46 Gta^{-1}. This consists of 23 Gta^{-1} from the Lambert Glacier [Allison, 1979], 14 Gta^{-1} from glaciers feeding the sides of the Amery Ice Shelf [Budd et al., 1967], and 9 Gta^{-1} of snow accumulation on the ice shelf [Budd et al., 1967]. The estimates of melting from the base of the ice shelf vary between 10.7 Gta^{-1} and 23 Gta^{-1}, this leaves a net loss from calving of between 35.3 Gta^{-1} and 23 Gta^{-1}. A mass flux of this size appears to be consistent with the ice shelf velocity and thickness measurements presented in Budd et al. [1982] for a survey line running east-west through G1 (Figure 3.3).

The data for surface elevation and the velocity of the ice shelf show very little change between 1968 and the present [Phillips, 1998]. This confirms that the ice shelf appears to be close to a balanced steady state over this period.

Chapter 4

Model background and setup

In this chapter the model which forms the basis of the investigations in the following chapters is presented. In the first section of this chapter a description of the continuous equations governing the model are presented. This is followed by the finite difference representation of the most important model equations. In the third section the various boundary conditions which are applied to the model cavity domain are detailed, including each of the different forms of the boundary conditions considered in Chapter 5. Following this, the origin of the water column thickness and ice shelf draft which describe the shape and extent of the cavity are presented. This is followed by the description of the restoring temperature and salinity fields at the ice front.

4.1 Model equations

The numerical model described here was first applied to studying cavities under ice shelves by Determann and Gerdes [1994] (see Section 2.3.5 for more details). The model is a three-dimensional, primitive equation ocean model, based on the work of Bryan [1969] and Cox [1984]. The model describes the evolution of the horizontal velocity components, potential temperature, salinity and additional passive tracers. Vertical velocity is calculated from the continuity equation for an incompressible fluid.

Cox-Bryan type models have traditionally been implemented using a z-coordinate approach. In the z-coordinate system a series of layers at fixed depths are used. In an ocean cavity beneath an ice shelf the changes in topography would then be represented by steps in the sea bed or the ice shelf draft. This method can lead to large localised vertical velocities which are generally unrealistic [Gerdes, 1993].

To reduce this problem, and allow a more realistic representation of the topographic changes in the ocean cavity, the vertical coordinate can be transformed by

$$\sigma = \frac{z}{H}, \tag{4.1}$$

where z is the depth below the ice shelf base and H is the water column thickness. Utilising this transformation forms the basis of the σ-coordinate system.

The main advantage of using a σ-coordinate system over a z-coordinate system, is that it allows for the convenient specification of the kinematic boundary conditions at the ice shelf-ocean interface and at the sea floor. This comes about as these two boundaries are respectively the top and bottom σ-layers.

Gerdes [1993] converted the Cox-Bryan model to a coordinate system using an arbitrary vertical coordinate (s-coordinate). The z-coordinate and σ-coordinate systems are special cases of the arbitrary vertical coordinate system. This also allows for some combination of the two coordinate systems, as was done by Grosfeld et al. [1997], in their combined ocean cavity and open ocean model domain, and in the studies presented in Chapter 7.

In this section, the σ-coordinate version of the equations and boundary conditions which underlie the model are outlined, these equations are based on the z-coordinate equations presented by Cox [1984] and the s-coordinate equations presented by Gerdes [1993].

The advection effects in the time evolution equations for the horizontal velocities and tracer equations can be described in terms of an advective operator. This operator $\Gamma(\mu)$ is

$$\Gamma(\mu) = \frac{1}{aH\cos\phi}\left(\frac{\partial}{\partial\lambda}(uH\mu) + \frac{\partial}{\partial\phi}(vH\mu\cos\phi)\right) + \frac{1}{H}\frac{\partial}{\partial\sigma}(\omega\mu), \tag{4.2}$$

where a is the Earth's radius, ϕ is latitude, λ is longitude, u and v are the horizontal velocities, and ω is the vertical velocity in the σ-coordinate system. The horizontal velocity terms are

$$u = a\cos\phi\frac{\partial\lambda}{\partial t} \tag{4.3}$$

$$v = a\frac{\partial\phi}{\partial t}. \tag{4.4}$$

The vertical velocity is

$$\omega = w + \frac{uH}{a\cos\phi}\frac{\partial\sigma}{\partial\lambda} + \frac{vH}{a}\frac{\partial\sigma}{\partial\phi}, \tag{4.5}$$

where $w = \frac{\partial z}{\partial t}$.

The continuity equation is used to solve for ω, and it can easily be described in terms of the advective operator. It is

$$\Gamma(1) = 0. \tag{4.6}$$

The main governing equations for the time evolution of the velocities are:

$$\frac{\partial u}{\partial t} + \Gamma(u) - fv = -\frac{1}{a\rho_0\cos\phi}\left(\frac{\partial p}{\partial\lambda} + \frac{\partial p}{\partial\sigma}\frac{\partial\sigma}{\partial\lambda}\right) + F^u, \tag{4.7}$$

$$\frac{\partial v}{\partial t} + \Gamma(v) + fu = -\frac{1}{a\rho_0}\left(\frac{\partial p}{\partial\phi} + \frac{\partial p}{\partial\sigma}\frac{\partial\sigma}{\partial\phi}\right) + F^v, \tag{4.8}$$

where f is the Coriolis parameter, p is the pressure, ρ is the density, ρ_0 is a reference density, and F^u and F^v are turbulent mixing terms.

The time evolution equation for the tracers, temperature and salinity, evolves with time in a similar way, i.e.,

$$\frac{\partial T}{\partial t} + \Gamma(T) = F^T, \tag{4.9}$$

where F^T is the turbulent mixing term for tracers.

The local vertical dependence on pressure is given by the hydrostatic relation

$$\frac{\partial p}{\partial \sigma} = -g\rho H. \tag{4.10}$$

In the model the density

$$\rho = \rho(\theta, S, p), \tag{4.11}$$

depends on pressure, potential temperature (θ), and salinity (S). It is represented by a polynomial approximation to the UNESCO equation of state, which is described in Mellor [1991].

Subgrid scale processes are implemented through the turbulent mixing terms, F^u, F^v and F^T. These are:

$$F^u = \frac{A_v}{H^2}\frac{\partial^2 u}{\partial \sigma^2} + \frac{A_h}{a^2}\nabla^2 u, \tag{4.12}$$

$$F^v = \frac{A_v}{H^2}\frac{\partial^2 v}{\partial \sigma^2} + \frac{A_h}{a^2}\nabla^2 v, \tag{4.13}$$

and

$$F^T = \frac{K_v}{H^2}\frac{\partial^2 T}{\partial \sigma^2} + \frac{K_h}{a^2}\nabla^2 T. \tag{4.14}$$

where

$$\nabla^2 \mu = \frac{1}{\cos^2\phi}\frac{\partial^2 \mu}{\partial \lambda^2} + \frac{1}{\cos\phi}\frac{\partial}{\partial \phi}\left(\cos\phi \frac{\partial \mu}{\partial \phi}\right). \tag{4.15}$$

In Equations 4.12 and 4.13, A_h and A_v are respectively the along σ-level and perpendicular to σ-level mixing coefficients. In Equation 4.14, K_h and K_v are the corresponding tracer mixing coefficients. In the studies presented in Chapters 5 and 6 the mixing coefficients take values of 30 m^2s^{-1}, 1×10^{-3} m^2s^{-1}, 100 m^2s^{-1}, 5×10^{-5} m^2s^{-1}, for A_h, A_v, K_h and K_v, respectively. In Chapter 7, where the open ocean domain is included, A_h is increased to 600 m^2s^{-1} [Grosfeld et al., 1997].

The time evolution equations for both velocity components (Equations 4.7 and 4.8) can be rearranged, taking into account the integral of Equation 4.10 from the σ-layer to the surface, to give

$$\frac{\partial u}{\partial t} = \frac{\partial u'}{\partial t} - \frac{1}{a\rho_0 \cos\phi}\frac{\partial p_S}{\partial \lambda}, \tag{4.16}$$

$$\frac{\partial v}{\partial t} = \frac{\partial v'}{\partial t} - \frac{1}{a\rho_0}\frac{\partial p_S}{\partial \phi}, \tag{4.17}$$

where p_S is the surface pressure which in the ice shelf cavity is the ice shelf draft, and

$$\frac{\partial u'}{\partial t} = -\Gamma(u) + fv - \frac{g}{a\rho_0 \cos\phi}\left(\int_\sigma^0 H\frac{\partial \rho}{\partial \lambda}\,d\sigma' + \rho\sigma\frac{\partial H}{\partial \lambda}\right) + F^u, \quad (4.18)$$

$$\frac{\partial v'}{\partial t} = -\Gamma(v) - fu - \frac{g}{a\rho_0}\left(\int_\sigma^0 H\frac{\partial \rho}{\partial \phi}\,d\sigma' + \rho\sigma\frac{\partial H}{\partial \phi}\right) + F^v. \quad (4.19)$$

This allows the momentum equations to be solved in two parts, the internal and external modes, which respectively represent the barotropic and baroclinic motion. The internal and external modes can be denoted by $\hat{\mu}$ and $\bar{\mu}$, respectively, where

$$\mu = \hat{\mu} + \bar{\mu} \quad (4.20)$$

and μ is either of the zonal (u) or meridional (v) velocities. Using this definition it can be shown, using Equations 4.16 and 4.17, that the time evolution equation for the internal mode can be written

$$\frac{\partial \hat{\mu}}{\partial t} = \frac{\partial \mu'}{\partial t} - \frac{\partial \bar{\mu}'}{\partial t} \quad (4.21)$$

where

$$\bar{\mu} = \int_{-1}^0 \mu\,d\sigma. \quad (4.22)$$

If all the terms on the right hand side of Equations 4.18 and 4.19 are known then the time evolution of the internal mode of momentum can be calculated.

Utilising the boundary conditions discussed in Section 4.3, in particular those related to the rigid lid approximation, the external mode of momentum can be represented in terms of a volume transport streamfunction, Ψ. The streamfunction is defined in terms of its derivatives by

$$\bar{u} = \frac{-1}{a}\frac{\partial \Psi}{\partial \phi}, \quad (4.23)$$

$$\bar{v} = \frac{1}{a\cos\phi}\frac{\partial \Psi}{\partial \lambda}. \quad (4.24)$$

Using the curl operator a time evolution equation for Ψ can be obtained;

$$\left|\nabla \times \left(\frac{\partial \bar{u}}{\partial t}, \frac{\partial \bar{v}}{\partial t}\right)\right| = \frac{1}{a\cos\phi}\left(\frac{\partial^2 \bar{v}}{\partial t \partial \lambda} - \frac{\partial^2(\bar{u}\cos\phi)}{\partial t \partial \phi}\right). \quad (4.25)$$

The equation

$$\frac{\partial}{\partial \lambda}\left(\frac{1}{a\cos\phi}\frac{\partial^2 \Psi}{\partial t \partial \lambda}\right) + \frac{\partial}{\partial \phi}\left(\frac{\cos\phi}{a}\frac{\partial^2 \Psi}{\partial t \partial \phi}\right) = \frac{\partial}{\partial \lambda}\left(\frac{\partial \bar{v}'}{\partial t}\right) - \frac{\partial}{\partial \phi}\left(\cos\phi\frac{\partial \bar{u}'}{\partial t}\right) \quad (4.26)$$

is found by substituting Equations 4.23 and 4.24 into Equation 4.25 to form the left hand side, and vertically integrating Equations 4.16 and 4.17, then substituting them into Equation 4.25 to form the right hand side of the equation.

This elliptic equation for $\frac{\partial \Psi}{\partial t}$, driven by the curl of the depth integrated acceleration enables the time evolution of the streamfunction to be found and from it the barotropic components of velocity.

The elliptic equation for $\frac{\partial \Psi}{\partial t}$ (Equation 4.26) is solved with the boundary equation

$$\frac{\partial \Psi}{\partial t} = 0. \tag{4.27}$$

The streamfunction evolves from an initial state where either the normal derivative or the streamfunction is specified on all boundaries. This translates the initial value problem in $\frac{\partial \Psi}{\partial t}$ to a boundary value problem for Ψ.

4.2 Finite difference formulation

The equations in the previous section may be solved numerically using finite difference techniques. The equations are divided into two groups, the prognostic equations (4.9, 4.21, 4.26), and the diagnostic equations (4.6, 4.11, 4.23, 4.24).

The formulation of the finite difference equations used in solving the model equations is grid dependent. On the constant σ-surfaces the staggered 'B' grid of Mesinger and Arakawa [1976] is used for distributing the velocity, streamfunction and tracer points. The vertical grid points are also staggered, with horizontal velocities and tracers defined at the centres of vertical boxes, and ω defined at the interfaces between boxes. The arrangement of grid points, for both horizontal and vertical sections is shown in Figure 4.1.

To simplify the representation of the finite difference equations, it is useful to define the following terms:

$$\delta_\beta \mu_m = \frac{\mu_{m+\frac{1}{2}} - \mu_{m-\frac{1}{2}}}{\Delta_m \beta}, \tag{4.28}$$

$$\langle \mu_m \rangle^\beta = \frac{\mu_{m+\frac{1}{2}} + \mu_{m-\frac{1}{2}}}{2}, \tag{4.29}$$

$$\langle \mu \rangle^* = \sum_{k=1}^{K} \mu_k \Delta\sigma, \tag{4.30}$$

where β represents any of the coordinates (λ, ϕ, σ), m represents the index of interest, and $\Delta_m \beta$ is the grid size over which the difference in Equation 4.28 is calculated. The indices i, j, and k are used to indicate the grid points of interest and apply to the coordinates λ, ϕ, and σ respectively (Figure 4.1). In Equations 4.28 and 4.29, if the index (m) is absent, the index will be implied by the coordinate (β) on which the operation is acting.

The representation of the time evolution of the internal mode of momentum equations (Equation 4.21), using central differences in time is

$$\delta_t \langle \hat{u} \rangle^t = \delta_t \langle u' \rangle^t - \langle \delta_t \langle u' \rangle^t \rangle^*, \tag{4.31}$$

$$\delta_t \langle \hat{v} \rangle^t = \delta_t \langle v' \rangle^t - \langle \delta_t \langle v' \rangle^t \rangle^*, \tag{4.32}$$

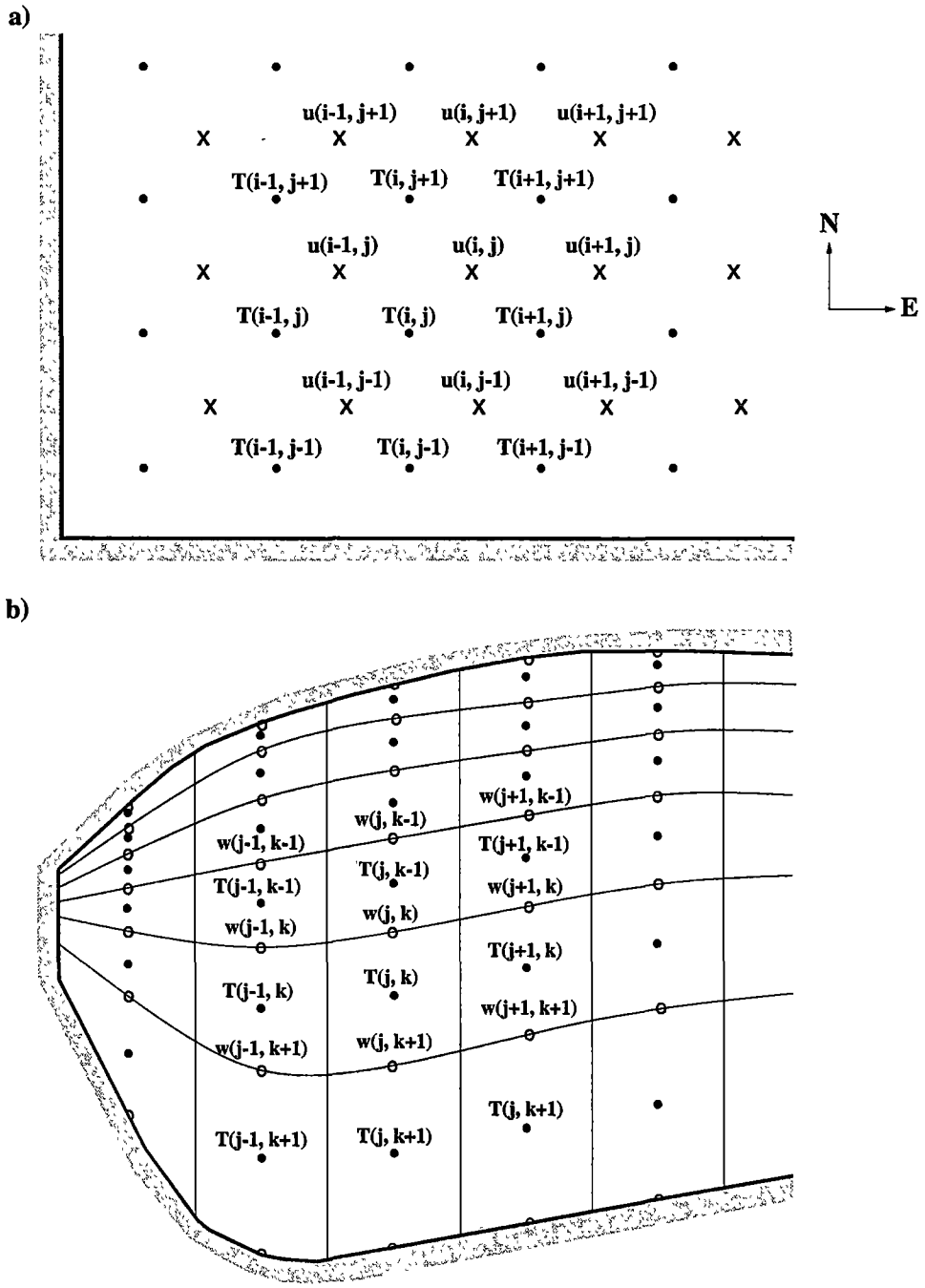

Figure 4.1: The (a) horizontal and (b) vertical arrangement of grid points. The dots are where the tracer and streamfunction are solved, the crosses are where the horizontal velocity $\mathbf{u}$, with components u and v, is solved, and the circles represent where the vertical velocity term (ω) is solved.

where, from Equations 4.18 and 4.19

$$\delta_t\langle u'\rangle^t = -\Gamma_M(u) + fv - \frac{g}{a\cos\phi}\left(\left\langle\sum_{k'=1/2}^{k-1/2}\delta_\lambda\langle\rho_{k'}\rangle^\sigma\langle\Delta_{k'}\sigma\rangle^\sigma\right\rangle^\phi + \langle\langle\rho\sigma\rangle^\lambda\delta_\lambda\langle H\rangle^\sigma\rangle^\phi\right) + \tilde{F}^u, \tag{4.33}$$

$$\delta_t\langle v'\rangle^t = -\Gamma_M(v) - fu - \frac{g}{a}\left(\left\langle\sum_{k'=1/2}^{k-1/2}\delta_\phi\langle\rho_{k'}\rangle^\sigma\langle\Delta_{k'}\sigma\rangle^\sigma\right\rangle^\phi + \langle\langle\rho\sigma\rangle^\lambda\delta_\phi\langle H\rangle^\sigma\rangle^\lambda\right) + \tilde{F}^v. \tag{4.34}$$

The finite difference representations of the turbulent mixing coefficients, $\tilde{F}^u$ and $\tilde{F}^v$, in the above equations are lagged one time step to enhance numerical stability, and are

$$\tilde{F}^u = \frac{A_v}{\langle H^2\rangle^{\lambda\phi}}\delta_\sigma\delta_\sigma u + \frac{A_h}{a^2}\tilde{\nabla}^2(u), \tag{4.35}$$

$$\tilde{F}^v = \frac{A_v}{\langle H^2\rangle^{\lambda\phi}}\delta_\sigma\delta_\sigma v + \frac{A_h}{a^2}\tilde{\nabla}^2(v), \tag{4.36}$$

where

$$\tilde{\nabla}^2(\mu) = \frac{1}{\cos^2\phi}\delta_\lambda\delta_\lambda\mu + \frac{1}{\cos\phi}\delta_\phi\left(\cos\phi\,\delta_\phi\mu\right). \tag{4.37}$$

The advective operator for the momentum equations, $\Gamma_M(\mu)$, is

$$\Gamma_M(\mu) = \frac{1}{\langle H\rangle^{\lambda\phi}}\delta_\sigma(\omega_m\langle\mu\rangle^\sigma) + \frac{1}{a\langle H\rangle^{\lambda\phi}\cos\phi}\left(\delta_\lambda(\langle\mu\rangle^\lambda\langle u\rangle^\lambda\langle H\rangle^{\lambda\phi}) + \delta_\phi(\cos\phi\langle\mu\rangle^\phi\langle v\rangle^\phi\langle H\rangle^{\lambda\phi})\right) \tag{4.38}$$

where ω_m is calculated from the kinematic boundary conditions (c.f. Section 4.3) and the continuity equation

$$\Gamma_M(1) = 0. \tag{4.39}$$

The streamfunction is solved on grid points which are displaced from the velocity grid points in both horizontal axes (Figure 4.1). The finite difference representation of the streamfunction evolution equation (Equation 4.26) is

$$\delta_\lambda\left(\frac{1}{\langle H\rangle^\phi a\cos\phi}\delta_\lambda\delta_t\langle\Psi\rangle^t\right) + \delta_\phi\left(\frac{1}{\langle H\rangle^\lambda a\cos\phi}\delta_\phi\delta_t\langle\Psi\rangle^t\right) = \frac{1}{\Delta\phi}\delta_\lambda\langle\langle\delta_t\langle v'\rangle^t\rangle^*\Delta\phi\rangle^\phi - \frac{1}{\Delta\lambda}\delta_\phi\langle\cos\phi\langle\delta_t\langle u'\rangle^t\rangle^*\Delta\lambda\rangle^\lambda. \tag{4.40}$$

From the solution of this equation, the finite difference representation of the external velocity modes, $\bar{u}$ and $\bar{v}$, can be found

$$\bar{u} = \frac{-1}{a}\delta_\phi\langle\Psi\rangle^\lambda, \tag{4.41}$$

$$\bar{v} = \frac{1}{a\cos\phi}\delta_\lambda\langle\Psi\rangle^\phi. \tag{4.42}$$

The time evolution of the tracer equation (Equation 4.9) becomes

$$\delta_t \langle T \rangle^t + \Gamma_T(T) = \tilde{F^T} + C. \tag{4.43}$$

The tracer advective operator Γ_T differs from the operator used in the momentum equations (Γ_M), because of the grid offset between the tracer grid points and velocity grid points. The operator for the tracer evolution equation is

$$\Gamma_T(T) = \frac{1}{\langle H \rangle^{\lambda\phi}} \delta_\sigma (\omega_T \langle T \rangle^\sigma) \tag{4.44}$$
$$+ \frac{1}{a \langle H \rangle^{\lambda\phi} \cos\phi} \left(\delta_\lambda \left(\langle T \rangle^\lambda \frac{\langle u \langle H \rangle^{\lambda\phi} \Delta\phi \rangle^\phi}{\Delta\phi} \right) + \delta_\phi \left(\langle T \rangle^\phi \cos\phi \frac{\langle v \langle H \rangle^{\lambda\phi} \Delta\lambda \rangle^\lambda}{\Delta\lambda} \right) \right).$$

In the model ω_T is calculated from the continuity equation

$$\Gamma_T(1) = 0. \tag{4.45}$$

In Equation 4.43, $\tilde{F^T}$ is the finite difference representation of F^T, (Equation 4.14) and is

$$\tilde{F^T} = \frac{K_v}{\langle H^2 \rangle^{\phi\lambda}} \delta_\sigma \delta_\sigma T + \frac{K_h}{a^2} \tilde{\nabla}^2 T. \tag{4.46}$$

The final term in Equation 4.43, C, was not included in the continuous version of the equation. This represents the process of convective adjustment. A convective mixing scheme is applied when the density stratification becomes unstable. The statically unstable sections of the water column are located. At each unstable section, the water is mixed by replacing the individual temperature and salinity values, with the mean values across the unstable section. This procedure is done for each unstable section. This scheme is repeated, as needed, until no instabilities remain in the water column.

4.3 Boundary conditions

The ocean cavity model domain has four different types of boundary: the sea bed, the ice shelf-ocean interface, the open ocean boundary, and the coast or grounding line. Of these the coast or grounding line and sea bed boundary conditions used here are similar to those used in other ocean models. The other two boundaries are more complex.

4.3.1 Grounding line or coast boundaries

Along the grounding line, which lies on velocity grid points, the boundary conditions ensure conservation of mass and tracers by ensuring no flow across the boundary wall. A no-slip condition on the velocities is also imposed. This implies the boundary conditions,

$$u = v = 0, \tag{4.47}$$
$$\frac{\partial T}{\partial n} = 0, \tag{4.48}$$

where n denotes the local normal derivative.

The velocity boundary conditions are imposed on the internal and external components separately. On the internal components,

$$\hat{u} = \hat{v} = 0, \tag{4.49}$$

is set on the velocity boundary points.

The boundary conditions for the external component of velocity are set via the streamfunction, and are

$$\frac{\partial \Psi}{\partial \phi} = \frac{\partial \Psi}{\partial \lambda} = 0. \tag{4.50}$$

These boundary conditions on the streamfunction are satisfied by having the streamfunction (Ψ) constant over the land mass around the domain, over any islands in the domain, and at the first internal grid point adjacent to the appropriate boundaries. The value of Ψ for the coast and grounding line has for convenience been set to zero.

For any islands in the domain the value of Ψ cannot be prescribed, as the value of Ψ reflects the net flow around the island. To solve the values for each island in the model domain, a hole relaxation method is used to solve for Ψ. This requires the divergence of the surface pressure to vanish along a line integral taken around the island. To solve for this Equations 4.16 and 4.17 are vertically averaged and integrated around the coast of the island. The contribution due to surface pressure is then set to zero. This gives the equation,

$$\int \left[\left(\frac{1}{H \cos\phi} \frac{\partial^2 \Psi}{\partial t \partial \lambda} \right) d\phi - \left(\frac{\cos\phi}{H} \frac{\partial^2 \Psi}{\partial t \partial \phi} \right) d\lambda \right] = a \int \left[\frac{\partial \bar{v}'}{\partial t} d\phi + \cos\phi \frac{\partial \bar{u}'}{\partial t} d\lambda \right]. \tag{4.51}$$

A version more suitable for solving in the model can be obtained using Stokes Theorem,

$$\begin{aligned} &\frac{1}{a} \int_A \left[\frac{\partial}{\partial \lambda} \left(\frac{1}{H \cos\phi} \frac{\partial^2 \Psi}{\partial t \partial \lambda} \right) + \frac{\partial}{\partial \phi} \left(\frac{\cos\phi}{H} \frac{\partial^2 \Psi}{\partial t \partial \phi} \right) \right] dA \\ &\quad = \int_A \left[\frac{\partial}{\partial \lambda} \left(\frac{\partial \bar{v}'}{\partial t} \right) - \frac{\partial}{\partial \phi} \left(\cos\phi \frac{\partial \bar{u}'}{\partial t} \right) \right] dA. \end{aligned} \tag{4.52}$$

4.3.2 Sea bed boundary conditions

The sea bed is a model coordinate surface so there is no flow through it. This gives the boundary condition

$$\omega = 0. \tag{4.53}$$

The sea bed could also apply drag to the ocean, this is included through the bottom stress components, τ_B^λ and τ_B^ϕ, where

$$\rho_0 A_v \frac{\partial u}{\partial \sigma} = H \tau_B^\lambda, \tag{4.54}$$

$$\rho_0 A_v \frac{\partial v}{\partial \sigma} = H \tau_B^\phi. \tag{4.55}$$

In this application a free-slip condition has been assumed, i.e.,

$$\tau_B^{\lambda} = \tau_B^{\phi} = 0. \tag{4.56}$$

This reduces the boundary conditions to

$$\frac{\partial u}{\partial \sigma} = \frac{\partial v}{\partial \sigma} = 0. \tag{4.57}$$

At the sea bed, as with the coast and grounding line boundary, no heat or salt flux across the boundaries is allowed, i.e.,

$$\frac{\partial T}{\partial \sigma} = 0. \tag{4.58}$$

4.3.3 Ice shelf base boundary conditions

The boundary between the ice shelf and the ocean is distinctive in ocean modelling. The features which make it unique were outlined in Chapter 1. Here the implementation of these processes within the model are presented.

At the ice shelf-ocean interface the potential temperature gradient can be calculated in terms of the heat flux, Q_T,

$$\rho_0 C_{pw} K_v \frac{\partial \theta}{\partial \sigma} = H Q_T, \tag{4.59}$$

where Q_T is given by

$$Q_T = \rho_0 C_{pw} \gamma_t (T_{ice} - T_w). \tag{4.60}$$

Here, ρ_0 is a typical water density (1028 kgm^{-3}), γ_t is the turbulent heat exchange coefficient (1×10^{-4} ms^{-1}) [Hellmer and Olbers, 1989], C_{pw} is the specific heat capacity (3950 Jkg^{-1}°C^{-1}), T_w is the water temperature adjacent to the ice shelf-ocean interface, and T_{ice} is the ice temperature at the interface. The ice is assumed to be at the in situ freezing temperature for water. This is calculated from

$$T_{ice} = a - bP_{ice} - cS_w, \tag{4.61}$$

where P_{ice} is the pressure at the ice shelf-ocean interface, which is equivalent to p_S in Equations 4.16 and 4.17, S_w is the salinity of the water adjacent to the ice shelf-ocean interface, and the coefficients a, b, and c are, respectively, 0.094°C, 7.53×10^{-8}°CPa^{-1}, and 0.057°C.

In this parameterisation of the heat flux, the argument of Determann and Gerdes [1994] is followed. If there is only a linear temperature gradient through the ice shelf then the sensible heat flux through the ice shelf may be ignored, as it is of order ~0.1 Wm^{-2}, significantly less than the other heat fluxes which are in the order of ~10 Wm^{-2}.

As the sensible heat flux into the ice shelf has been ignored, Q_T is balanced by the latent heat flux, Q_T^B, i.e. $Q_T = Q_T^B$. The latent heat flux is

$$Q_T^B = -\rho_{ice} L m \tag{4.62}$$

where ρ_{ice} is a typical density for ice (915 kgm^{-3}), L is the latent heat of fusion (3.34×10^5 Jkg^{-1}), and m is the melt (freezing) rate of ice.

The salt flux is dependent on the salinity of the ice at the base of the ice shelf. Analysis of marine ice sampled on the Ronne Ice Shelf [Oerter et al., 1992] found salinities much less than those found in sea ice, suggesting that almost all of the salt is rejected during freezing. This is supported by the findings of Morgan [1972], who found low salinities in what he considered was marine ice, near the base of the Amery Ice Shelf. Thus, the salinity of the salt flux can be assumed to be independent of whether marine ice or meteoric ice is melting or freezing. Using this assumption, the salt flux at the top of the water column, Q_S, can be formulated in terms of the melt rate and a reference salinity ($S_0 = 35.0$ PSU);

$$Q_S = -\rho_{ice} m S_0. \tag{4.63}$$

The boundary condition on the salinity can be formulated in a similar way to the condition for potential temperature;

$$\rho_0 K_v \frac{\partial S}{\partial \sigma} = H Q_S. \tag{4.64}$$

In addition to the tracer boundary conditions, there are two other boundary conditions. Both are similar to those at the sea bed. The first,

$$\omega = 0, \tag{4.65}$$

ensures no flow from the ocean into the ice shelf. The second,

$$\rho_0 A_v \frac{\partial u}{\partial \sigma} = H \tau_S^\lambda, \tag{4.66}$$

$$\rho_0 A_v \frac{\partial v}{\partial \sigma} = H \tau_S^\phi, \tag{4.67}$$

relates to the surface stress, τ_S^λ and τ_S^ϕ, applied to the top of the water column. In most applications of ocean models τ_S^λ and τ_S^ϕ are wind stresses. Under the ice shelf no wind stress is able to act on the top of the water. It is also assumed the ice shelf is a free-slip surface. Hence the boundary condition reduces to

$$\frac{\partial u}{\partial \sigma} = \frac{\partial v}{\partial \sigma} = 0. \tag{4.68}$$

4.3.4 Open ocean tracer boundary conditions

Along the open ocean the tracer boundary conditions used in the model are based on those used in the Fine Resolution Antarctic Model [The FRAM Group, 1991]. These boundary conditions were described by Stevens [1990, 1991].

In the model the open ocean boundary is set to lie along a line of constant latitude, and any flow across the boundary is assumed to occur perpendicular to the boundary.

The boundary conditions for the tracers are implemented differently depending on whether the boundary point is located in an inflow or outflow region.

This distinction is made since if the velocity on the open boundary is directed out of the domain, then it is likely that the values of tracers on the open ocean boundary will have been determined by processes inside the domain. Similarly, in inflowing regions it would be expected processes outside the domain would be most important and hence boundary forcing values should influence the model.

The value of tracers at the boundary in outflow regions are found using an approach developed by Orlanski [1976]. This approach allows plane waves to pass through the boundary. This condition has been further developed by Stevens [1990, 1991] with the inclusion of diffusive terms and a correcting phase speed, c_T, designed to enhance the propagation of internal waves out through the boundary. The equation used in outflow regions is

$$\frac{\partial T}{\partial t} + \frac{v + c_T}{a}\frac{\partial T}{\partial \phi} = F^T. \tag{4.69}$$

The correcting phase speed is calculated, just inside the boundary at the previous time step in the model, from the finite difference form of the equation

$$\frac{\partial T}{\partial t} + \frac{c_T}{a}\frac{\partial T}{\partial \phi} = 0, \tag{4.70}$$

by using forward and upstream differencing. This gives the expression

$$c^n_{T\,i,k} = -\frac{a\Delta\phi}{\Delta t}\frac{T^n_{i,J-1,k} - T^{n-1}_{i,J-1,k}}{T^{n-1}_{i,J-1,k} - T^{n-1}_{i,J-2,k}} \tag{4.71}$$

for $0 \leq c^n_{T\,i,k} \leq \frac{a\Delta\phi}{\Delta t}$, where i and k are any points on the boundary row J, and n denotes the current time step. Model stability requires $c^n_{T\,i,k}$ to remain within these bounds, and it is reset to $\frac{a\Delta\phi}{\Delta t}$ if it exceeds the bounds.

The finite difference form of Equation 4.69 used in the model is

$$\frac{T^{n+1}_{i,J,k} - T^n_{i,J,k}}{\Delta t} = -\frac{c^n_{T\,i,k} + v^n_{i,J-1,k}}{a}\frac{T^n_{i,J,k} - T^n_{i,J-1,k}}{\Delta\phi} + F^{T\,n}_{i,J,k}. \tag{4.72}$$

In this equation forward differences are used instead of the usual central differences for time differencing. The advective term is in a non-conservative form using upstream differencing. This enables the advective term to be retained without including unknown terms from outside the domain. In the diffusion terms, any unknown terms from outside the domain which are required by the second derivatives, are set equal to the value on the boundary.

The application of the outflow boundary condition is dependent on the values of v and c_T. One or both of v and c_T must be positive at the outflow, if either term is negative it is set to zero. If both terms are negative or zero then the inflow boundary conditions are used.

In the inflow regions tracer values on the boundary can in principle be set to any prescribed value. However, to avoid sharp discontinuities at the boundary between inflowing and outflowing regions and between different time steps when a region may change between inflow and outflow, the tracer field inside the domain is relaxed to a prescribed field, i.e.,

$$\frac{\partial T}{\partial t} = \frac{1}{\alpha}(T_b - T), \tag{4.73}$$

where α is the time scale over which relaxation takes place, and T_b is the tracer value prescribed on the boundary. The impact of varying α on the model results are considered in Section 5.4.

The prescribed salinity and potential temperature fields used in this model are described in Section 4.6.

4.3.5 Open ocean velocity and streamfunction boundary conditions

The boundary conditions for the velocity and streamfunction are important in determining the flow across the ice front. In the model the barotropic (external mode) and baroclinic (internal mode) components of velocity are solved separately, so boundary conditions are required for both components.

For the internal mode velocities, $\hat{u}$ and $\hat{v}$, the velocity field at the open boundary is calculated from linear forms of Equations 4.7 and 4.8. The nonlinear terms can be neglected safely along the boundary, as they are generally small in comparison with other terms in the equation. The equations are

$$\frac{\partial \hat{u}}{\partial t} - f\hat{v} = -\frac{1}{a\rho_0 \cos\phi}\left(\frac{\partial p}{\partial \lambda} + g\rho H \frac{\partial \sigma}{\partial \lambda}\right) + F^u, \tag{4.74}$$

$$\frac{\partial \hat{v}}{\partial t} + f\hat{u} = -\frac{1}{a\rho_0}\left(\frac{\partial p}{\partial \phi} + g\rho H \frac{\partial \sigma}{\partial \phi}\right) + F^v. \tag{4.75}$$

The omission of the nonlinear advection terms also has the advantage that unknown velocity values from outside the domain are not required. Any terms required for calculating the diffusion which lie outside the boundary are reset to the value on the boundary, in a similar manner to the outflow tracer boundary conditions.

The boundary condition for the barotropic components of velocity is to specify either the streamfunction or its gradient along the open boundary, as $\bar{u}$ and $\bar{v}$ are found through the time evolution equation for the streamfunction (Ψ). The tracer and baroclinic velocity boundary conditions are found by modifying the usual time evolution equations to account for boundary processes. A similar approach cannot easily be used as the time evolution equation for the streamfunction (Equation 4.26) has no generally useful simplifications [Stevens, 1990]. Here two possible boundary conditions are proposed. The impact of the different boundary conditions on the results of the model is then considered fully in Chapter 5.

The large step in the water column thickness which occurs at the ice front between the cavity and the open ocean, could be expected to form a barrier to cross-boundary barotropic flow. Thus setting $\Psi = 0$ may be a suitable boundary condition. Setting $\Psi = 0$ will restrict only the barotropic velocity component, it will not eliminate all cross-boundary exchange as $\hat{u}$ and $\hat{v}$ are not necessarily zero. There is also exchange through the tracer and baroclinic velocity boundary conditions. Although the net mass transport in each column at the ice front will vanish.

Flow across the ice front is likely to strongly influence the ocean cavity through the transport of heat, salt and momentum across the ice front, hence damping the barotropic transport may be unrealistic. Stevens [1990, 1991] suggested the streamfunction gradient along the boundary could be found from the Sverdrup balance. This is unsuitable for this model, because for the Sverdrup balance to be calculated non-zero surface stresses at the ice front would be needed.

An alternative method of prescribing a streamfunction at the boundary is to utilise the prescribed potential temperature and salinity fields, already required for the tracer boundary conditions. By assuming the potential temperature and salinity fields are in geostrophic balance, the depth integrated velocity across the ice front can be determined, and from this the streamfunction gradient along the ice front is implied.

Using the assumption of geostrophic balance, the vertical gradient of the horizontal velocity is given by

$$\frac{\partial v_g}{\partial \sigma} = \frac{gH}{af\rho\cos\phi}\frac{\partial \rho}{\partial \lambda}. \tag{4.76}$$

This equation is solved to give the geostrophic velocity v_g, at each grid cell on the boundary, using central differences for the derivative of ρ. The vertical velocity derivatives are then integrated vertically from the sea bed, assuming it is a level of no motion. Conservation of mass is not guaranteed when calculating geostrophic velocity fields. To ensure mass is conserved in the cross-boundary flow a correcting velocity, v_c, is found so

$$\int\int (v_g - v_c)\, d\sigma\, d\lambda = 0. \tag{4.77}$$

On a significant portion of the boundary in the present model $v_g = 0$ and applying a correcting velocity in these areas would introduce a cross-boundary flow inconsistent with the $\frac{\partial \rho}{\partial \lambda} = 0$ density gradient. A piecewise correcting velocity is used to avoid this problem. It is defined as

$$v_c = 0 \quad \text{if} \quad v_g = 0, \tag{4.78}$$

$$v_c = \frac{1}{A}\int\int v_g\, d\sigma\, d\lambda \quad \text{if} \quad v_g \neq 0. \tag{4.79}$$

The integral in Equation 4.79 is taken over the area (A) where $v_g \neq 0$.

With the geostrophic and correcting velocities prescribed, the boundary condition for the streamfunction can be found. Using Equations 4.22 and 4.24 it becomes,

$$\frac{\partial \Psi}{\partial \lambda} = a\cos\phi \int_{-1}^{0} (v_g - v_c)\, d\sigma. \tag{4.80}$$

Although Equation 4.24 indicates the specification of a boundary condition for the longitudinal derivative of the streamfunction would specify the cross-boundary barotropic velocity components, in the model this does not follow directly. The offset between the streamfunction grid points and the velocity grid points (Figure 4.1a) means the calculation of the barotropic components

Table 4.1: Vertical layer thicknesses as a percentage of the water column depth, numbered from top to bottom.

layer	1	2	3	4	5	6	7	8	9	10
%	2.5	3.2	4.2	5.4	6.9	9.0	11.5	14.8	18.8	23.7

of velocity involves utilising values of Ψ at the surrounding four streamfunction grid points. Hence, if the streamfunction boundary condition is applied only on the streamfunction boundary row, only half of the four streamfunction values required to determine $\bar{v}$ are specified.

The method of solving for Ψ in the model allows for the possibility of the streamfunction being specified on only the streamfunction boundary row, or on both the streamfunction boundary row and the row adjacent to the boundary inside the domain. If the streamfunction is only specified on the boundary row, then the barotropic velocities are partly determined by the solution of the streamfunction in the model interior. If the streamfunction is specified on both the boundary and adjacent streamfunction rows, then the barotropic components of velocity on the velocity boundary row are set by the boundary condition.

The two different methods of specifying the mass transport at the boundary are likely to lead to different solutions of the model. The probable reason for this is the extra freedom the model has in determining the circulation near the ice front, when the boundary conditions are only set on the streamfunction boundary row. This choice could have a potentially significant impact on the temperature and salinity structure in the domain. This is because changes in the circulation will change the areas where inflow and outflow occur, thus changing the exchange of heat and salt across the open ocean boundary.

When both the boundary and the adjacent row are specified, there are potential problems in effectively ensuring conservation of mass through the boundary velocity row. These arise from the need to specify through the streamfunction both the along boundary ($\bar{u}$) and the across boundary ($\bar{v}$) velocities. The simplest approach to this problem is to assume that the along boundary is zero, i.e., $\bar{u} = 0$. Then the across boundary velocity can be set by using the same streamfunction on the boundary row and the row adjacent to the boundary. In the case of the $\Psi = 0$ boundary condition this will also set $\bar{v} = 0$.

As the model allows for two alternate specifications of each boundary condition on the streamfunction, and by implication on the barotropic velocity, it is important both are trialled to examine which is more representative of the physical system being modelled.

4.4 Other model details

The model equations and boundary conditions described in the preceding sections are applied to the ocean cavity formed by the water column thickness

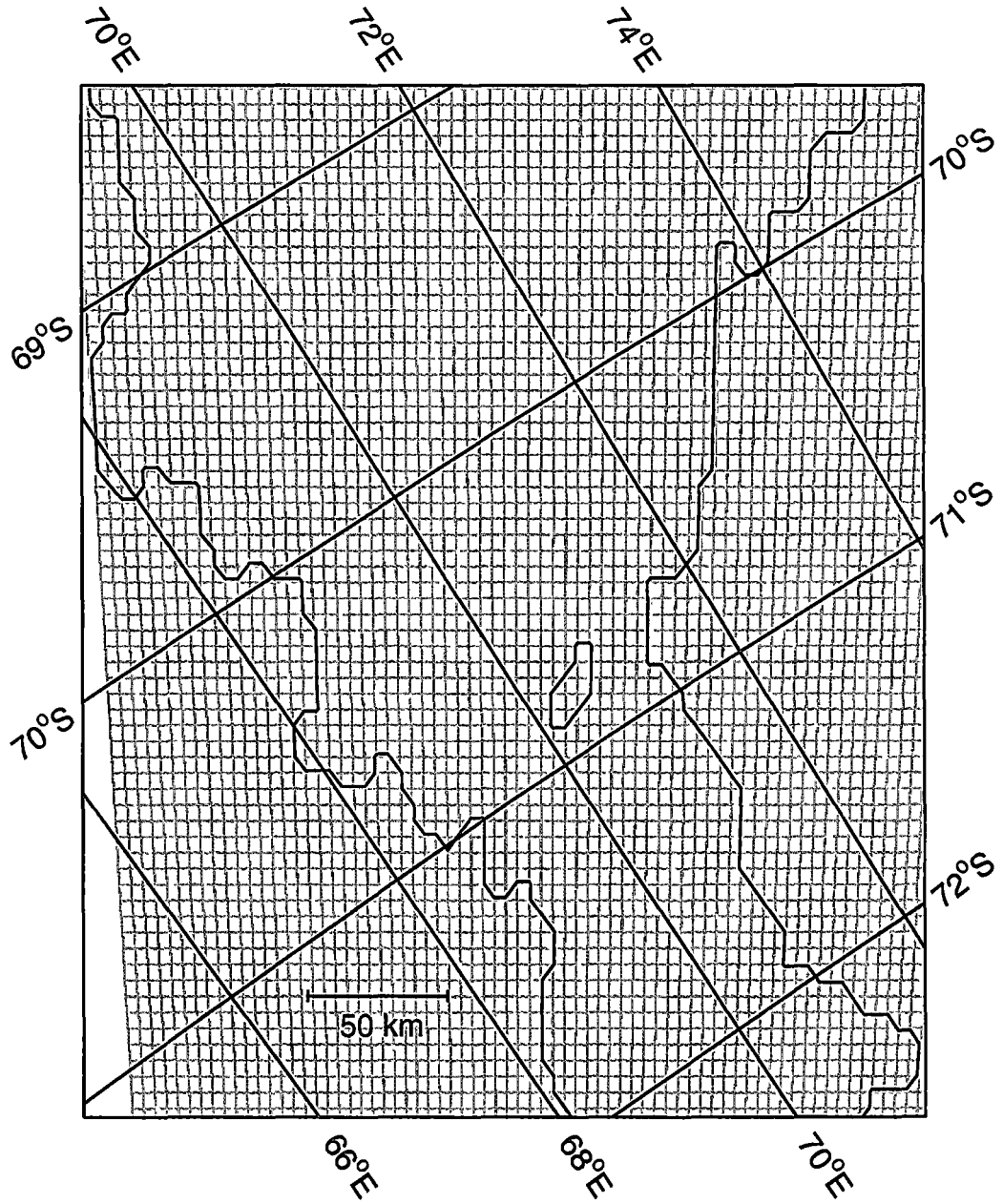

Figure 4.2: The horizontal grid used on the model domain. The outline of the ice shelf grounding line has been superimposed. Velocity points are solved where the grid lines intersect and tracer and streamfunction are solved in the middle of the boxes.

described in the following section. In the application used here the model has 10 σ-levels. The percentage thicknesses for all the layers are shown in Table 4.1. The 66 by 71 model grid, shown in Figure 4.2, has a resolution in the rotated coordinates of 0.05° by 0.1°. This gives a mean resolution of 5.5 km by 4.3 km.

For all of the different model scenarios the model was spun up from the same initial conditions for 5×10^8 s (~15.8 years). This spin up time is approximately six times the estimated flushing time for the cavity under the Amery Ice Shelf.

The temperature of each column of water was set at the in situ freezing temperature at the top of the water column, for a salinity of 35 PSU. To ensure the water column was initially stratified the salinity was increased down the water column by 0.01 PSU per model level. The salinity at the top of water column (S_T) was fixed by the depth of the ice shelf draft (d) at $S_T = 34.65 - 2.8 \times 10^{-4} d$.

4.5 Model topography

The finite difference model equations are implemented on a σ-coordinate version of the Arakawa 'B' grid (Section 4.2). The horizontal extent of the model domain that this grid is applied to is defined by the water column thickness, which is the thickness of the ocean between the ice shelf and the sea bed. To find the water column thickness for the Amery Ice Shelf, the depth below sea level of the ice shelf draft and sea bed were found and the difference taken.

An important constraint on the grid imposed by the model design is that the ice front has to be straight, and run along a single model latitude line. The natural ice front of the Amery Ice Shelf fulfils neither of these criteria. To fulfil the criteria the ice front was straightened, and the model domain was rotated by 12° (Figure 4.3).

The ice shelf draft was calculated from ice shelf thickness data collected using airborne radio echo sounding (RES), by the Australian Antarctic Division in the 1988-89 and 1989-90 summer seasons [Ian Allison, Pers. Comm.]. The flight-lines along which the data was collected are shown in Figure 4.3. As can be seen from the figure these flight-lines were irregularly spaced and quite sparse near the ice front. These observations were processed to remove any doubtful observations, including those where the RES had most likely found the interface between the meteoric and marine ice. This processing is the cause of the gaps in the flight-lines shown in Figure 4.3.

The high resolution grid being used in the model (Figure 4.2), required the ice thickness to be smoothed and interpolated. This was done after the data was rotated from latitude and longitude coordinates to the model coordinates. The interpolation of the ice shelf thickness at grid point (i, j) was done using the inverse distance method. This gave an ice shelf thickness $z'(i, j)$ of

$$z'(i,j) = \frac{\sum(w_k^{-4} z_k)}{\sum w_k^{-4}}, \tag{4.81}$$

where z_k, is the 'clean' RES ice shelf thickness data, and w_k, is the distance between the model grid point and the position of the RES ice shelf thickness

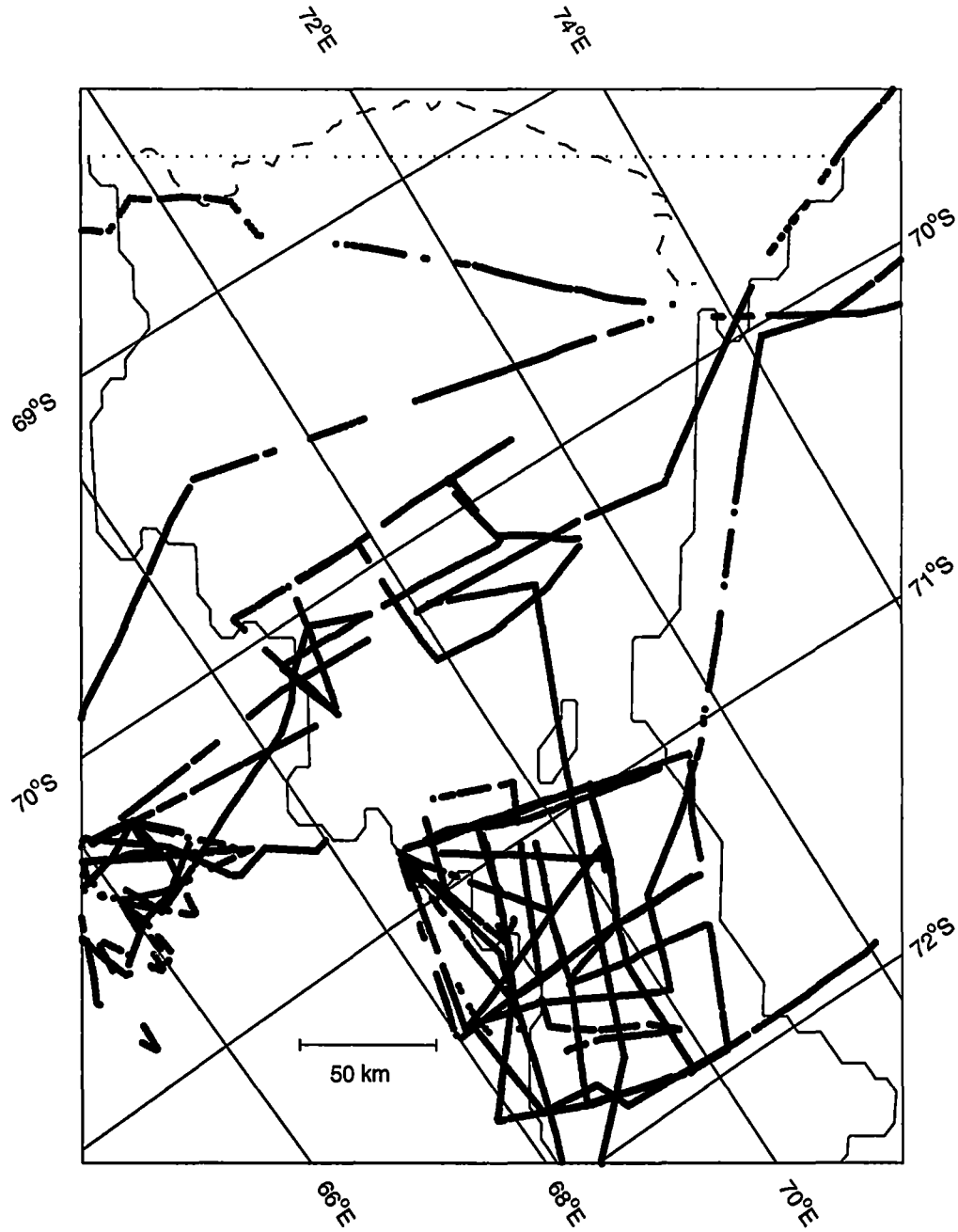

Figure 4.3: The model ice shelf extent, showing RES observations where individual non-zero ice thicknesses were recorded (dots). The original (1988) ice front position (dashed line) is also shown along with the model ice front position (dotted line).

observation.

No maximum distance between grid point and the RES data positions was used, this allowed the interpolation scheme to interpolate in areas where the data was particularly sparse, and to extend the ice shelf in areas out to the straight ice front edge needed by the model. The risk in having no maximum or cutoff distance in the inverse distance interpolation is that large numbers of RES data positions at a distance from the interpolation grid point can swamp a small amount of data close to the grid point. This effect has been minimised by taking the inverse distance to the power of four. This strongly enhances weighting for RES data close to the model grid points.

After interpolation the ice shelf thickness was converted to ice shelf draft by applying the following buoyancy relation [Jenkins and Doake, 1991]:

$$d = \frac{\rho_i}{\rho_w}(z_f - z'), \tag{4.82}$$

where d is the ice shelf draft, ρ_i is the density of ice (920 kgm^{-3}), ρ_w is the density for water (1028 kgm^{-3}) and z_f represents the 'thickness' of air in the firn layer of the ice shelf. The values for the densities and firn thickness were determined empirically for this study from surface elevation, and ice thickness data for the central flowline (Figure 3.3) presented in Budd et al [1982].

Using the data from Budd et al [1982], $z_f = 15.6$ m was the mean value for z_f calculated at 30 positions along the approximately north-south traverse line. Comparison of the draft calculated from Equation 4.82 and the observed ice shelf draft along the traverse line, shows a difference of less than 5% for most of the ice shelf. In the 50 km nearest the ice front the difference trend increased reaching ~30% at the ice front. This reflects changes in the mean density near the ice front, either from increased accumulation on the surface, which would generate a thicker layer of firn, or from the accumulation of marine ice on the base of the ice shelf.

The other data field needed to calculate the water column thickness is the sea bed position. The sea bed position under an ice shelf can be determined from seismic observations. Using the bedrock map produced by Kurinin and Aleshkova [1987], the contours of constant depth under the ice shelf were extracted.

The contours were then treated in a similar manner to the ice shelf thickness data. The sea bed contours were interpolated onto a similar grid using the same inverse distance method, and then rotated on to the model grid.

After calculating the sea bed position and the ice shelf draft it was possible to calculate the actual extent of the ocean cavity under the Amery Ice Shelf by calculating the water column thickness. The model has several constraints on the water column thickness, which were also applied. These constraints were based on model resolution and numerical stability concerns. In no part of the domain was the water column thickness allowed to be less than 50 m. A water column of this thickness would lead to very thin σ-layers near the top of the water column, which would restrict the length of the time step needed to ensure numerical stability in the model. For similar reasons, three or more grid points were generally needed to resolve any channels around islands or grounded

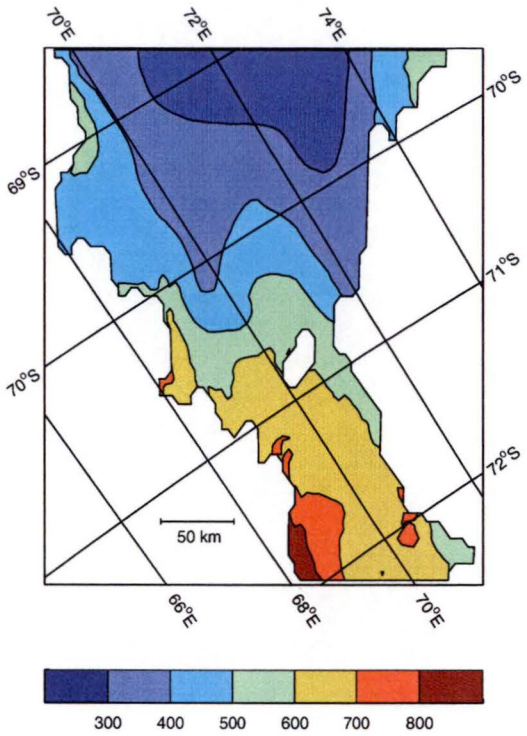

Figure 4.4: The model ice shelf draft in metres.

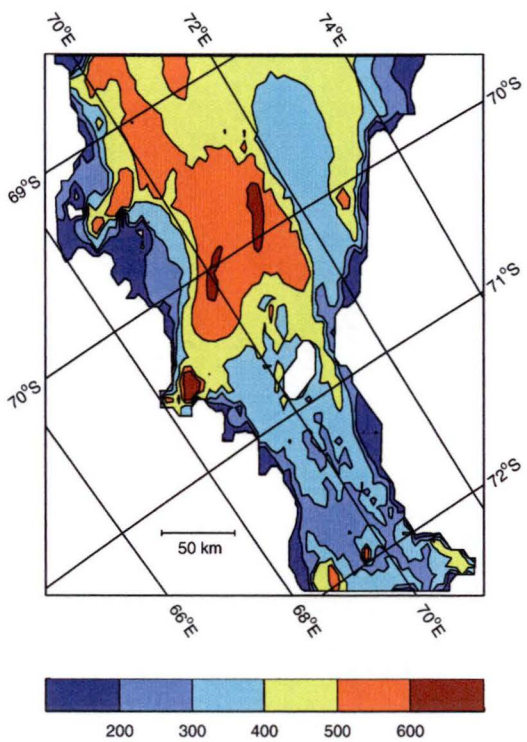

Figure 4.5: The model water column thickness in metres.

zones in the model. Implementation of these rules excluded some areas with a positive water column thickness from the main cavity. These areas were ignored by setting the water column to zero.

After determining the extent of the ocean cavity by calculating the water column thickness, the ice shelf draft data set was reduced. Only values over the ocean cavity were retained. In addition the ice shelf draft was smoothed. This was partly an attempt to reduce the bad fit in some areas, but was mainly done to reduce noise in the ice shelf melting and freezing rates. This noise occurred because of localised 'ice pumps' forming between neighbouring grid cells. The final smoothed version of the ice shelf draft is presented in Figure 4.4.

Any substantial changes resulting from the smoothing of the ice shelf draft were assimilated by altering the water column thickness, so that the sea bed position remained constant. The water column thickness used in the model is shown in Figure 4.5

The ice shelf draft and water column thickness shown in Figures 4.4 and 4.5 have several features which may be artifacts of the processing. The most distinct of these is the island in the ocean cavity at 70.8°S 71.5°E. This has been named the Central Grounded Zone. In this area there is a prominent sea-mount [Kurinin and Aleshkova, 1987], which comes close to the base of the ice shelf. It is unclear if the ice shelf is fully grounded on this feature. In this study it has been treated as fully grounded, because there is insufficient water column thickness between the sea mount and the ice shelf base.

4.6 Open ocean boundary data sets

Along the northern boundary of the model the ocean cavity interacts with the waters of Prydz Bay through a series of boundary conditions described in Section 4.3.4. Where water is flowing into the domain, its temperature and salinity are relaxed to prescribed salinity and temperature fields. These temperature and salinity fields are based on CTD profile data collected during the FISHOG cruise (Section 3.1).

Data used was from the CTD profiles near the ice front. The profiles chosen were 114, 115, 116, 117, 118, 142, and 143, the locations of which are shown in Figure 3.1. The latitude and longitude of each data point was translated into the model coordinates, and then by ignoring the 'latitude' part of the model coordinate each profile was mapped to the ice front.

This gave an unevenly spaced data set in one dimension, the model 'longitude', and regularly spaced data in the vertical dimension, as the profile data was binned with 2 db intervals. To achieve the desired data set, the profiles had to be fitted to an evenly spaced grid, with 0.1° intervals in the horizontal and 10 m intervals in the vertical. The vertical gridding was done by binning the 2 db data into 10 m bins.

This data was then turned into a rectangular data set so it could be interpolated horizontally, and also to ensure there were no gaps between the profile bottom, and the sea bed along the ice front. The gaps could arise from the horizontal projection of the profiles onto the ice front, and the possible change

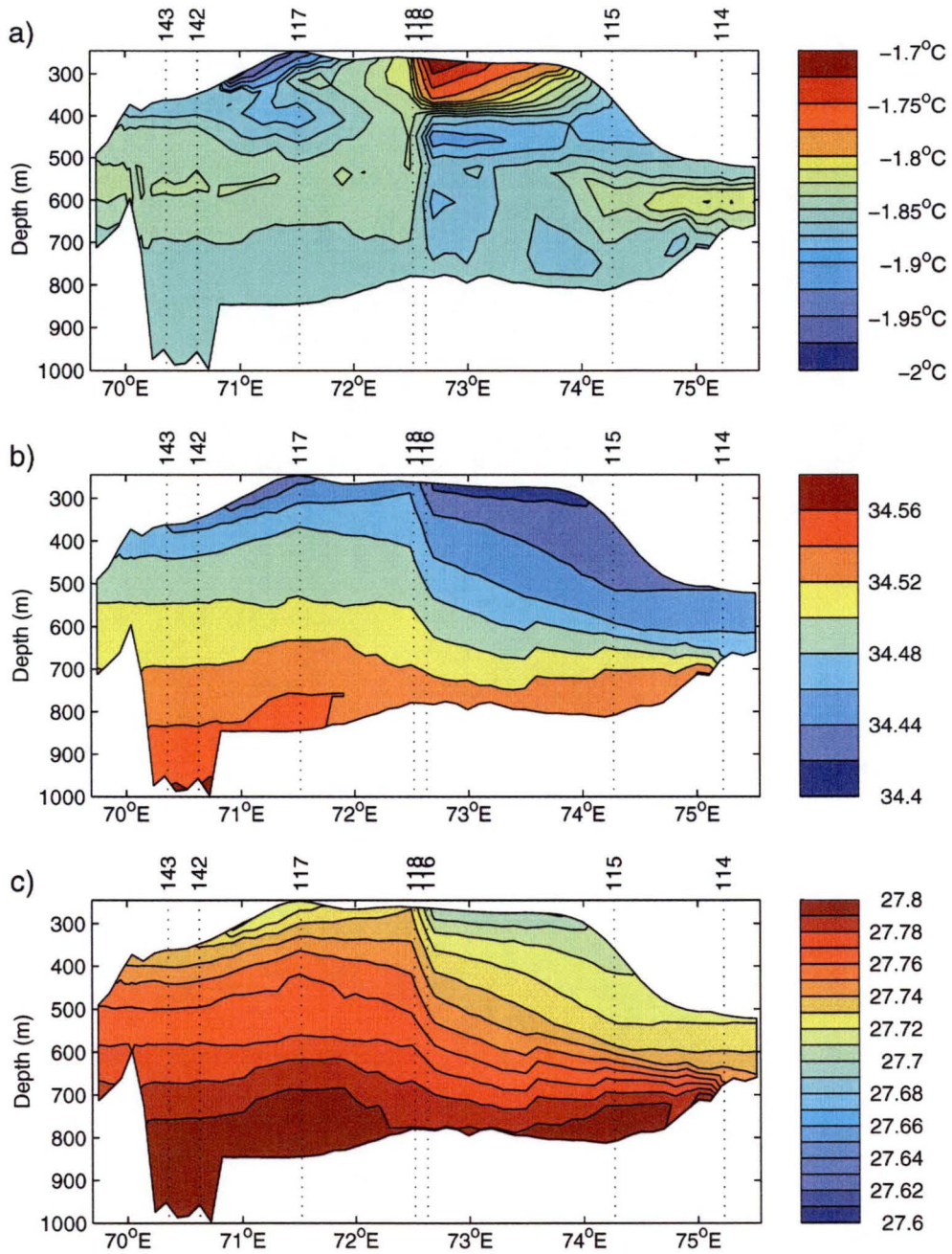

Figure 4.6: The a) potential temperature, b) salinity along the open ocean boundary, and c) potential density. The numbered dotted lines indicate the positions in the potential temperature, and salinity fields of the FISHOG CTD casts used in the interpolation.

in depth from where the casts were collected to their location on the ice front. The dimensions of the rectangular data set were chosen so all profiles reached to the depth of the deepest profile. This extension of the data set was done by filling in the rest of the data set with the nearest deeper cast. This was performed for convenience, under the assumption that most of the data below the normal profile bottom would be ignored in the process of fitting the gridded data to the σ-levels.

With the new profile data now reaching to the same depth on all profiles, they were linearly interpolated in the horizontal to give a column of data for each model grid point along the ice front.

The vertically and horizontally gridded temperature data sets were fitted within the model code to the σ-levels, by mapping the closest boundary data grid point above the σ-layer on to the σ-layer. This is done independently for each σ-layer on each column along the ice front.

The temperature, salinity and the corresponding potential density fields at the ice front, used within the model, are shown in Figure 4.6. In the temperature field there are four noticeable features. These are the cold area of Ice Shelf Water around 71.2°E, the warm core of water adjacent to the ice shelf near 73°E, the cold waters beneath this, and the core of -1.85°C water on the eastern side on the section. Apart from these four features the temperature is relatively constant across the section. This contrasts with the salinity which has a distinct stratification between the top and the bottom of the water column. The stratification of the salinity leads to a stable water column, This can be seen in the potential density field, which is clearly dominated by salinity.

Chapter 5

Investigating different open ocean boundary conditions

In this chapter the effects of different momentum boundary conditions at the ice front on the ocean circulation, temperature and salinity distribution, and the mass balance of the Amery Ice Shelf are investigated.

The chapter is divided into two parts: first, a general description of the results from the numerical model runs using the different boundary conditions, and second, a comparison between the results and observations. Because of the lack of subice shelf observations the comparison between model results and observations is not direct. Instead the model results are used to derive quantities for comparison with observations.

The first four sections in this chapter discuss the model results. First the simplest case, that of a closed northern boundary is considered. The next two sections consider the effects of applying boundary conditions to either the streamfunction or the barotropic velocity, as discussed in Section 4.3.5. The first scenario considers this problem for a zero streamfunction on the boundary. The second scenario considers the geostrophically based along boundary streamfunction gradient. In both sections setting the streamfunction is not equivalent to setting the barotropic velocities, because of the offset between the streamfunction and velocity grid points (Figure 4.1a). This offset means that the four streamfunction points around each velocity point are used in determining the velocities, so that the barotropic velocities in the boundary velocity row at the ice front are partly determined by the prescribed streamfunction and partly by the internally evolved streamfunction.

The boundary conditions for temperature and salinity are applied, as outlined in Section 4.3.4, in all of the scenarios examined, except the closed ocean boundary run. When the tracer boundary conditions are applied, it is important to consider what relaxation time scale should be imposed. In other studies of ocean circulation under ice shelves using this model Determann and Gerdes [1994] used a time period of 100 days for their theoretical ice shelf. Determann et al. [1994] also used a time period of 100 days for the ocean cavity under the Filchner-Ronne Ice Shelf. In this study, 80 days has been selected as a suitable time scale for the relaxation constant. This reflects the smaller cavity size of the Amery Ice Shelf, and hence an expectation that the flushing time for the ocean

cavity would be smaller than for the Filchner-Ronne Ice Shelf. The affects of varying this parameter are also investigated.

5.1 Closed ocean boundary

A closed boundary is the simplest boundary condition which can be applied at the northern boundary. It is worth considering as an initial model scenario for the ocean cavity under the Amery Ice Shelf, despite a closed ocean boundary being unrealistic. This is because it allows the influence of the open ocean in later model runs on the ocean circulation, temperature structure and ice shelf-ocean interaction to be clearly seen. The northern boundary is closed by using the same boundary conditions which are used on the coast or grounding line boundaries (Section 4.3.1).

The ocean circulation under the ice shelf is intimately linked to the forcing provided by the ice shelf. This forcing is dominant when the additional exchange of heat and salt across the ice front, which is important for real ocean dynamics, is eliminated. The amount of interaction between the ice shelf and the ocean can be characterised by the rates of melting and freezing at the ice shelf-ocean interface. Where melting occurs the top of the water column is cooled and freshened, and where freezing occurs salt is rejected and heat is transfered to the ocean. For a fixed ice shelf draft and an ocean initially at rest this typically generates a thermohaline circulation through the buoyancy of the freshened melt water.

Figure 5.1 shows the mean rates of melting and freezing at the ice shelf-ocean interface over the last approximately three months of the model run[1]. The highest rates of melting occur where they are expected, in the south-east and south-west of the domain where the ice shelf is thickest. High rates of melting also occur in areas where the ice shelf draft is not the determining factor. In these areas (e.g., around 70.1°S 71.5°E) horizontally advected water comes into contact with a thickening ice shelf. Here, the steep ice shelf draft gradients drive the water down slope where it is able to drive melting, because of the increased temperature gradient between the water and the ice shelf. The temperature gradient is increased in down slope flow conditions, because the ice shelf-ocean interface, which is at the in situ freezing temperature, cools with the increase in pressure.

The areas of freezing seem to be more closely linked to the underlying ocean circulation. The three extensive regions of freezing, in the channel to the east of the Central Ground Zone, around 70°S 70°E, and along the ice front, are all in areas where water cooled and freshened by melting at depth is rising in contact with the ice shelf.

The smaller localised areas of freezing, particularly in the south of the domain where the ice shelf is still comparatively thick, are caused by the same mechanism that generates the high freezing rates within the significant areas

[1]The melting and freezing rates in the thesis are mean rates calculated over the last 1×10^7 s of the model run

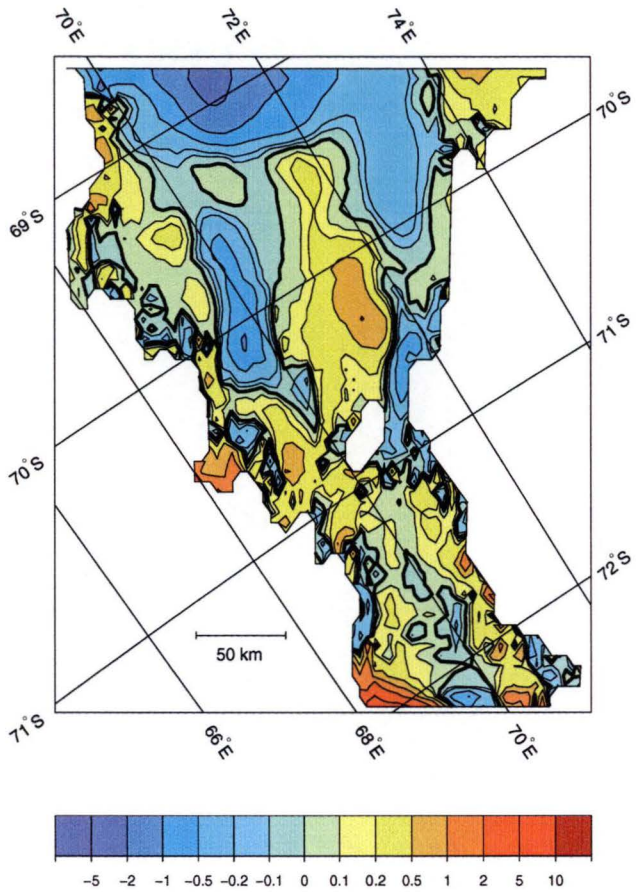

Figure 5.1: Melting (+) and freezing (-) rates for the closed boundary run in ma^{-1}. The bold contour denotes the boundary between melting and freezing.

of freezing; that is, steep local ice shelf gradients. These allow the rapid rise of supercooled water, which drives high freezing rates.

The overall effect of the melting and freezing at the ice shelf-ocean interface leads to a zero net mass loss to the ice shelf. This is as expected in this run, because with the northern boundary closed the only opportunity for mass exchange is with the ice shelf. The boundary conditions here do not allow for heat (or salt) loss through the ice shelf, so the ice shelf and ocean effectively form a closed system. The heat and salt exchange with the ice shelf is required to match the heat and salt exchange with the ice front, so with the ice front boundary closed heat and salt conservation ensure this is zero.

As with other applications of this model [Determann and Gerdes, 1994; Determann et al., 1994], the horizontal circulation is significantly stronger than the vertical (overturning) circulation. The horizontal circulation is mostly vertically coherent and is described clearly in terms of the vertically integrated streamfunction.

Figure 5.2 shows the vertically integrated streamfunction for the model run with a closed northern boundary[2]. Comparison between this figure and the water column thickness (Figure 4.5), shows the generally barotropic nature of

[2]The streamfunction presented is for the final time step of the model run

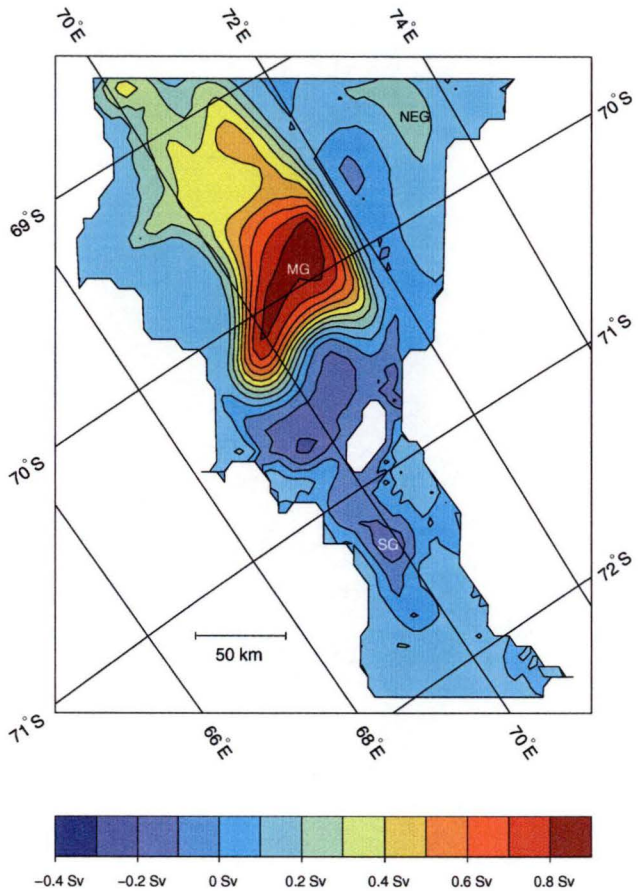

Figure 5.2: Vertically integrated streamfunction for the model run with a closed northern boundary. The main features discussed in the text, the Northeastern Gyre (NEG), the Main Gyre (MG) and the Southern Gyre (SG), are marked. Circulation is clockwise about positive features.

the flow. The major feature is the large clockwise circulating gyre in the north of the domain, the Main Gyre, which is bounded by the water column thickness on the south and east. It has a strength of approximately 0.87 Sv in its centre (69.8°S 71.7°E) which is situated in the area of greatest water column thickness. This gyre dominates flow in the north of the domain and accounts for most of the north-south transport.

The other major features of the horizontal circulation are the Northeastern Gyre, situated in the north-east corner of the domain and centred at about 69.5°S 73.5°E; the area of counterflow between the Northeastern Gyre and the Main Gyre; the South-Central Gyre, which lies to the south of the Main Gyre and to the west of the Central Grounded Zone; and the Southern Gyre, to the south of the Central Grounded Zone, is centred at about 71.3°S 69.7°E.

The flow south of the Main Gyre can be described in terms of the South-Central and Southern Gyres. These two gyres form part of a larger gyre which directs flow around and to the south of the Central Grounded Zone. Flow goes south along the western boundary, before turning east and flowing towards the Central Grounded Zone. Here it turns southwest and flows back towards the

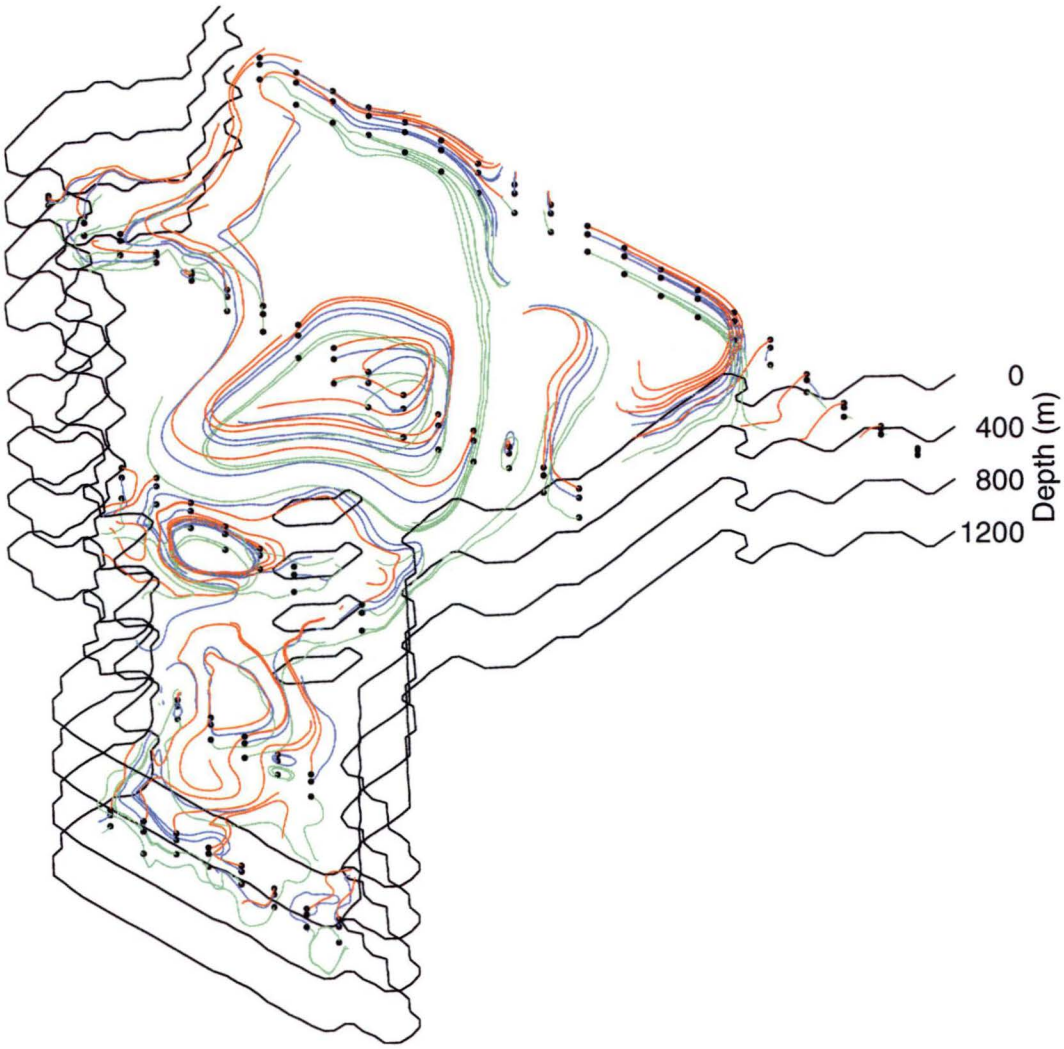

Figure 5.3: Pseudo-lagrangian tracer paths for the closed run. The dots show the release points for each tracer. The colours indicate the σ-layer on which the tracers were released: red layer 2, blue layer 5, and green layer 8.

western boundary, and from about 71.0°S it follows the western boundary until turning north from about 71.5°S. The general trend of this circulation is that from the southernmost point of the Southern Gyre the flow returns to the north before turning east and flowing through the channel to the east of the Central Grounded Zone. Between 71.5°S and the southern boundary the circulation is more complex and not easy to describe in terms of gyres or similar structures.

The area of counter flow between the Main and Northeastern Gyres forms in an area where the sea bed is shallow. This inhibits water from the Northeastern Gyre flowing far to the south. A strong current on the western side of the Main Gyre follows the topography. This is important, as it is an area of strong return flow from the south of the domain to the northern boundary.

The strength of the horizontal circulation in comparison to the vertical circulation can be seen in the pseudo-lagrangian tracer paths shown in Figure 5.3[3].

[3]The pseudo-lagrangian tracer paths presented are from the final time step of the model

The tracer paths are found by tracking particles through the three-dimensional velocity field from the spun up model run. They are not true lagrangian tracers as the velocity field is not time evolving but reused for each stepping calculation.

In Figure 5.3 the vertical circulation in most of the domain is weak with the flow being generally vertically coherent. This is the case in the areas of the Main, South-Central and Southern Gyres, all of which can be clearly seen in Figure 5.3. South of the Southern Gyre near the grounding line the tracer paths indicate the circulation is not vertically coherent. The lack of vertical coherence suggests that the topographic steering effects which influence the rest of the domain are much smaller. There are indications in the tracer paths that the deeper waters (green) are flowing south in some places, while the dominant trend of the upper level tracers (red) is northward. This indicates there is some vertical overturning occurring close to the grounding line. Since no pseudo-lagrangian tracers appear to follow an overturning path, vertical diffusion may be the dominant source of vertical mixing.

In other applications of this model [Determann and Gerdes, 1994; Grosfeld et al., 1997] the overturning circulation under the ice shelf was able to be partly described in terms of the zonally integrated streamfunction. In this model the zonally integrated streamfunction gives little useful information. This is for two reasons: the large variations in the zonal extent, and the vertically coherent flow in opposite directions in the cavity, e.g., in the area of the Main Gyre. These lead to biases in any estimation of the overturning streamfunction. Hence it is not presented in this thesis.

The local change in density levels shows the localised movement of water masses. In areas of heavy melting a cold and fresh melt-water layer forms at the top of the water column. As the locations of heavy melting are generally where the ice shelf is thick, the melt-water layer flows up the ice shelf. This allows warm and salty water to up-well and continue driving the melting. In areas of high melt this leads to very steep vertical gradients in density.

In contrast, areas of freezing lead to a more vertically coherent water column. As freezing effectively warms the water, and since the model assumes the frozen on ice has zero salinity, salt is rejected into the top of the water column. This warm, salty water drives strong overturning in the water column, which leads to gentle vertical density gradients in the water column. The effect of these mechanisms on the water column can be seen in three temperature cross-sections through the model domain. The locations of the cross-sections are shown in Figure 5.4.

Figure 5.5 shows three temperature cross-sections through the model domain. Sections A and B run north-south and Section C runs east-west[4]. The salinity cross-sections have not been shown, as processes occurring in the salinity cross-sections are similar to those occurring in the temperature cross-sections.

At the southern end of Section A (Figure 5.5a) there is a steep temperature gradient close to the ice shelf. This gradient is partly formed by the small amount of melting near the grounding line, but mainly by the westwards

run

[4]The temperature cross-sections presented are from the final time step of the model run.

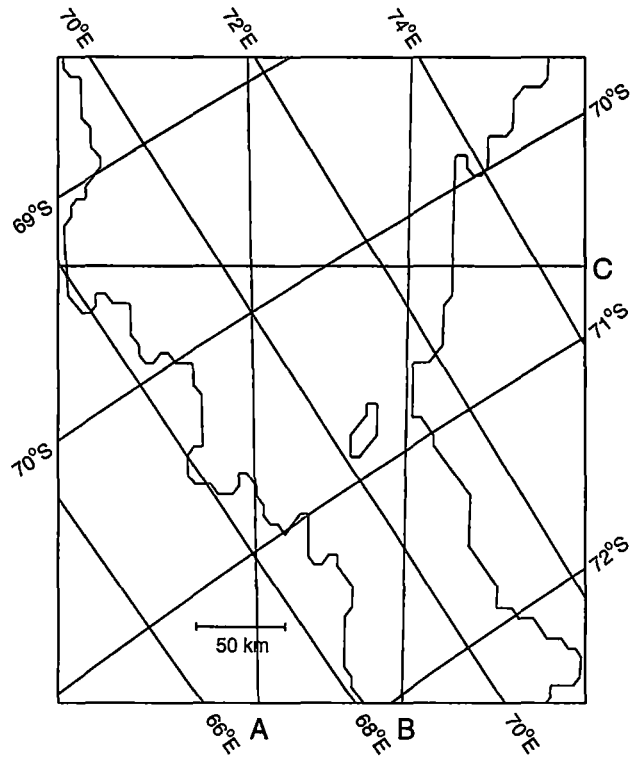

Figure 5.4: Positions of the three temperature cross-sections shown in Figure 5.5 and other figures.

advection of melt water through the section by the South-Central and Main Gyres. The supply of melt water helps drive the high freezing rates seen along the section (Figure 5.1). The freezing in the section leads to the thinning of the melt-water layer near 70°S. Continuing northwards the increased freezing drives enhanced vertical mixing through salt rejection. With continued freezing the distinct surface layer near the ice shelf disappears and the water becomes vertically well-mixed near the northern end of the cross-section. This is driven by salt rejection from freezing near the ice front, with peak freezing rates of ~ 3 ma^{-1} (Figure 5.1).

In Section B (Figure 5.5b) freezing near the ice front again forms a homogeneous water column. Close to the ice front the warmest and saltiest water is found in the domain. It forms because the weak local circulation in the Northeastern Gyre allows salt to be rejected over a longer time period. This compensates for freezing rates which are lower than in other areas. As with Section A melting is seen forming a cold and fresh melt-water layer at the top of the water column, between 70.8°S and 72°S. Upwelling is again occurring close to the southern grounding line. The melt-water layer thins rapidly while flowing through the channel to the east of the Central Grounded Zone (between 70.8°S and 71.0°S), as a large amount of freezing in the channel thins the melt-water layer. This behaviour is similar to that seen with the Plume Model by Jenkins [1991] (Section 2.3.2). It occurs in the channel to the east of the Grounded Zone, as here the mean flow direction allows melt-water to flow up

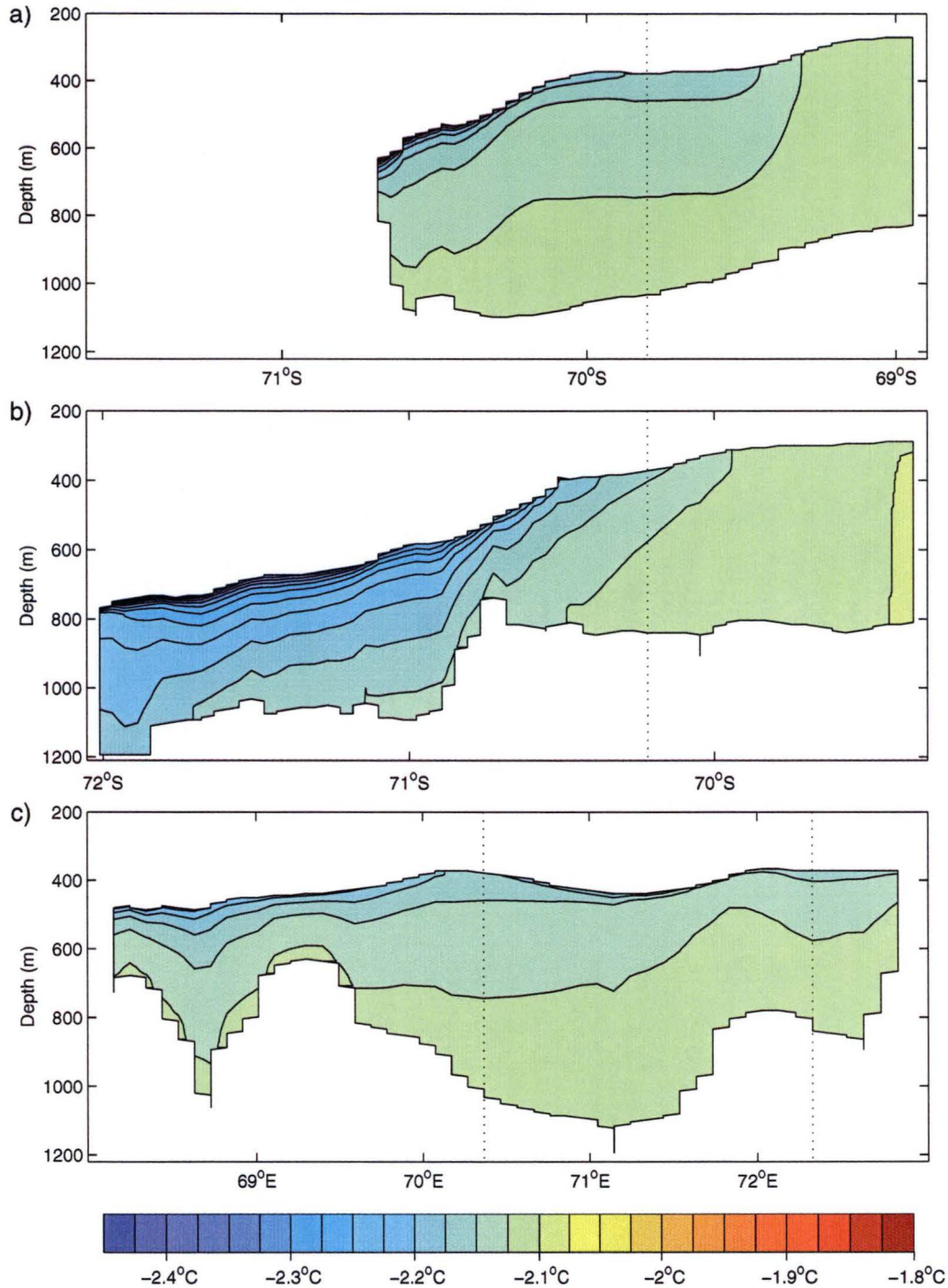

Figure 5.5: Temperature cross-sections of the model domain for the closed boundary run. a) Section A, b) Section B, and c) Section C. The locations of the cross-sections are shown in Figure 5.4. The dotted lines indicate where the cross-sections intersect.

slope in the channel, as was assumed in the Plume Model.

Section C (Figure 5.5c) is different from the other two sections as it runs east-west, perpendicular to the orientation of the overturning circulation assumed by two-dimensional models. It highlights features of the circulation not seen in Sections A and B, particularly in the Main Gyre through which it runs.

In the area of the Main Gyre (approximately between 69.8°E and 71.8°E) the water mass being transported south on the eastern side of the gyre is warmer and better mixed than the northbound water on the western side of the gyre. On both sides of the gyre the anticipated vertical temperature structures from the high melting or freezing rates seen in Figure 5.1 are not generated. On the eastern side of the gyre (~71.3°E), where the model reports melt rates of up to ~0.75 ma^{-1}, no significant melt-water layer forms. The layer of melt-water on the western side of the gyre does not appear to thin significantly, in an area where freezing rates of up to ~0.6 ma^{-1} are reported. The most likely cause of this variation from the behaviour seen in Sections A and B, is the strong horizontal velocities on the edges of the Main Gyre. The effect of the strong horizontal velocities is amplified by Section C being perpendicular to the mean flow direction. The mean velocities are respectively, ~8 cms^{-1} and ~5 cms^{-1} on the eastern and western sides of the gyre. This suggests the melt-water on the eastern side is moved by the gyre before a melt-water layer can form.

5.2 Zero streamfunction on the open boundary

In the present ocean model a closed ocean boundary where cross-boundary flow is expected is unrealistic as it allows no exchange of heat, salt or momentum across the boundary. There are two alternative boundary conditions explored, in this and the following section.

In all the open boundary model runs the tracer and internal (baroclinic) velocity terms at the boundary can be described in terms of an Orlanski-type radiation condition and a linearisation of the time evolution equation for velocity, as described in Sections 4.3.4 and 4.3.5. Both of these boundary conditions are modifications of the usual time evolution equation for each quantity. The behaviour of the external (barotropic) velocity boundary condition is more complex, because of the manner in which it is solved through the streamfunction. This is further complicated by the lack of useful simplifications for the streamfunction time evolution equation (Equation 4.26), which could be applied along an ocean boundary [Stevens, 1990].

The simplest boundary condition to achieve exchange across the open ocean boundary is $\Psi = 0$, and a rationale for this boundary condition was given in Section 4.3.5. With the $\Psi = 0$ boundary condition the model then relies on the tracer and internal velocity modes for heat, salt and mass exchange across the ocean boundary.

The $\Psi = 0$ boundary condition implies, through Equation 4.24, that the cross-boundary barotropic velocity on the boundary would be zero. This is not automatically the case for the finite difference system in the model. The offset between the streamfunction and velocity grid points (Figure 4.1a) in effect

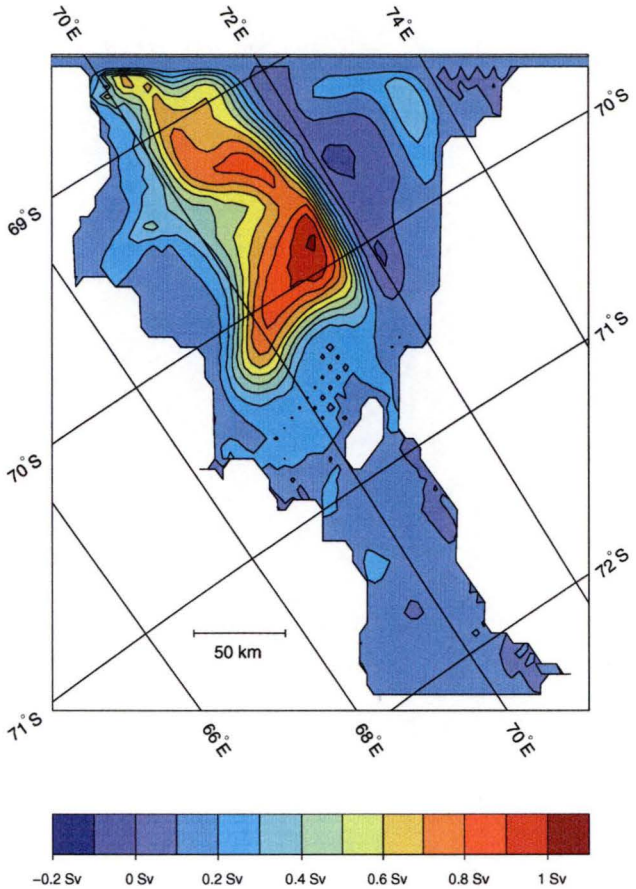

Figure 5.6: Vertically integrated streamfunction for the $\text{AIS}_{\bar{u},\bar{v}=0}$ run. Circulation is clockwise about positive features.

allows two options for setting the boundary condition. Either the barotropic velocities on the velocity boundary row are set to zero, or on the streamfunction boundary row Ψ is set to zero. In the later case some cross-boundary barotropic flow will be generated by the internal evolution of the streamfunction.

5.2.1 Zero barotropic velocities on the ocean boundaries

Opening the ocean boundary of the model substantially changes the tracers and circulation in the ocean cavity under the Amery Ice Shelf. In this section the $\Psi = 0$ boundary condition is applied on the velocity grid-points. This sets $\bar{u}$ and $\bar{v}$ to zero. This model run has been labelled $\text{AIS}_{\bar{u},\bar{v}=0}$.

The general structure of the horizontal circulation in the $\text{AIS}_{\bar{u},\bar{v}=0}$ run is similar to the closed boundary run. This can be seen by comparing the streamfunction for the $\text{AIS}_{\bar{u},\bar{v}=0}$ run, shown in Figure 5.6, with the streamfunction for the closed boundary run (Figure 5.2). The similarity in the horizontal circulation is because of the strong tendency of the circulation to follow the contours of water column thickness (Figure 4.5).

There are some differences between the circulation in the north of the domain in the $\text{AIS}_{\bar{u},\bar{v}=0}$ run and the closed boundary run. In particular, the Main Gyre

is stronger near the ice front in the $AIS_{\bar{u},\bar{v}=0}$ run. This increased transport is because the water column is not as homogeneous in the $AIS_{\bar{u},\bar{v}=0}$ run, as it is in the closed boundary run (Figure 5.7a). The increased density gradients near the ice front are formed by interaction with the prescribed tracer fields on the boundary. This interaction strengthens the overall gyre, as well as dramatically increasing circulation in the north of the domain.

South of the Main Gyre changes also occur from the introduction of limited cross-boundary exchange. Here the circulation is much weaker than in the closed boundary run, with the maximum strength reducing from ~-0.27 Sv to ~-0.1 Sv. The South-Central Gyre, which was situated between the Main Gyre and the Central Grounded Zone in the closed boundary run (Figure 5.2), is no longer present. In its place there is a weak flow in the same direction as the Main Gyre.

Three temperature sections for the $AIS_{\bar{u},\bar{v}=0}$ run are shown in Figure 5.7. The locations of the three sections are shown in Figure 5.4, they are the same as for the closed boundary run. The effect of an open boundary on the vertical circulation can be seen in these sections. In the upper part of the water column near the ice front in Section A (Figure 5.7a) freezing at the ice shelf-ocean interface (Figure 5.8) is causing vertical mixing. Unlike the closed boundary case the vertical mixing is not occurring in the whole water column. Instead the bottom ~260 m of the water column contains a relatively warm mixture of the water mass generated by freezing and vertical mixing, and water which has come from interaction with the ocean boundary.

Section A also highlights features of the horizontal circulation. Near the ice front a small temperature inversion occurs in the otherwise well-mixed water column. This intrusion is indicative of the west to east flow in the north of the Main Gyre. The inversion remains stable because of the strong stratification in the salinity field (not shown).

The effect of the Main Gyre can also be seen in Section A, where between 69.7°S and 70.2°S, the isotherms are very flat. The streamfunction in this part of the Main Gyre has a strong east-west gradient, and a weak north-south gradient.

Near the ice front in Section B (Figure 5.7b) the water column is still well-mixed, and has the same temperature as the water at the base of the water column in Section A. Across the middle of Section B the isotherms indicate less vertical mixing and greater stratification than in the closed boundary run. In the channel to the east of the Central Grounded Zone (between 70.2°S and 70.8°S) there is a change in the horizontal circulation, from northward flowing in the closed boundary run to southward. (There is still some northward flow on the west side of the channel (Figure 5.6).) The southward flow gives a warmer water column along Section B, this leads to increased melting of the ice shelf in this part of the domain (Figure 5.8). The effect of this extra melting is not apparent in Section B, because most of the increased melt flows along the western side of the channel.

The horizontal circulation for the $AIS_{\bar{u},\bar{v}=0}$ and closed boundary runs south of the Central Grounded Zone is similar. This generates isotherm gradients

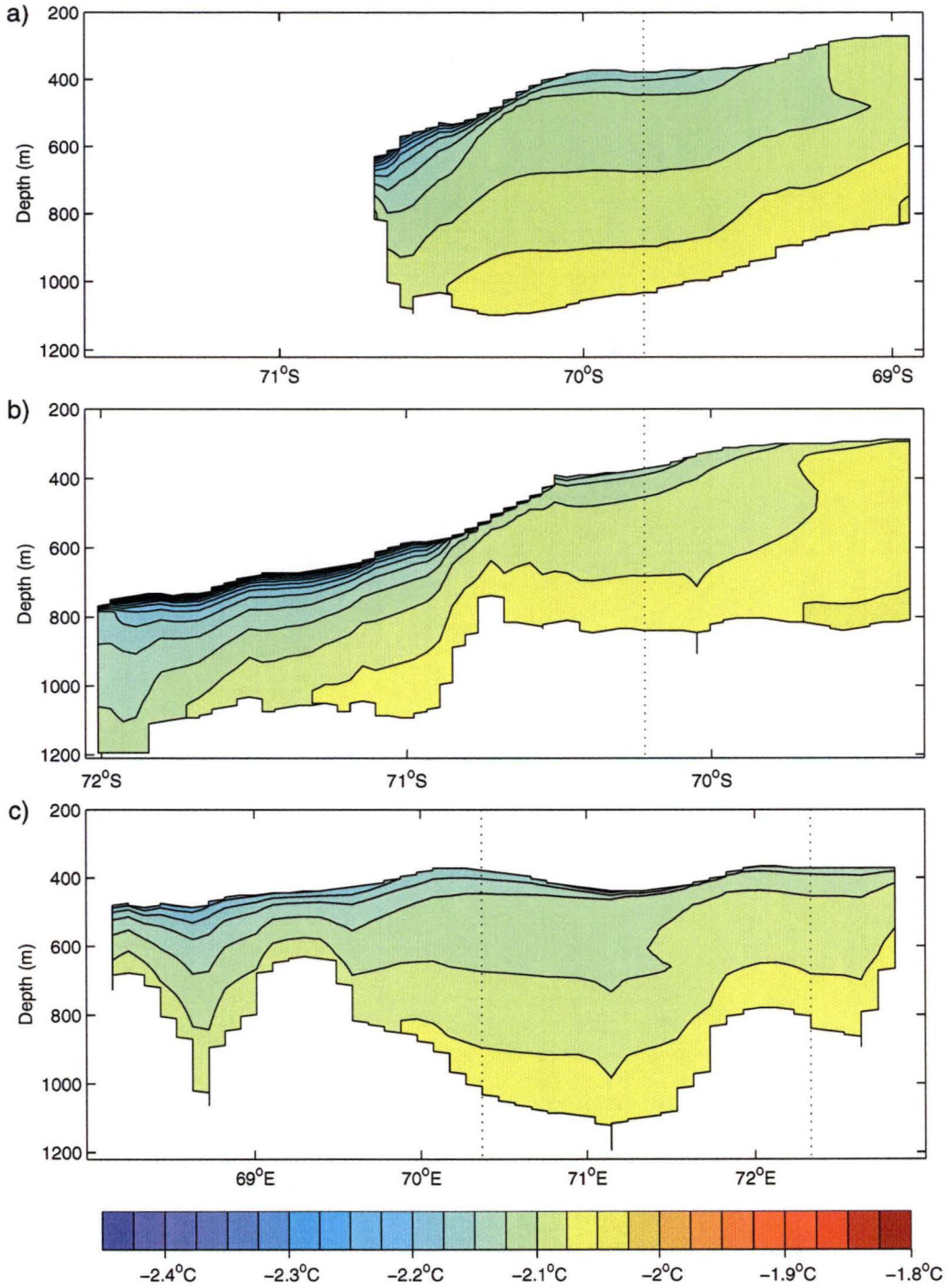

Figure 5.7: Temperature cross-sections of the model domain for the $\text{AIS}_{\bar{u},\bar{v}=0}$ run. a) Section A, b) Section B, and c) Section C. The location of the cross-sections is shown in Figure 5.4. The dotted lines indicate where the cross-sections intersect.

at the southern end of Section B in the $AIS_{\bar{u},\bar{v}=0}$ run which are similar to the same section for the closed boundary run (Figure 5.5b). The isotherm gradients suggest the vertical mixing and circulation near the grounding line and in the southern part of the cavity, are similar in the $AIS_{\bar{u},\bar{v}=0}$ and closed boundary runs. There are some small differences which arise from the additional heat available from across the ice shelf boundary in the $AIS_{\bar{u},\bar{v}=0}$ run. This additional heat has sharpened the melt-water layer which forms in the high melt rate areas, and increased the temperature at the bottom of the water column.

The east-west section, Section C (Figure 5.7c), shows a similar temperature structure in the upper part of the water column, for the $AIS_{\bar{u},\bar{v}=0}$ and closed boundary runs. The lower half of the water column, however, differs. In the $AIS_{\bar{u},\bar{v}=0}$ run this is more stratified than in the closed boundary run. This partly comes from the heat exchange across the ice front, but also from a general reduction in vertical mixing, caused by less freezing near the ice front (Figure 5.8). In this area of the closed boundary model substantial amounts of vertical mixing, through the convective adjustment scheme, were driven by high rates of freezing which gave a homogeneous water column.

The difference in the temperature at the ice front in Sections A and B from that specified in the boundary conditions (Figure 4.6a), is caused partly by the design of the boundary conditions (Section 4.3.4) and partly by the strong control which the internal circulation has over the circulation near the ice front. In this model run the barotropic velocity components are zero along the ice front. Thus all transport is via the baroclinic component which is generally weak at the ice front. Thus there is little to force agreement between the boundary conditions and the model tracer fields at the ice front, except for the weak restoring (Equation 4.73).

The opening of the northern boundary for the exchange of heat and salt has a significant affect on the melting and freezing rates at the ice shelf-ocean interface. The melting and freezing rates for the $AIS_{\bar{u},\bar{v}=0}$ run are shown in Figure 5.8. The large area of freezing along the ice front, found in the closed boundary run, is reduced. This is because the integrated heat and salt fluxes at the ice shelf-ocean interface over the whole ice shelf no longer have to be in balance. Instead the fluxes at the ice shelf-ocean interface are in balance with the heat and salt flux across the ice front boundary.

The top layer of water in the western side of the Main Gyre contains melt-water, either from the southern part of the domain, or from melt which occurs on the eastern side of the Main Gyre. The strong area of freezing near the ice front is driven by this flow of melt-water in the Main Gyre. At the boundary insufficient cold water is able to leave the domain, keeping the water below the in situ freezing temperature and generating the excess freezing. This is caused by the restriction of zero net flow in each boundary column, both across and along the boundary. The most noticeable example of this is around 68.9°S 71.5°E, where freezing rates of $\sim$2.2 ma^{-1} are found. Here the effect on the water column can be seen in Section A (Figure 5.7a), where there is strong vertical coherence in the upper part of the water column.

Away from the ice front the patterns of melting and freezing are very similar

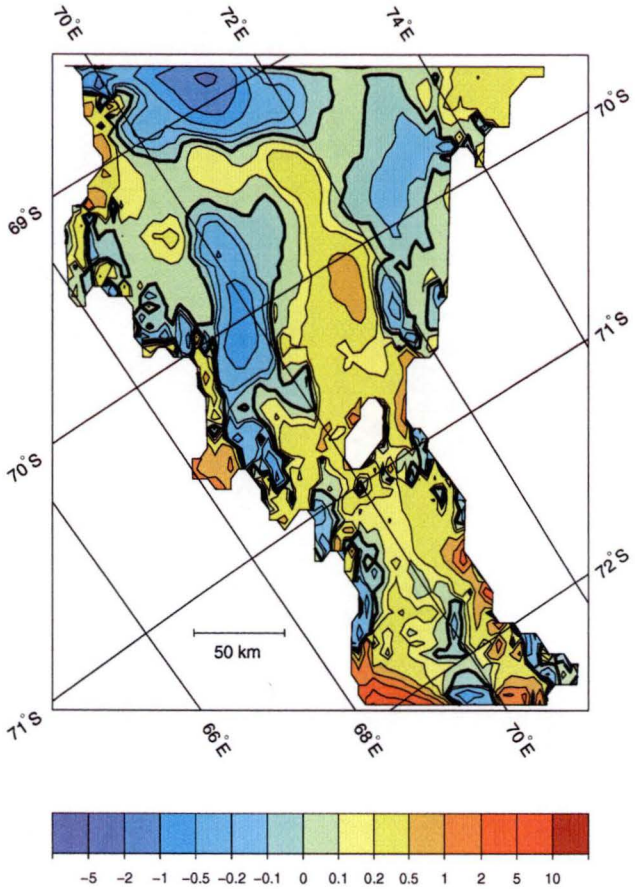

Figure 5.8: Melting (+) and freezing (-) rates for the $AIS_{\bar{u},\bar{v}=0}$ run in ma^{-1}. The bold contour denotes the boundary between melting and freezing.

between the $AIS_{\bar{u},\bar{v}=0}$ run and the closed boundary run, except to the east of the Central Grounded Zone. In the $AIS_{\bar{u},\bar{v}=0}$ run there is a strong area of melting in this area rather than the freezing seen in the closed boundary run. This occurs because a reversal in the direction of the horizontal circulation removes the rising flow of potentially supercooled melt-water from south of the Central Grounded Zone and replaces it with southward flowing warm water. The vertically stable warm water intersects the draft of the ice shelf to drive significant amounts of melting at the ice shelf base.

5.2.2 Zero streamfunction

As we saw in the previous section opening the northern boundary made a substantial change to the horizontal circulation in the model. Changing the way in which the $\Psi = 0$ boundary condition is applied also changes the circulation and thermohaline structure in the model domain. In this section the results of applying the $\Psi = 0$ boundary condition on the streamfunction boundary row are discussed. This run has been labelled $AIS_{\Psi=0}$.

The major change in the horizontal circulation can be seen in the streamfunction which is shown in Figure 5.9. Here the single Main Gyre, seen in

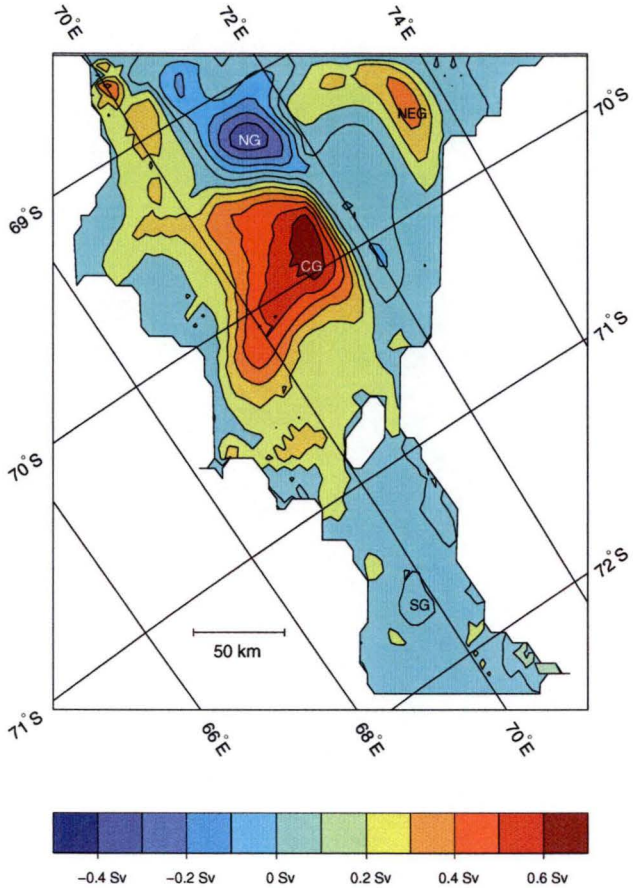

Figure 5.9: Vertically integrated streamfunction for the $AIS_{\Psi=0}$ run. The main features discussed in the text, the Northeastern Gyre (NEG), the Central Gyre (CG), the Northern Gyre (NG) and the Southern Gyre (SG), are marked. Circulation is clockwise about positive features.

the closed boundary (Figure 5.2) and $AIS_{\bar{u},\bar{v}=0}$ runs (Figure 5.6), has changed to a pair of gyres. The more southern of these gyres, which has the greater transport of the pair, and is the dominant feature of the new circulation in the ocean cavity, will be referred to as the Central Gyre. This is to differentiate it from the circulation in the closed boundary and $AIS_{\bar{u},\bar{v}=0}$ runs, which are characterised by the Main Gyre. The other gyre of the pair has been named the Northern Gyre. The strength of the Central Gyre is reduced in comparison with the Main Gyre circulation in the $AIS_{\bar{u},\bar{v}=0}$ run.

Along the northern boundary of the domain cross-boundary flow is generally vertically coherent. This can be seen in the cross-boundary velocity field shown in Figure 5.10. The largest area of inflow is in a deep trench which runs to the east of the 70.0°E meridian. In some of this region the vertical coherence breaks down and here the inflow is near the bottom and outflow is located at the top of the water column. Weaker inflow occurs near 74.0°E where the ice shelf thickens sharply, and also to the west of the 72.0°E meridian. These areas of weak inflow are separated by areas of weak outflow. The strongest area of outflow is in the west. It is the boundary representation of the western boundary current.

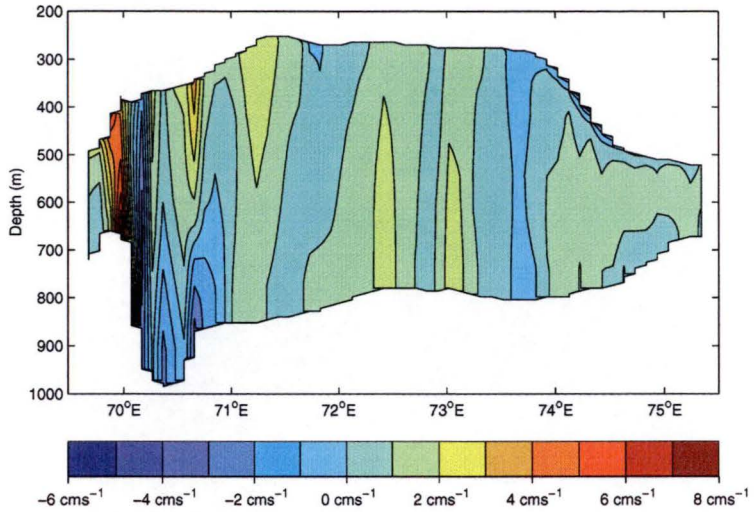

Figure 5.10: The ice front cross-boundary velocity field for the $\text{AIS}_{\Psi=0}$ run. Positive velocities are northward (or into the page).

In the streamfunction (Figure 5.9) it can be seen that most of the inflow from the western inflow regions is collected in the Northern Gyre. The flow from west of 71.0°E circulates through the western side of the Northern Gyre where it is joined by flow along the base of the deep trench. From here the flow divides, with the bulk of the flow going east and then south as part of the Central Gyre. A smaller amount recirculates and flows back towards the boundary. This combines with flow from the Northeastern Gyre before flowing out of the domain between 72.0°E and 73.0°E.

South of the Central Gyre the circulation is similar to the $\text{AIS}_{\bar{u},\bar{v}=0}$ run, with a small peripheral gyre between the Central Gyre and the Central Grounded Zone. This is a strengthening of the weak flow in the region in the $\text{AIS}_{\bar{u},\bar{v}=0}$ run. The change in the circulation to the west of the Central Grounded Zone affects the exchange of heat and salt between the northern and southern parts of the domain.

The flow south of the Central Grounded Zone is not clear in the streamfunction. This is because it is comparatively weak and is not clearly represented by the contours in Figure 5.9. In can be seen more clearly in the pseudo-lagrangian tracer paths shown in Figure 5.11.

The circulation south of the Southern Gyre is not vertically coherent in comparison to the circulation linked to the gyres in the rest of the domain (Figure 5.11). Near the southern grounding line it appears flow is southward in the lower layer (green paths), while nearer to the ice shelf the flow is northward. The top tracer levels (red paths) released near the southern grounding line are flowing along the base of the ice shelf in a 'plume' like manner. Once away from the southern grounding line the 'plume' follows, and becomes part of the gyres. This differs from the assumptions made in the Plume Model (Section 2.3.2), where the plume would follow the steepest ice shelf gradient.

In addition to the changes in the horizontal circulation, the rates of melting and freezing also differ from the closed boundary and $\text{AIS}_{\bar{u},\bar{v}=0}$ runs. The rates

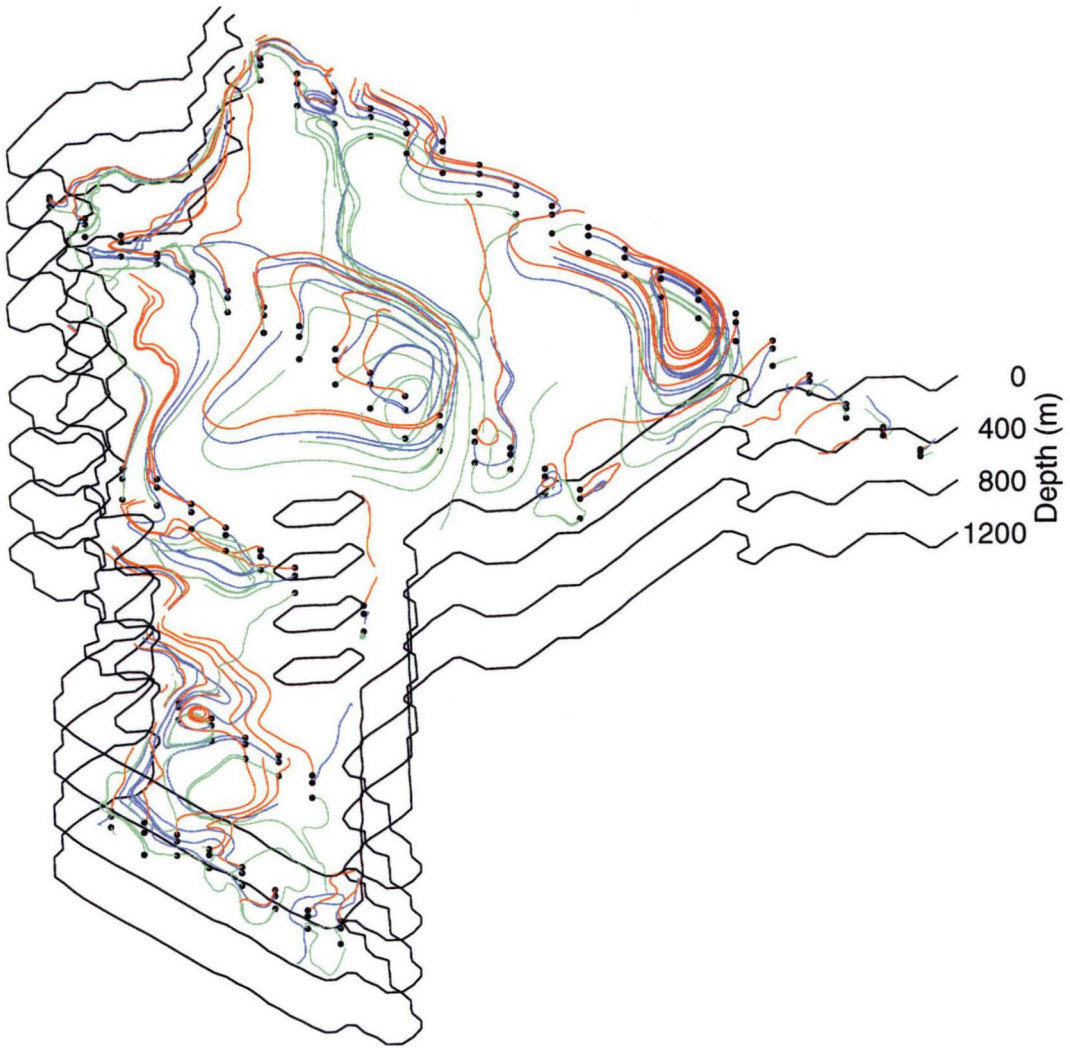

Figure 5.11: Pseudo-lagrangian tracer paths for the $AIS_{\Psi=0}$ run. The dots show the release points for each tracer. The colours indicate the σ-layer on which the tracers were released: red layer 2, blue layer 5, and green layer 8.

of melting and freezing for the $AIS_{\Psi=0}$ run are shown in Figure 5.12. Most of the change in melting and freezing between the $AIS_{\bar{u},\bar{v}=0}$ and $AIS_{\Psi=0}$ run is a small shift in the local rate of melting or freezing. The exception to this is the disappearance of the area of strong freezing in the northwest of the domain. In this area the strong freezing is replaced with a broad region of weak freezing, which includes two areas with higher freezing rates.

Figure 5.13 shows the temperature along the three cross-sections shown in Figure 5.4. The most noticeable difference between the temperature cross-sections shown in Figure 5.13 and those for the $AIS_{\bar{u},\bar{v}=0}$ run (Figure 5.7) is the general increase in temperature within the model domain. The water at the bottom of all the cross-sections is warmer than in the $AIS_{\bar{u},\bar{v}=0}$ run by $\sim$0.1°C. With the ice shelf base still near the in situ freezing temperature there is consequently more stratification.

In Section A (Figure 5.13a) the temperature section south of 69.6°S is very

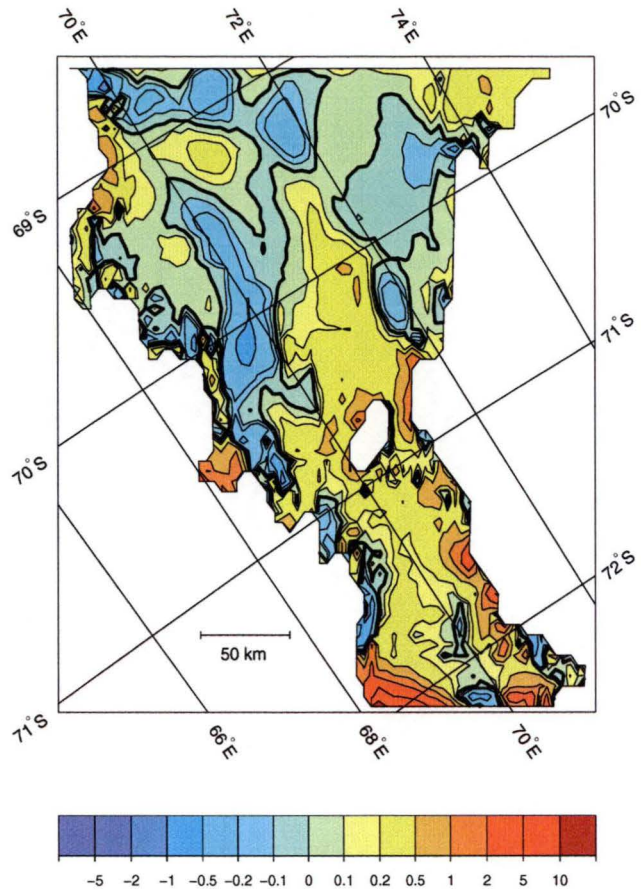

Figure 5.12: Melting (+) and freezing (-) rates for the $\text{AIS}_{\Psi=0}$ run in ma^{-1}. The bold contour denotes the boundary between melting and freezing.

similar to the $\text{AIS}_{\bar{u},\bar{v}=0}$ run. This similarity is unsurprising as the horizontal circulation is very similar in this part of the domain in the two models. North of 69.6°S, the isotherm gradients are very different. In place of the well-mixed upper water column and warm inflow water near the bottom, in the $\text{AIS}_{\bar{u},\bar{v}=0}$ run the upper water column is heavily stratified. The warmest water in the section is also restricted to the bottom of this small part of the section. The bottom water for the rest of the cross-section has the characteristics of mid-depth water north of 69.6°S. This structure is caused by the Northern Gyre bringing in water near the bottom of the cavity, but instead of it then mixing into the Central Gyre it flows out of the domain.

South of 70°S, Section B (Figure 5.13b) differs little between the $\text{AIS}_{\bar{u},\bar{v}=0}$ run and the $\text{AIS}_{\Psi=0}$ run. North of 70°S the change in the method of implementation of the $\Psi = 0$ boundary condition has an effect. There is still some strong mixing near the ice front, but in general the level of stratification has increased. This is in line with the general warming of the cavity.

The major change in Section C (Figure 5.13) is the restriction of the warmer waters to the area of the Northeastern Gyre. This occurs partly because of the sill which stops the warm water flowing as a gravity current from the eastern basin into the Central Gyre basin. Any flow above the sill is also blocked by the

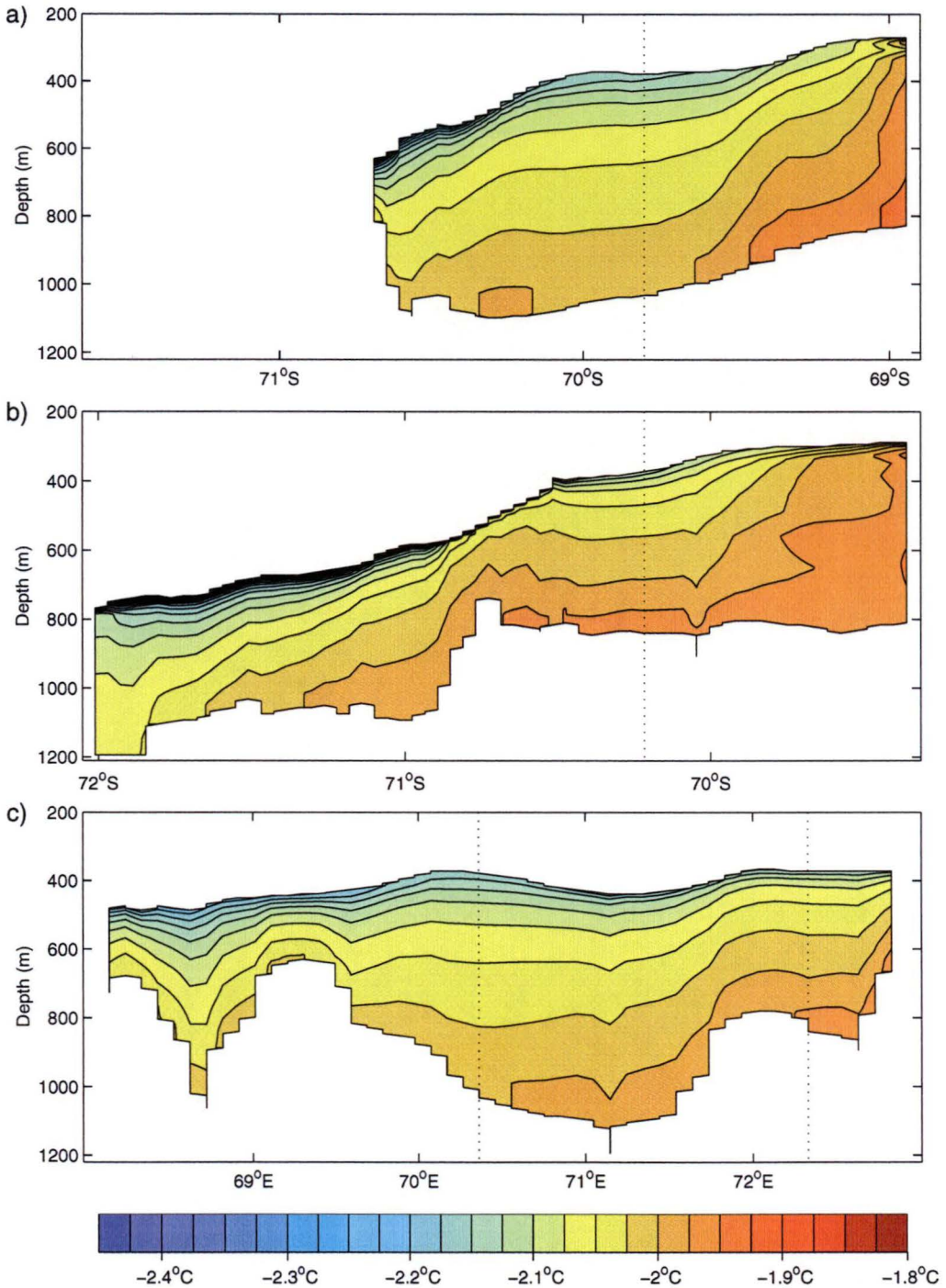

Figure 5.13: Temperature of the model domain, for the $AIS_{\Psi=0}$ run. a) Section A, b) Section B, and c) Section C. The locations of the cross-sections are shown in Figure 5.4. The dotted lines indicate where the cross-sections intersect.

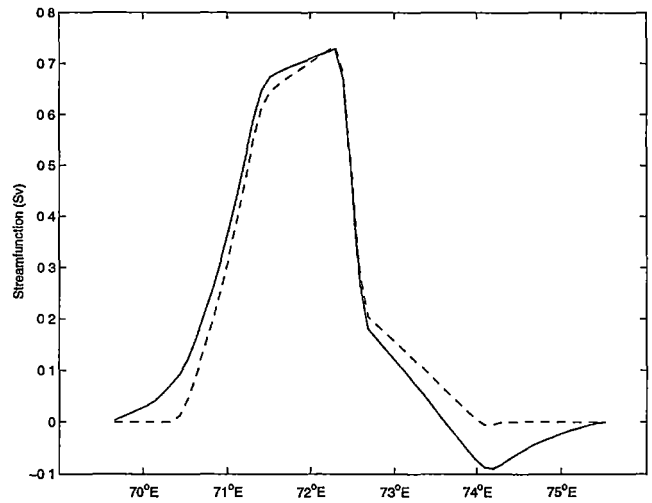

Figure 5.14: Streamfunctions specified along the northern boundary. The dashed line is the streamfunction calculated applying a correcting velocity where $v_g \neq 0$, and the solid line is the streamfunction applying a correcting velocity across all points. See Section 4.3.5 for full details.

eastward flow, which occurs in the zone between the Central and Northeastern Gyres.

5.3 Along boundary streamfunction gradient conditions

In the previous sections the boundary condition for either the streamfunction or the barotropic velocity component was set to zero. The open boundary condition can also be specified in terms of the streamfunction gradient along the open boundary ($\frac{\partial \Psi}{\partial \lambda}$). As previously mentioned the streamfunction time evolution equation (Equation 4.26) has no useful reductions [Stevens, 1990]. For the open ocean boundaries Stevens [1990, 1991] suggests a streamfunction gradient based on the Sverdrup balance. In discussions in Section 4.3.5 this was deemed inappropriate, because it has been assumed there is zero surface stress under the ice shelf. The strategy presented here, as outlined in Section 4.3.5, is to assume the prescribed temperature and salinity forcing fields at the ice front are in geostrophic balance.

As discussed in Section 4.3.5 the boundary condition can be imposed on either the streamfunction boundary row only or on both the streamfunction boundary row and adjacent interior row. In this section these two methods of setting the streamfunction gradient are compared, utilising the geostrophically derived streamfunction gradient. The first scenario examined is the prescribed velocity run ($\text{AIS}_{\text{P}\bar{v}}$). The second scenario, sets the streamfunction gradient along the boundary ($\text{AIS}_{\text{P}\partial\Psi}$).

In Section 4.3.5, where the derivation of the along front streamfunction was described, two possible correcting velocities were mooted: a uniform correcting

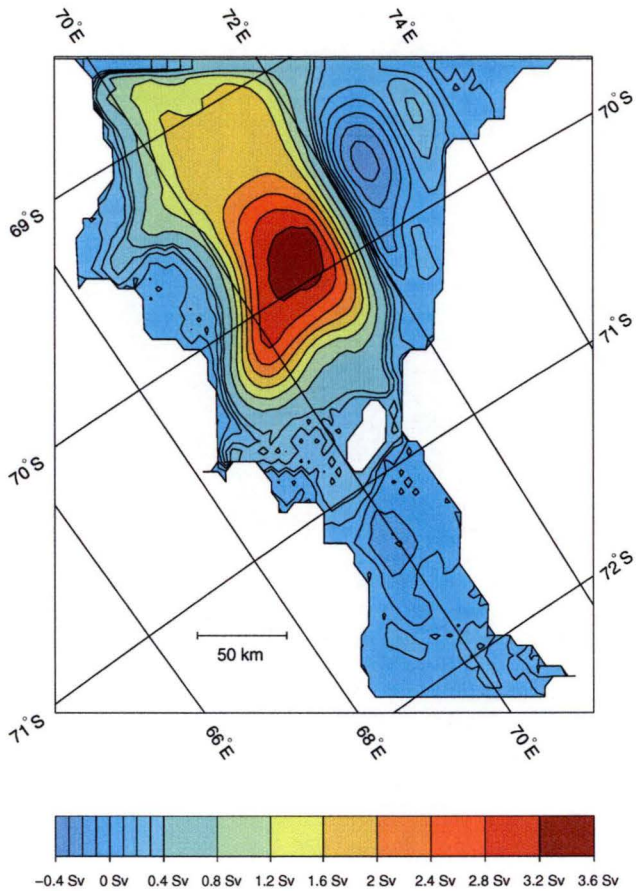

Figure 5.15: Vertically integrated streamfunction for the $AIS_{P\bar{v}}$ run. Circulation is clockwise about positive features.

velocity, and a non-uniform correcting velocity. The use of different correcting velocities results in different streamfunctions and hence gradients. The two derived streamfunctions are shown in Figure 5.14. There are some similarities in the two streamfunctions, for instance the main peak. This suggests for the bulk of cross-boundary flow the method used to correct for mass conservation is unimportant. However, outside the main peak there are differences between the two figures. The use of a uniform correcting velocity increases the flow near the coastline at each end of the open boundary. These increases in inflow are in areas where the observations used in calculating the geostrophic velocities suggest there is little or no flow.

Model runs with both uniform and non-uniform correcting velocities were made, for both the $AIS_{P\bar{v}}$ and $AIS_{P\partial\Psi}$ runs. The difference in each run between the uniform and non-uniform boundary conditions is localised to the ice front and is significantly less than the difference between the $AIS_{P\bar{v}}$ and $AIS_{P\partial\Psi}$ runs. Accordingly in the following sections only the results for the runs where a non-uniform correcting velocity is used are discussed.

5.3.1 Prescription of cross-boundary velocities

As would be expected changing the streamfunction boundary condition along the open ocean boundary has a large impact on the horizontal circulation. This can be seen in the streamfunction for the $AIS_{P\bar{v}}$ run, which is shown in Figure 5.15. The structure of the circulation, with a single Main Gyre dominating the circulation, is similar to the closed boundary and $AIS_{\bar{u},\bar{v}=0}$ runs. Here the circulation in the Main Gyre is much greater than in the other runs. The maximum transport in the centre of the gyre is ~3.59 Sv, this is over three times larger than for the Main or Central Gyres in any of the other model runs. The strength of the circulation in most of the remainder of the domain is also slightly greater than in other model runs. South of the Central Grounded Zone the maximum transport is ~-0.21 Sv, this is approximately a three fold increase on the $AIS_{\bar{u},\bar{v}=0}$ run, where the maximum transport in the same region was ~-0.07 Sv. The general increase in the circulation also affects the area of reverse flow between the Main and Northeastern Gyres. This area of flow is significantly stronger than the other runs, and is a product of the increased circulation in the Main Gyre.

The circulation in the Northeastern Gyre does not increase by a factor of three, it remains at a very similar magnitude to the $AIS_{\bar{u},\bar{v}=0}$ and $AIS_{\Psi=0}$ runs. The lack of change in the strength of the Northeastern Gyre is most likely due to its linkages to the open ocean and the restoring of heat and salt this would allow along the boundary.

The effect of the boundary conditions in directing areas of inflow and outflow can be clearly seen along the boundary, particularly for the outflow. Here, the flow from the western side of the Main Gyre is directed along the northern boundary until it reaches the area for outflow around 71.0°E. This area of outflow is directed by the streamfunction used to prescribe the forcing (Figure 5.14).

The increase in the strength of the horizontal circulation has a noticeable effect on the strength of the melting and freezing rates at the ice shelf-ocean interface, these are shown in Figure 5.16. Both the rate of melting and the rate of freezing have increased dramatically in the area of the Main Gyre. In the previous runs both the melting and freezing rates have been less than 1 ma^{-1} in the north of the domain, except near the ice front where flow constraints have forced higher freezing rates.

In the $AIS_{P\bar{v}}$ run ice redistribution from the east to west sides of the Main Gyre benefits greatly from the increased transport in the Main Gyre. This mechanism can be likened to the 'ice pump' mechanism described by Melling and Lewis [1984], except it works in the horizontal rather than the vertical. On both sides of this horizontal 'ice pump' the rates of melting and freezing are high. On the eastern side of the gyre the melt rates are greater than 2 ma^{-1}, while on the western side the freezing rates are greater than 1 ma^{-1}. The area of freezing is also fed by increased amounts of melting in the south of the domain.

The amount of melting at the southern grounding line has also increased a small amount on the other runs. The peak melt rate is 14.4 ma^{-1}; this contrasts with 12.5ma^{-1} for the $AIS_{\Psi=0}$ and 10.6 ma^{-1} for the $AIS_{\bar{u},\bar{v}=0}$ run.

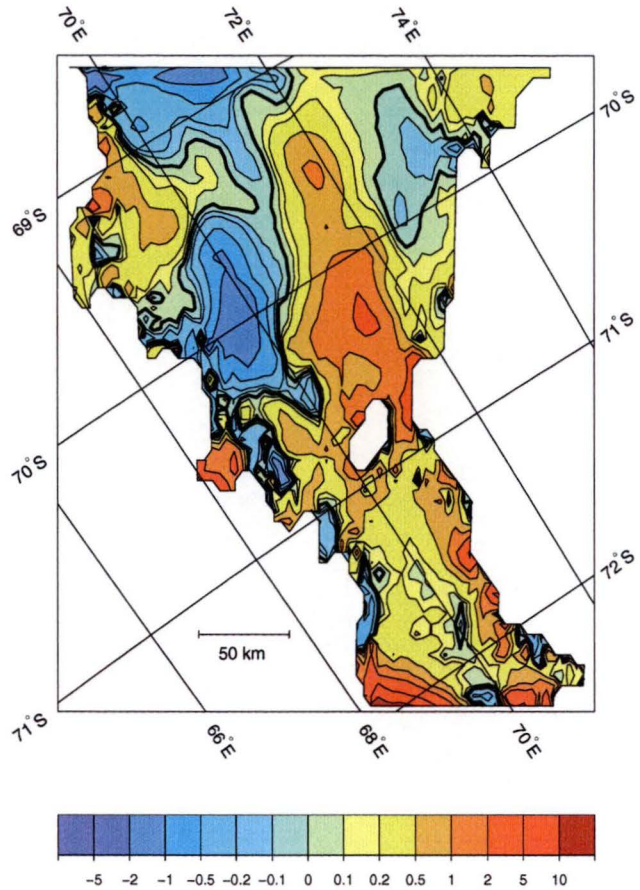

Figure 5.16: Melting (+) and freezing (-) rates for the $AIS_{P\bar{v}}$ run in ma^{-1}. The bold contour denotes the boundary between melting and freezing.

In the northeastern part of the domain, the area where freezing occurs is slightly smaller than in either the closed boundary, $AIS_{\bar{u},\bar{v}=0}$, or $AIS_{\Psi=0}$ runs. This is also caused by increased temperatures in the water column, a consequence of cross-boundary flow.

The large horizontal transport in the northern part of the domain generates a thick well-mixed layer at the bottom of the water column. This well-mixed layer can be seen in all three of the temperature cross-sections, presented in Figure 5.17.

The changes to the water column structure are most noticeable in Section A (Figure 5.17a). Here a warm (and salty) water mass fills up most of the water column. The melt-water layer is constrained to a thin heavily stratified layer adjacent to the ice shelf-ocean interface. This layer thins further because of freezing at the ice shelf-ocean interface (Figure 5.16). However, it then thickens near the ice front, as the Main Gyre drives water from the west through the section.

The source of heat which drives the heavy melting in the channel to the east of the Central Grounded Zone (between 70.6°S and 71.0°S) is evident in Section B (Figure 5.17b). Here the warm mixed layer is extending to the south and out-cropping where the ice shelf draft deepens. There is a thin melt-water

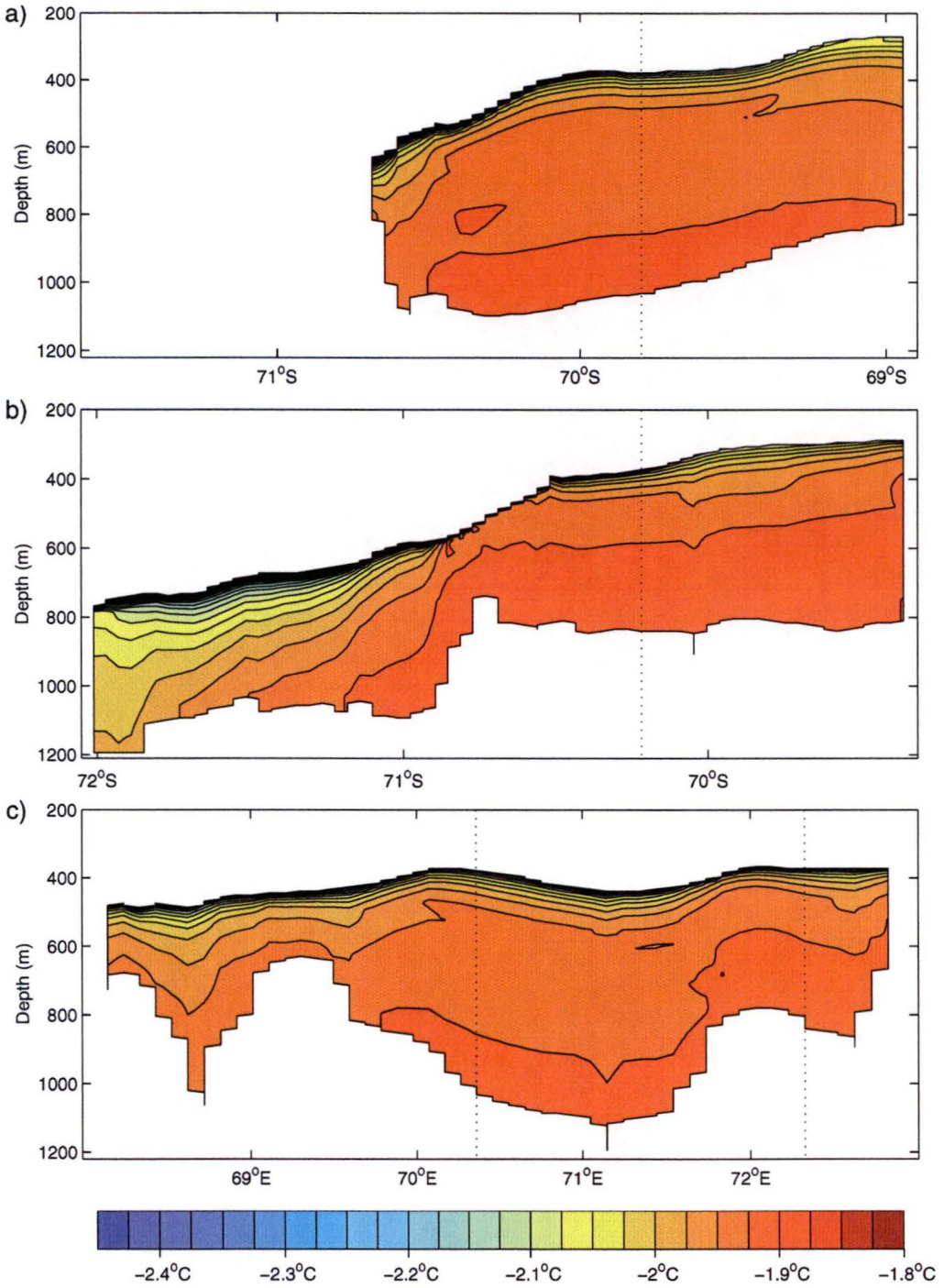

Figure 5.17: Temperature cross-sections of the model domain for the $\mathrm{AIS}_{\mathrm{P}\bar{0}}$ run. a) Section A, b) Section B, and c) Section C. The locations of the cross-sections are shown in Figure 5.4. The dotted lines indicate where the cross-sections intersect.

layer indicating large velocities next to the ice shelf. These strong velocities are removing the protective layer of melt-water, thus increasing the temperature gradient between the water close to the ice shelf and the ice shelf itself.

The structure in the remainder of the cross-section is otherwise similar to the same cross-section in the other model runs. In the south of the domain, the increased melting close to the grounding line is being driven by the extra heat in the water column. The bottom temperature at the grounding line on Section B is about 0.05°C warmer than in the other runs.

The additional melting and freezing across the Main Gyre is not apparent in the temperature in Section C (Figure 5.17c). Instead of an expected east-west variation, from melting thickening the layer and freezing thinning the layer, it has a consistent thickness. This is because the high velocities on each side of the Main Gyre are removing the products of the melting or freezing, before they are able to mix with the rest of the water column. This prevents, either thinning of the stratified layer in the west from freezing, or it thickening from melting in the east.

The other notable feature in Section C is a temperature inversion at 71.4°E. This is warm water from the upper layers between 73°E and 74°E at the ice front (Figure 4.6a). This water mass is advected at mid-depths from the ice front, and reduces in volume with distance from the front. The temperature inversion beneath the water parcel does not destabilise the water column as the salinity, which dominates the density at these temperatures, is still well stratified.

5.3.2 Specification of along boundary streamfunction gradient

Applying the geostrophically based streamfunction gradient only to the streamfunction, and not to the cross-boundary barotropic velocity component, produces a similar contrast between the $\text{AIS}_{\text{P}\bar{v}}$ and $\text{AIS}_{\text{P}\partial\Psi}$ runs to that produced between the $\text{AIS}_{\bar{u},\bar{v}=0}$ and $\text{AIS}_{\Psi=0}$ runs.

The horizontal circulation in the $\text{AIS}_{\text{P}\partial\Psi}$ run, as represented by the streamfunction in Figure 5.18, shows that the general circulation in the area south of the Central Grounded Zone and in the northeastern part of the cavity is very similar to the other model runs. The circulation in the north-eastern part of the domain is of similar strength to the $\text{AIS}_{\Psi=0}$ and $\text{AIS}_{\text{P}\bar{v}}$ runs. The Southern Gyre is weaker than in the $\text{AIS}_{\Psi=0}$ run, but of similar strength to the $\text{AIS}_{\text{P}\bar{v}}$ run.

The major change in the horizontal circulation occurs in the area to the north of the Central Gyre between 72.0°E and the western grounding line. Here the general pattern of the circulation is more like the $\text{AIS}_{\Psi=0}$ run, than the closed boundary, $\text{AIS}_{\bar{u},\bar{v}=0}$, or $\text{AIS}_{\text{P}\bar{v}}$ runs, with several gyres making up the flow rather than a single Main Gyre. All the flow is stronger than in the $\text{AIS}_{\Psi=0}$ run, but not to the same extent as the $\text{AIS}_{\text{P}\bar{v}}$ run. In the $\text{AIS}_{\text{P}\partial\Psi}$ run the Central Gyre has a maximum transport of $\sim$1.25 Sv, compared with the $\sim$0.61 Sv of the $\text{AIS}_{\Psi=0}$ run.

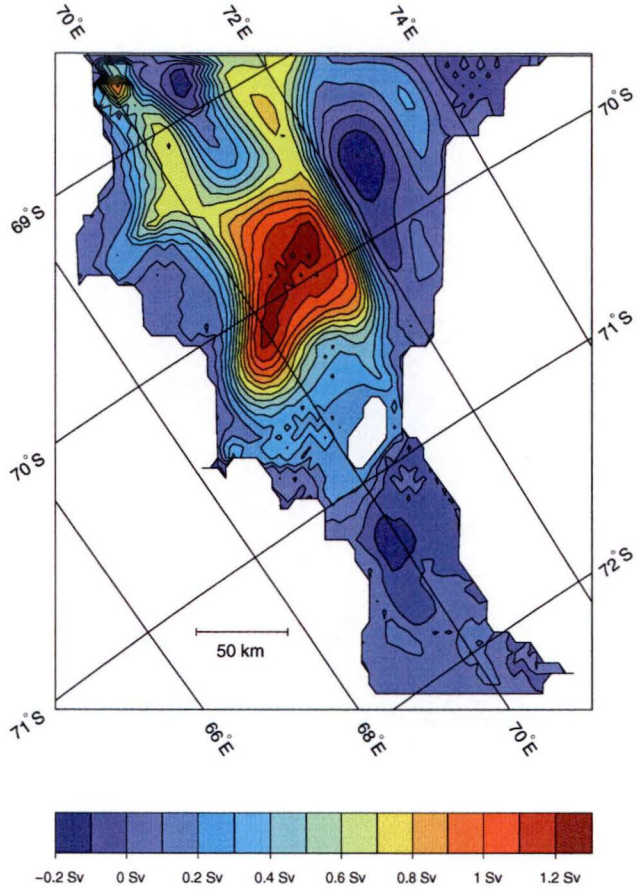

Figure 5.18: Vertically integrated streamfunction for the $AIS_{P\partial\Psi}$ run. Circulation is clockwise about positive features.

North of the Central Gyre the flow is made up of three parts. A western boundary current, and two gyres. The western boundary current is a narrow extension of the Central Gyre. To the east of this are the two gyres, an anticlockwise gyre to the west of a clockwise gyre. Both gyres interact with the cross-boundary flow and the Central Gyre. The form of these two gyres is directed by the specification of the streamfunction gradient along the boundary. This gives a different circulation in comparison to the $AIS_{\Psi=0}$ run. The anticlockwise circulating gyre is an alternate version of the Northern Gyre described for the $AIS_{\Psi=0}$ run. It connects the inflow region near 70.5°E with the Central Gyre.

Unlike the $AIS_{\Psi=0}$ run, where all the cross-boundary flow into the Central Gyre came from the Northern Gyre, the clockwise gyre (an extension of the Central Gyre) provides an additional source of heat for the Central Gyre. The effect of this additional heat can be seen in the higher melt rates in the area of the eastern side of the Central Gyre (Figure 5.20).

The specification of the cross-boundary flow impacts on the areas where inflow and outflow occur. This can be seen in the cross-boundary velocity shown in Figure 5.19 that differs from the cross-boundary flow shown for the $AIS_{\Psi=0}$ run (Figure 5.10). The most significant change occurs in the eastern side of the

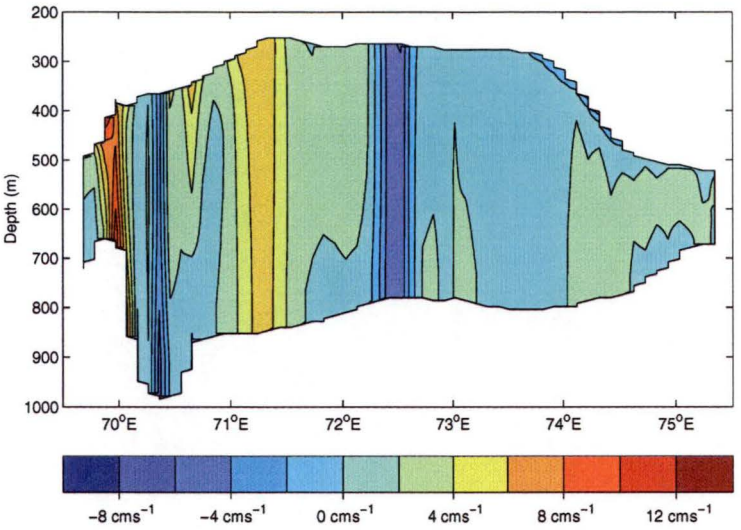

Figure 5.19: The ice front cross-boundary velocity field for the $AIS_{P\partial\Psi}$ run. Positive velocities are northward (or into the page).

front, here two areas of weak outflow have disappeared, and an area of weak inflow has strengthened dramatically. This increase in the current strength also impacts on the outflow, which although reduced in area has increased in velocity, particularly in the west of the domain where the western boundary current is flowing out, and between 70.5°E and 71.5°E. The changes in the pattern of inflow and outflow lead to an increase in the inflow and outflow components of mass transport across the ice front. In the $AIS_{\Psi=0}$ and the $AIS_{P\bar{v}}$ runs the individual components are ~0.49 Sv and ~0.84 Sv, respectively. In the $AIS_{P\partial\Psi}$ run the components are ~1.02 Sv.

The different ocean circulation in the $AIS_{P\partial\Psi}$ run is coupled to a different pattern of melting and freezing at the ice shelf-ocean interface. The melting and freezing rates are shown in Figure 5.20.

North of the Central Grounded Zone the pattern of melting and freezing, for the $AIS_{P\partial\Psi}$ run, has similarities with both the $AIS_{\Psi=0}$ and $AIS_{P\bar{v}}$ runs. This model run does not have a large amount of freezing adjacent to the ice front in the north-west, as was seen in the melting and freezing rates for the $AIS_{P\bar{v}}$ run. However, it does have the strong melt-freeze pattern across the Central Gyre, although the contrast is not as great as in the $AIS_{P\bar{v}}$ run. The other changes are: a shift in the position of the freezing area which lies in the northwest corner of the domain, and in the eastern side of the domain the area where freezing occurs is much smaller than in any of the other runs.

South of the Central Grounded Zone there is a small shift in the rates of melting and freezing between the $AIS_{P\partial\Psi}$ run and the other runs.

The changes in the horizontal circulation and the melting and freezing rates at the ice shelf-ocean interface can be seen in the three temperature cross-sections shown in Figure 5.21. The increased interaction with the open ocean can be seen in the warmer temperatures in all three sections. The amount of warming is slightly more than is seen with the prescription of velocities along

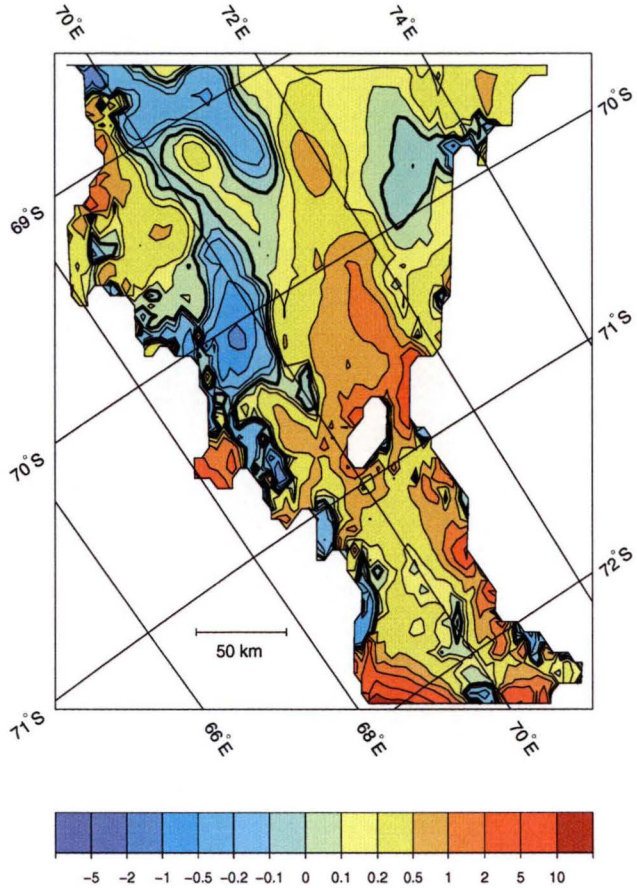

Figure 5.20: Melting (+) and freezing (-) rates for the $AIS_{P\partial\Psi}$ run in ma^{-1}. The bold contour denotes the boundary between melting and freezing.

the open boundaries in the $AIS_{P\bar{v}}$ run.

Section A (Figure 5.21a) has a well-mixed water column, similar to that for the $AIS_{P\bar{v}}$ run. In the northern part of the section centred around 69.4°S the impact of the Northern Gyre can be seen. The Northern Gyre has the effect of thickening the stratified layer at the top of the water column. The gyre overlaps part of an area of weak melting, and part of an area of freezing (Figure 5.20). The melting in the southern side of the gyre thickens the stratified layer, but on the northern freezing side the salt rejection thins the stratified layer by driving mixing in the water column. The close linkage between the melting and freezing regions helps create steep density gradients on both sides of the thick stratified region. This assists in driving the Northern Gyre as geostrophic processes are dominant in the ocean cavity.

Section B (Figure 5.21b) is very similar in the southern part of the domain to the same section in the $AIS_{P\bar{v}}$ run (Figure 5.17b). This similarity arises from the inflow at the ice front in the area of the section. Under the stratified layer at the top of the water column, the well-mixed layer still extends to the south, and outcrops in the channel to the east of the Central Grounded Zone (around 70.7°S). A similar feature was seen in the $AIS_{P\bar{v}}$ run. Also in the channel the effects of the local circulation in this area can be seen, with small temperature

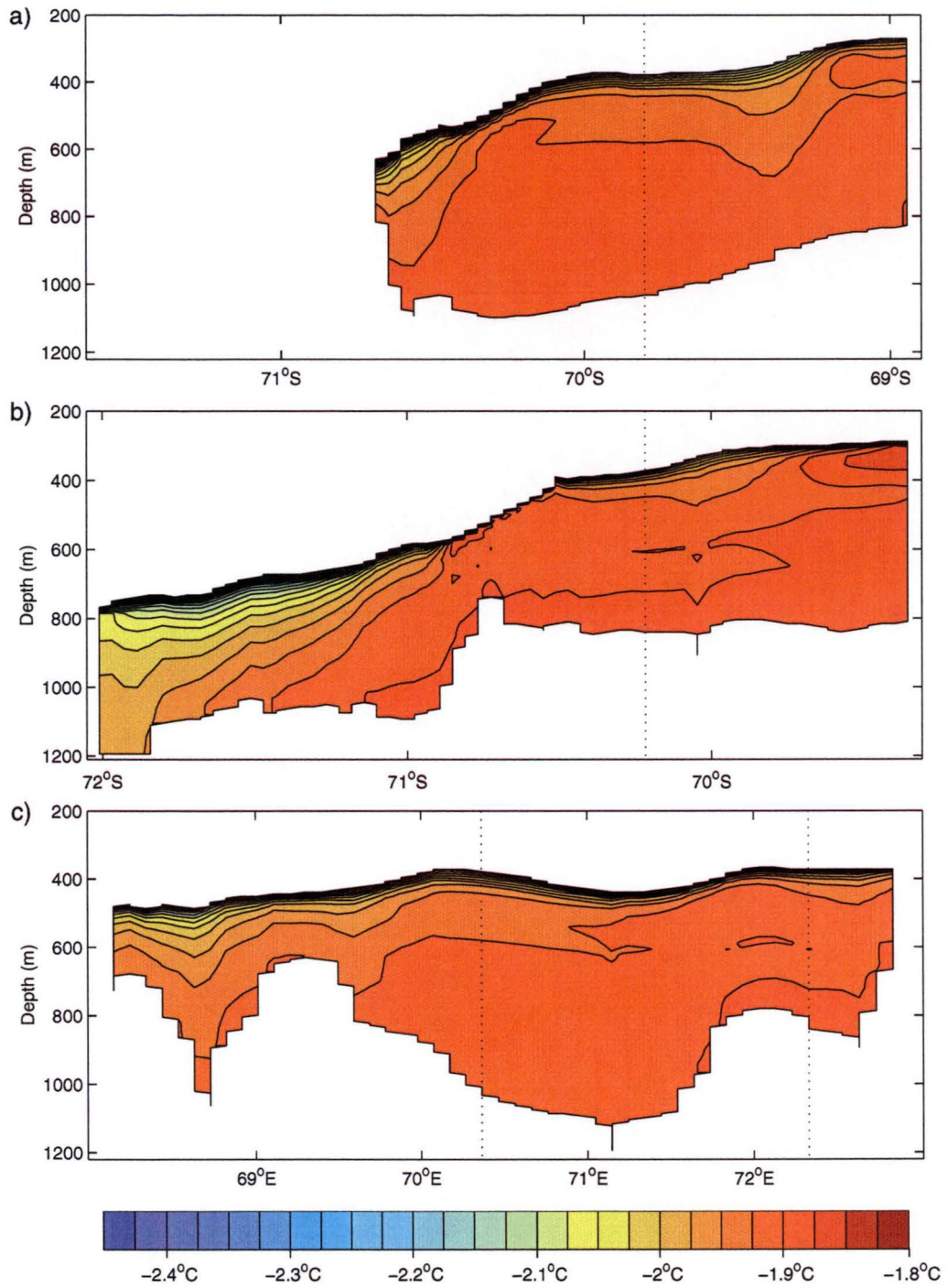

Figure 5.21: Temperature cross-sections of the model domain for the $\text{AIS}_{\text{P}\partial\Psi}$ run. a) Section A, b) Section B, and c) Section C. The locations of the cross-sections are shown in Figure 5.4. The dotted lines indicate where the cross-sections intersect.

inversions occurring in the same area as the out-cropping of the mixed layer.

The east-west temperature structure in Section C in the $AIS_{P\partial\Psi}$ run (Figure 5.21c) has a complex structure. As in the $AIS_{P\bar{v}}$ run, west of the Central Gyre basin the temperature gradient is much sharper adjacent to the ice shelf. This reflects the much greater heat in the water column.

The other notable feature in Section C, which was also observed in the $AIS_{P\bar{v}}$ run, is a parcel of relatively warm water in the upper water column. This is again warm water from the upper layers at the ice front between 73.8°E and 74.0°E (Figure 4.6a) being advected south. Part of this parcel is also shown in Section B at about 70.2°S. This feature is seen only in the $AIS_{P\bar{v}}$ and $AIS_{P\partial\Psi}$ runs. In the other open boundary model runs the area between 73°E and 74°E at the ice front is an area of outflow.

The salinity in the model domain is shown along Sections A, B, and C in Figure 5.22. The salinity fields in these three cross-sections are typical of the salinity for most of the model runs presented. In all three of the salinity sections the salinity is well stratified. This is mainly because the salinity forcing (Figure 4.6b) is itself well stratified, and as the density is largely determined by the salinity, the convective adjustment scheme will remove any salinity inversions or similar structures in the water column. The other effect which keeps the water column well stratified is the dominance of melting at the ice shelf-ocean interface. This adds freshwater at the top of the water column, which will enhance stratification in the water column.

The only scenario where the salinity field is significantly different is the closed boundary case. In the closed boundary model the salinity structure is significantly different because the high freezing rates at the ice shelf led to extensive salt rejection during the spin up to equilibrium circulation, raising overall salinities dramatically within the domain.

Apart from the very high salinities seen in the closed boundary run, the salinity range in the different model runs only changed with variations in the mass transport across the ice front. The waters at the bottom of the ice shelf cavity tended to be saltier, by approximately 0.02 PSU, in the $AIS_{P\bar{v}}$ and $AIS_{P\partial\Psi}$ runs compared with the $AIS_{\bar{u},\bar{v}=0}$ or $AIS_{\Psi=0}$ runs.

5.4 Variation of the time restoring constant

On the open ocean boundary an active boundary condition is used where the circulation indicates water is flowing into the domain. Instead of simply specifying the temperature and salinity of the inflowing water mass, the boundary tracer values are restored towards the boundary data with a prescribed relaxation time (Equation 4.73). The use of this restoring time scale (α) reduces the possibility of discontinuities in the tracer quantities on boundary points which change between inflow and outflow points on short time scales. For a model which is spun up to a steady state there should be no variation in the locations of inflow or outflow along the ice front. Changing the time restoring constant should not affect this. Realistically, most of the model runs can only be considered to be in a quasi-steady state, despite the ~15.8 year spin up time. So

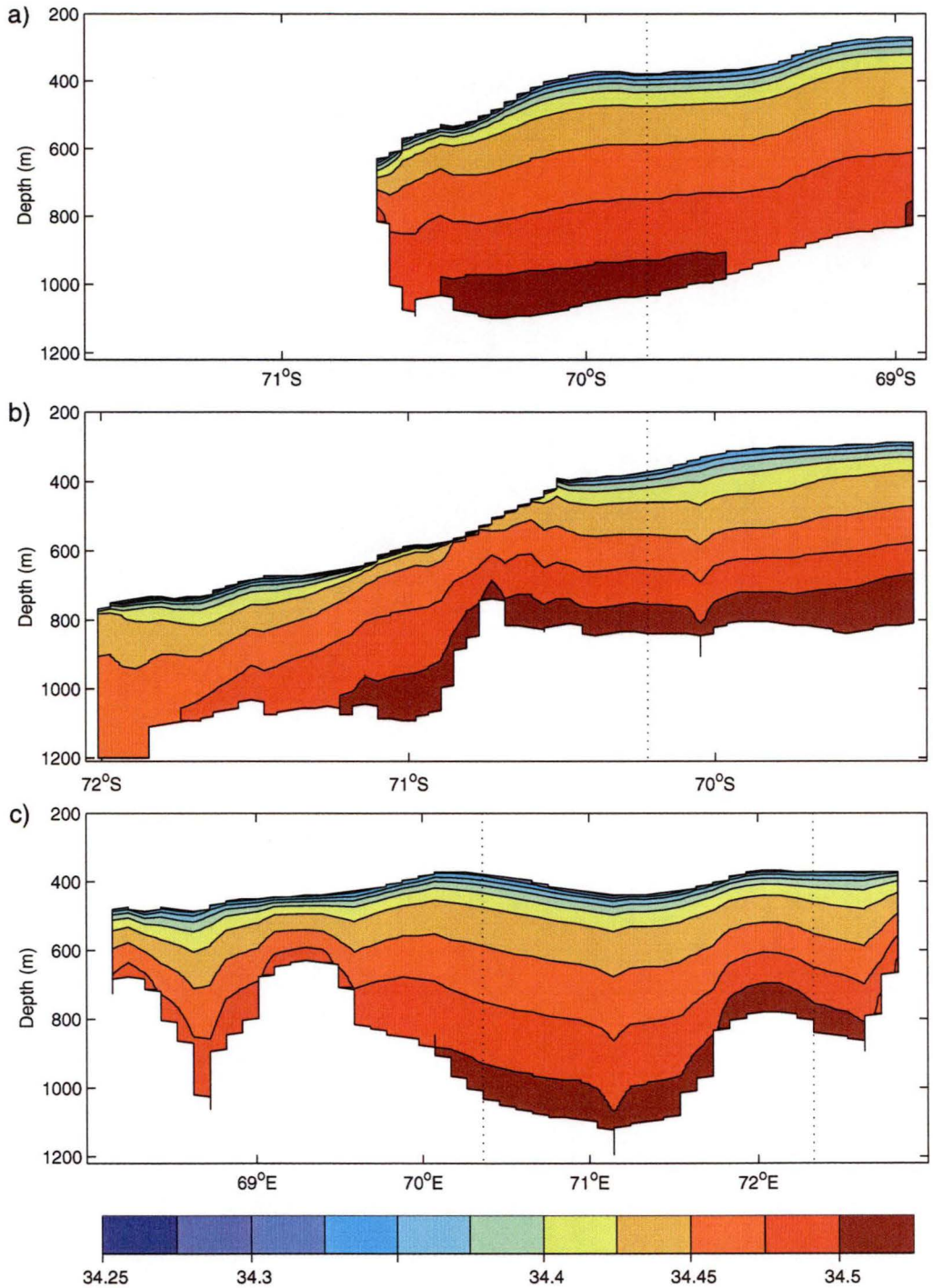

Figure 5.22: Salinity of the model domain, for the $AIS_{P\partial\Psi}$run. a) Section A, b) Section B, and c) Section C. The locations of the cross-sections are shown in Figure 5.4. The dotted lines indicate where the cross-sections intersect.

some changes are still occurring along the ice front boundary, these include the locations of inflow at the ice front.

Modifying the time restoring constant from the standard 80 days affects the ocean circulation, the distribution of temperature and salinity, and the melting and freezing at the ice shelf-ocean interface. For each transport condition on the boundary, there is no consistent trend with α in changes in the ocean circulation and the distribution of temperature and salinity. There is a consistent trend in the changes in rates of melting and freezing. For α time scales less than the 80 days used in the standard run the amount of melting at the ice shelf-ocean interface increases, with the reverse occurring for α time scales greater than 80 days. This is discussed in more detail in Section 5.6.2.

There is no trend in the ocean circulation and temperature and salinity distribution, with the results from different barotropic velocity or streamfunction boundary conditions being similar. Here only the results from the $AIS_{\Psi=0}$ run are discussed. This boundary condition is selected as it shows the largest amount of variation with respect to changes in the time restoring constant, and hence represents the bounds on changes in α.

For α values of 10, 50, and 200 days the horizontal circulation is very similar to the standard run (Figure 5.9). There are, however, a few changes in the strengths of some of the gyres. In the $\alpha = 10$ run the Central Gyre increases in strength in comparison with the standard $AIS_{\Psi=0}$ run (Figure 5.9), from $\sim$0.67 Sv to $\sim$0.75 Sv, and the Northern Gyre changes from $\sim$-0.47 Sv to $\sim$-0.41 Sv. The transport in the other gyres north of the Central Grounded Zone differs between the two runs by a similar amount. In the $\alpha = 50$ and $\alpha = 200$ runs, the opposite change occurs, with the Northern Gyre transport increasing, but the Central Gyre transport decreasing. In the $\alpha = 50$ run the transport in the Central Gyre is $\sim$0.53 Sv and in the Northern Gyre $\sim$-0.56 Sv. In the $\alpha = 200$ run the Central Gyre changes to $\sim$0.56 Sv and the Northern Gyre to $\sim$-0.58 Sv.

The structure of the horizontal circulation for $\alpha = 20$ days and for $\alpha = 100$ days, which are shown in Figure 5.23, differs noticeably from the circulation for the standard run. The change in the circulation is largely restricted to the north of the domain, with the circulation south of the Central Grounded Zone being similar to the other model runs.

In the $\alpha = 20$ run the Northern Gyre is replaced by two smaller gyres, with transports less than half that of the Northern Gyre in the main run. Both of the gyres are anticyclonic and are separated by a small shear zone. The western most of the two gyres is centred at 68.8°S 71.0°E. This is in approximately the same location as that of a small peripheral gyre in the $AIS_{\Psi=0}$ run ($\alpha = 80$ days) (Figure 5.9). The easternmost of the two gyres is centred at 69.3°S 71.6°E, this is slightly to the east of the centre of the Northern Gyre in the standard run. The similarity in the position of the centres of the two gyres to distinct features in the Northern Gyre of the $AIS_{\Psi=0}$ ($\alpha = 80$ days) run, suggests the change in α allows the gyre closest to the boundary (the western most of the two gyres) to dominate.

In the $\alpha = 100$ run an enhanced version of the Northern Gyre develops. The

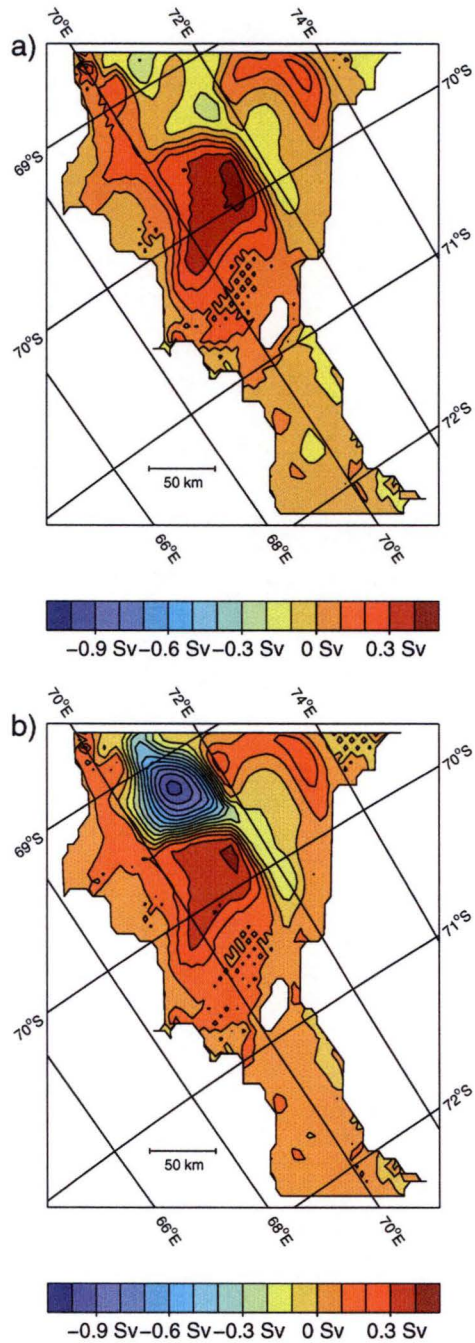

Figure 5.23: Vertically integrated streamfunction for the $\text{AIS}_{\Psi=0}$ run, with different α values. a) $\alpha = 20$ days and b) $\alpha = 100$ days. Circulation is clockwise about positive features.

maximum transport in the gyre is ~-1.03 Sv. This is greater than twice the transport in the Northern Gyre in the $AIS_{\Psi=0}$ (α = 80 days) run. This enhanced transport also causes a reduction in the transport in the Central Gyre. It reduces from ~0.67 Sv to ~0.43 Sv. However, the transport in the Northeastern Gyre is not as effected. The reduction in the strength of the Central Gyre occurs because less heat and salt is transported across the Northern Gyre, reducing the density gradients in the area of the Central Gyre.

Despite the difference in the ocean circulation between the α = 20 day, α = 100 day, and other α values, the temperature and salinity structure does not vary significantly from those for the $AIS_{\Psi=0}$ run (Figure 5.13). There is a small amount of variation in the melting and freezing rates, which when integrated over the whole ice shelf varies noticeably (this is discussed in Section 5.6.2).

The mass exchange at the ice front also varies with α. The changes in the inflow and outflow transport components follow no clear trend, with the mass transport for the α = 200 day run being the same as in the $AIS_{\Psi=0}$ (α = 80 day) run (~0.49 Sv). For α's less than the standard run the mass transport increases, with the maximum inflow and outflow transport component being ~0.57 Sv for the α = 10 day run.

The value of α reflects the strength with which restoring is applied on tracer inflow points along the ice front. Variation in α does impact on the model results, but the impact is less than the differences found between the model runs with different ice front streamfunction boundary conditions. This suggests the determination of appropriate boundary conditions for the streamfunction and barotropic velocity is more important.

As it is unclear from the studies in which α is varied, what a realistic value for α should be, there appears to be no reason for modifying the value of α from that chosen as standard (80 days). An α of 80 days was chosen as standard for several reasons. It is less than the 100 day restoration time chosen by Determann et al. [1994] for the Filchner-Ronne Ice Shelf. Thus an 80 day restoration time reflects both the higher resolution grid used in this model, and the smaller ice shelf cavity under the Amery Ice Shelf. A time scale of 80 days is also consistent with the circulation time scale of the central or main gyre. The retention of a standard value of α eases intercomparisons between different model runs.

5.5 Comparison of model results with oceanographic observations

There are presently no observations of the oceanographic properties under the Amery Ice Shelf. If we wish to test the ability of the model to reproduce ocean observations, the only available observations are along the ice front. There is a risk in using these observations for testing the model results. Reasonable agreement would be expected, because the observations are used in specifying the tracer boundary conditions. Despite this, the design of the tracer boundary

conditions still allows limited testing.

In the tracer fields specified on the ice shelf boundary several different water masses can be identified, including Ice Shelf Water (ISW). ISW can only form when water comes into contact with ice at depth, as its distinguishing characteristic is its temperature, which is less than the surface freezing point (~-1.9°C). Hence any ISW in the boundary tracer fields (Figure 4.6) is highly likely to be flowing out of the ocean cavity.

Water with similar characteristics to ISW is only observed at 12 of the 590 model points in the boundary forcing data set. For the $AIS_{\bar{u},\bar{v}=0}$, $AIS_{P\partial\Psi}$ and $AIS_{P\bar{v}}$ runs, the model reproduces outflowing ISW in the same location as in the forcing field. The area where ISW is flowing out is larger than the small area where it was observed. In the $AIS_{\Psi=0}$ runs the number of points which agree with the observations varies with the time restoring constant used. The best result is for the $\alpha = 50$ days run, where there is outflow for all the ISW points on the boundary. The worst result is for the $\alpha = 10$ days run, where only two-thirds of the 12 ISW points match.

5.6 Comparison of model results with glaciological observations.

Using the melting and freezing rates derived at the ice shelf-ocean interface it is possible to calculate estimates of two glaciological quantities and compare these with observations. The first is the marine ice layer thickness on the base of the ice shelf. The second is the basal component of the ice shelf mass balance. The method for calculating the marine ice layer thickness is described in Appendix A. It is similar to the method used by Nicholls and Jenkins [1993] for an ice stream on the Ronne Ice Shelf.

5.6.1 Marine ice layer thickness

The marine ice layer thickness is calculated, using the method described in Appendix A, along three flowlines in the ice shelf for each model run. The locations of the three flowlines are shown in Figure 5.24. The flowlines were extracted from a new digital elevation map of the Amery Ice Shelf from examination of surface features [H. Phillips, Pers. Comm.]. To calculate the marine ice layer thickness velocities along the length of each flowline are required. For ease the same velocity profile is used along each flowline. The velocity profile used (Figure 5.25) is found by fitting a polynomial to the observations reported by Budd et al. [1982], for velocities along the centre line of the ice shelf (Figure 3.3). The polynomial fit to the data is extrapolated to give a velocity profile to the southern most extent of Flowline 2, and to the ice front in all three flowlines. The velocity profile and the Budd et al. velocities are shown in Figure 5.25.

The marine ice thicknesses for four different model runs are shown in Figure 5.26. The marine ice thicknesses are calculated along the flowlines shown in Figure 5.24. All the model runs show similar features, with a thick marine ice

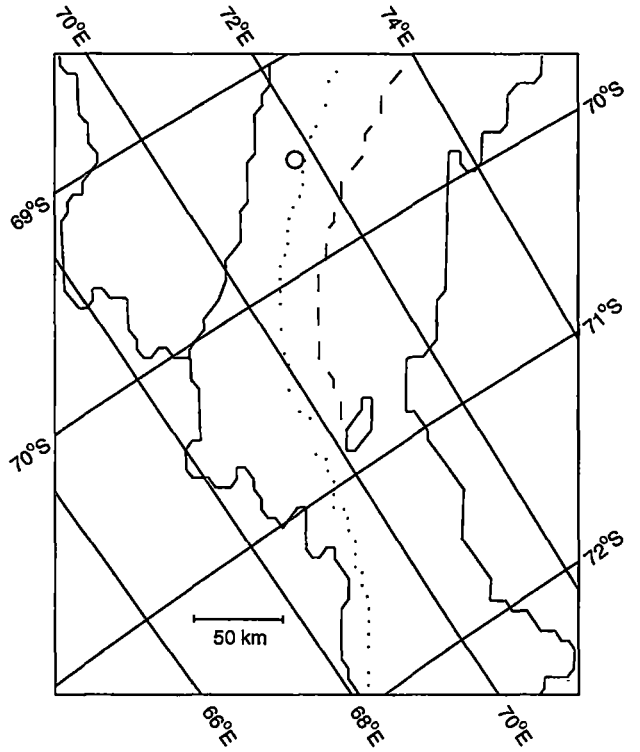

Figure 5.24: Locations of the flowlines along which the marine ice thickness, shown in Figure 5.26, are calculated. The solid line is Flowline 1, the dotted line is Flowline 2 and the dashed line is Flowline 3. The approximate position of the G1 drill site is marked by the circle.

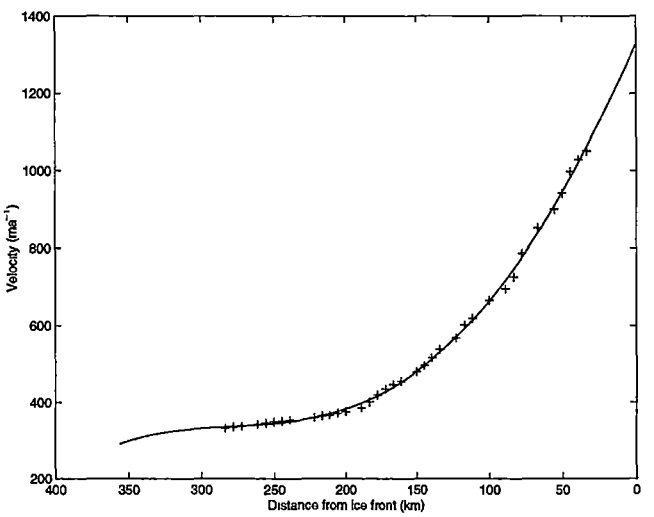

Figure 5.25: The along flowline ice velocity profile. The line is the interpolated velocity field, and the crosses indicate the positions of the Budd et al. [1982] observations.

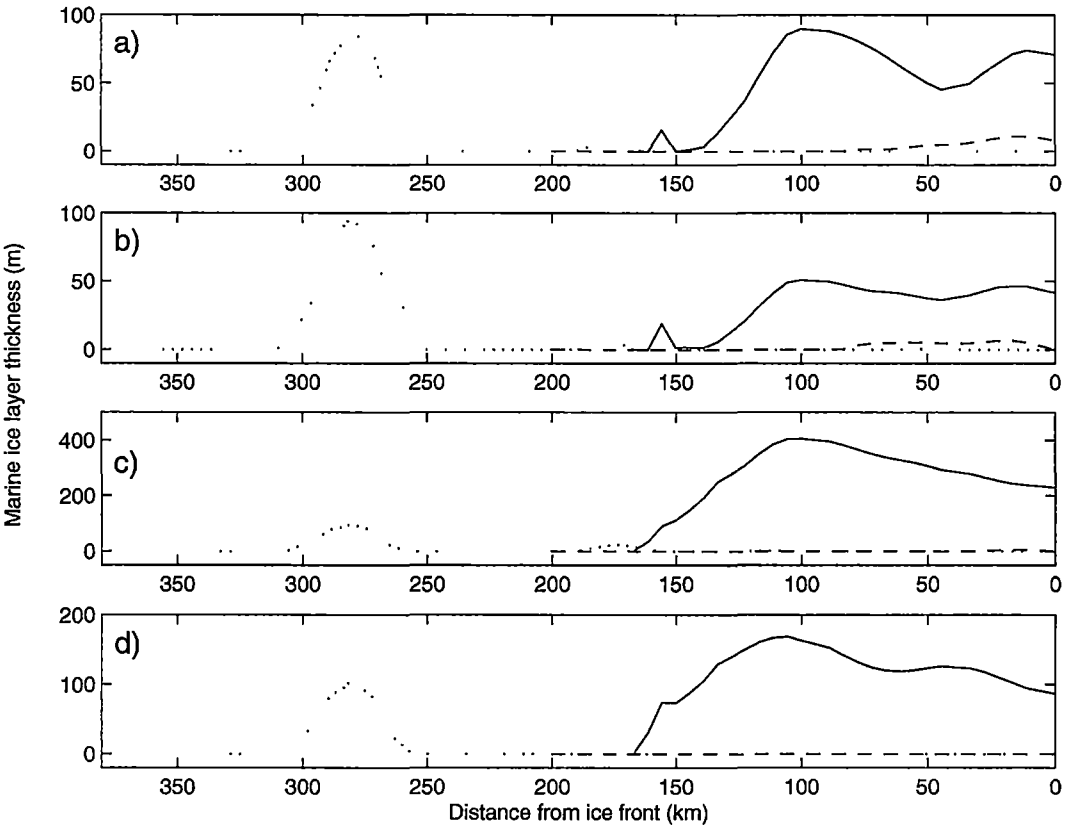

Figure 5.26: Marine ice layer thicknesses for, a) the $AIS_{\bar{u},\bar{v}=0}$ run, b) the $AIS_{\Psi=0}$ run, c) the $AIS_{P\bar{v}}$ run, and d) the $AIS_{P\partial\Psi}$ run. The solid line is Flowline 1, the dotted line is Flowline 2 and the dashed line is Flowline 3. The locations of the flowlines is shown in Figure 5.24.

layer forming along Flowline 1, little or no marine ice layer forming along Flowline 3, and a thick marine ice layer forming along Flowline 2, which then melts away. The variation in the marine ice thicknesses between the different model runs, shows the affect on individual flowline of different patterns of melting and freezing at the ice shelf-ocean interface.

At the G1 site, also shown on Figure 5.24, the marine ice thickness was estimated by Morgan [1972] at ~168 m. Flowline 2 runs closest to G1, but in the vicinity of G1 no marine ice layer is present. To the west, along Flowline 1, all the model runs shown in Figure 5.26 have substantial marine ice layers. In the $AIS_{P\partial\Psi}$ run the marine ice layer thickness along Flowline 1, at the same distance from the ice front as G1, has a marine ice layer approximately the same thickness as observed at G1. The $AIS_{P\bar{v}}$ run has a marine ice layer approximately twice the observed thickness.

The estimated marine ice layer thicknesses clearly indicate the model is capable of generating ice-ocean interaction which leads to the sustained accumulation of marine ice on the base of the Amery Ice Shelf. Additionally, the difference in the marine ice layers along Flowlines 1 and 2, suggests there is a substantial region of marine ice to the west of G1 which will persist to the ice front. There is evidence that such a layer does persist to the ice front from

Table 5.1: Estimates of the mass balance rates at the base of the Amery Ice Shelf.

Amery Model Run (AIS)	Mean Rates for Freezing Zone (ma^{-1})	Mean Rates for Melting Zone (ma^{-1})	Mean Rates for Whole (Loss) (ma^{-1})	Area of Melt (%)	Mass Change Rates Freezing (Gta^{-1})	Mass Change Rates Melting (Gta^{-1})	Mass Change Rates Net Loss (Gta^{-1})
Closed	0.37	0.32	0.00	53.6	8.8	8.8	0.0
$\bar{u},\bar{v}$=0	0.26	0.33	0.11	63.0	4.9	10.7	5.8
Ψ=0	0.16	0.40	0.21	66.6	2.8	13.4	10.6
P$\bar{v}$	0.38	0.66	0.35	70.4	5.9	23.9	18.0
P$\partial\Psi$	0.28	0.60	0.39	76.6	3.4	23.6	20.2

Note: The total area of the ice shelf is 5.6 x 10^4 km^2.

analysis of ice cores collected from green icebergs which are believed to come from the Amery Ice Shelf [Warren et al., 1993].

5.6.2 Ice shelf basal mass balance

One of the reasons for developing an understanding of the circulation under the Amery Ice Shelf is to estimate the amount of ice lost from melting at the base of the ice shelf. This can also be used in estimating the success of the model by comparing the calculated mass balance with previous estimates, which were discussed in Section 3.3. By calculating the heat and salt fluxes across various CTD sections in Prydz Bay, Wong et al. [1998] estimated the basal component of ice shelf mass balance at between 10.7 Gta^{-1} and 21.9 Gta^{-1}, with a mean of 14.7 Gta^{-1}.

Table 5.1 contains several different measures of the basal component of ice shelf mass balance. They are derived from the melting and freezing rates calculated at the ice shelf-ocean interface. The first two columns contain mean rates of freezing and melting, in areas where freezing or melting is occurring. The third column contains the mean rate of melting for the whole ice shelf. The next column contains the percentage of the ice shelf base area where melting is occurring. The fifth and sixth columns contain the mass accretion from freezing, and the loss from melting, in areas where either freezing or melting is occurring, respectively. The last column is the net mass loss from the ice shelf from basal melting.

The closed boundary run has a total mean melt rate and a net accretion rate of zero. The rates are this size, as apart from the ice shelf-ocean interaction, this is a closed system and total mass should be conserved.

The net basal mass loss estimates of the $AIS_{\Psi=0}$, $AIS_{P\bar{v}}$ and $AIS_{P\partial\Psi}$ runs span the range of basal mass loss estimates of Wong et al. [1998]. The net mass loss estimate for the $AIS_{\bar{u},\bar{v}=0}$ run is less than those of Wong et al.

It is interesting to note the mass loss from the model run with the most vigorous internal circulation, the $AIS_{P\bar{v}}$ run, does not experience the largest amount of mass loss. The mass loss from the $AIS_{P\partial\Psi}$ run is larger. The reason

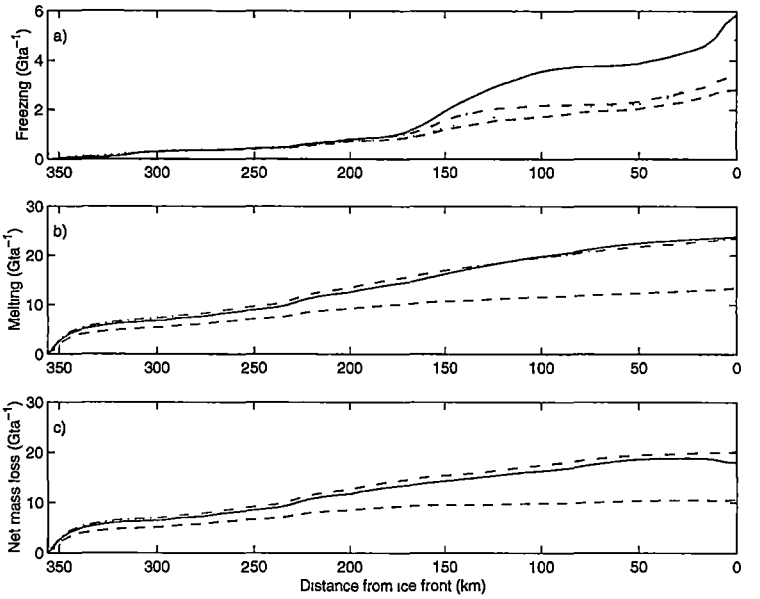

Figure 5.27: Cumulative a) freezing, b) melting, and c) net mass loss rates for the four different open boundary model runs. The dotted line represents the $\mathrm{AIS}_{\bar{u},\bar{v}=0}$ run, the dashed line the $\mathrm{AIS}_{\Psi=0}$ run, the solid line the $\mathrm{AIS}_{\mathrm{P}\bar{v}}$ run and the dash-dot line the $\mathrm{AIS}_{\mathrm{P}\partial\Psi}$ run.

for this is the $\mathrm{AIS}_{\mathrm{P}\partial\Psi}$ run has warmer temperatures in the ocean cavity. The temperature is most likely warmer because of the greater mass transport across the ice front, which will generate greater heat flux into the domain.

Changing the time restoring constant has an effect on the mass balance of the ice shelf. This occurs because the tracer restoration boundary terms form part of the flux of heat and salt into the model domain. If the change in heat and salt flux from changing the time restoring constant (α) is not counteracted by the other terms in the heat and salt fluxes at the ice front, then the fluxes at the ice shelf-ocean interface will change to ensure heat and salt conservation. The amount of variation with α depends on whether the streamfunction gradient is imposed or not. In the $\mathrm{AIS}_{\Psi=0}$ run the net mass loss varies between 6.9 Gta^{-1} for $\alpha = 200$ days, and 13.8 Gta^{-1} for $\alpha = 10$ days. Less variation is found for the $\mathrm{AIS}_{\mathrm{P}\partial\Psi}$ run. It varies between 17.9 Gta^{-1} for $\alpha = 200$ days, and 21.9 Gta^{-1} for $\alpha = 10$ days.

From the melting and freezing rates it is possible to show where the ice shelf is losing the bulk of its mass. The cumulative freezing, melting and net mass loss for the open boundary models is shown in Figure 5.27. The largest amount of melting in all the models is occurring near the southern grounding line. Once away from near the grounding line the amount of mass lost from the ice shelf follows an approximately linear trend towards the ice front. Near the ice front the effect of the large areas of freezing can be seen, as a reverse in the increasing net melt trend. This change is particularly prominent in the $\mathrm{AIS}_{\bar{u},\bar{v}=0}$ and $\mathrm{AIS}_{\mathrm{P}\bar{v}}$ runs, reflecting the magnitude of the freezing near the ice front.

5.7 Discussion and conclusions

The application of different boundary conditions, on either the streamfunction or the barotropic velocity component along the open ocean boundary, affects the oceanographic conditions of the cavity under the Amery Ice Shelf. The choice of the boundary conditions strongly influences the structure of the horizontal circulation in the cavity. The rest of the oceanography and the interaction with the ice shelf, through the heat and salt fluxes at the ice shelf-ocean interface follow from the horizontal circulation.

The structure of the ocean circulation in the cavity forms two distinct patterns depending on which boundary conditions are considered. In the closed boundary, $\mathrm{AIS}_{\bar{u},\bar{v}=0}$ and $\mathrm{AIS}_{\mathrm{P}\bar{v}}$ runs the circulation is dominated by a single cyclonic circulating gyre, which is named the Main Gyre (see for example Figure 5.6). In contrast, the horizontal circulation in the $\mathrm{AIS}_{\Psi=0}$ and $\mathrm{AIS}_{\mathrm{P}\partial\Psi}$ runs has several gyres in the same area—these are a cyclonic Central Gyre to the south and some form of anticyclonic Northern Gyre (see for example Figure 5.9).

The distinction between the boundary condition groups is the method of application of the boundary conditions, either on the streamfunction boundary row ($\mathrm{AIS}_{\Psi=0}$ and $\mathrm{AIS}_{\mathrm{P}\partial\Psi}$ runs), or on the velocity boundary row ($\mathrm{AIS}_{\bar{u},\bar{v}=0}$ and $\mathrm{AIS}_{\mathrm{P}\bar{v}}$ runs). In the model runs where the barotropic velocity component across the ice front ($\bar{v}$) is specified, the model forces the barotropic velocity along the ice front ($\bar{u}$) to be zero. The difference in the circulation could thus arise from the restriction on $\bar{u}$ near the ice front. With $\bar{u}$ prescribed to be zero there is less space for the development of more complex gyre structures within the model cavity. This would encourage the development of a single gyre, rather than several interacting gyres.

In the rest of the domain the circulation is similar for all the model runs. This similarity in the circulation is due to the strong influence that the topography has on the horizontal circulation. Both the Central and Main Gyres (depending on which boundary conditions is applied), and the Northeastern Gyre are topographically trapped on most sides, either by basins in the sea bed, or by ridges in the ice shelf draft.

The rates of melting and freezing at the ice shelf-ocean interface are strongly linked to both the ice shelf draft gradient and the ocean circulation. The influence of the ice shelf draft gradient on the rates of melting is similar to that seen in the Plume (Section 2.3.2) or HO Model (Section 2.3.4). In those models the ice shelf draft gradient controls the rising velocity of the melt-water layer adjacent to the ice shelf. In areas of low velocity (gentle gradients) the melt-water layer would thicken and thus melt rates would drop because the temperature gradient is less. Conversely, if the ice shelf draft gradient is steep the velocities would be higher and the melt-water layer thinner and thus heat fluxes would be larger. In the results in this chapter this process is modified by the horizontal circulation as the velocities adjacent to the ice shelf are not solely determined by a combination of the ice shelf draft gradient and the buoyancy of the melt-water layer. This is particularly important, as the horizontal circulation will drive a flow which intersects with the ice shelf, effectively giving a near ice shelf down slope flow. These are processes not considered by any of

the non-three-dimensional models.

The largest impact the horizontal circulation has on the melting rates is across the Central or Main Gyre. The southward flowing water on the eastern side of the gyre drives significant amounts of melting in all the model runs. The melt water, however, does not form a noticeable melt-water layer, because of the high velocities associated with the edges of the gyre. This stops a protective layer of melt water forming, allowing the melting to be continually fed by warm water transported from the ice front by the gyre. The bulk of the melt-water which forms is moved in the gyre to its western side. It provides an important source of melt-water feeding the large area of freezing on the western side of the Central or Main Gyre. Given the presence of melt-water, which can easily become supercooled, the rate of freezing is more dependent on the gradient of the ice shelf draft. This is because the changes in the ice shelf draft allow the necessary changes in pressure for water to become colder than the in situ freezing temperature.

The temperature and salinity structure in the model is dependent on heat and salt exchange across the ice front. In the open boundary runs the exchange of heat and salt across the ice front allows supercooled melt-water to, in effect, flow out of the domain and be replaced with inflowing water. This influences the temperature and salinity in the model domain. The degree of influence is dependent on two factors, the time restoring constant, and the cross-boundary velocity. The magnitude of the cross-boundary velocities affects the amount of melt-water advected out of the domain and the rate at which heat and salt from inflow regions is advected into the model interior. The time restoring constant has a smaller effect because it is only able to influence the inflowing tracer values. However, varying the time scale over which restoring occurs does influence the heat and salt fluxes at the ice front.

There is the potential the rates of melting and freezing in the model may be effected by the choice of boundary condition parameterisation at the ice shelf-ocean interface. Any significant changes in the rates of melting and freezing could potentially affect the temperature and salinity structure in the model domain, and thus through the density structure, the circulation in the cavity. To test what effect a different parameterisation could have, an exploratory study was completed and is presented in Appendix B. It was found the temperature and the salinity structure in the cavity changed little, although the relative melting and freezing rates did change. Despite the change in the magnitudes of the melting and freezing rates the net basal mass balance remained similar.

By comparing the results of the different model runs with observable quantities, it was hoped to determine which of the model runs could be considered to most realistically represent the oceanography of the ocean cavity under the Amery Ice Shelf. Three different measures were considered: comparison between the ocean observations along the ice front, and the temperature and salinity in the model boundary row; estimates of marine ice thickness along three glaciological flowlines; and estimates of the basal component of ice shelf mass balance.

Comparison between the model results along the open boundary and the

ocean observations was inconclusive for the purposes of determining a realistic representation of the oceanography. Most of the models were able to reproduce outflowing ISW, in the area where ISW was observed.

None of the marine ice layers calculated from the ocean model derived melting and freezing results, were able to reproduce exactly the single marine ice thickness observed at G1. This was perhaps an unrealistic aim because of the uncertainties in calculating the ice shelf draft from sparse radio echo sounding thickness data (Section 4.5), and the dependence of the ocean circulation, which influences where freezing occurs on the ocean cavity topography. It is important that the results consistently predict in parts of the model domain, marine ice layers with thicknesses similar to that observed at G1.

The estimates of the basal component of the ice shelf mass balance were potentially more useful in assessing the different models. The range of the basal component of mass balance estimates against which the model results were compared is large. Wong et al. [1998] estimates ranged from 10.7 Gta^{-1} to 21.9 Gta^{-1}, with a mean of 14.7 Gta^{-1}. The estimate of Jacobs et al. [1992] at 23.0 Gta^{-1} was dependent on the model results of Hellmer and Jacobs [1992], which contain their own uncertainties.

With these thoughts in mind, the choice of which design of the open boundary models most realistically represents the circulation under the Amery Ice Shelf is difficult to make. It seems unlikely the $\mathrm{AIS}_{\bar{u},\bar{v}=0}$ run is very realistic. This can be argued from the comparison between observations and the model results, and also from the model physics. The basal mass estimates are well outside the estimates of Wong et al. [1998]. The restriction to no barotropic flow, adjacent to or across the ice front, is also not realistic. That model is more important for considering if this restriction would reduce the cross-boundary flow to an overturning circulation, similar to those assumed for the Plume and HO Models (Chapter 2); in general this did not occur.

The constraint on the along front barotropic velocity in the $\mathrm{AIS}_{\mathrm{P}\bar{v}}$ run, i.e., $\bar{u} = 0$ suggests this run may be unrealistic. However, if the across front velocities ($\bar{v}$) are significantly larger than the along front velocities ($\bar{u}$), setting the along front velocities to zero may not have a significant effect. The $\mathrm{AIS}_{\mathrm{P}\bar{v}}$ and the $\mathrm{AIS}_{\mathrm{P}\partial\Psi}$ runs are dependent on the streamfunction gradient specified along the boundary. As discussed earlier, the method used in finding and applying the correcting velocity, does not significantly alter the results for either the $\mathrm{AIS}_{\mathrm{P}\bar{v}}$ run or the $\mathrm{AIS}_{\mathrm{P}\partial\Psi}$ run.

The two different methods for specifying the streamfunction boundary condition along the ice front, effectively allows different streamfunctions to evolve internally for the same boundary condition. This is because in the $\mathrm{AIS}_{\Psi=0}$ and $\mathrm{AIS}_{\mathrm{P}\partial\Psi}$ model runs cross-boundary flow is partly determined by the internal circulation, so in effect, the model can disagree with the flow prescribed by the streamfunction boundary condition. In the $\mathrm{AIS}_{\Psi=0}$ run the $\Psi = 0$ boundary condition effectively damps the cross-boundary flow determined by the internal circulation. In the $\mathrm{AIS}_{\mathrm{P}\partial\Psi}$ run where $\frac{\partial\Psi}{\partial\lambda}$ is prescribed, there is the potential for a complicated circulation along the ice front to develop as the circulation attempts to reconcile the differences between the circulation desired by the

internal circulation and the prescription of $\frac{\partial \Psi}{\partial \lambda}$ on the boundary. This effect, however, is difficult to eliminate without a boundary treatment that allows inflow to be prescribed, and outflow to freely evolve.

The limited number of observations make it unclear which model run is the most realistic. Because of this, the results from all except the closed boundary and $\mathrm{AIS}_{\bar{u},\bar{v}=0}$ runs should be considered as possible estimates of the oceanographic conditions in the ocean cavity under the Amery Ice Shelf. This also suggests that moving the open ocean boundary away from the ice front is desirable as a long term solution. This is investigated in Chapter 7, where the model domain is expanded to include part of the ocean to the north of the ocean cavity under the Amery Ice Shelf.

The results presented in this chapter are sufficiently encouraging to warrant using this model for a study of the impact of changing ocean climates near the Amery Ice Shelf in the next chapter.

Chapter 6

Impact of ocean temperature change on ocean circulation and the mass balance of the Amery Ice Shelf

Melting at the base of Antarctic ice shelves is a major source of ice loss from the Antarctic Ice Sheet. For any given situation the rate of melting is dependent on the temperature difference between the ice shelf and the underlying ocean. With ocean temperatures expected to increase in most global climate change scenarios [Mikolajewicz et al., 1990; Manabe and Stouffer, 1994; Gordon and O'Farrell, 1997], the impact of this on the mass balance of Antarctic ice shelves could be quite significant.

In this chapter the responses to several different ocean climate change scenarios are presented. For each scenario the change in ocean circulation, the temperature and salinity distributions, and the affect on the ice shelf mass balance are discussed. In addition to ocean warming scenarios, two cooler ocean scenarios are considered.

Several of the climate change scenarios presented in this chapter were discussed by Williams et al. [1998b]. The difference in the results presented here and those of Williams et al. comes from a change in the tracer boundary conditions at the open ocean boundary. These boundary conditions are particularly important in considering temperature changes along the ocean boundary, as they partly control the inflow of heat at the model boundary. The boundary conditions used by Williams et al. were similar to those presented in Section 4.3, but contained additional restoration terms. These terms applied restoring on the outflowing water masses in addition to the inflowing water masses. This effect may not be significant in present climate scenarios, where it could be considered to constrain the outflow to the observations. Restoring on outflow effectively allows heat and salt to move against the direction of flow, hence its impact in climate change scenarios could be both large and undesirable.

6.1 Estimates of ocean temperature change

Estimates of likely ocean temperature changes near the Amery Ice Shelf can be taken from modelling studies of various climate change scenarios. The studies discussed here [Mikolajewicz et al., 1990; Manabe and Stouffer, 1994; Gordon and O'Farrell, 1997] consider as their climate change scenario the affects of increases in the concentration of atmospheric CO_2.

Mikolajewicz et al. [1990] drove an Ocean General Circulation Model (OGCM) with monthly mean anomalies of surface air temperature based on the doubling of atmospheric CO_2. These surface air temperature anomaly fields were derived from four equilibrium-response experiments conducted with Atmospheric General Circulation Models (AGCMs), each coupled to a mixed layer ocean model [Hansen et al., 1984; Wetherald and Manabe, 1986; Schlesinger and Zhao, 1989; Wilson and Mitchell, 1987]. The results from all four AGCMs were interpolated onto the OGCM grid and averaged to provide an annual cycle of monthly mean anomalies of surface air temperature. In addition to the run forced by the doubled atmospheric CO_2 field a control run was done. In the control run the OGCM was forced with restoring fields calculated over the last 500 years of the 10 000 year spin up period of the OGCM.

Fifty years after applying the mean anomaly surface air temperature field, a comparison of the sea surface temperature field between the AGCM forced run and the control run was made [Figure 4, Mikolajewicz et al., 1990]. Along the coast of Antarctica at the longitude of the Amery Ice Shelf this temperature change was $\sim$2°C.

In contrast to the work of Mikolajewicz et al. [1990], Manabe and Stouffer [1994] and Gordon and O'Farrell [1997] used fully coupled Ocean-Atmosphere General Circulation Models to study the impacts of increased atmospheric CO_2 concentration.

Manabe and Stouffer [1994] looked at two different climate change scenarios, a doubling of atmospheric CO_2 concentration, and a four-fold increase in CO_2 concentration, in addition to a control run (no change in atmospheric CO_2 concentration). In both runs the increase in CO_2 was applied at the rate of $1\%a^{-1}$. This led to a doubling in CO_2 after 70 years and a four-fold increase after 140 years. The impact on the ocean temperature field was greater in the four-fold increase study, than in the doubling of CO_2 run.

Several different ocean temperature fields featuring the four-times CO_2 ($4\times CO_2$) run and the control run were presented by Manabe and Stouffer [1994]. They show the latitude-height (or depth) distribution of the zonally averaged mean temperature in the Atlantic and Pacific Oceans, both for the model initial conditions and for the 400-500 model year average for the $4\times CO_2$ run. Comparison between the initial conditions and the $4\times CO_2$ run provides an estimate of temperature change. At depths on the Antarctic coast, where interaction between the Southern Ocean and the ice shelf cavity is expected, the temperature changes in the Atlantic and Pacific Oceans were $\sim$4°C and $\sim$3°C, respectively. Manabe and Stouffer also present the geographical distribution of the annual mean difference for the sea surface temperature between the control and $4\times CO_2$ runs. Two time periods are shown, an average for the period 130-150 years (ap-

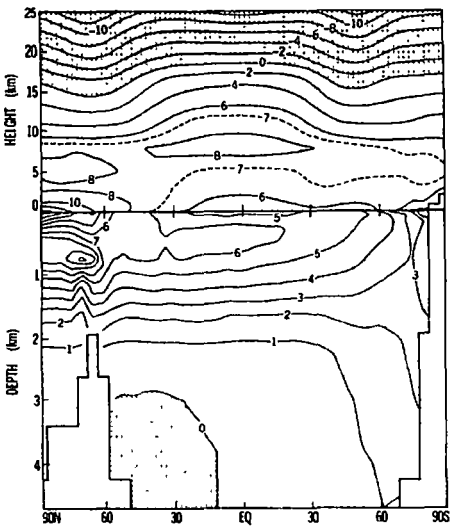

Figure 6.1: Latitude-height (or depth) distribution of zonally averaged, annual mean difference in temperature (°C) between the $4\times CO_2$ run and the control run for integrations averaged over the 400-500 year period [Figure 17, Manabe and Stouffer, 1994].

proximately when the four-fold increase in CO_2 concentration was reached), and an average for the period 400-500 years. The figures respectively show sea surface temperature differences of ~0°C and ~2°C, on the Antarctic Coast at the longitude of the Amery Ice Shelf. In Figure 6.1, the zonally averaged mean temperature difference between the $4\times CO_2$ and control runs is shown. At the latitude of the front of the Amery Ice Shelf (69°S) and at depths where there is ocean exchange with the ice shelf cavity, the temperature change was ~3°C. This may be larger than would be observed, because of the lack of a continental shelf which might be expected to keep the warming away from the ice shelf.

Gordon and O'Farrell [1997] used a similar rate of increase for atmospheric CO_2 concentrations in their coupled model run. Unlike Manabe and Stouffer [1994] they did not continue increasing the atmospheric CO_2 concentration after it had doubled. Gordon and O'Farrell [1997] also did a control run with no change in the atmospheric CO_2 concentration. The only result Gordon and O'Farrell provide is for temperature change estimates is the sea surface temperature [Figure 19, Gordon and O'Farrell, 1997]. At the longitude of the Amery Ice Shelf on the coast of Antarctica the change in the sea surface temperature was ~-0.05°C.

In O'Farrell et al. [1997] ocean temperature anomaly fields, based on the results of Gordon and O'Farrell [1997] are presented. These ocean temperature anomaly fields were developed (along with appropriate atmospheric forcing) to drive a model of the Antarctic Ice Sheet, including the major ice shelves. Figure 6.2 shows the ocean temperature anomaly below 100 m used in forcing the ice sheet model, upon reaching atmospheric conditions of $3\times CO_2$, after 180 years. This temperature anomaly field provides a good estimate of the temperature anomaly near the Amery Ice Shelf. Unlike sea surface temperature estimates,

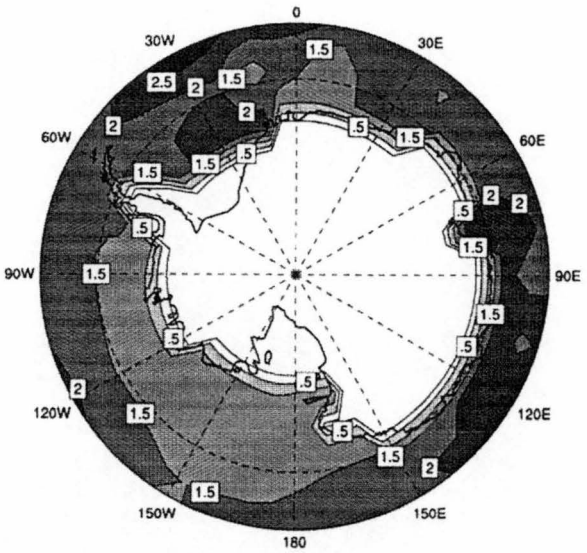

Figure 6.2: Mean ocean temperature anomaly field below 100 m, from a transient model run at the time of reaching a three-fold increase in atmospheric CO_2 concentration [Figure 2d, O'Farrell et al., 1997].

this temperature field is at a depth where water exchange occurs with the ocean cavity under the Amery Ice Shelf. A suitable estimate from Figure 6.2 would be in the range of ~1°C to ~2°C.

The three different studies suggest that with increased atmospheric CO_2, ocean temperatures in the vicinity of the Amery Ice Shelf will change by between ~-0.05°C (at the surface) and ~3°C, with the most likely temperature change about 2°C.

Most climate change model studies do not include any form of coupling between the ocean and the Antarctic Ice Sheet. This eliminates any possible feedback from ice shelves melting which would cool and freshen the adjacent ocean. To allow for the possibility of the estimated temperature changes being too large, several warming studies were done with different degrees of warming for the water at the ice shelf cavity front. This also allows estimates of the effect of warming on shorter time scales than the time scale on which large temperature change is expected.

6.2 Boundary conditions

In the previous chapter several different prescriptions of the open ocean boundary conditions were discussed. Several of the model runs could be considered as representative of the present conditions as they give reasonable agreement with observations. For consistency one boundary condition on the streamfunction needs to be used for the different climate change scenarios. Two of the boundary conditions in the previous chapter seem suitable, these are those used for the $AIS_{\Psi=0}$ and $AIS_{P\partial\Psi}$ runs.

The other two boundary conditions (those used in the $AIS_{\bar{u},\bar{v}=0}$ and $AIS_{P\bar{v}}$

runs) both specify the barotropic velocity components on the boundary velocity row. Specification of across front velocities constrains circulation close to the front and specifies the across front mass exchange. This will affect the heat and salt fluxes at the open ocean boundary. Of the two suitable boundary conditions the $AIS_{\Psi=0}$ is the more preferable streamfunction boundary condition. This is because the prescribed streamfunction gradients along the boundary in the $AIS_{P\partial\Psi}$ run are determined by assuming the tracer forcing at the ice front is in geostrophic balance.

In the climate change scenarios these tracers are modified to reflect the climate change scenarios. If the prescribed streamfunction is not modified then inconsistencies between the prescribed flow and the density gradient may arise. This has the potential to cause anomalous circulation features to develop as the model attempts to accommodate any inconsistencies. Indeed this was found to be the case, as in tests of the prescribed streamfunction boundary condition the model did not reach a steady state. If the streamfunction is modified to reflect the new density structure at the ice front, this removes a level of consistency between the different climate change scenarios.

To maintain consistency with the studies in the previous chapter a relaxation time scale of 80 days is used. The ocean circulation and ice shelf for the $AIS_{\Psi=0}$ run was discussed in Section 5.2.2. In this chapter this model run is relabelled AIS_{pres}.

6.3 Responses to a cooler ocean

In addition to the general warming trend predicted by coupled climate models it is worth considering the general effects of variation in the climate. This includes the possibility that the current climate is warmer than other historical climates. There is also a need to consider colder climates to assess the sensitivity of the model, and attempt to find conditions of minimal ice shelf melting. In this section two climate scenarios are considered before the warmer climate scenarios are presented in the next section.

The water along the ocean boundary is already close to the surface freezing temperature. This restricts the amount of cooling which can be applied to the water column as only two likely mechanisms for cooling the water exist. The first is that individual water parcels have been cooled at the surface via interaction with the atmosphere, and then moved down the water column. The second is that water parcels have been cooled by interaction with the ice shelf, before moving down the water column. In the second case the most likely place this could occur is at the ice front. Taking into account these mechanisms two cooler ocean scenarios are considered.

In the first cooler run, labelled AIS_{cool}, the ocean temperature fields prescribed along the ocean front (Figure 4.6a) are cooled at each depth level to the salinity dependent surface freezing temperature, except where the present temperature is less than the surface freezing temperature where it is unchanged. At the ice front boundary the mean temperature change is $\sim$-0.03°C, with a maximum change of $\sim$-0.25°C.

In the second cooler run, labelled AIS_{cold}, the waters are cooled to the salinity dependent in situ freezing temperature at the minimum ice shelf draft (235 m). With this cooling mechanism the mean temperature change is ~-0.20°C, and the maximum change is ~-0.43°C.

The temperature change is applied to the open boundary and the model is spun up from the same initial state as used for the AIS_{pres} run. (No change is made to the salinity.) Both the AIS_{cool} and AIS_{cold} runs are run for the same length of time as the standard model (~15.8 years).

Ocean circulation

The pattern of horizontal circulation does not change significantly between the AIS_{pres} run and the AIS_{cool} run. The main circulation features are located in the same positions (Figure 6.3). However, the strengths of the various gyres are different between the two runs. The Central Gyre weakens slightly with the maximum circulation dropping from ~0.67 Sv in the AIS_{pres} run to ~0.53 Sv for the AIS_{cool} run. The largest anticlockwise circulating gyre, the Northern Gyre, does not weaken in the same manner as the Central Gyre. Instead, it strengthens in the AIS_{cool} run from ~-0.47 Sv to ~-0.56 Sv, becoming the gyre with the largest transport.

The additional cooling applied in the AIS_{cold} run does change the horizontal circulation (Figure 6.4). The two largest changes are in the northeast of the domain and south of the Central Gyre. In both of these areas the streamfunction changes sign, indicating a reversal in the direction of flow. In the north a single gyre with several local maxima forms. The single gyre includes the Northern and the now reversed Northeastern Gyre, in addition to the area between the Central and Northeastern Gyres. South of the Central Gyre, the now anticlockwise flowing gyre fills the area between the Central Gyre and a more northerly positioned Southern Gyre. This includes flow to the east of the Central Grounded Zone, where circulation is now reversed in direction. (The effects of this can also be seen in the temperature cross-section (Figure 6.6b).) In addition to these major changes the Central and Northern Gyres both weaken to ~0.49 Sv and ~-0.40 Sv, respectively. The weakening of these two gyres decreases the strength of the current along the western boundary.

Cooling the boundary temperature fields also affects the temperature and salinity within the model. Figures 6.5 and 6.6 show three different temperature cross-sections for the AIS_{cool} and AIS_{cold} runs. The temperature change on any of the three sections between the AIS_{pres} (Figure 5.13) and the AIS_{cool} runs is not large. Most of the change occurs at the northern (ice front) ends of Sections A and B. Here the thermocline is less steep than in the AIS_{cool} run. This removes small temperature inversions near the ice shelf in Section A and through the whole water column in Section B.

Greater changes can be seen between the AIS_{cold} run and the AIS_{pres} run. The most obvious change is the near homogeneous water column at the northern end of Section B (Figure 6.6b). A similar feature can be seen on the northern end of Section A (Figure 6.6a). This is not as distinct as the one on Section B, and it contains a noticeable temperature inversion. The water column only

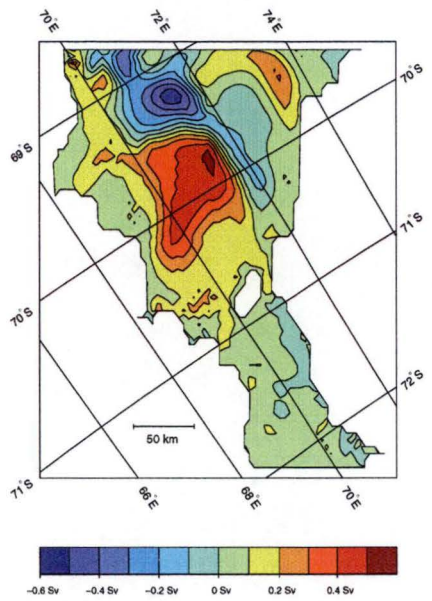

Figure 6.3: Vertically integrated streamfunction from the AIS_{cool} run. Circulation is clockwise around positive features.

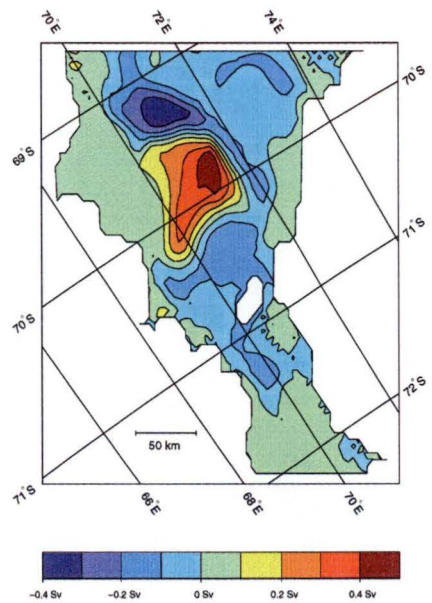

Figure 6.4: Vertically integrated streamfunction from the AIS_{cold} run. Circulation is clockwise around positive features.

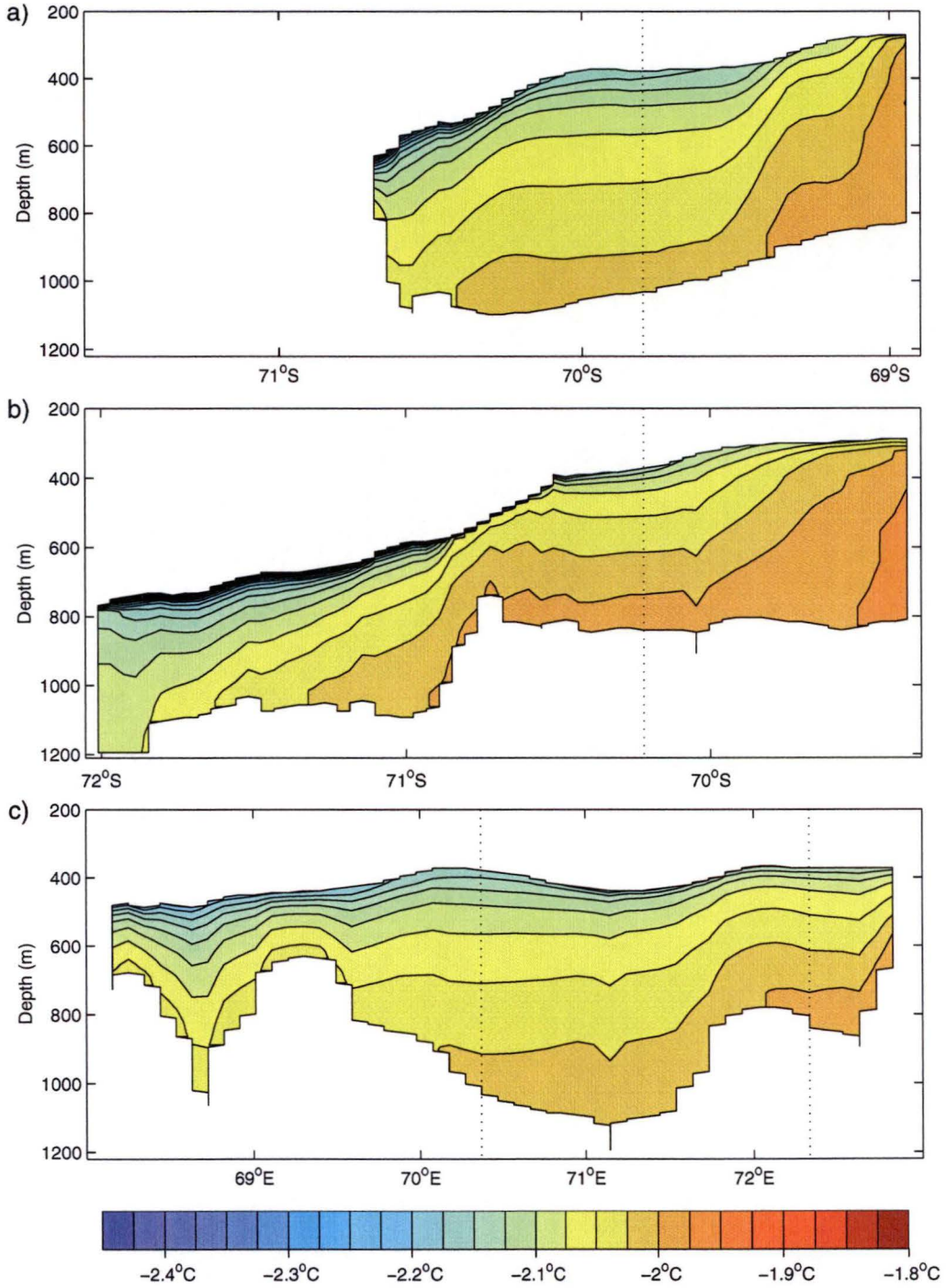

Figure 6.5: Three temperature sections through the water column, for the AIS_{cool} run. a) Section A, b) Section B, and c) Section C. The location of the sections is shown in Figure 5.4. The dotted lines indicate where the cross-sections intersect.

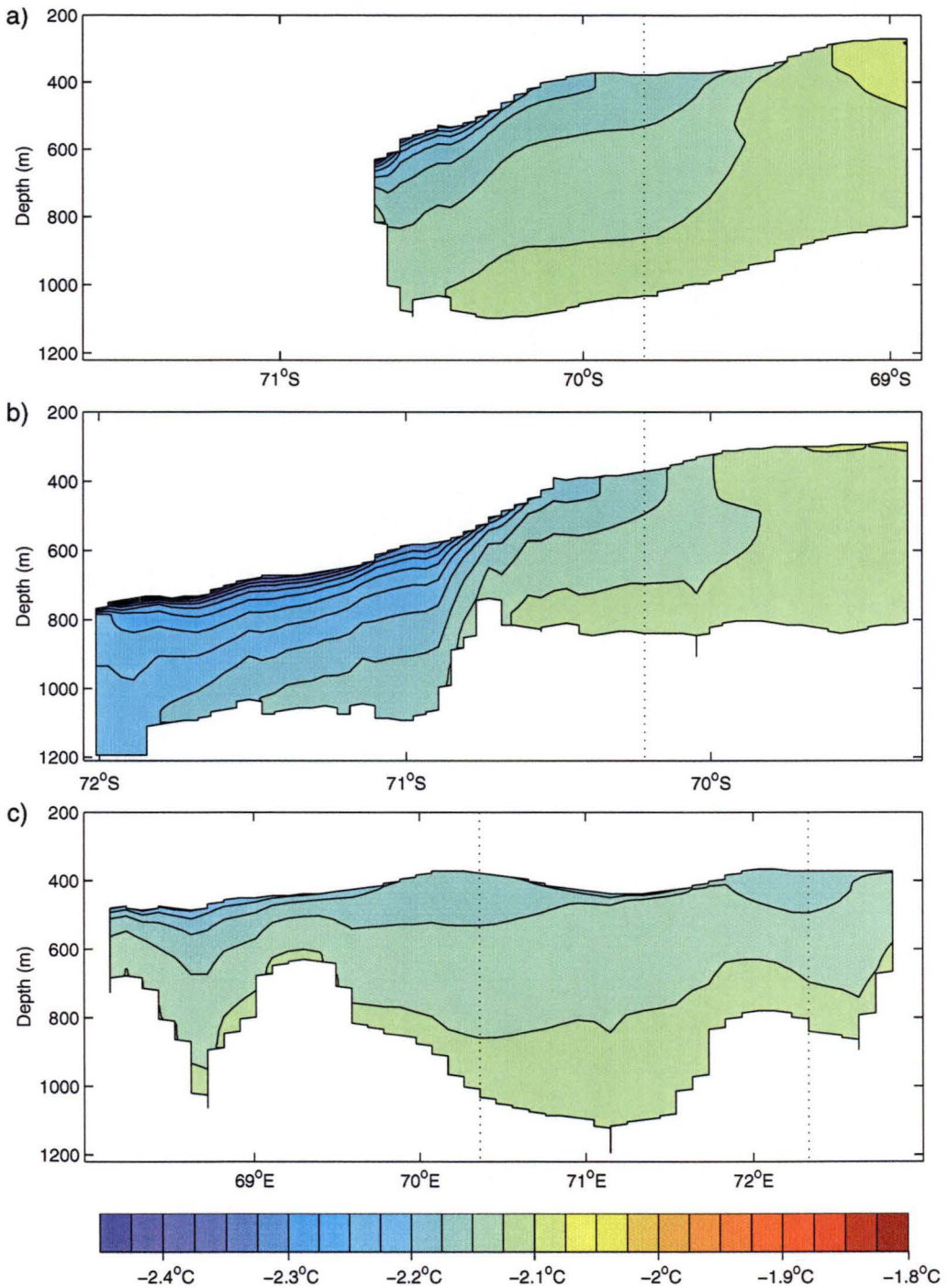

Figure 6.6: Three temperature sections through the water column, for the AIS_{cold} run. a) Section A, b) Section B, and c) Section C. The location of the sections is shown in Figure 5.4. The dotted lines indicate where the cross-sections intersect.

Table 6.1: Estimates of the basal component of mass balance at the base of the Amery Ice Shelf, under present and colder ocean conditions.

Amery Model Run (AIS)	Mean Rates for Freezing Zone (ma^{-1})	Mean Rates for Melting Zone (ma^{-1})	Mean Rates for Whole (Loss) (ma^{-1})	Area of Melt (%)	Mass Change Rates Freezing (Gta^{-1})	Mass Change Rates Melting (Gta^{-1})	Mass Change Rates Net Loss (Gta^{-1})
pres	0.16	0.40	0.21	66.4	2.8	13.4	10.6
cool	0.16	0.38	0.19	64.7	2.9	12.4	9.5
cold	0.20	0.25	0.05	55.5	4.5	7.1	2.6

Note: The total area of the ice shelf is 5.6 x 10^4 km^2.

remains stable because of the strong salinity gradient in the area. The salinity gradient is maintained by the strong localised freezing above the northern part of Section A (Figure 6.8). These features in both sections are associated with the large single gyre in this part of the domain, combined with the lack of warm ($> -2°C$) water circulating in the domain. The warm water is absent because the temperature change on the boundary effectively stops warm water masses from entering the ocean cavity.

The reduction of the warm water in the domain can also be seen in Section C (Figure 6.6c). Here the deep basin, around which the Central Gyre circulates, is filled with considerably colder water in the AIS_{cold} run than in either the AIS_{cool} run or the AIS_{pres} run.

Ice shelf basal mass balance

The changes in ocean circulation between the AIS_{pres} run and the two cooler runs affects the mass balance of the ice shelf. Most of the change in the mass balance occurs from the changed temperature gradient at the ice shelf-ocean interface.

The cooler waters circulating under the ice shelf reduce the melt rates near the grounding zone and in the other major melting regions. However, the weaker circulations in the AIS_{cool} and AIS_{cold} runs reduce the velocity of water adjacent to the ice shelf, allowing a more complete use of the heat capacity of the water in contact with the ice shelf. This has the additional effect of thickening the melt-water layer at the top of the water column (see Figures 6.5 and 6.6), hence increasing the potential for supercooling as the melt-water layer moves to shallower ice shelf drafts.

In Figures 6.7 and 6.8, the shift in the position of the zero contour line, which indicates the boundary between melting and freezing, increases the area in the north of the domain where freezing is occurring. A slight shift in the boundary between melting and freezing also occurs in the south of the domain. The shift in the south of the domain is less significant as both the area and freezing rates are small. The most noticeable change is the transition from melting to freezing in the channel to the east of the Central Grounded Zone. This is caused by

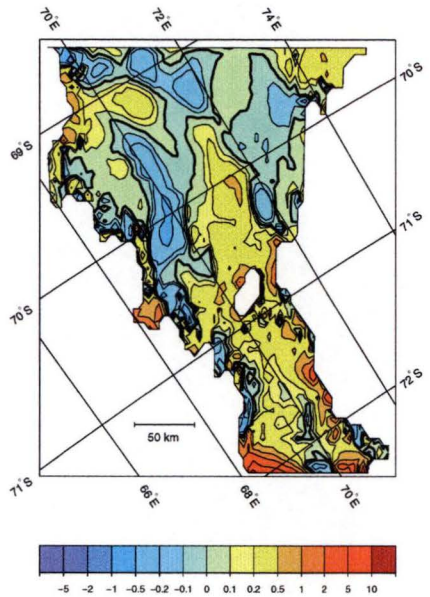

Figure 6.7: Rates of melting (+) and freezing (-) from the AIS_{cool} run in ma^{-1}. The bold contour denotes the boundary between melting and freezing.

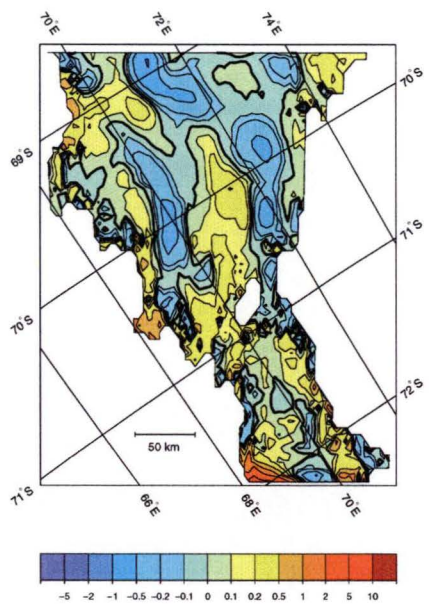

Figure 6.8: Rates of melting (+) and freezing (-) from the AIS_{cold} run in ma^{-1}. The bold contour denotes the boundary between melting and freezing.

the change of direction in this part of the domain. The locations of the peak areas of freezing, both in the south and north, do not change in comparison to the results for the AIS_{pres} run. In the AIS_{cool} run the peak rate of freezing ($\sim$0.73 ma^{-1}) does not change from the AIS_{pres} run, in contrast the peak rate of freezing increases to $\sim$1.00 ma^{-1} in the AIS_{cold} run.

The melt rates follow the opposite trend. They decline with increased cooling. This can be seen in the mean rates in Table 6.1 and in the peak melting rates. The peak melt rate at the southern grounding line, changes from $\sim$12.6 ma^{-1} in the AIS_{pres} run, to $\sim$11.9 ma^{-1} in the AIS_{cool} run and $\sim$8.2 ma^{-1} in the AIS_{cold} run.

In Table 6.1 several different measures of the change in the basal component of ice shelf mass balance are presented. The melting rates in the first three columns are the area averaged rates, over regions where freezing or melting occur, and for the total ice shelf area. The next column contains the percentage of the ice shelf base where melting is occurring. The fifth and sixth columns contain the mass accretion from freezing, and the loss from melting, in areas where either freezing or melting is occurring, respectively. The last column is the net mass loss from the ice shelf from combined basal melting and freezing.

The trend shown in Table 6.1 is for a decrease in melting for all the measures shown. This is as expected given the reduction of melting shown in Figures 6.7 and 6.8. It is also consistent with the cooling of the water column, which makes less heat available for melting at the ice shelf-ocean interface.

6.4 Responses to a warmer ocean

The various climate change studies discussed in Section 6.1 suggest ocean warming of up to $\sim$3°C could occur in the vicinity of the Amery Ice Shelf. A temperature change of this magnitude is unlikely to occur without salinity also changing in the region of the ice shelf front. At present formation of sea ice maintains the cold water in Prydz Bay. In the climate change scenarios, which were discussed earlier, the reduction of sea ice formation allows the warmer and more saline Circumpolar Deep Water to encroach upon the continental shelf in Prydz Bay. However, any initial change in salinity is likely to be very small, and climate change experiments with temperature changes of up to 1.0°C may be done without considering changes in salinity. Five experiments are run with temperature increases of +0.1°C, +0.2°C, +0.3°C, +0.5°C and +1.0°C. These runs are labelled: $AIS_{+0.1°C}$, $AIS_{+0.2°C}$, $AIS_{+0.3°C}$, $AIS_{+0.5°C}$ and $AIS_{+1.0°C}$.

For temperature increases larger than 1.0°C in the restoring temperatures on the model boundary, the inflowing salinity is restored to a single salinity on the open boundary. This modifies the salinity, so it is similar to that expected from the encroachment of Circumpolar Deep Water onto the continental shelf. The new salinity is kept constant for the model runs with temperature changes greater than 1.0°C. This eliminates the effects of salinity change in comparisons between model runs. Two temperature increases are considered: +2.0°C ($AIS_{CS+2.0°C}$) and +3.0°C ($AIS_{CS+3.0°C}$). The change in salinity is also required for model stability in the higher temperature warming runs.

Additional runs with the same constant salinity are also presented. These allow the effects of changing the salinity independent of the temperature to be determined, and hence will allow the assessment of the warming trends at the higher levels of temperature change. For these purposes the temperature increase runs of +0.5°C and +1.0°C were repeated with the increased salinities. These were labelled $AIS_{CS+0.5°C}$ and $AIS_{CS+1.0°C}$, respectively.

The warming scenarios were applied, by changing the salinity and temperature fields prescribed along the front of the ice shelf. The model runs were then spun up from the common initial state described in Section 4.4.

6.4.1 Temperature increases up to 1.0°C

Ocean circulation

The vertically integrated streamfunctions for the initial series of warming runs are shown in Figures 6.9 to 6.13. The streamfunction strengthens with the increasing temperature changes. In addition to the increase in the strength of the circulation, there are some changes in the circulation pattern.

In the $AIS_{+0.1°C}$ (Figure 6.9) and $AIS_{+0.2°C}$ (Figure 6.10) runs, the biggest change from the present circulation is the breakdown and reversal of the Northern Gyre. In the AIS_{pres} run (Figure 5.9) the Northern Gyre is an anticlockwise rotating gyre, which strongly interacts with the inflow and outflow across the Northern Boundary. In the $AIS_{+0.1°C}$ run this has disappeared and the cross-boundary flow is now being driven by two smaller gyres, which in the AIS_{pres} run are part of the Northern Gyre. The circulation which develops in the absence of the Northern Gyre is more obvious in the $AIS_{+0.2°C}$ run (Figure 6.10). In the $AIS_{+0.2°C}$ run a clockwise rotating gyre can be clearly seen. It is centred in approximately the same position as the Northern Gyre in the AIS_{pres} run.

In the $AIS_{+0.3°C}$ run (Figure 6.11) the Northern Gyre is more like the circulation in the AIS_{pres} run, than in either the $AIS_{+0.1°C}$ or $AIS_{+0.2°C}$ runs. However, there are some changes from the circulation in the AIS_{pres} run. In particular, in the area between the centre of the Northern Gyre and the ice front (69.0°S 71.5°E), where a weak clockwise gyre has developed which is connected with the cross-boundary flow. This gyre replaces the extensions of the Northern Gyre, which in the AIS_{pres} run connects with the cross-boundary flow.

Further warming of the boundary tends to make the circulation in the area of the Northern Gyre similar to that seen in the AIS_{pres} run. This is particularly true for the $AIS_{+1.0°C}$ run (Figure 6.13) where the circulation north of the Central Grounded Zone follows the same pattern as the AIS_{pres} run, but with a more vigorous circulation.

In all the increased temperature model runs the western boundary current increases in strength at a greater rate than the Central Gyre. In the AIS_{pres} run the western boundary current has a strength of ~0.25 Sv, and in the $AIS_{+1.0°C}$ run it has a strength of ~0.80 Sv. Between the same runs the Central Gyre transport increases from ~0.67 Sv to ~0.84 Sv and the Northern Gyre transport changes from ~-0.47 Sv to ~-0.74 Sv.

The Northeastern Gyre also strengthens with the increased temperatures

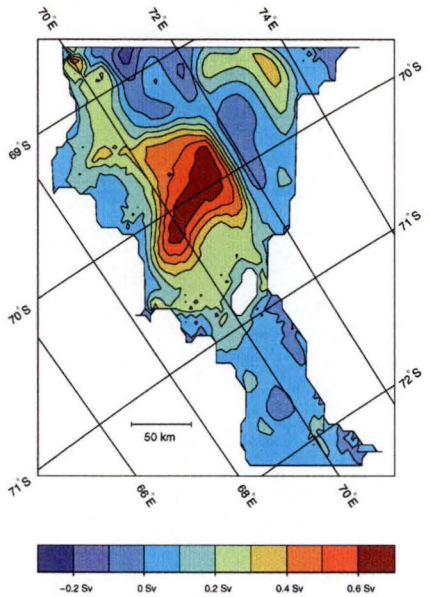

Figure 6.9: Vertically integrated streamfunction for the $AIS_{+0.1°C}$. Circulation is clockwise around positive features.

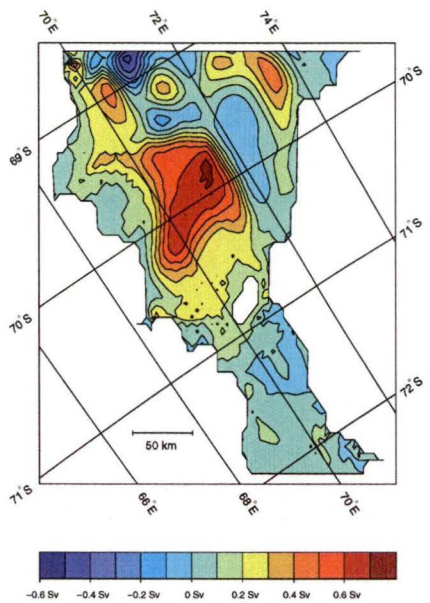

Figure 6.10: Vertically integrated streamfunction for the $AIS_{+0.2°C}$. Circulation is clockwise around positive features.

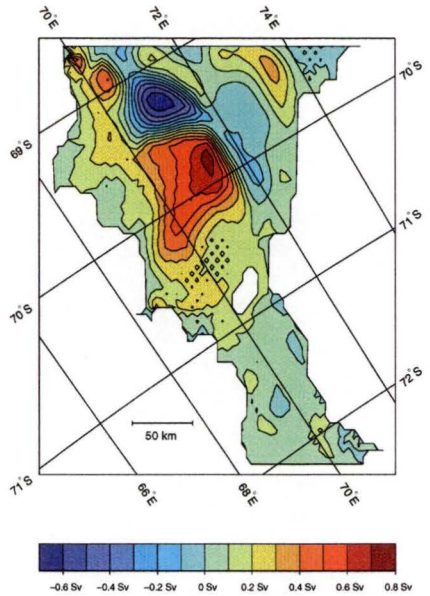

Figure 6.11: Vertically integrated streamfunction for the $AIS_{+0.3°C}$. Circulation is clockwise around positive features.

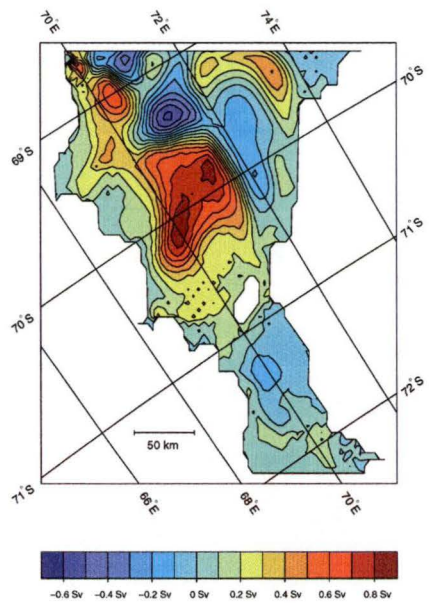

Figure 6.12: Vertically integrated streamfunction for the $AIS_{+0.5°C}$. Circulation is clockwise around positive features.

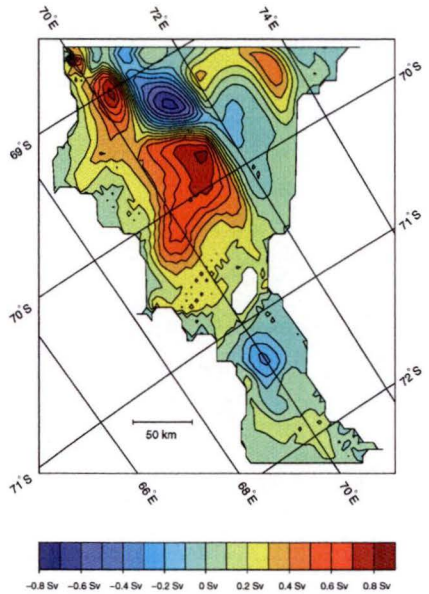

Figure 6.13: Vertically integrated streamfunction for the $AIS_{+1.0°C}$. Circulation is clockwise around positive features.

along the open ocean boundary. In the AIS_{pres} run it has a transport of ~0.26 Sv. This increases to ~0.49 Sv in the $AIS_{+1.0°C}$ run.

South of the Central Grounded Zone the changes in the horizontal circulation are much smaller in the different warming runs. The largest change is the shift in the position of the Southern Gyre. In the warmer runs it is situated further to the north than in the AIS_{pres} run. It also changes in strength as it moves north from ~-0.07 Sv to ~-0.32 Sv in the $AIS_{+1.0°C}$ run.

Increasing the temperature along the open boundary affects the water column structure and hence the vertical circulation within the model domain. Figures 6.14 to 6.18, show the temperature structure for the warmer runs: $AIS_{+0.1°C}$, $AIS_{+0.2°C}$, $AIS_{+0.3°C}$, $AIS_{+0.5°C}$, and $AIS_{+1.0°C}$. The most obvious change is an increase in the temperature of the warmest waters within the ocean cavity. These are found on Section C. (The coldest temperatures do not change as they are fixed by the interaction at the ice shelf-ocean interface.) The increase in temperature at the boundary does not increase the ocean cavity temperature by a similar amount. In the AIS_{pres} run the maximum temperature at the bottom of the basin under the Central Gyre is ~-1.96°C, this contrasts with temperatures of ~-1.90°C for the $AIS_{+0.1°C}$ run (Figure 6.14c) and ~-1.63°C for the $AIS_{+1.0°C}$ run (Figure 6.18c). A similar magnitude temperature change can be seen at depth at the southern end of Sections A and B for all the temperature runs.

The biggest changes in the structure of the water column are linked with the changes in the horizontal circulation and the salt and heat fluxes at the ice shelf-ocean interface. This can be most clearly seen in Figure 6.15a, which shows the temperature on Section A. It runs through the reversed Northern Gyre in the $AIS_{+0.2°C}$ run. In this section the isotherms at the northern end have changed their structure to reflect the strength of the reversed Northern Gyre.

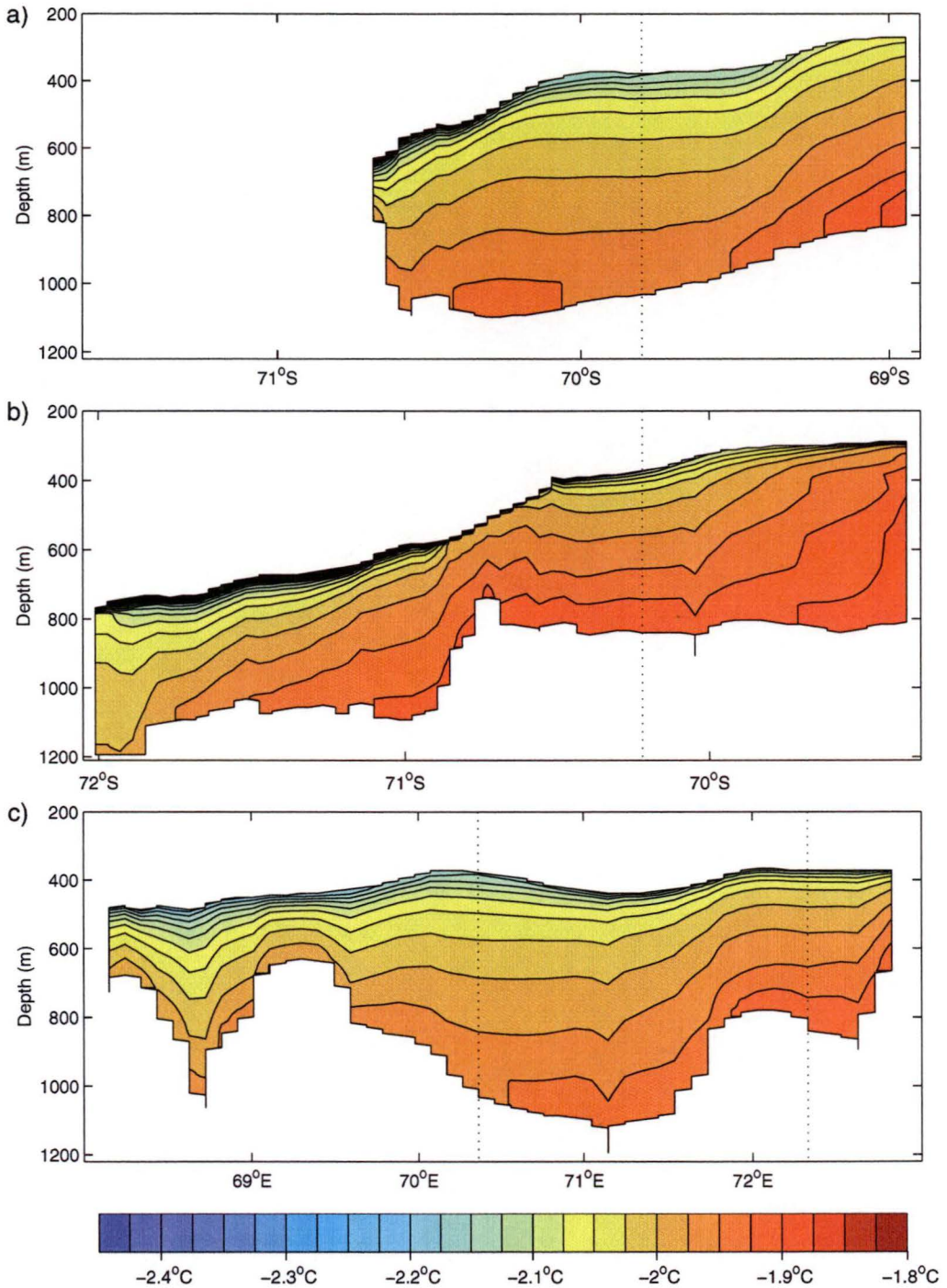

Figure 6.14: Three temperature sections through the water column, for the $AIS_{+0.1°C}$ run. a) Section A, b) Section B, and c) Section C. The location of the sections is shown in Figure 5.4. The dotted lines indicate where the cross-sections intersect.

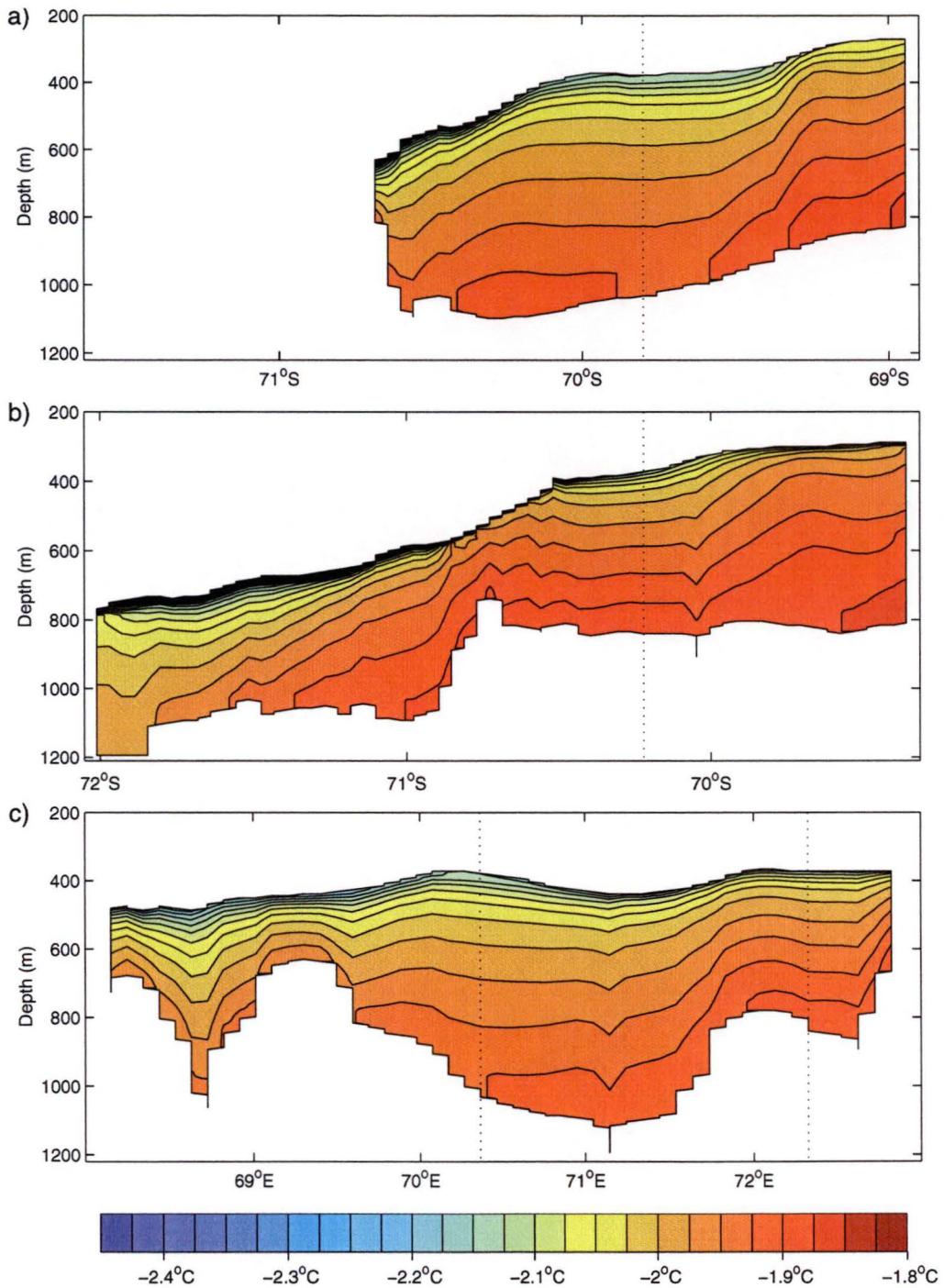

Figure 6.15: Three temperature sections through the water column, for the $AIS_{+0.2°C}$ run. a) Section A, b) Section B, and c) Section C. The location of the sections is shown in Figure 5.4. The dotted lines indicate where the cross-sections intersect.

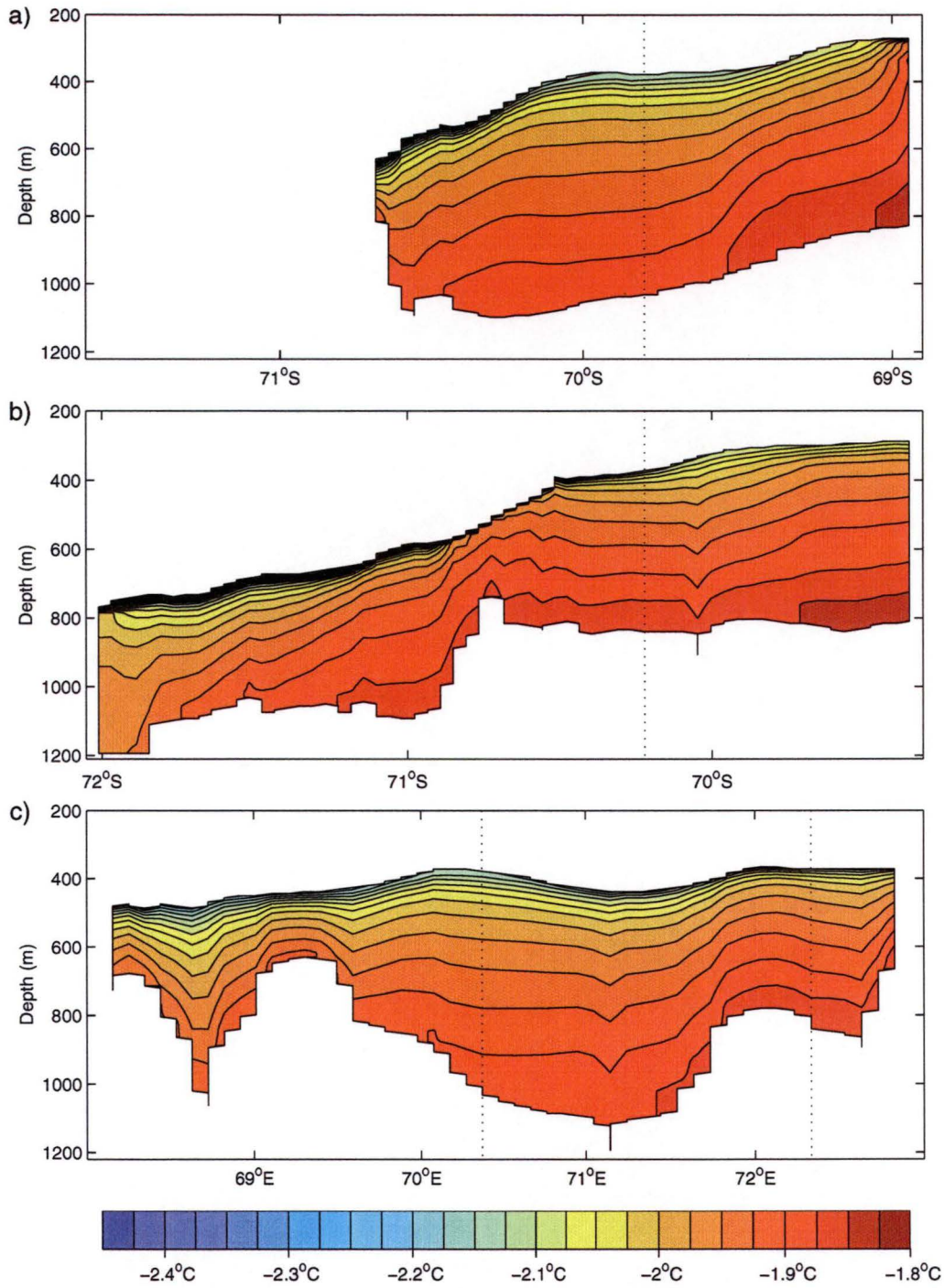

Figure 6.16: Three temperature sections through the water column, for the $AIS_{+0.3°C}$ run. a) Section A, b) Section B, and c) Section C. The location of the sections is shown in Figure 5.4. The dotted lines indicate where the cross-sections intersect.

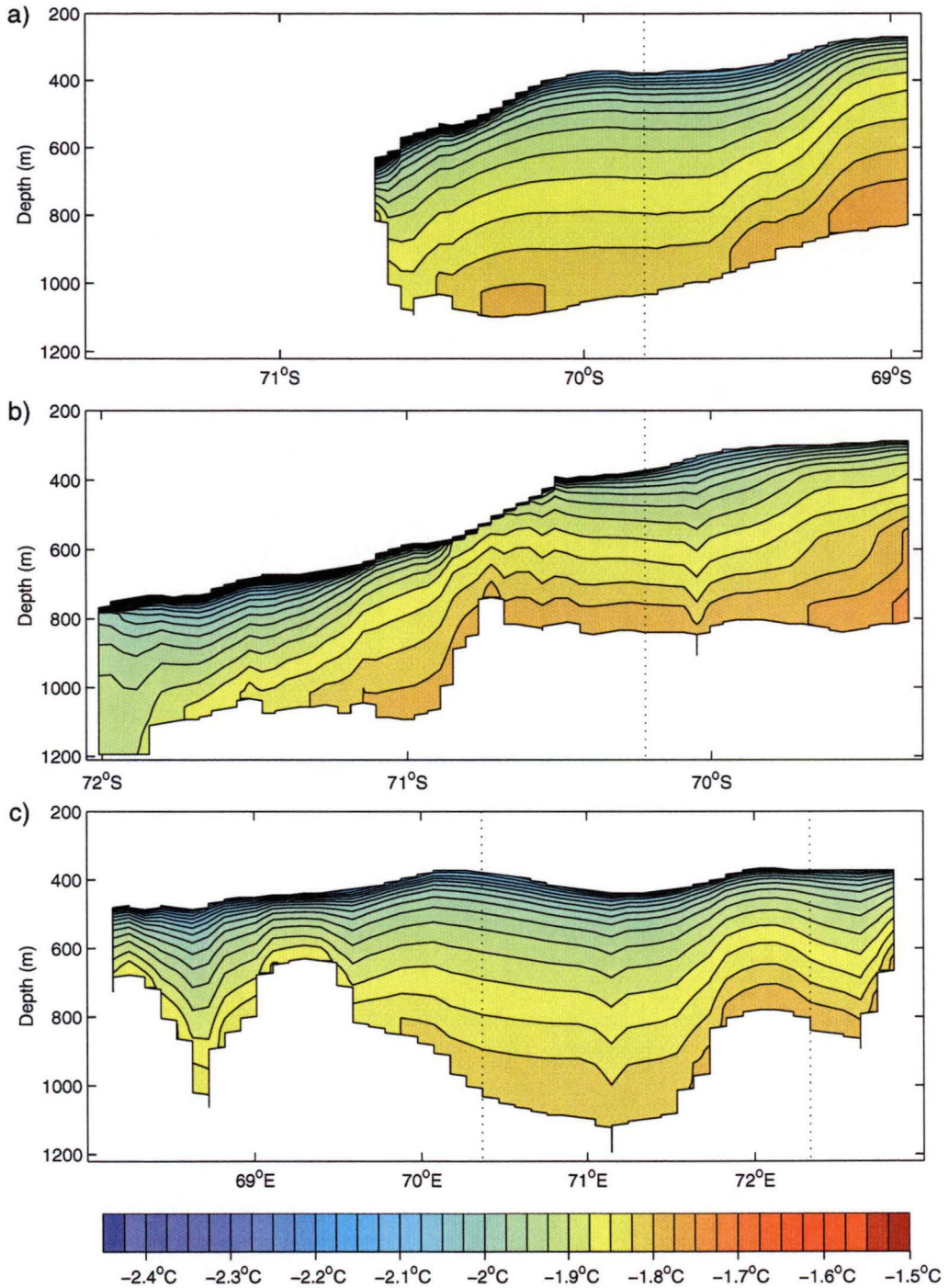

Figure 6.17: Three temperature sections through the water column, for the $AIS_{+0.5°C}$ run. a) Section A, b) Section B, and c) Section C. The location of the sections is shown in Figure 5.4. The dotted lines indicate where the cross-sections intersect.

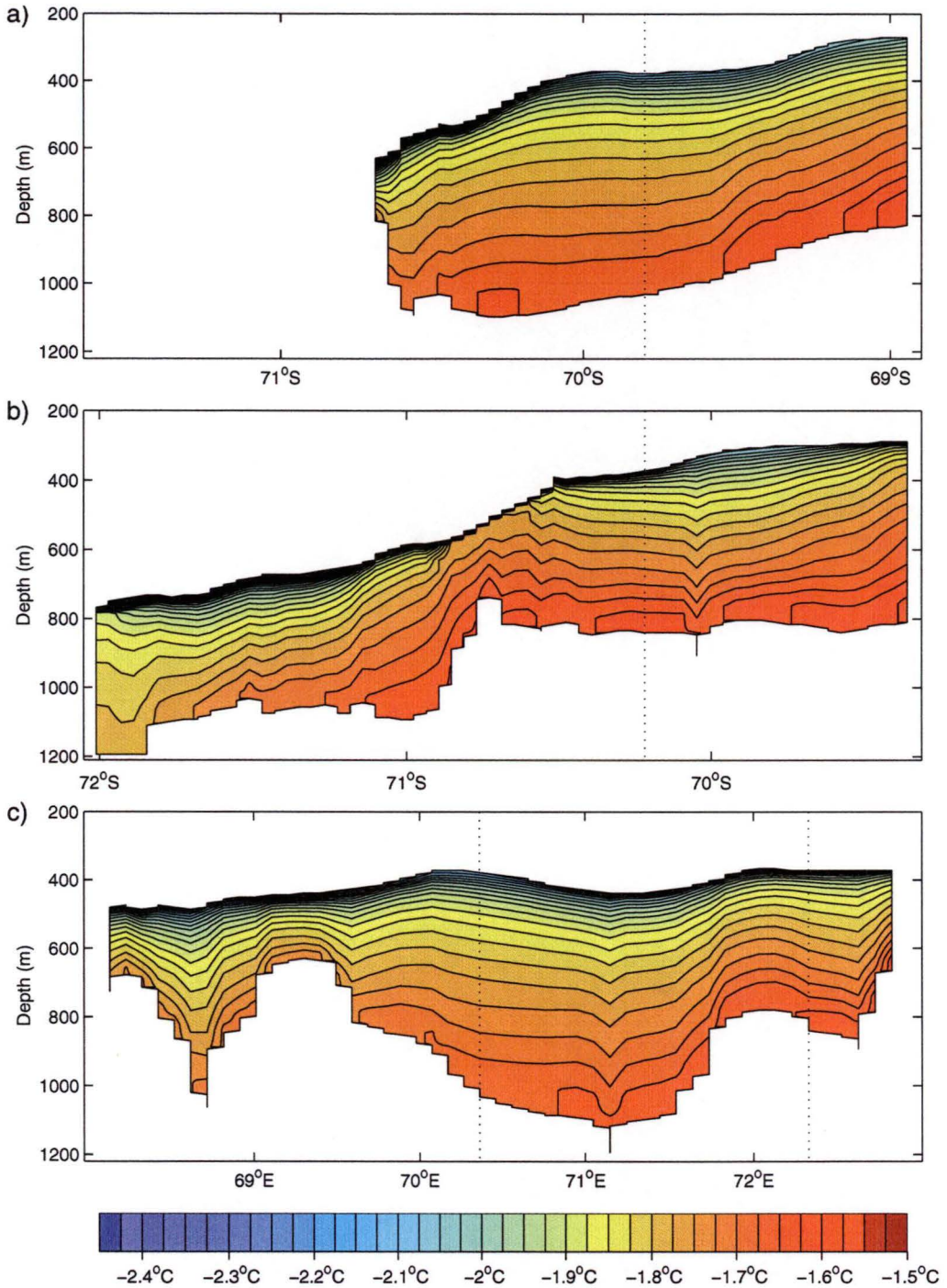

Figure 6.18: Three temperature sections through the water column, for the $AIS_{+1.0°C}$ run. a) Section A, b) Section B, and c) Section C. The location of the sections is shown in Figure 5.4. The dotted lines indicate where the cross-sections intersect.

This contrasts with the general trend which is for the thermocline to become more evenly stratified with warming. This effect is caused by the change from a freezing to melting environment in this part of the ocean cavity (see for example Figure 6.20). This change removes the vertical mixing which is driven by the salt rejection that accompanies freezing, and accordingly the previous homogeneity of the water column is reduced. Instead with melting the stratification of the water column is enhanced by adding fresh water to the top of the water column. The increased stratification of the water column can be seen in the Figures 6.14 to 6.18, with the stratification becoming more pronounced with increased ocean warming.

Ice shelf basal mass balance

The change in the temperature along the northern boundary of the model has a significant effect on the mass balance of the Amery Ice Shelf. This can be seen in Figures 6.19 to 6.23 which show the melting and freezing rates at the ice shelf-ocean interface in model runs $AIS_{+0.1°C}$, $AIS_{+0.2°C}$, $AIS_{+0.3°C}$, $AIS_{+0.5°C}$ and $AIS_{+1.0°C}$. In most of the domain the direction of change in the melting and freezing rates is the same in each warming scenario. The only exception to this is in the north of the domain, in the area around the Northern Gyre (69.3°S 71.2°E). In this area different behaviour from the other warming scenarios occurs in the $AIS_{+0.1°C}$ and $AIS_{+0.2°C}$ runs. This is because of differences in the horizontal circulation (Figures 6.19 and 6.20).

In the remainder of the domain the warming scenarios all show the same trend. In most of the domain we see an increase in the melting rates or a decrease in the freezing rates. Large rate changes can occur in areas where the melt rate is already strong. This occurs because of the additional heat which reaches these areas from the warmer water circulating in the domain. In turn, the amount of freezing increases in the small areas where it occurs, as these areas now have an increased supply of supercooled water. This has only a local effect as the increased velocities also increase mixing, so the freezing potential is rapidly lost.

The effect of these changes is shown in Table 6.2. The table shows several different measures of the change in the basal component of the Amery Ice Shelf mass balance under the different warming scenarios. The general trend is for an increase in melting with increases in temperature. What might be unexpected is that the increase in net mass lost from the ice shelf comes, not from a decrease in freezing, but from an increase in melting. The steadiness of the mass gain from freezing comes from a sharp increase in the rates of freezing where freezing occurs, but there is a general trend of decrease in the area of freezing.

The rise in the net melt from the ice shelf comes from substantial increases in the melt rates near the southern grounding line, east of the Central Grounded Zone, in the southwestern melting zone, and along the southeastern grounding line. There is also a change of freezing areas to melting areas. Most of the increase in melt occurs in the areas where melting was already occurring. The maximum rate of melting changes from $\sim$12.5 ma^{-1} in the AIS_{pres} run to $\sim$20.4 ma^{-1} in the $AIS_{+1.0°C}$ run.

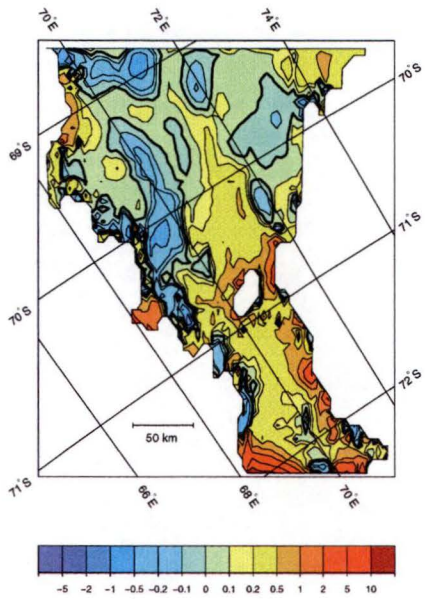

Figure 6.19: Rates of melting (+) and freezing (-) from the $AIS_{+0.1°C}$ run in ma^{-1}. The bold contour denotes the boundary between melting and freezing.

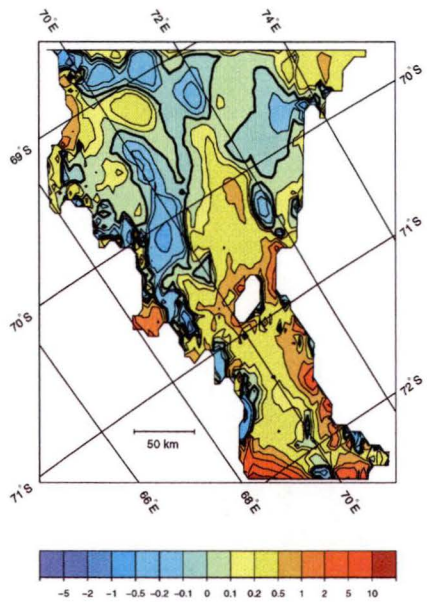

Figure 6.20: Rates of melting (+) and freezing (-) from the $AIS_{+0.2°C}$ run in ma^{-1}. The bold contour denotes the boundary between melting and freezing.

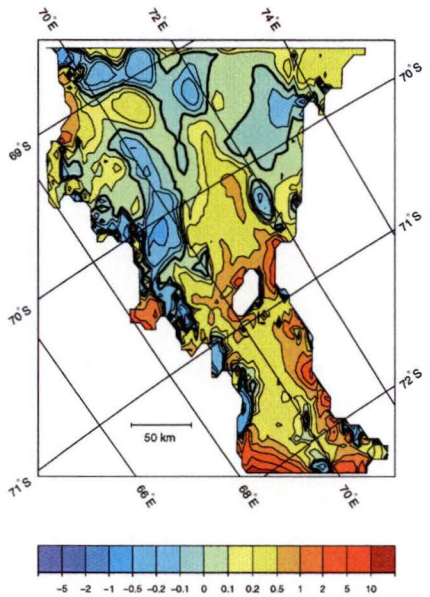

Figure 6.21: Rates of melting (+) and freezing (-) from the $AIS_{+0.3°C}$ run in ma^{-1}. The bold contour denotes the boundary between melting and freezing.

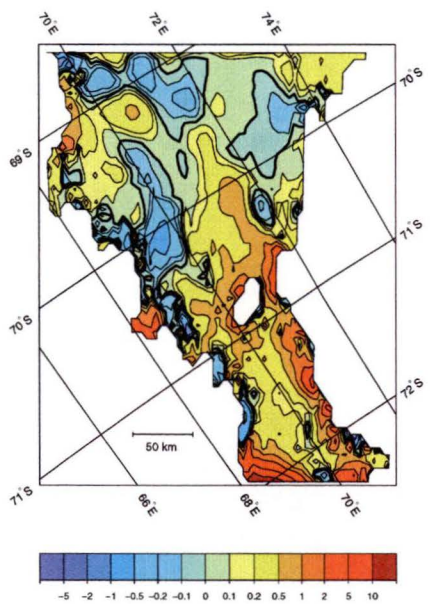

Figure 6.22: Rates of melting (+) and freezing (-) from the $AIS_{+0.5°C}$ run in ma^{-1}. The bold contour denotes the boundary between melting and freezing.

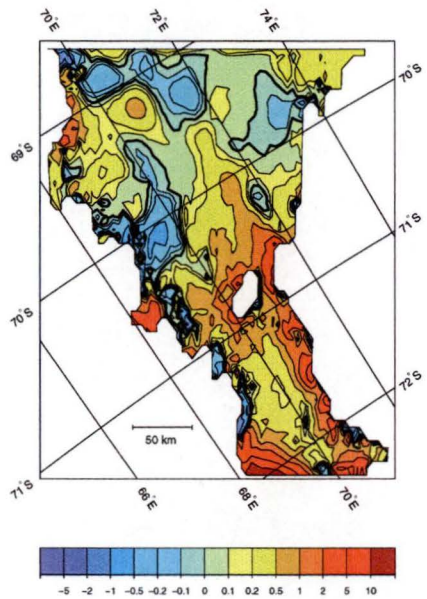

Figure 6.23: Rates of melting (+) and freezing (-) from the $AIS_{+1.0°C}$ run in ma^{-1}. The bold contour denotes the boundary between melting and freezing.

Table 6.2: Estimates of the basal component of mass balance at the base of the Amery Ice Shelf, under warmer ocean conditions.

Amery Model Run (AIS)	Mean Rates for Freezing Zone (ma^{-1})	Mean Rates for Melting Zone (ma^{-1})	Mean Rates for Whole (Loss) (ma^{-1})	Area of Melt (%)	Mass Change Rates Freezing (Gta^{-1})	Mass Change Rates Melting (Gta^{-1})	Mass Change Rates Net Loss (Gta^{-1})
pres	0.16	0.40	0.21	66.4	2.8	13.4	10.6
+0.1°C	0.18	0.46	0.27	70.4	2.8	16.6	13.8
+0.2°C	0.18	0.49	0.28	69.3	2.8	17.5	14.7
+0.3°C	0.18	0.54	0.33	70.8	2.7	19.4	16.7
+0.5°C	0.21	0.62	0.40	73.3	2.8	23.2	20.4
+1.0°C	0.24	0.79	0.54	76.6	2.9	30.7	27.8

Note: The total area of the ice shelf is 5.6 x 10^4 km^2.

The general trend in Table 6.2 of increasing melting with increased warming, has one small exception. The exception is the $AIS_{+0.2°C}$ run. Although the total mean melting rate and net melt rate follow the general trend, the area of the ice shelf where melting occurs decreases, against the trend. This decrease is coupled to the change in circulation in the area of the Northern Gyre (Figure 6.20). The circulation change is allowing outflowing supercooled water to ascend the ice shelf and drive freezing. In the other warming runs the flow is in the opposite direction, so warm inflowing water is driving melt instead. The freezing rate in the additional area where freezing is occurring is relatively low, so there is a negligible change in the rate of mass accretion from the other runs.

6.4.2 Temperature and salinity changes in the ocean climate

Increasing the ocean warming along the open boundary by uniform shifts in temperature restoring field above 1.0°C introduces instabilities in the temperature and salinity fields specified along the model boundary. The change in temperature leads to a change in the density structure, so it is no longer stable with the current salinity profile. At temperatures close to the surface freezing point the density gradient is largely determined by the salinity gradient. However, as temperatures increase by even a few degrees temperature becomes more important in determining density.

For temperature change runs with constant salinity, the salinity is fixed along the northern boundary. A salinity of 34.95 PSU is used. Although this salinity is well above the salinity of the CDW, this value is the minimum value for which all of the $AIS_{CS+0.5°C}$, $AIS_{CS+1.0°C}$, $AIS_{CS+2.0°C}$, and $AIS_{CS+3.0°C}$ model runs will spin up to a steady state. Having a single value across the different model runs is considered desirable here for sensitivity studies, so that any observed trend can be attributed solely to changes in temperature. In reality the response to climatic warming can be expected to involve transient changes which would involve an interactive coupling between the cavity model and the external domain. This is beyond the scope of the present study which addresses primarily the response to increasing ocean temperature.

Constant salinity +0.5°C and +1.0°C runs

The first two constant salinity runs, $AIS_{CS+0.5°C}$ and $AIS_{CS+1.0°C}$, repeat the $AIS_{+0.5°C}$ and $AIS_{+1.0°C}$ runs, but with the salinity field changed. This allows the effects of the salinity field on the circulation and the mass exchange at the ice shelf to be considered.

Changing the salinity along the boundary has a noticeable affect on the horizontal circulation. This can be seen by comparing the streamfunction for the $AIS_{CS+0.5°C}$ and $AIS_{CS+1.0°C}$ runs, which are shown in Figures 6.24 and 6.25, with the streamfunctions for the $AIS_{+0.5°C}$ and $AIS_{+1.0°C}$ runs (Figures 6.12 and 6.13). The effect on the $AIS_{CS+0.5°C}$ run is most noticeable in the area close to the open boundary. In the model the Northeastern Gyre has changed from a distinct clockwise gyre which is separated from the Central Gyre. It is instead

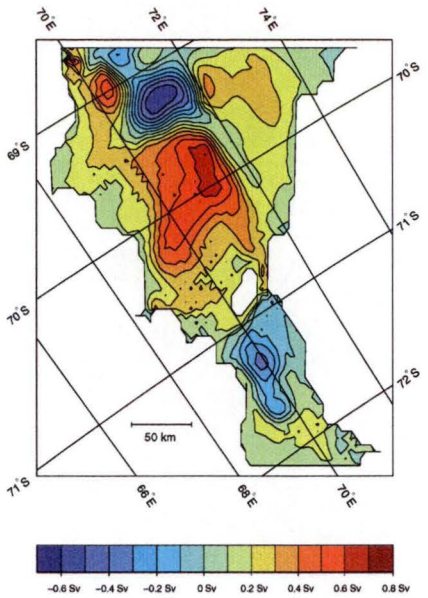

Figure 6.24: Vertically integrated streamfunction for the $AIS_{CS+0.5°C}$ run. Circulation is clockwise around positive features.

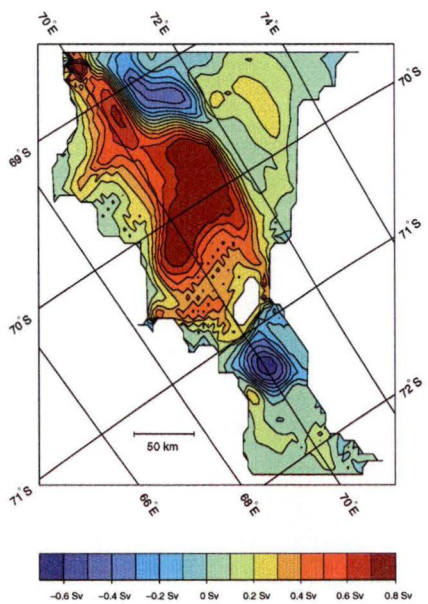

Figure 6.25: Vertically integrated streamfunction for the $AIS_{CS+1.0°C}$ run. Circulation is clockwise around positive features.

an area of low velocities with a generally weak clockwise circulation, which connects with the Main Gyre. The Northern Gyre also changes, but it still resembles the gyre in the $AIS_{+0.5°C}$ run. The Northern Gyre's interconnection with the boundary is slightly modified, with the small gyres in the north-west portion of the domain connecting directly to the Central Gyre. In the remainder of the domain the $AIS_{CS+0.5°C}$ run is similar to the $AIS_{+0.5°C}$ run, except for changes in the strengths of some of the gyres. The Central Gyre decreases in strength. Its maximum transport is ~0.70 Sv in the $AIS_{CS+0.5°C}$ run, compared with ~0.88 Sv in the $AIS_{+0.5°C}$ run. In contrast the Southern Gyre transport increases in strength from ~0.18 Sv to ~0.35 Sv.

In the $AIS_{CS+1.0°C}$ run the changes close to the ice front are similar to the changes between the two +0.5°C runs. In the remainder of the domain the change in the salinity field at the boundary is more noticeable between the two +1.0°C runs than it was between the two +0.5°C runs. The change is perhaps most noticeable south of the Central Grounded Zone. Here the Southern Gyre has increased significantly in strength and size, from a transport of ~-0.33 Sv in the $AIS_{+1.0°C}$ run to ~-0.70 Sv in the $AIS_{CS+1.0°C}$ run. Previously, the velocities along the eastern and western boundaries in the area of the southern gyre were relatively weak, these have been replaced by strong along boundary velocities.

The temperature structure in the ocean cavity is affected by the changes in the salinity along the model boundary. The temperature cross-sections for the $AIS_{CS+0.5°C}$ run are shown in Figure 6.26. The changes are relatively small compared with the $AIS_{+0.5°C}$ run (Figure 6.17) and like the changes in the streamfunction, they are generally restricted to near the ice front. In Section A (Figure 6.26a) the bottom water is slightly warmer. This is the only noticeably different feature from the $AIS_{+0.5°C}$ run (Figure 6.17a). The differences in Section B (Figure 6.26b), between the two +0.5°C runs are a slight cooling in the warmest waters in the section, and a levelling out of the thermocline near the ice front. This levelling out is consistent with the small gradients in the streamfunction in this area, which indicate low velocities associated with the density gradient. In Section C (Figure 6.26c) the temperature structure has changed slightly between the two +0.5°C model runs. The $AIS_{CS+0.5°C}$ run has both slightly warmer and slightly colder water in the section, compared with the same section for the $AIS_{+0.5°C}$ run (Figure 6.17c). The warmest water is constrained to the eastern side of the section and does not fill the bottom of the Central Gyre basin.

The difference between the temperature sections for the two +1.0°C model runs is significant. All three of the temperature sections shown in Figure 6.27 for the $AIS_{CS+1.0°C}$ run have warmer waters than in the $AIS_{+1.0°C}$ run, with the largest change an increase of ~0.1°C. Apart from the increase in the water temperatures, there is little difference in the temperature structure of Section A (Figure 6.27a) between the $AIS_{CS+1.0°C}$ run and the $AIS_{+1.0°C}$ run.

Section B (Figure 6.27b) has more significant changes, particularly in the middle of the section. In the $AIS_{+1.0°C}$ run the water near the ice shelf is ~-1.75°C. In the $AIS_{CS+1.0°C}$ run it is ~-1.65°C. The warmer water from deep in the cavity is being drawn to the surface. This is related to the increased melting

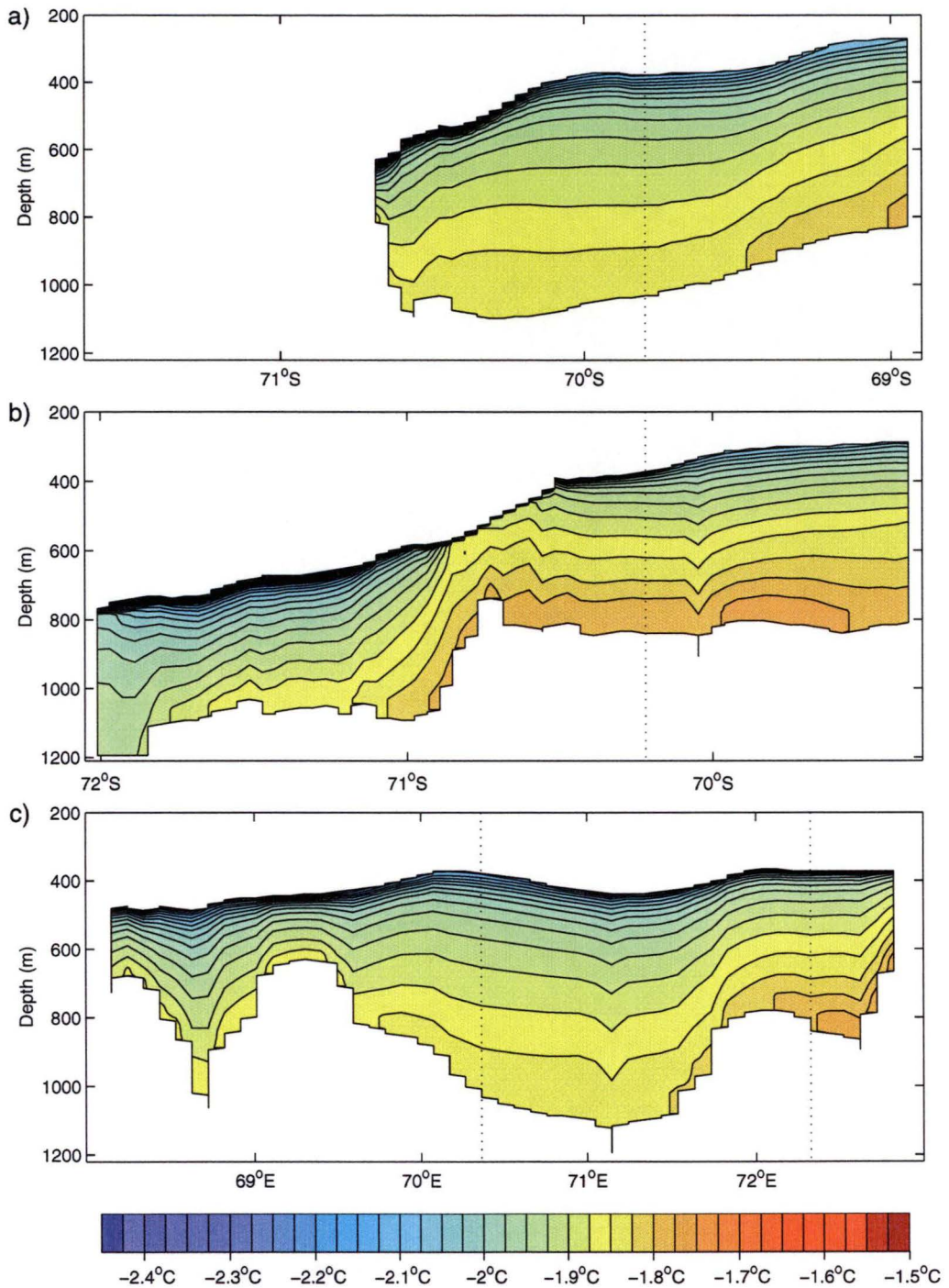

Figure 6.26: Three temperature sections through the water column, for the $AIS_{CS+0.5°C}$ run. a) Section A, b) Section B, and c) Section C. The location of the sections is shown in Figure 5.4. The dotted lines indicate where the cross-sections intersect.

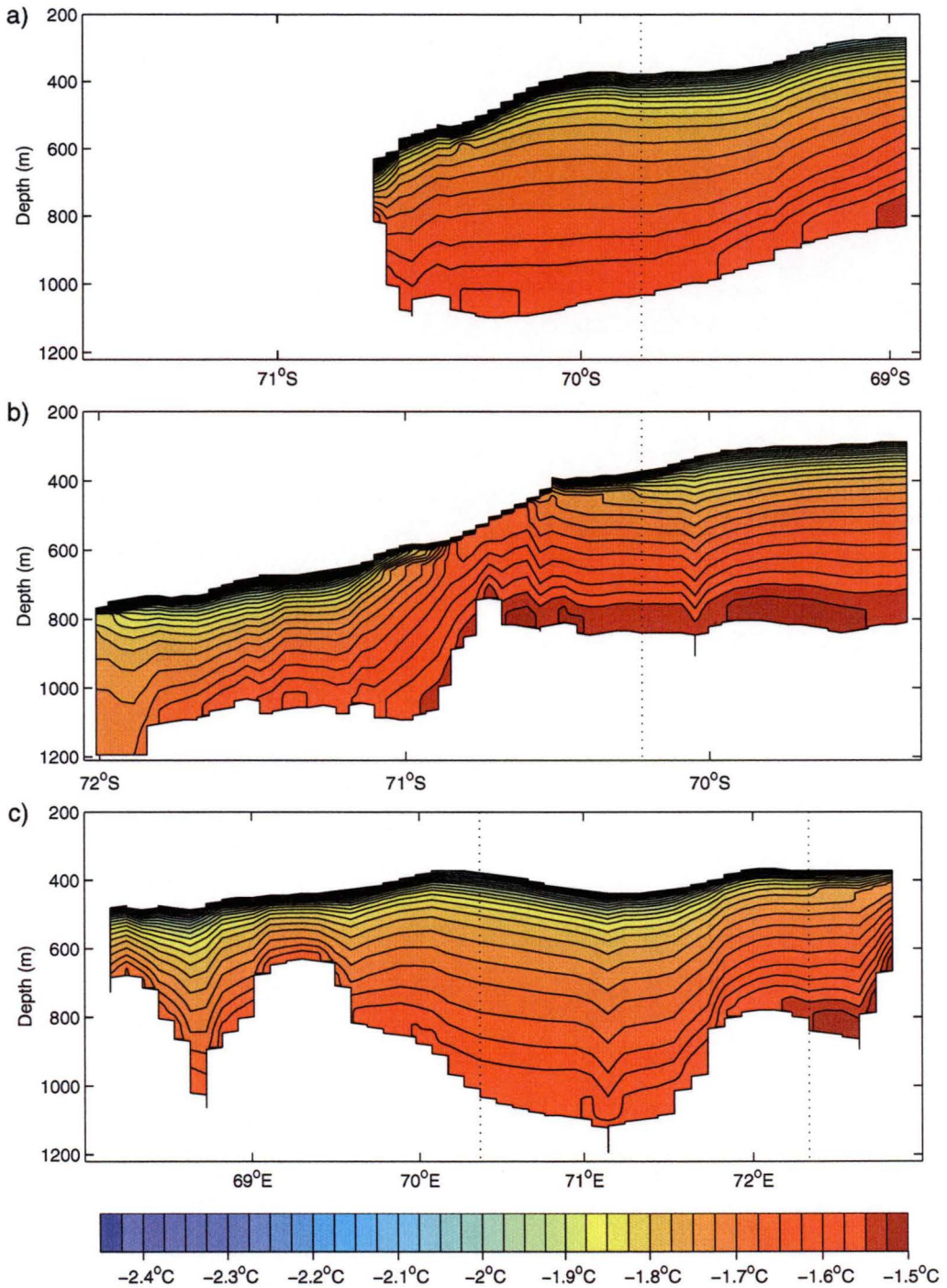

Figure 6.27: Three temperature sections through the water column, for the $AIS_{CS+1.0°C}$ run. a) Section A, b) Section B, and c) Section C. The location of the sections is shown in Figure 5.4. The dotted lines indicate where the cross-sections intersect.

in this area (Figure 6.29) in comparison to the $AIS_{+1.0°C}$ run. The additional melting increases the vertical velocities adjacent to the ice shelf in this area and changes the temperature gradient. The changes in Section C (Figure 6.27c) between the two +1.0°C runs are similar to those between the two +0.5°C runs. The most noticeable change is that the warmest water is confined to the eastern side of the cavity.

The melting and freezing rates for the two +0.5°C runs are similar. The small differences are caused by changes in the circulation as discussed above. These changes do not impact significantly on the overall mass exchange with the ice shelf. The melting and freezing rates for the $AIS_{CS+0.5°C}$ run are shown in Figure 6.28.

In contrast to the two +0.5°C runs, the +1.0°C runs differ significantly in the rates of melting and freezing at the ice shelf-ocean interface. This difference can be seen by comparing Figures 6.23 and 6.29, which show the melting and freezing rates for the $AIS_{+1.0°C}$ and $AIS_{CS+1.0°C}$ runs, respectively. The main change in the pattern of melting and freezing is a reduction in the area of freezing in the north-east part of the domain. There is also an increase in the area where melt rates are high, particularly around the Central Grounding Zone.

The difference in the melting and freezing rates also impacts on the estimates of the basal component of the ice shelf mass balance. In the $AIS_{CS+1.0°C}$ run the amount of ice lost from the ice shelf has increased by 10 Gta^{-1}, compared with the mass lost in the $AIS_{+1.0°C}$ run (see Tables 6.2 and 6.3). This increase in mass loss of approximately ~37%, comes from increases in both the area where melting is occurring and the mean rate of melting. In contrast the agreement for the melting and freezing rates between the $AIS_{CS+0.5°C}$ and $AIS_{+0.5°C}$ runs is within 2%.

+2.0°C and +3.0°C warming runs

The results of the two +0.5°C runs are largely similar, suggesting the effect of the salinity change can be safely ignored for smaller levels of temperature change. Accordingly, the $AIS_{CS+2.0°C}$ and $AIS_{CS+3.0°C}$ runs are compared with the AIS_{pres} run rather than with an intermediate warming scenario.

The streamfunction for the $AIS_{CS+2.0°C}$ run is presented in Figure 6.30. The circulation is similar in structure to the AIS_{pres} run except to the south of the Central Grounded Zone. Here the Southern Gyre is situated further north and closer to the Central Grounded Zone. Along with this shift in position the Southern Gyre also increases in strength from ~-0.07 Sv to ~-0.62 Sv. This is particularly important as it will impact on the heat exchange into and out of the southern part of the domain. The circulation in the remainder of the domain is also stronger.

The three temperature cross-sections for the $AIS_{CS+2.0°C}$ run, shown in Figure 6.31, have similar structures in most of the domain to the AIS_{pres} run, if the expanded temperature range in the $AIS_{CS+2.0°C}$ run is considered. The expanded temperature range is driving the increased circulation.

The main differences in the temperature are in Sections A (Figure 6.31a) and

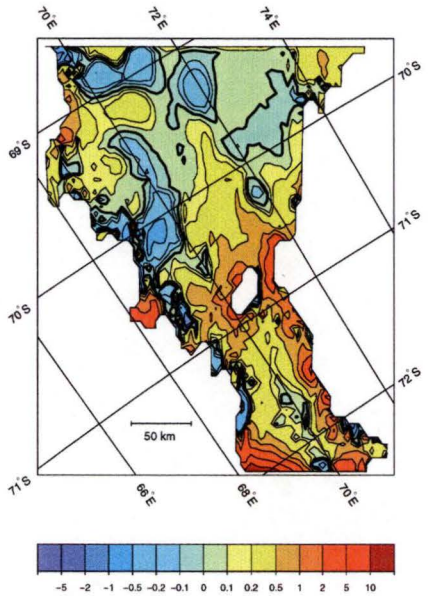

Figure 6.28: Rates of melting (+) and freezing (-) from the $AIS_{CS+0.5°C}$ run in ma^{-1}. The bold contour denotes the boundary between melting and freezing.

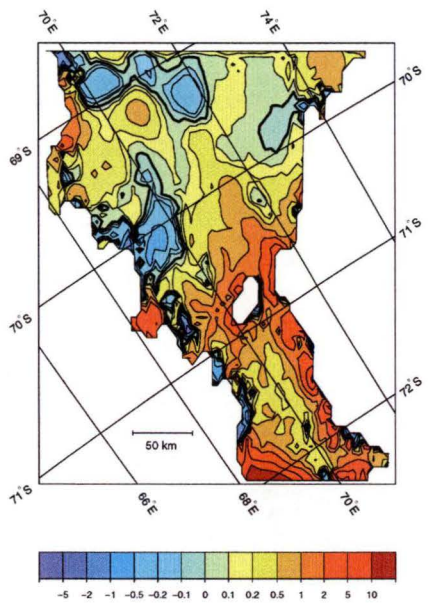

Figure 6.29: Rates of melting (+) and freezing (-) from the $AIS_{CS+1.0°C}$ run in ma^{-1}. The bold contour denotes the boundary between melting and freezing.

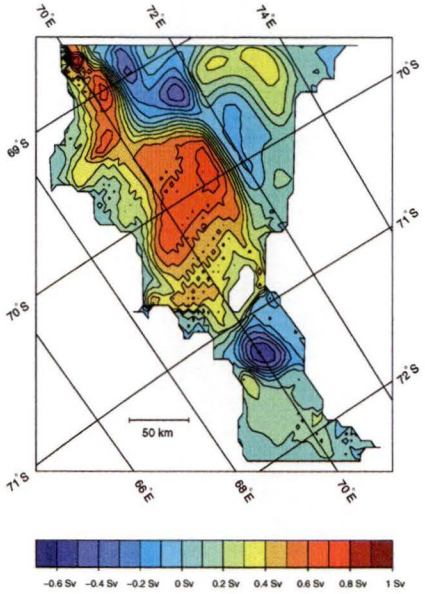

Figure 6.30: Streamfunction for the $AIS_{CS+2.0°C}$ run. Circulation is clockwise around positive features.

B (Figure 6.31b) close to the ice front. Here the isotherm gradient is smoother. This is caused by the change from freezing to melting close to the ice front in these sections. In the AIS_{pres} run the freezing leads to some vertical mixing near the ice front. The change from freezing to melting extends and thickens the melt-water layer adjacent to the ice shelf over the whole section.

Also visible in Section B are two lenses in the melt-water layer, these are centred about 69.7°S and 71.5°S. The lenses have both formed in gyres, the northern lens in the Northeastern Gyre, and the southern lens in the Southern Gyre.

With further warming the circulation again changes. In the $AIS_{CS+3.0°C}$ run the streamfunction, shown in Figure 6.32, has distinct differences from earlier circulation patterns. The Central Gyre and the gyres close to the open ocean boundary change. In the north-east the shape of the Northeastern Gyre changes as it expands and connects more with the Central Gyre. The expansion does not affect the strength of the gyre — it is similar to that seen in the AIS_{pres} run. Also in the north-east corner of the domain a small anticyclonic gyre has formed with ~0.3 Sv of transport. This gyre has developed from a current formed by the steep ice shelf draft gradient along the ice front in this area. Another small gyre (69.9°S 71.5°E) has also formed in the vicinity of the Northern Gyre.

Perhaps the most important change is in the Central Gyre, it is no longer constrained on the western side by the large basin in the centre of the domain (Figure 4.5). It is instead constrained by the grounding line on the western side of the model domain. Similarly, the Central Gyre has expanded to the east and south. The southern part of the Central Gyre now drives strong flow around the Central Grounded Zone. It is in contact with the grounding line on the eastern side, just to the north of the Central Grounded Zone. This leads to a weakening of the velocities in the middle of the Central Gyre.

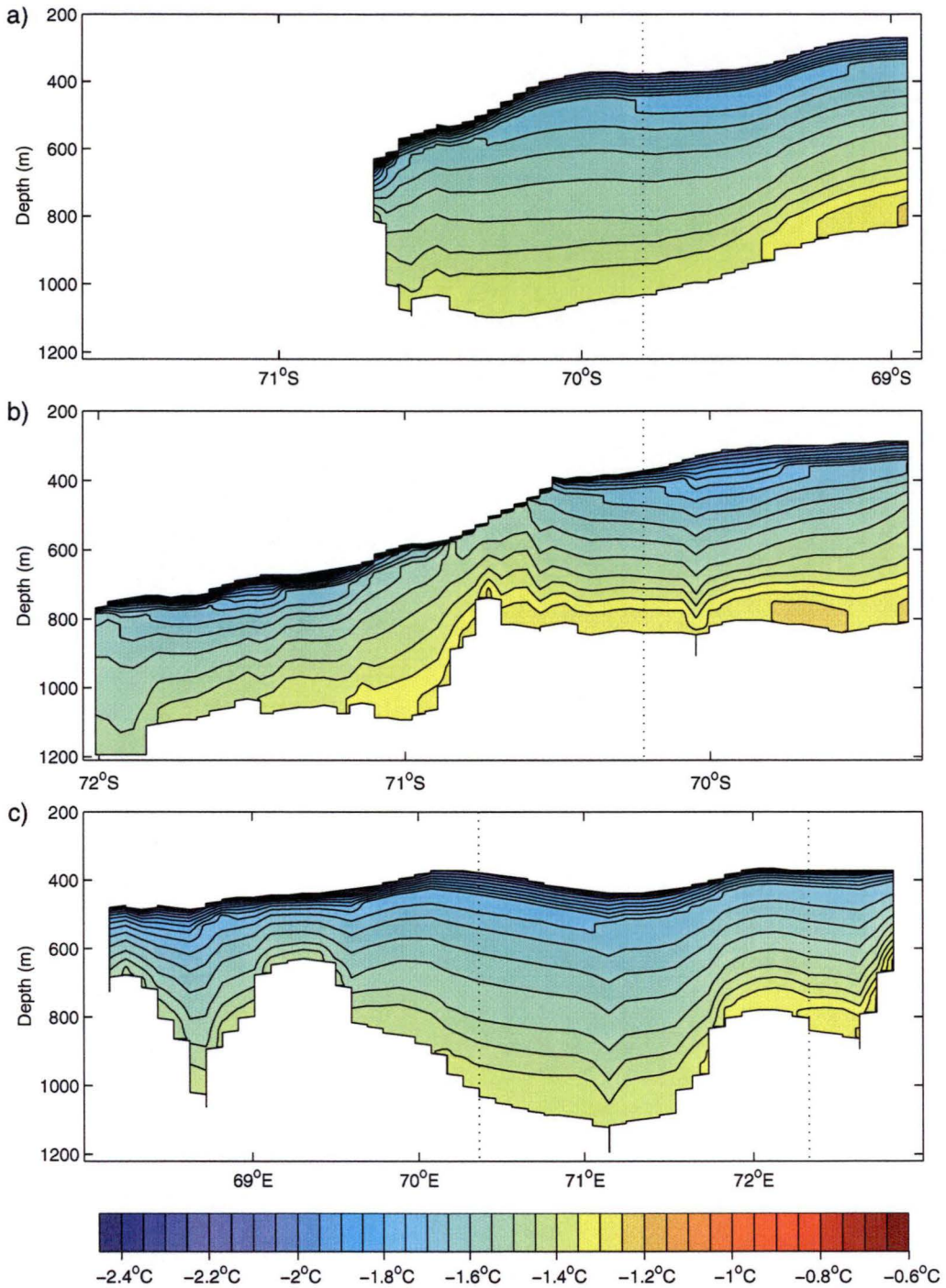

Figure 6.31: Three temperature sections through the water column, for the $AIS_{CS+2.0°C}$ run. a) Section A, b) Section B, and c) Section C. The location of the cross-sections is shown in Figure 5.4. The dotted lines indicate where the cross-sections intersect.

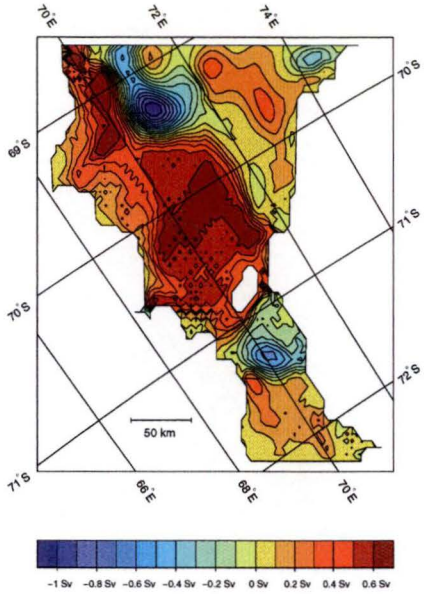

Figure 6.32: Streamfunction for the $AIS_{CS+3.0°C}$ run. Circulation is clockwise around positive features.

The change in the circulation in the northeastern part of the domain affects the temperature structure in the domain. The three temperature cross-sections are shown in Figure 6.33. In the west of the domain, there is little change along Section A (Figure 6.33a) except for the expected broadening of the temperature range from the available additional heat. In the north-east portion of the domain, particularly in the north of Section B (Figure 6.33b) and the eastern side of Section C (Figure 6.33c) there are slight changes. In Section B the warmest water in the section is no longer present at the ice front, nor does it reach into the south of the domain through the channel to the east of the Central Grounded Zone. This change in the temperature structure has been caused by the change in the horizontal circulation. The strengthening of the Central Gyre driven circulation around the Central Grounded Zone is isolating the channel from the warmer waters in the Northeastern Gyre.

The increased warming of the ocean leads to increasing areas of melting and the restriction of freezing to a few locations. This can be seen in the melting and freezing rates for the $AIS_{CS+2.0°C}$ and $AIS_{CS+3.0°C}$ runs, which are shown in Figures 6.34 and 6.35, respectively. These figures show the continued decline in the areas where freezing occurs and the continued increase in areas where melt rates are very high.

The mass balance statistics associated with all the constant salinity runs are presented in Table 6.3.

In Table 6.3 the continuing increase in mass loss from the ice shelf with continued warming can be clearly seen. This increase, as in the earlier warming scenarios, comes from slight increases in the area where melting is occurring, but mainly from increases in the mean rate of melting. The peak rates of melting also increase significantly. In the $AIS_{CS+2.0°C}$ run the peak melt rate is 30.0 ma^{-1} and in the $AIS_{CS+3.0°C}$ run it is 37.3 ma^{-1}.

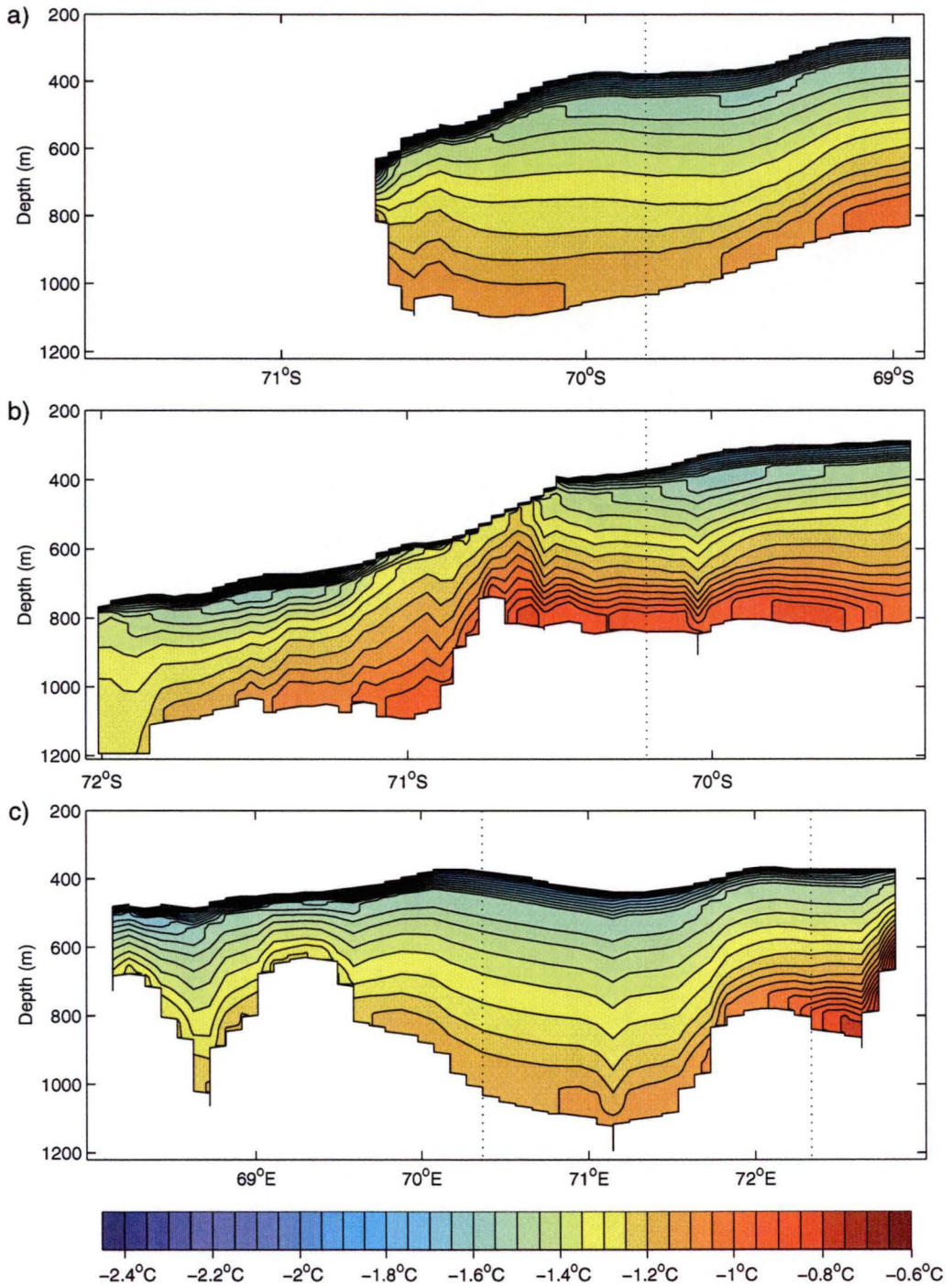

Figure 6.33: Three temperature sections through the water column, for the $AIS_{CS+3.0°C}$ run. a) Section A, b) Section B, and c) Section C. The location of the cross-sections is shown in Figure 5.4. The dotted lines indicate where the cross-sections intersect.

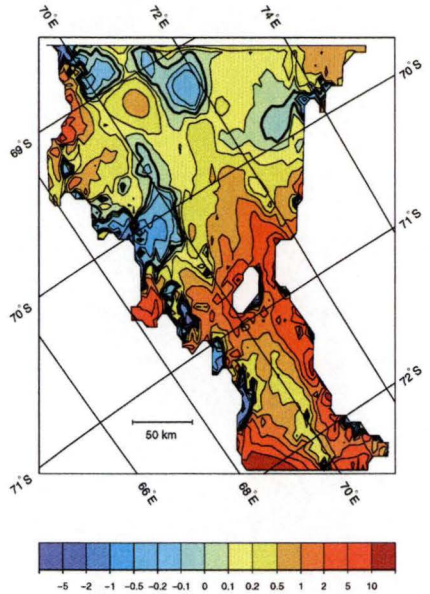

Figure 6.34: Rates of melting (+) and freezing (-) from the $\text{AIS}_{\text{CS+2.0°C}}$ run in ma^{-1}. The bold contour denotes the boundary between melting and freezing.

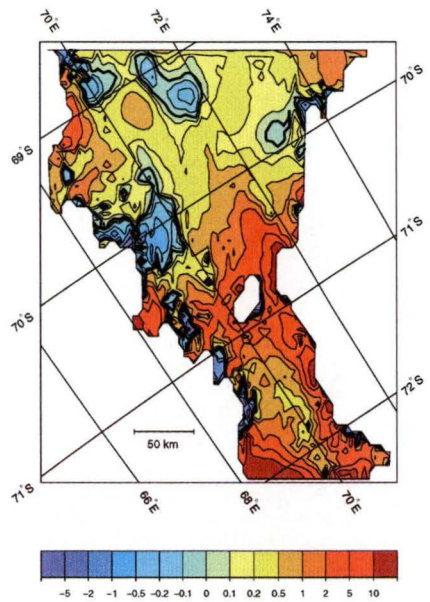

Figure 6.35: Rates of melting (+) and freezing (-) from the $\text{AIS}_{\text{CS+3.0°C}}$ run in ma^{-1}. The bold contour denotes the boundary between melting and freezing.

Table 6.3: Estimates of the mass balance rates at the base of the Amery Ice Shelf, under warmer ocean and constant salinity conditions.

Amery Model Run (AIS)	Mean Rates for Freezing Zone (ma^{-1})	Mean Rates for Melting Zone (ma^{-1})	Mean Rates for Whole (Loss) (ma^{-1})	Area of Melt (%)	Mass Change Rates Freezing (Gta^{-1})	Mass Change Rates Melting (Gta^{-1})	Mass Change Rates Net Loss (Gta^{-1})
pres	0.16	0.40	0.21	66.4	2.8	13.4	10.6
CS+0.5°C	0.21	0.62	0.41	74.2	2.8	23.5	20.7
CS+1.0°C	0.33	1.00	0.74	80.8	3.2	41.2	38.0
CS+2.0°C	0.42	1.35	1.05	83.0	3.7	57.3	53.6
CS+3.0°C	0.62	1.90	1.54	85.8	4.5	83.2	78.7

Note: The total area of the ice shelf is 5.6 x 10^4 km^2.

Also of interest in Table 6.3 is the increase in ice freezing onto the ice shelf. In the $AIS_{CS+3.0°C}$ run 4.42 Gta^{-1} of ice is accreted to the ice shelf. This is approximately the same amount as was accreted in the AIS_{cold} run (Table 6.1) and is about 1.5 times the amount of ice accreted in the AIS_{pres} run. This increase in accretion can also be clearly seen in Figure 6.36.

In Figure 6.36 the effect on the cumulative ice shelf mass balance for the AIS_{pres} and the four constant salinity model runs is shown. The main feature in this figure is the consistent increase in melting over the length of the ice shelf. There is no significant change in freezing for the $AIS_{CS+0.5°C}$ and $AIS_{CS+1.0°C}$ model runs over the AIS_{pres} run. There are several trends in the melting and net mass loss which appear in all of the model runs. The ice shelf generally loses about a quarter of the overall net loss near the grounding line. This increases to about half the mass loss in the region between the grounding line and 230 km from the ice front. The mass loss then increases at an approximately constant rate over the 230 km closest to the ice front

The location of the major melt zones can also be seen in the cumulative ice shelf mass balance. These are near the grounding line and between approximately 230 km and 240 km from the ice front.

6.5 Discussion and conclusions

In the first set of warming scenarios presented in this chapter, for oceanic temperature increases of up to 1°C, it was assumed the salinity along the ocean boundary was unchanged. For warmer scenarios and also for repetitions of the +0.5°C and +1.0°C warming scenarios, the salinity was changed. The salinity field along the open ocean boundary was set to a constant 34.95 PSU. This was required to ensure all the model runs using the constant salinity field were numerically stable. No water masses observed in the vicinity of Prydz Bay have a salinity this high [Wong et al., 1998]. However, setting the restoring salinity this high does not necessarily generate water masses this saline in the model

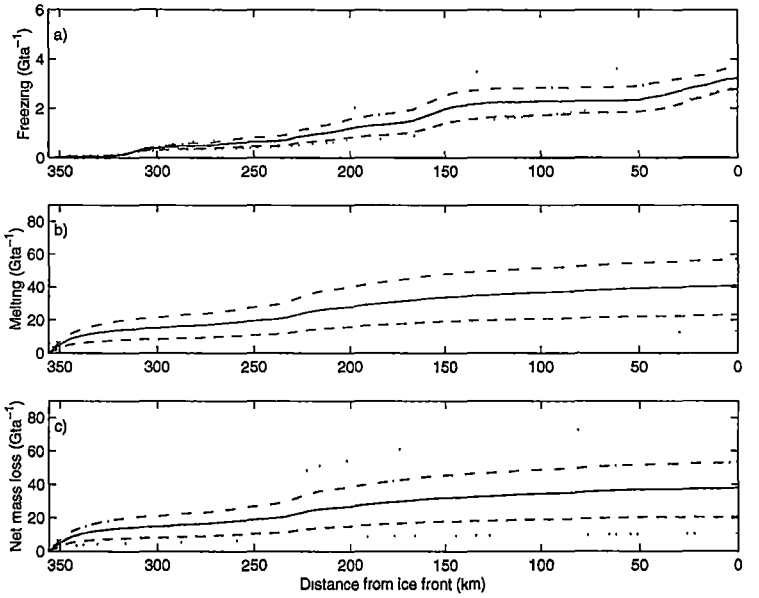

Figure 6.36: Cumulative a) freezing, b) melting, and c) net mass loss rates for the present and four different open boundary model runs. The lower dotted line represents the AIS_{pres} run, the dashed line the $AIS_{CS+0.5°C}$ run, the solid line the $AIS_{CS+1.0°C}$ run, the dash-dot line the $AIS_{CS+2.0°C}$ run, and the upper dotted line represents the $AIS_{CS+3.0°C}$ run.

interior.

In the $AIS_{CS+0.5°C}$ and $AIS_{CS+1.0°C}$ runs the salinities found in the model are saltier than in the comparable model run without the change in the salinity field. The range of the salinities in the $AIS_{CS+0.5°C}$ run is 34.40 PSU to 34.71 PSU; in the $AIS_{CS+1.0°C}$ run it is 34.25 PSU to 34.65 PSU. The salinity in both of these model runs places the water mass effectively flowing into the model domain as Modified Circumpolar Deep Water (MCDW) (Table 3.1). This is a water mass currently present on the continental shelf in Prydz Bay, but not observed close to the ice front [Wong et al., 1998]. An anticipated method for warmer waters to be found on the continental slopes around Antarctic is for Circumpolar Deep Water to encroach on to the shelf. A reasonable precursor of this would be an increase in the amount of MCDW on the continental shelf.

In the two warmest runs the salinity ranges simulated by the model in the cavity were in the range of observed water masses. In the $AIS_{CS+2.0°C}$ run the water in the domain had a maximum salinity of 34.60 PSU, and a maximum temperature of -1.25°C. The maximum salinity and temperature in the $AIS_{CS+3.0°C}$ run were respectively 34.40 PSU and -0.75°C. The broad classification of MCDW ($-1.5 < \theta < 1.0$, $34.2 < S < 34.67$) also includes these water masses, although they are warmer and fresher than in the $AIS_{CS+0.5°C}$ and $AIS_{CS+1.0°C}$ runs.

Generally the different climate change scenarios led to different circulations in the ocean cavity. The most consistent trend was in the expansion and strengthening of the Southern and Central Gyres. As the ocean temperatures were increased, the gyres tended to expand, with the areas of maximum

Table 6.4: Inflow and outflow mass transport components.

Run	AIS_{pres}	$AIS_{+0.1°C}$	$AIS_{+0.2°C}$	$AIS_{+0.3°C}$
Transport (Sv)	0.49	0.49	0.67	0.70
Run	$AIS_{+0.5°C}$	$AIS_{+1.0°C}$	$AIS_{CS+0.5°C}$	$AIS_{CS+1.0°C}$
Transport (Sv)	0.75	0.81	0.71	0.96
Run	$AIS_{CS+2.0°C}$	$AIS_{CS+3.0°C}$		
Transport (Sv)	1.10	1.40		

barotropic velocity moving away from the centre of each gyre. In the Southern Gyre this expansion was limited to the north by the Central Grounded Zone and to the east and west by the grounding line. The situation in the Central Gyre is slightly different, it does not expand evenly in all directions, but remains strongly confined in the north-east. It does not expand significantly to the east until it has already expanded to the south. The expansion to the south is limited by the Central Grounded Zone. The westward expansion of the Central Gyre leads to the formation of a strong western boundary current, as the Central Gyre becomes restricted by the grounding line on the western side of the ocean cavity.

The behaviour of the Northern and Northeastern Gyres varies between the different climate scenarios. The Northern Gyre changes from an anticyclonic gyre in the AIS_{pres} run to a cyclonic gyre in the $AIS_{+0.2°C}$ run. In the warmer scenarios the form of the Northern Gyre is similar to that seen in the AIS_{pres} run. The Northeastern Gyre appears more susceptible to the changes in salinity, rather than the changes in temperature. This is also supported by the form of flow which develops, that is, a gyre with weak barotropic velocities driven by gentle density gradients in the area of the gyre. These changes were seen in the $AIS_{CS+0.5°C}$ and $AIS_{CS+1.0°C}$ runs, but not in the $AIS_{+0.5°C}$ and $AIS_{+1.0°C}$ runs. This suggests the absence of salinity gradients, either horizontal or vertical in the forcing has some localised effects on the circulation near the ice front. The Northeastern Gyre also changes form in the $AIS_{CS+3.0°C}$ run, however, it is harder to determine if this is caused by the change in salinity or the increase in the temperature, as the circulation in the $AIS_{CS+2.0°C}$ run is similar to the AIS_{pres} run.

Coupled with the increases in the strength of the circulation is an increase in the mass transport across the ice front for the different warming scenarios. This can be seen in Table 6.4. This suggests part of the variation in the heat fluxes across the ice front, which balance with the heat fluxes used to generate the net mass loss from the ice shelf, comes from the variation in the mass transport across the ice front. This is particularly relevant given that the difference in the transport components for the $AIS_{+1.0°C}$ and $AIS_{CS+1.0°C}$ runs mirrors the variation in the net mass loss rate at the ice shelf-ocean interface (Tables 6.2 and 6.3).

In the colder climate scenarios the temperature changes also affected the

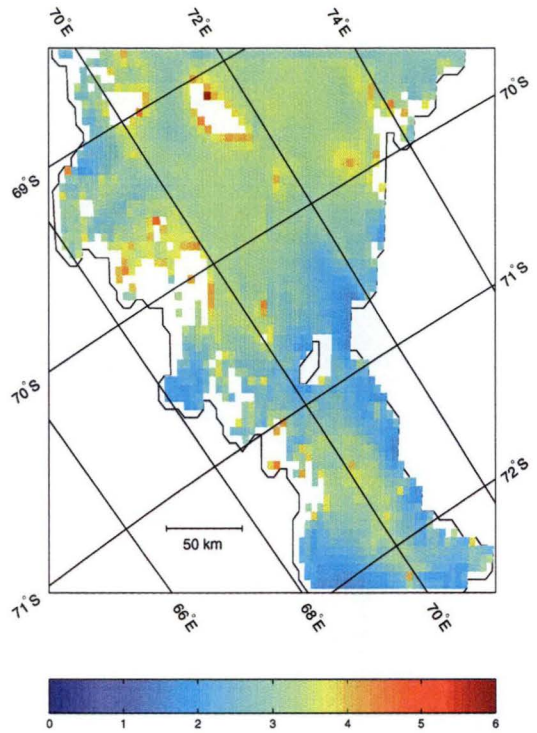

Figure 6.37: The melt-through time for the increased melting rates between the AIS_{pres} and the $AIS_{CS+3.0°C}$ runs. The colour scale is exponential (base 10) years, with white indicating mass gain by the ice shelf.

ocean circulation. The effect was small in the AIS_{cool} run because of the comparatively small change in the temperature at the open boundary (a mean change of -0.03°C). In the AIS_{cold} run the change was more substantial (a mean change of -0.20°C). The direction of the Northeastern Gyre changed; it formed part of a large gyre to the north and north-east of the Central Gyre.

A limit on the applicability of the warming studies may arise from the assumption of a steady state ice shelf. As warming increases it is reasonable to expect that the mass balance changes to the ice shelf seen in this study would affect the shape and dynamics of the ice shelf. A full assessment of the changes is beyond the scope of this study. However, the appropriateness of assuming an unchanging ice shelf in the different climate scenarios should be considered.

Here the time that would be taken for the increased melting rates in the $AIS_{CS+3.0°C}$ run to melt through the ice shelf is estimated. This is found by dividing the thickness of the ice shelf by the difference in melt rates between the AIS_{pres} run and the $AIS_{CS+3.0°C}$ run. The difference is taken as the ice shelf in the AIS_{pres} run is assumed to be in a steady state, hence any change in the melt rate will directly affect the ice shelf. The melt-through times are shown in Figure 6.37 using an exponential scale. From this figure the smallest change in the melt-through time is 1.504, which corresponds to a melt-through time of ~32 years. It should be noted, it is unlikely the calculated melt rates would remain as high as were modelled, particularly near the southern grounding line. Changes in the thickness of the ice shelf will reduce the ability of cavity waters

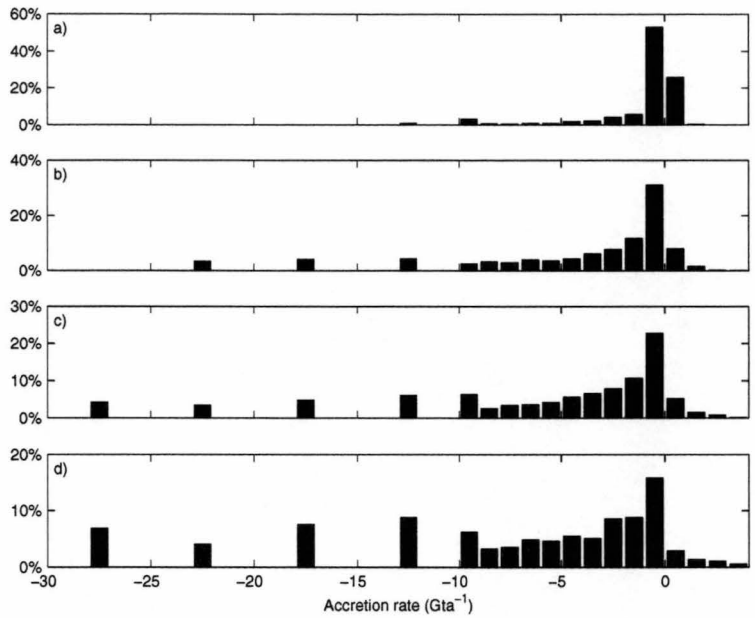

Figure 6.38: Frequency distribution of melting (-) and freezing rates (+) for the a) AIS_{pres}, b) $AIS_{CS+1.0°C}$, c) $AIS_{CS+2.0°C}$ and d) $AIS_{CS+3.0°C}$ model runs. Bin size = 0.2 ma^{-1}.

to melt the ice shelf as the associated pressure change will increase the in situ freezing temperature, thus reducing the heat flux out of the ocean. Therefore the values calculated for the melt-through times are the minimum period in which the ice shelf could melt-through in these locations. The results indicate changes in the ice shelf would occur over longer time scales than the flushing period of the cavity (~2.5 years; calculated from the volume of the cavity and the transport across the ice front). However, the time scales for change in some parts of the ice shelf, particularly in the south and near the Central Grounded Zone, are likely to be on time scales similar to the increase in ocean warming. Although the assumption of a constant ice shelf is useful in this study, a full assessment of the impact and persistence of high localised melt rates could only realistically be done with a coupled ice shelf-ocean model.

The changes in the ocean circulation and the temperature in the ocean cavity impact upon the melting and freezing rates at the ice shelf-ocean interface. These changes in turn affect the mass balance of the Amery Ice Shelf.

The impact of the warming runs on the rates of melting and freezing can be seen in various figures in this chapter. The bulk of the change in the melt rate occurs from shifts in the melt rate. This is highlighted by Figures 6.38 and 6.39. Figure 6.38 shows the frequency distribution of melting and freezing rates for the AIS_{pres}, $AIS_{CS+1.0°C}$, $AIS_{CS+2.0°C}$, and $AIS_{CS+3.0°C}$ model runs. The frequency distributions which are shown have been cropped at melt rates of 10 ma^{-1}. The percentage of melt rates less than this is shown in the most negative bin. The general trend with warming shows a shift in the melt rates, which increases the net amount of melting. Figure 6.39 shows the accumulated net mass loss from the ice shelf base, against the same melting and freezing rates in

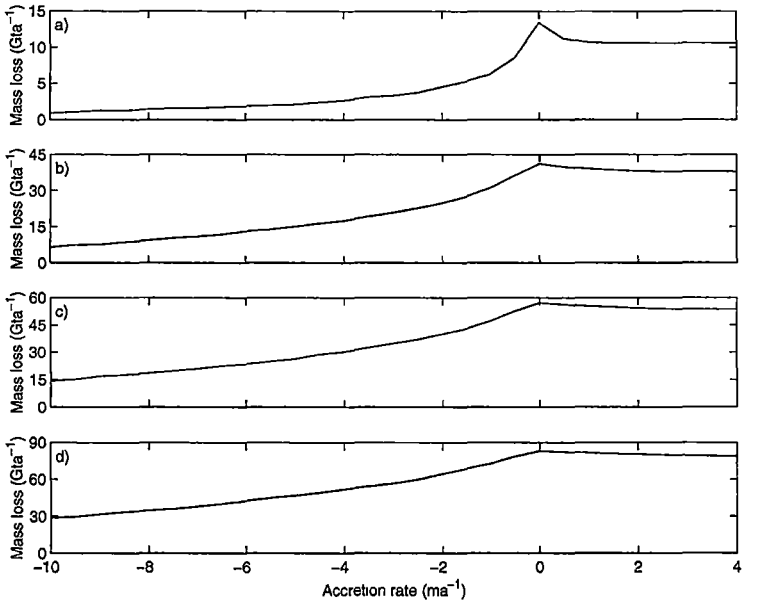

Figure 6.39: Accumulated mass balance by melting (-) and freezing rates (+) for the a) AIS_{pres}, b) $AIS_{CS+1.0°C}$, c) $AIS_{CS+2.0°C}$ and d) $AIS_{CS+3.0°C}$ model runs.

Figure 6.38. The accumulated mass balance suggests as the waters under the ice shelf are warmed up to one third of the melting at the ice shelf base occurs at the small number of locations with high melt rates. The remainder of the melting occurs in areas where the melt rate has only shifted marginally. This is also consistent with the cumulative ice shelf mass balance shown in Figure 6.36, where approximately the same fraction of net mass loss occurred in the same parts of the ice shelf in all of the warming scenarios.

In the warming scenarios the amount of ice lost from the ice shelf increased with the temperature. This change came from increases in both the area of melting and the rate of melting. These combined to give an increase in the total rate of melting. The amount of ice lost and the total melt rate for the ice shelf increased approximately linearly with the change in temperature. The total melt rate changed by $\sim$0.45 ma^{-1}°C^{-1}, and the net ice loss changed by $\sim$22.0 Gta^{-1}°C^{-1}. The linear trend is common to both the constant salinity model runs and the unchanged salinity runs. This is possibly surprising as the melt rates and mass loss rates from the two +1.0°C experiments did not agree. Comparison between the AIS_{pres} run and the $AIS_{+1.0°C}$ run gives a change in the mean melt rate of $\sim$0.36 ma^{-1}°C^{-1}, and a change in the net ice loss of $\sim$18.0 Gta^{-1}°C^{-1}. The corresponding values obtained from comparing the $AIS_{CS+1.0°C}$ run and the AIS_{pres} run are $\sim$0.57 ma^{-1}°C^{-1}, and $\sim$28.5 Gta^{-1}°C^{-1}, respectively. The variation between the two +1.0°C runs brackets the general trend and represents the uncertainty associated with the possible salinity changes accompanying the temperature increases.

The results in this chapter differ from the results presented in Williams et al. [1998b], where it was found for present conditions the mean melt rate was 0.16 ma^{-1}, and the net melting from the ice shelf was 7.8 Gta^{-1}. The

reason these differ is because of the design of the tracer boundary conditions, which were discussed earlier. However, the results of Williams et al. cannot be fully dismissed as a similar rate of change in the melt rate and net loss from the ice shelf was found. For temperature changes of up to +1.0°C, with no changes in salinity the total melt rate changed at $\sim$0.5 $ma^{-1}°C^{-1}$, and the net ice loss varied at $\sim$25 $Gta^{-1}°C^{-1}$. These values are similar to those found in this study. This suggests the change in total net melting with a warming trend is less sensitive to parameterisations of boundary conditions than expected. However, as the melt rate and mass loss rate of Williams et al. increases at a greater rate, this suggests that the tracer boundary condition used in Williams et al. increases the heat flux across the ice front, in the warmer temperature runs, somewhat more than occurs in the runs described here.

Two results which one might expect from warming the ocean are an increase in the mean melt rate and a decrease in the mean freezing rate. The first of these occurred in all the warming scenarios, but the second did not occur. The area of freezing did decrease and the area of melting increased. This decrease in the area of freezing occurred, because where freezing is marginal under present conditions the introduction of warmer waters can change the area from freezing to melting. This feature of increasing accumulation from freezing was also seen by Grosfeld and Gerdes [1998] in their climate change scenarios.

Grosfeld and Gerdes [1998] looked at possible climate change scenarios and their impact on the ocean circulation and the ice shelf mass balance using the three-dimensional ocean model of Grosfeld et al. [1997]. The area they studied included the Filchner Trough and the ocean cavity under the Filchner Ice Shelf. The two climate change scenarios they examined were an increase in ocean temperatures, and a reduction in sea ice formation rates in the open ocean part of their model domain. Grosfeld and Gerdes suggested the reduction in sea ice scenario was the more likely, as warm waters, e.g., Circumpolar Deep Water, would be unable to directly access the continental shelves and interact with the ice shelves in either the Ross or Weddell Sea. Whereas sea ice retreat over the continental shelves from climate change will reduce the production of High Salinity Shelf Water (HSSW).

In their first climate change scenario they increased the ocean temperature by altering the water masses entering the domain. It was changed from HSSW to Modified Warm Deep Water, which has a temperature of -1.3°C. The effect of this was to increase the temperature along the northern boundary by 0.6°C. Over the whole ice shelf Grosfeld and Gerdes reported a net melt rate of 0.81 ma^{-1} for the warming scenario. This is over twice the melt rate reported in their control run (0.35 ma^{-1}). As a warming trend this gives a change of $\sim$0.76 $ma^{-1}°C$, which is approximately twice the size of the trend found in this study. Over the area of the Filchner Ice Shelf (7.18×10^5 km^2) this gives a mass balance change of $\sim$55.6 $Gta^{-1}°C^{-1}$.

The second climate change scenario involved reducing the formation of HSSW from sea ice processes in the Filchner Trough. Grosfeld and Gerdes achieved this by switching off the HSSW restoring in the open ocean part of the domain. This changed the circulation under the Filchner Ice Shelf, and

lowered the temperatures in the ocean cavity under the ice shelf filling it with ISW. In this scenario it was found the mean melt rate of the ice shelf changed to 0.29 ma^{-1} for the whole ice shelf, a decrease in the melt rate of 0.06 ma^{-1}. This change in the melt rate is between the two cooler than present scenarios in this study. This was the climate scenario considered most likely by Grosfeld and Gerdes, and they concluded that the immediate response to climate warming would be the thickening of ice shelves.

This scenario however neglects the deeper ocean warming which could be expected to accompany the reduction in sea ice formation, as found in the coupled climate models [e.g., Gordon and O'Farrell, 1997].

Other numerical studies of the impact of ocean temperature change on ice shelves have been done by Jenkins [1991] and Hellmer and Jacobs [1995]. Jenkins [1991] found the mean melt rate on the base of the Ronne Ice Shelf increased from 0.6 ma^{-1} to 2.6 $m^{-1}$when the HSSW layer with a temperature of -1.91°C, was rapidly replaced with a layer of Modified Warm Deep Water, with a temperature of -1.3°C. Hellmer and Jacobs [1995] gradually warmed the ocean forcing at each end of the cavity model they used by 0.01°Ca^{-1} for 100 years. After this time period they found the melt rate had increased from a mean of 0.18 ma^{-1} to a mean of 1.38 ma^{-1}. In a further experiment, Hellmer and Jacobs also changed the salinity. The salinity forcing field was decreased by 0.02 $PSUa^{-1}$ over the same time scale. This changed the mean melt rate to 0.98 ma^{-1}. Both the models used by Jenkins [1991] and Hellmer and Jacobs [1995] are more likely to force warmer waters into contact with the ice shelf because of the overturning circulation assumed by these models. Where this is occurring the melt rates at the ice shelf-ocean interface will be raised. In most of the model domain seen in this study the warmest waters remain at the bottom of the ice shelf cavity, and generally do not come into direct contact with the ice shelf.

Nicholls [1997] has also suggested the response of the Filchner-Ronne Ice Shelf to ocean warming would be for it to thicken, i.e., net melting from the ice shelf would decrease. In estimating this response Nicholls assumes that the seasonal variation of about 0.1°C, observed in oceanographic moorings under the Ronne Ice Shelf was analogous to the effects of climate warming. In calculating this estimate Nicholls assumes the Southern Weddell Sea circulation remains unchanged, particularly the domination of HSSW on the continental shelf and in the ocean cavity under the ice shelf. A constant ocean circulation ensures that the heat flux across the ice front is only able to vary because of temperature change. The results from the present study and Grosfeld and Gerdes [1998] show this is probably not a valid assumption, as both studies have found the circulation to be dependent on the temperature and salinity at the ice front. The results in this study also suggest thickening of the ice shelf is unlikely to happen without cooling of the open ocean temperatures. The long-term applicability of Nicholls [1997] assumptions need to be questioned. In the warming scenarios presented here the temperature increased in the south of the domain by about an order of magnitude larger than the seasonal change observed by Nicholls. This would suggest that observed seasonal change may not be a reliable guide for estimating the effects of significant climate change

Table 6.5: Melt rates of fresh ice in ocean water as a function of temperature After Russell-Head, [1980] and Budd et al. [1994].

Water Temp (°C)	-1.3	-0.8	-0.3	+0.2	+0.7	+1.2	+1.7	+2.2
Melt rate (ma^{-1})	2.2	6.6	12.0	18.6	25.6	34.3	43.0	52.6

Table 6.6: Maximum melt rates for the climate warming scenarios.

Run	AIS_{pres}	$AIS_{+0.1°C}$	$AIS_{+0.2°C}$	$AIS_{+0.3°C}$
Melt rate (ma^{-1})	12.5	14.3	14.8	15.7
Run	$AIS_{+0.5°C}$	$AIS_{+1.0°C}$	$AIS_{CS+0.5°C}$	$AIS_{CS+1.0°C}$
Melt rate (ma^{-1})	17.2	20.4	16.7	23.9
Run	$AIS_{CS+2.0°C}$	$AIS_{CS+3.0°C}$		
Melt rate (ma^{-1})	30.0	37.3		

under ice shelves.

Budd et al. [1994] presented a series of melt rates for ice shelves, which are shown in Table 6.5. The melt rates were based on laboratory studies by Russell-Head [1980] and inferences made from icebergs by Hamley and Budd [1986]. The differences in the melt rate with temperature follow a non-linear trend and are substantially larger than the mean melt rates found in this study. For a temperature increase of 0.5°C the mean melt rate increase with temperature is 7.2 ma^{-1}. At temperatures close to the surface in situ freezing temperature the rate of change is 4.4 ma^{-1} for 0.5°C. For temperature change between 2.5°C and 3.0°C above freezing (0.7°C and 1.2°C) the change in melt rate is larger at 8.7 ma^{-1}.

The differences in the rate of change for the melt rates between those presented by Budd et al. [1994] and the mean melt rates presented here can be attributed to the ability of the ice shelf to protect itself from warm water. It does this by forming a layer of melt-water adjacent to the ice shelf. The melt-water layer has temperatures close to the freezing point so melt rates are reduced. A free drifting iceberg, on which the melt rates of Budd et al. are based, is unlikely to be able to form such a protective layer. Under an iceberg any melt water is likely to rise from the base of the iceberg to the ocean surface, because the melt-water is relatively fresh and hence less dense. This was seen by Russell-Head [1980] in his laboratory experiments. Under the ice shelf the product of melting will rise, however, it still remains under the ice shelf effectively protecting another part of the ice shelf upstream of the melt. There is also the potential of the melted ice to freeze back on the ice shelf, further reducing the net impact of melting on the ice shelf.

Although the rate of change with temperature presented by Budd et al. [1994] is substantially different from the trend presented here for the mean melt rates, there is some similarity with the change in maximum melt rates, which

are shown in Table 6.6. For example the difference between the AIS_{pres} and the $AIS_{+0.5°C}$ runs is $\sim$4.7 ma^{-1}, which is similar to the change in the Budd et al. [1994] melt rates for between -1.3°C water and -0.8°C water.

The immediate response of the ice shelf to climate change is highly dependent on the response of the sea ice and the ocean at the ice front. If sea ice retreats and the ability of the ocean to be cooled by the increased air-sea heat exchange is larger than the warming of the ocean from increased atmospheric CO_2, then the ocean temperatures at the ice front will be cooled. It is unlikely the waters will be cooled more than the amount assumed for the AIS_{cool} run, so the change in the ice shelf mass balance is likely to be in the order of 1 Gta^{-1}. A change of this magnitude is unlikely to significantly alter the ice shelf. If the warming of the ocean is more significant than the increased heat loss to the atmosphere, then the net amount of ice lost from the Amery Ice Shelf will increase. The climate studies with coupled climate models, discussed in Section 6.1, all indicate a rise in ocean temperatures at depths below 200 m around the Antarctic coast. This favours the assumption the ocean will warm in front of the ice shelf.

The results in this chapter have ramifications beyond the scope of this study. The changes in the basal component of the ice shelf mass balance indicate the ice shelf mass budget will change under expected climate change scenarios. It is realistic to expect that changes in the mass budget will lead to changes in ice shelf geometry and dynamics, particularly at the ice front and grounding lines. Any changes which might occur in grounding line positions, or ice shelf thickness would also impact upon the glaciers flowing into the ice shelf, potentially extensively modifying flow in these glaciers from the reduction in back pressure from the ice shelf.

The results presented here show general agreement with those of studies of other ice shelves [Jenkins, 1991; Hellmer and Jacobs, 1995; Grosfeld and Gerdes, 1998]. The trend in all the studies was for an increase in melting with an increase in ocean temperature. This agreement between the different studies suggests the increased melting response found in this study for ocean warming may be indicative of the expected changes to be found on other large Antarctic ice shelves for ocean warming around Antarctica.

Chapter 7

Interaction between Prydz Bay and the ocean cavity under the Amery Ice Shelf

The main aim of this chapter is to determine the interaction between Prydz Bay and the ocean cavity under the Amery Ice Shelf. To achieve this aim an extended model domain which includes Prydz Bay is used. This will allow the mass, heat and salt exchange across the ice front to evolve freely in the interior of the model. Hence, removing the need to prescribe this interaction in terms of boundary conditions at the ice front on the cavity domain model.

In the extended domain model runs the domain is expanded to include Prydz Bay and a portion of the abyssal ocean to the north of Prydz Bay. A reasonable sized expansion of the domain is needed so that any circulation in Prydz Bay which interacts with the ocean cavity can form away from the influence of the model boundaries. To achieve this expansion of the domain some changes to the model, which was discussed in Chapter 4, are required. In addition to the changes needed to expand the model domain, a simple data assimilation scheme is also introduced in the open ocean part of the domain. The aim of introducing this scheme is to attempt to ensure that the temperature and salinity in the open ocean part of the domain are sufficiently similar to observations. By using an assimilation scheme it is hoped to remove the need to use sea ice models and schemes for the artificial restoring of water masses.

In the first section of this chapter the changes needed to use the model in the extended model are discussed. The section which follows discusses the results of several studies using the extended domain. These include the effects of different assimilation time scales, wind stress regimes, and a modification to the assimilation data set. In the third section the results of the extended domain model runs are compared with oceanographic observations in Prydz Bay. In the fourth section the estimates for the basal component of the ice shelf mass balance from the extended domain model are presented. In the final section the results are discussed and conclusions drawn.

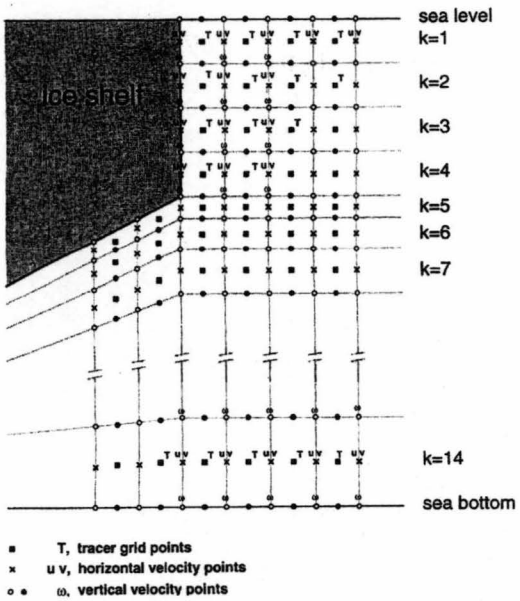

Figure 7.1: Arrangement of grid points and variables at the ice front [Figure 1, Grosfeld et al., 1997].

7.1 Model changes

The numerical model used to simulate the ocean in the extended domain is an adaptation of the model described in Chapter 4. The changes made to implement the model on the combined open ocean-cavity configuration were originally detailed by Grosfeld et al. [1997]. In this section the changes needed to extend the model domain, and the modifications made to the model for the studies in this chapter are described.

7.1.1 Changes to the model domain

The extension of the model domain introduces a large step between the cavity and the open ocean in the water column thickness along the ice front. This step has the potential to cause significant problems in a σ-layer model, as the σ-layers would be forced to rapidly change depth across the ice front. This would introduce large gradients in the σ-layers, and potentially breach the condition of 'hydrostatic consistency' which is associated with the σ-coordinate system [Haney, 1991].

To alleviate this problem in models with a combined open ocean and ocean cavity domain, Grosfeld et al. [1997] introduced additional model levels above the existing levels in the open ocean part of the domain. These additional levels are of fixed thickness and are able to be combined with the σ-layers beneath because of the generalised vertical coordinate scheme of Gerdes [1993] through which the model is implemented. The four additional levels are of equal thickness, and when combined match the draft of the ice shelf along the ice front. This also places a constraint on the ice shelf draft, it must now be constant at the ice front. Beneath the four fixed layers, the ten σ-layers under

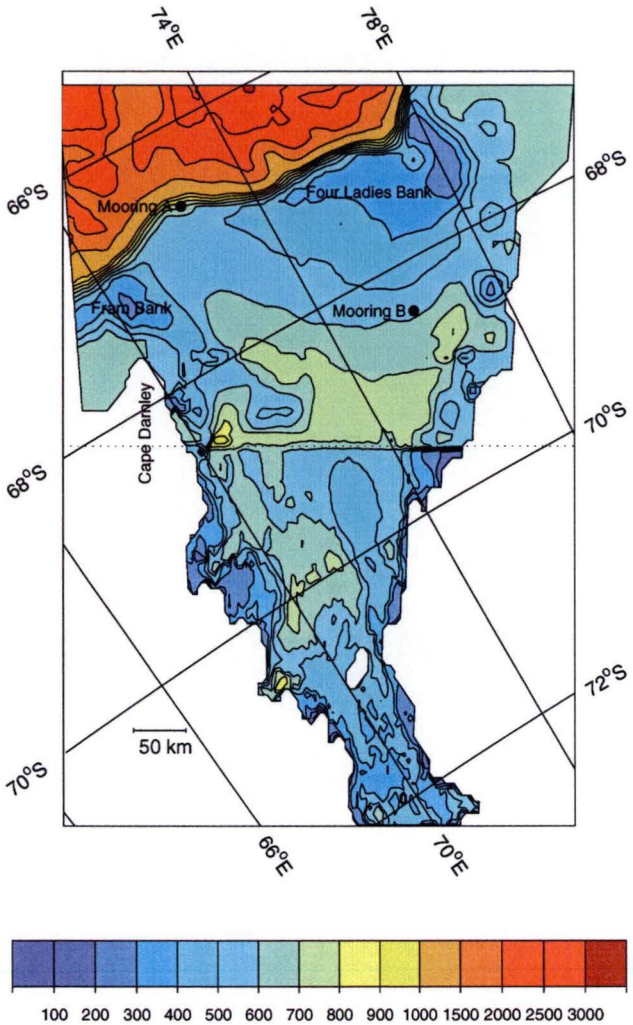

Figure 7.2: Water column thickness over the extended domain in metres. The dotted line indicates the position of the ice front. At the locations of Moorings A and B current meter data is available.

the ice shelf are extended out into the open ocean part of the domain. The vertical layout of the extra layers and the model grid points is shown in Figure 7.1.

In addition to increasing the number of vertical levels the horizontal domain is substantially expanded. The increase in the model area can be seen in the water column thickness for the extended domain. This is shown in Figure 7.2. North of the ice front the water column thickness is the bathymetry. South of the ice front the water column thickness is defined, as in the earlier model runs, as the difference between the ice draft and the sea floor. The bathymetry to the north of the ice front is calculated from ship track data [P. O'Brien, Pers. Comm.] in the region. This data is rotated and gridded in a similar way to the ice shelf draft and water column thickness data in the cavity model (Section 4.5). The bathymetry is then joined to the bathymetry under the ice shelf, found by combining the water column thickness and the ice shelf draft. Some additional smoothing is done on the open ocean side of the ice front to ensure a continuous

bathymetry across the ice front. Although the open ocean bathymetry should be more accurate, the need to retain a consistent ocean cavity under the ice shelf with the previous models is considered more important.

Further changes are made to the bathymetry in the open ocean to accommodate the ten σ-layers below the fixed levels. In some areas of the open ocean after the water column thickness for the top four layers are removed the remaining water column is less than the minimum 50 m needed to ensure numerical stability. In these regions the water column thickness is increased to accommodate the σ-layers. This occurs mainly on the Four Ladies Bank, but also in some places near the coast.

The northernmost row of the ice shelf draft is changed to a constant thickness of 160 m, this is the total thickness of the four fixed layers in the open ocean. The remainder of the ice shelf draft is unchanged.

The horizontal resolution of the model grid is the same as for the cavity model used in Chapters 5 and 6. However, to accommodate the expanded domain the number of grid points is increased, from 66×71 to 130×99. The distribution of the ten σ-levels within the ocean cavity is the same as in the previous model (Table 4.1).

7.1.2 Model forcing

In the previous chapters forcing is applied to the model domain through the boundary conditions at the northern ocean boundary and at the ice shelf-ocean interface (Section 4.3). In the extended domain model these two types of forcing are still used, however, they are supplemented by additional boundary conditions in the open ocean.

The boundary conditions along the northern ocean boundary are similar to those used in the cavity model. For the barotropic component of velocity or streamfunction boundary condition, $\Psi = 0$ was assumed along the northernmost streamfunction row (as used in the $\text{AIS}_{\Psi=0}$ run). The boundary conditions for the tracers and the baroclinic component of velocity are implemented in the same manner as was used in the cavity domain model (Section 4.3). The eastern and western open ocean boundaries are treated as fully closed boundaries and no exchanges of heat, salt, or mass are made across them.

The heat and salt fluxes at the surface of the open ocean are implemented using the simplest method presented by Grosfeld et al. [1997]. The surface temperature is held fixed at the surface freezing point for sea water ($T_f = -1.9°\text{C}$), and the heat fluxes across the surface are calculated from the temperature difference between T_f and the uppermost ocean layer. The temperature difference is also used to calculate a melt rate for sea ice. (Sea ice is by implication always assumed to be present.) This melt rate is then used to determine the salt flux. This method of calculating the heat and salt fluxes is similar to the method used at the ice shelf-ocean interface (Section 4.3.3), except that T_f is fixed. This simple heat and salt flux calculation is used in place of a full sea ice model as the assimilation of temperature and salinity throughout the water column in the open ocean part of the model (Section 7.1.3), should make surface heat and salt fluxes less influential in water mass generation.

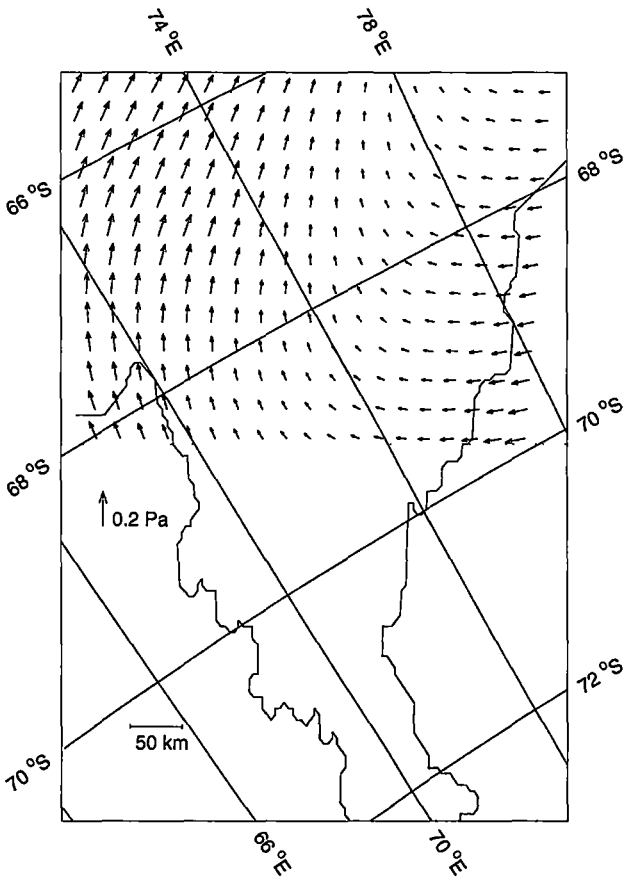

Figure 7.3: Wind stress field in the open ocean part of the model domain. The wind stress field [Trenberth et al., 1989] has been interpolated onto the model grid points. The wind stress is shown at every fifth grid point.

On the top layer of the open ocean part of the domain the surface stress changes from the zero stress environment under the ice shelf. It is important that the surface stress components are included, as they help to introduce processes such as Ekman transport in the top layers of the open ocean. These are important in determining the vertical velocities near the ice front, and they possibly assist in the development of the gyre which is known to form in Prydz Bay [Wong, 1994; Wong et al., 1998]. The surface stress components τ_S^λ and τ_S^ϕ (Equations 4.66 and 4.67) are set to reflect a mean seasonal wind stress for the months January to March. This period is chosen so the wind forcing and assimilation data are seasonally consistent. The FISHOG data set used in the assimilations was collected between February 18 and March 5, 1992.

The wind stress data comes from the Trenberth et al. [1989] global ocean wind stress climatology. This climatology is based on analyses from the European Centre for Medium Range Weather Forecasting between 1980 and 1986. The 2.5° by 2.5° resolution of the Trenberth et al. [1989] data set is rotated and interpolated onto the model grid. The wind stress field at every fifth grid point is shown in Figure 7.3.

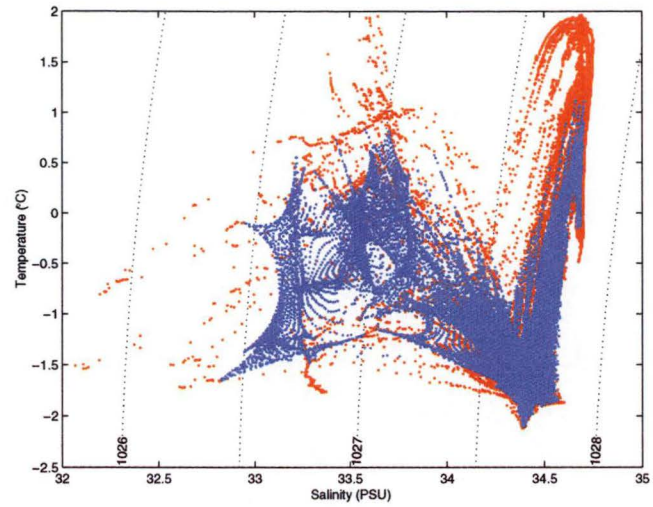

Figure 7.4: Temperature-salinity plot of the FISHOG observations (red) and the assimilation data set (blue). The dotted lines are isopycnals.

7.1.3 Tracer assimilation scheme

The changes made in the previous two sections are related to preparing data for the combined open ocean and cavity domain model of Grosfeld et al. [1997]. In this section the changes are specific to this study.

The assimilation scheme is introduced in the open ocean part of the model domain with the aim of nudging the temperature and salinity in the model close to the observations from the FISHOG data set (Section 3.1). This data set is highly suitable as the extent of the observations (Figure 3.1) is greater than the model domain (Figure 7.2). To implement the nudging scheme a restoring term is added to the time evolution equation for temperature and salinity. This changes the evolution equation for a tracer T (Equation 4.9) to

$$\frac{\partial T}{\partial t} + \Gamma(T) = F^T + \frac{1}{\gamma}(T_{ass} - T), \tag{7.1}$$

where γ is the time scale over which the nudging takes place, and T_{ass} is the prescribed data field being assimilated into the model.

The prescribed data field, used to define T_{ass} in Equation 7.1, is derived from the FISHOG data set. To provide data at each open ocean model point the FISHOG data set (Section 3.1) is interpolated onto the model grid. The latitude and longitude of each CTD cast is rotated into the model coordinate system. After rotation the CTD profiles are interpolated on each horizontal level of the CTD data set using an inverse distance weighted mean. This provides a series of horizontal grids which have 2 db resolution in the vertical. This data set is then fitted to the σ-levels by assigning the values in the interpolated data set below each σ-level to that σ-level.

The fit of the assimilation data in temperature and salinity space to the FISHOG observations is shown in Figure 7.4. The warmest and saltiest waters in the FISHOG data set do not appear in the assimilation data set, as they are

observations collected outside the current model domain. However, they are used in the interpolation process along the model boundaries.

Figure 7.5 shows the temperature along three cross-sections in the open ocean part of the model domain. The locations of the three cross-sections are shown in Figure 7.6. These temperature cross-sections are presented for later comparison with the model results. The cross-sections presented in Figures 7.5a and 7.5b are northward extensions of Sections A and B, respectively

7.2 Results from the extended model domain

An initial assimilation time scale (γ) of 360 days is chosen. This is based on values used by The FRAM Group [1991] for the Fine Resolution Antarctic Model. Initial evaluations suggest the time scale is too long, and shorter time scales are experimented with.

Here the results from the initial assimilation run with a time scale of 360 days are presented. Although the assimilation time scale is too long, the features of this model discussed are common to all of the model runs. This model run is labelled EXDOM$_{\gamma=360}$.

Following the discussion of the EXDOM$_{\gamma=360}$ run, the effects of change on the assimilation time scale and running the model without assimilation are considered. Two shorter time scales of 50 days (EXDOM$_{\gamma=50}$) and 100 days (EXDOM$_{\gamma=100}$) are presented. The discussion of the effect of the assimilation time scale on the model results is followed by an investigation of the importance of the wind stress on the circulation. In the final part of this section the assimilation data set is modified and the impact of this is discussed.

7.2.1 Initial assimilation run

The horizontal circulation shown by the vertically integrated streamfunction for the EXDOM$_{\gamma=360}$ run is presented in Figure 7.7. The dominant feature of the circulation is the large gyre which connects the circulation under the Amery Ice Shelf with the circulation in Prydz Bay. This gyre has two distinct centres, one in the ocean cavity and the other in Prydz Bay. Previous researchers [e.g., Wong et al., 1998] have referred to the part of the gyre north of the ice front as the Prydz Bay Gyre, this nomenclature will be retained for this part of the gyre. The whole gyre will be referred to as the Dominant Gyre.

Examination of the vertical circulation in the Dominant Gyre shows it is generally vertically coherent. The gyre is constrained in the ocean cavity by the same topographic features which constrain the Main or Central Gyres, as discussed in Chapter 5. North of the ice front the Prydz Bay Gyre is topographically trapped by the Four Ladies and Fram Banks to the northeast and west, and the coast on the eastern side of the gyre (Figure 7.2). The Prydz Bay Gyre is not topographically constrained in the northwest where it fills a sill between the Four Ladies and Fram Banks. Here the gyre is able to interact with the deep ocean, which provides an important source for the transfer of

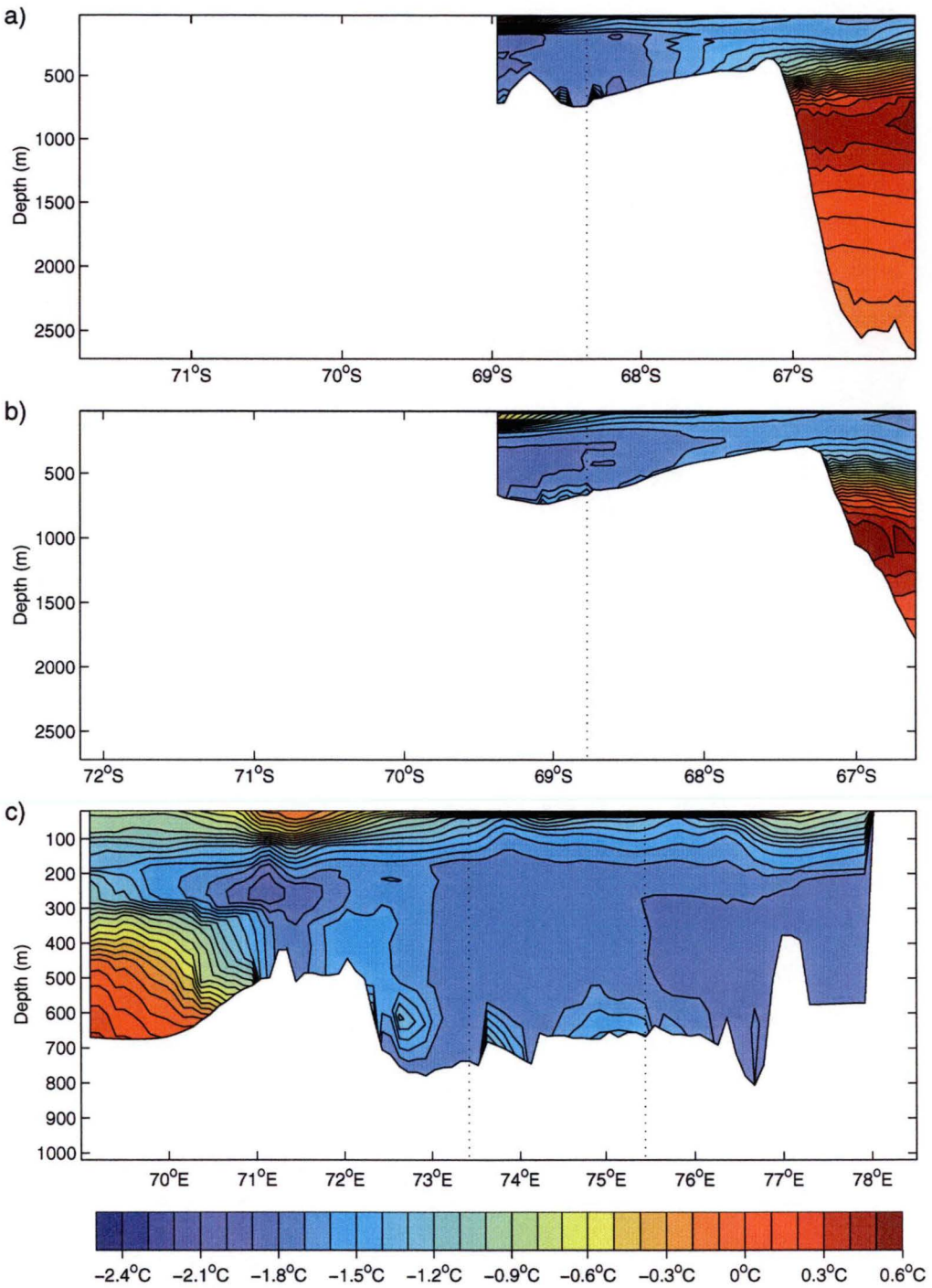

Figure 7.5: Temperature cross-sections for assimilation data set a) Section A′, north of the ice front, b) Section B′, north of the ice front, and c) Section D. The scales of Sections A′ and B′ are set consistent with the other sections presented later. The location of the cross sections is shown in Figure 7.6.

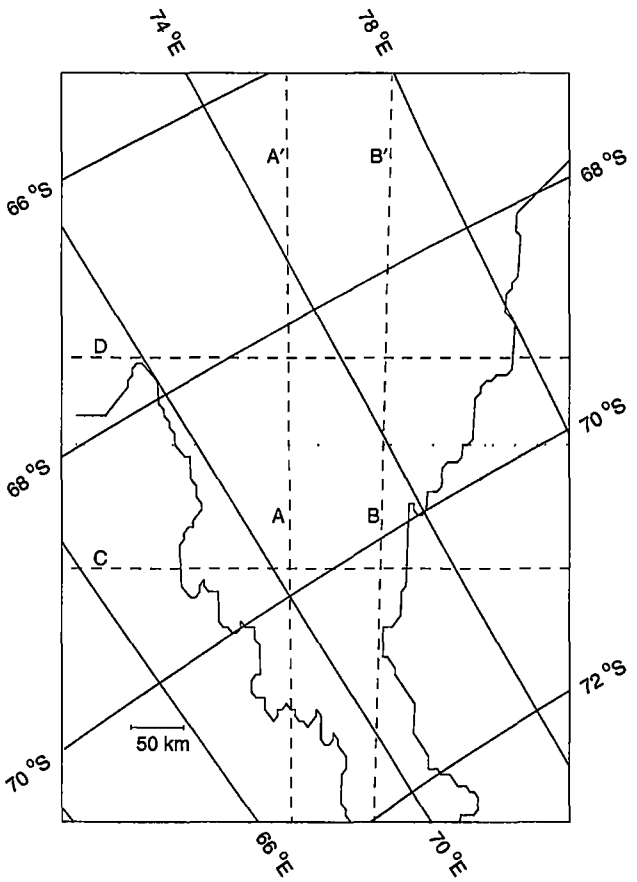

Figure 7.6: Positions of the temperature cross-sections shown. Sections A and B are the parts of Sections A′ and B′ within the ocean cavity, and Sections A, B and C, are along identical model grid rows to the sections with the same name presented in Figure 5.4. The dotted line indicates the position of the ice front.

heat and salt from the warm water masses north of the shelf break on to the shelf.

Off the shelf break the circulation forms a series of weak gyres. These gyres are the product of restrictions in horizontal transport by the continental slope and the boundaries of the model domain. Accordingly, they are unlikely to realistically represent the ocean circulation to the north of Prydz Bay. The gyres do, however, influence the transport and orientation of the slope current.

Inside the ice shelf cavity the horizontal ocean circulation is similar to that seen in the cavity models for the $AIS_{\bar{u},\bar{v}=0}$ and $AIS_{P\bar{v}}$ model runs (Chapter 5). The part of the Dominant Gyre inside the ocean cavity is similar to the Main Gyre seen in both of these model runs (Figures 5.6 and 5.15), although the strongest part of the circulation is now near the ice front, rather than near the Central Grounded Zone. The remainder of the ocean cavity is also similar, except in the northeastern part of the cavity where no Northeastern Gyre is present. South of the Central Grounded Zone the circulation in the Southern Gyre has a similar structure to that seen in previous experiments, with a transport of ~-0.2 Sv.

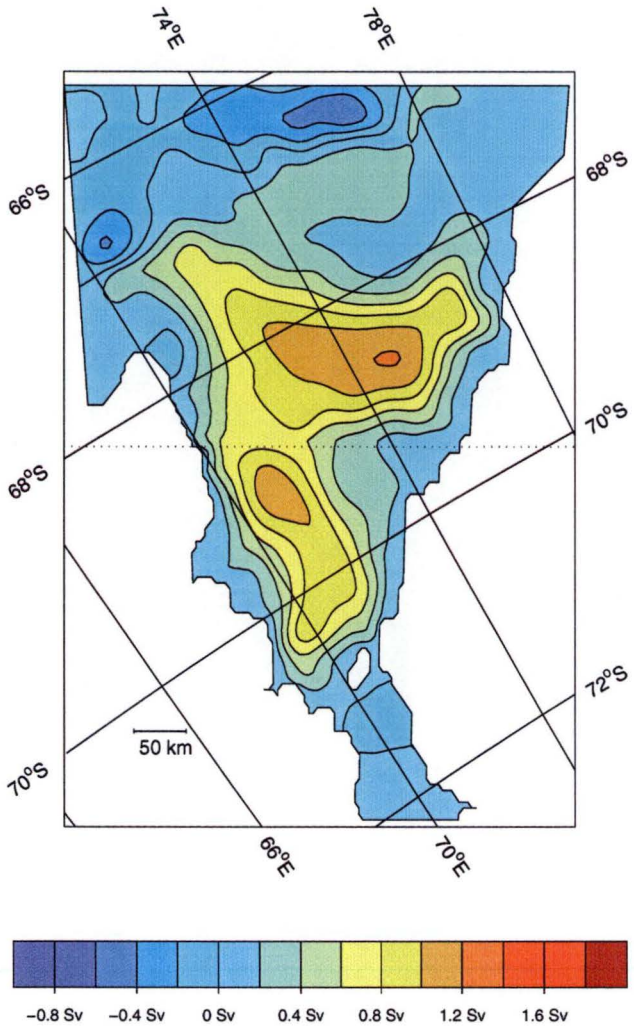

Figure 7.7: Vertically integrated streamfunction for the EXDOM$_{\gamma=360}$ run. The circulation is clockwise about positive values. The dotted line indicates the position of the ice front.

The vertical circulation north of the ice front differs between the top and bottom of the water column. In the top 160 m of the water column the vertical velocities are very small and there is little movement in the pseudo-lagrangian tracers between the upper and lower parts of the water column. The lower part of the water column is better mixed.

The circulation in the ocean cavity is vertically coherent, with small vertical velocities in the area of the Dominant Gyre. Outside the gyre the vertical flow is dominated by the buoyancy effects, particularly in the south of the domain and around the Central Grounded Zone where melt rates are high.

The part of the circulation of most interest is the flow across the ice front. To identify the processes taking place at the ice front the paths of several pseudo-lagrangian tracers were determined. The initial positions of the tracers are one model row to the north of the ice front. These are shown in Figures 7.8 and 7.9. The tracer paths agree with the streamfunction (Figure 7.7), in that there

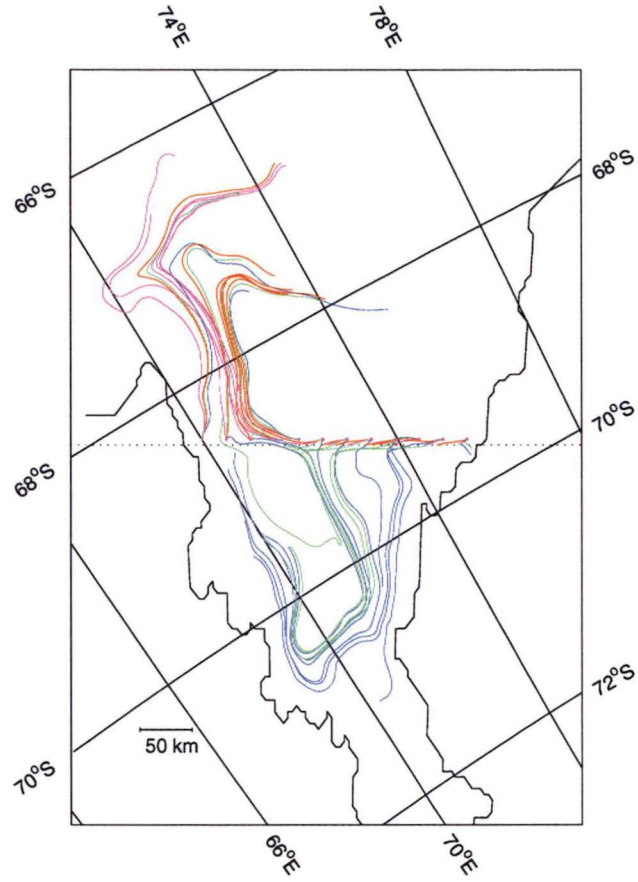

Figure 7.8: Pseudo-lagrangian tracer paths viewed from above the model domain. The tracers are released one model row north of the ice front on σ-levels 2 (magenta), 6 (red), 9 (green) and 12 (blue). The dotted line indicates the position of the ice front.

is a broad area of inflow in the eastern side of the domain while the outflow is constrained to the western side. The tracer paths highlight which part of the open ocean circulation is interacting with the ocean cavity. At the deepest initial tracer layer (σ-layer 12), all the tracer paths, except those released in the outflow region, run into the ice shelf cavity. At intermediate depths, reflected by the release of tracers in σ-layer 9, the cross-boundary flow is mixed with some tracer paths running into the ocean cavity. In Figure 7.9 only the tracer paths deeper than the ice shelf draft are able to enter the ocean cavity. This restricts the tracers released in σ-layers 2 or 6 from flowing under the ice shelf. Outside of the ice shelf cavity both these layers are at depths less than the ice shelf draft. Hence the water masses flowing into the ocean cavity are derived from the deep waters on the shelf off the ice front.

In Figures 7.10 and 7.11 several temperature cross-sections are shown. The locations of the cross-sections are presented in Figure 7.6. The cross-sections shown in Figure 7.11 are taken in identical locations to the temperature cross-sections shown in Chapters 5 and 6. The cross-sections shown in Figures 7.10a (Section A′) and 7.10b (Section B′) are extensions of Sections A and B to include

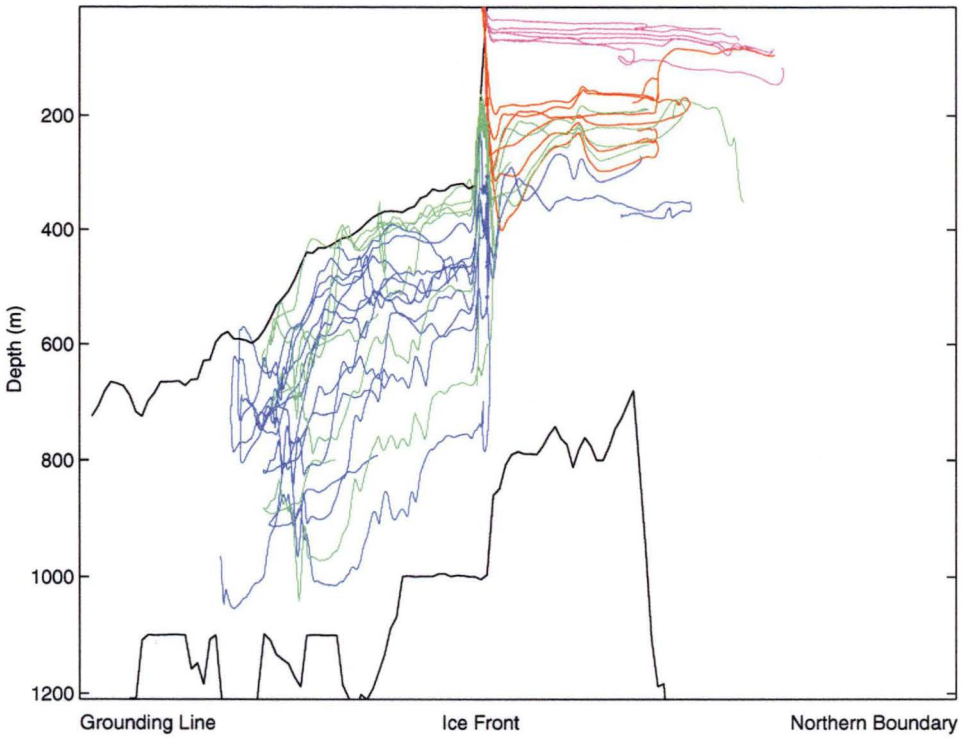

Figure 7.9: Pseudo-lagrangian tracer paths from the east of the domain. The tracers are released one model row north of the ice front on σ-levels 2 (magenta), 6 (red), 9 (green) and 12 (blue). The ice shelf draft shown is the mean zonal draft, and the bathymetry is the zonal maximum.

the open ocean.

At the northern end of Sections A′ and B′ the warm waters off the shelf break have formed from the assimilation of the FISHOG data set into the model domain and from the tracer boundary conditions along the northern boundary. This can be seen by comparing these figures with those in Figure 7.5. The temperature structure off the shelf is, however, different from that in the assimilation data sets. In the model the water adjacent to the continental slope is homogeneous and well mixed, reflecting circulation on the slope. In the assimilation data sets the waters warmer than -0.8°C are below the level of the shelf break, and do not encroach onto the northern portion of the continental shelf. In the model these warmer waters are located higher in the water column and on the shelf.

In Section D (Figure 7.10c) and in the continental shelf parts of Sections A′ and B′, the temperature structure in the $\text{EXDOM}_{\gamma=360}$ run bears little resemblance to the temperature structure in the assimilation data set. The most significant difference is the presence in the model runs of a layer of warm water at the bottom of the water column. This is warmer than found in the assimilation data sets. The other noticeable difference is the lack of warm water at the top of the water column. In the assimilation data set this is present in Section D, and adjacent to the ice front in Sections A′ and B′.

In Section D the model does not reproduce either of the areas of water cooler

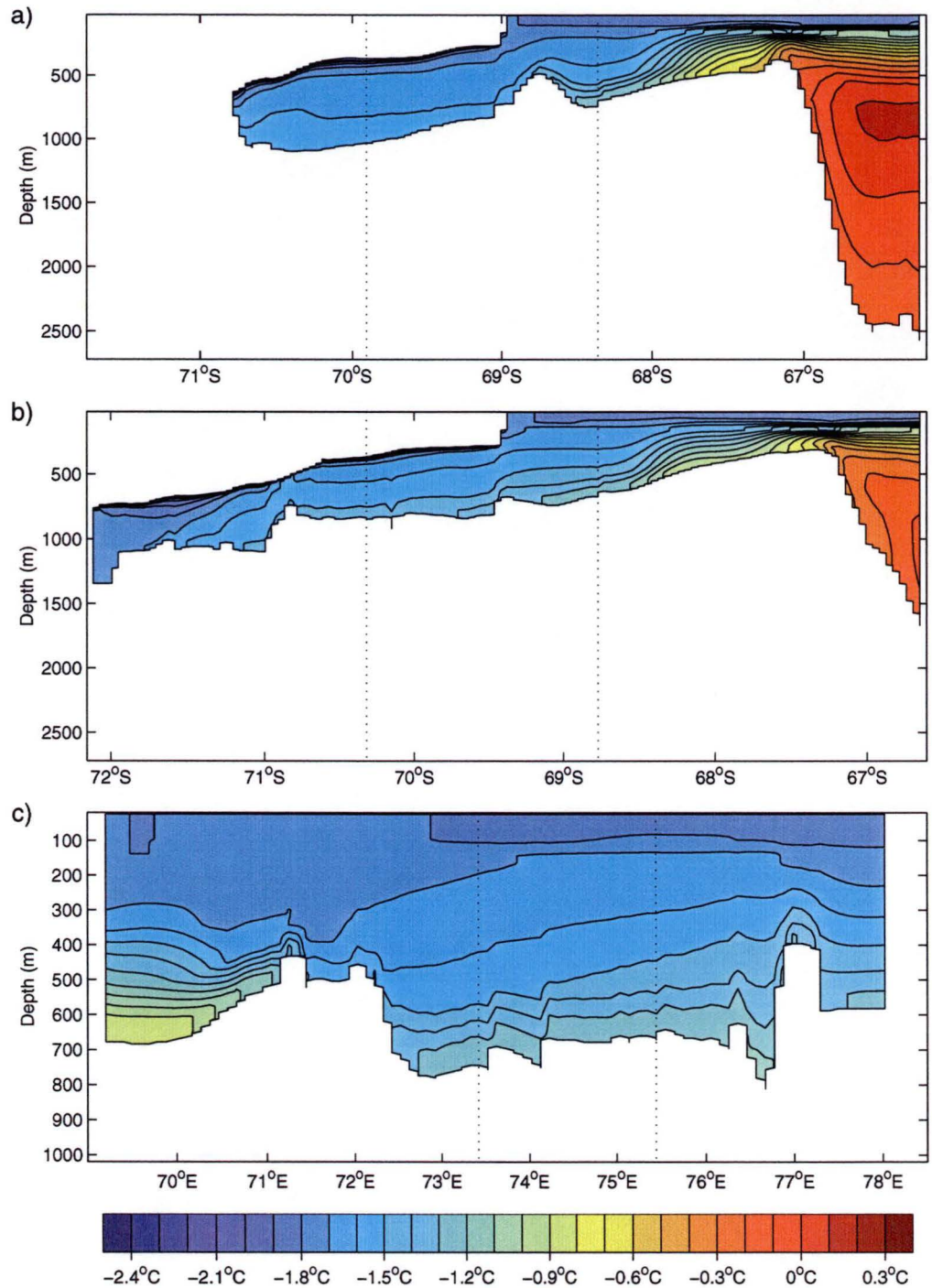

Figure 7.10: Temperature cross-sections for the EXDOM$_{\gamma=360}$ run. a) Section A′, b) Section B′, c) Section D. The locations of the cross-sections is shown in Figure 7.6. The dotted lines indicate where the cross-sections intersect.

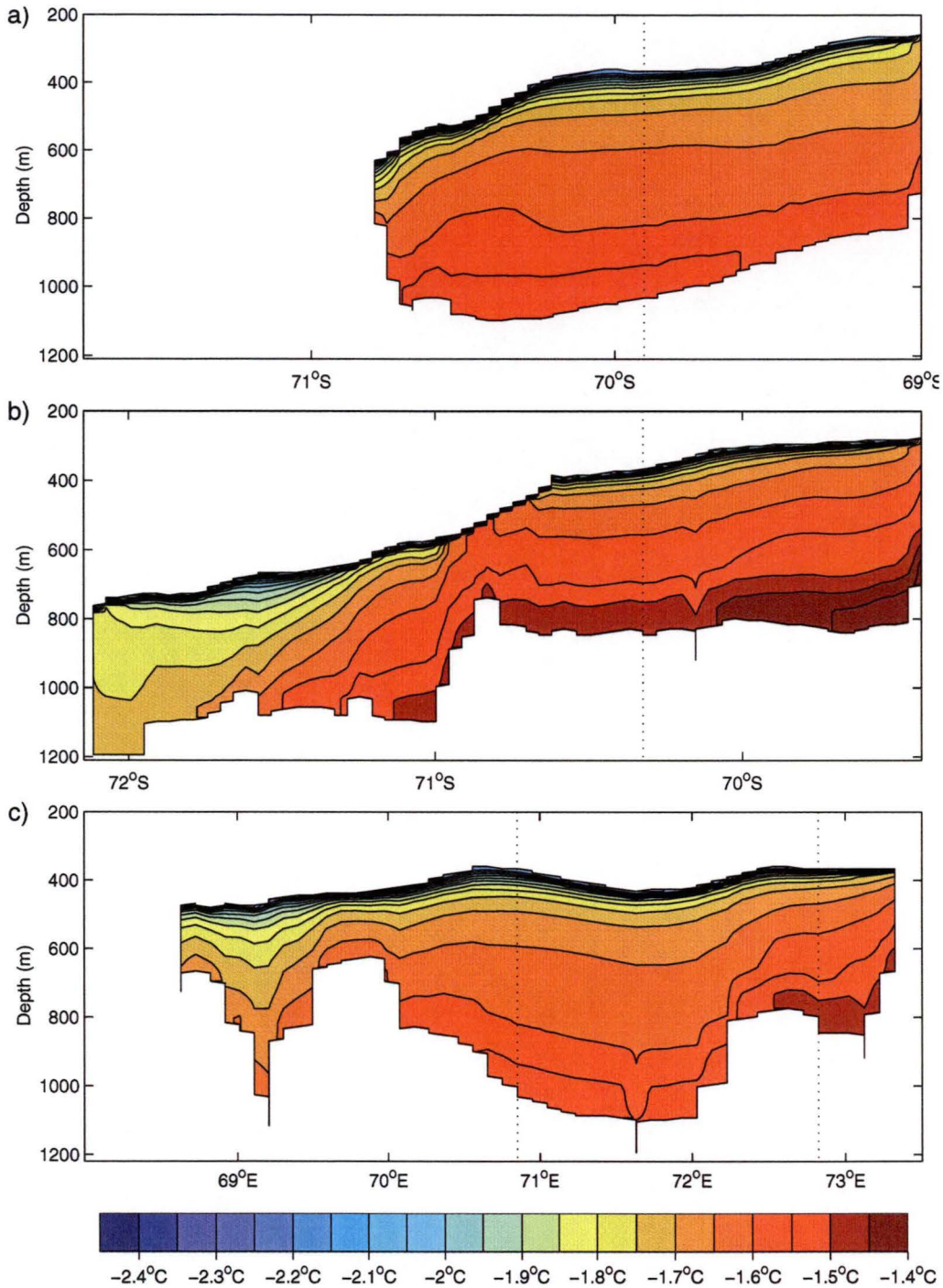

Figure 7.11: Temperature cross-sections in the ocean cavity for the EXDOM$_{\gamma=360}$ run. a) Section A in the ocean cavity, b) Section B in the c) Section C. The locations of the cross-sections is shown in Figure 7.6. The dotted lines indicate where the cross-sections intersect.

than -1.8°C found in the section. The model does produce an area of warmer water on the western end of Section D, although the temperature of that water is approximately 1°C cooler than in the assimilation data set.

In the ice shelf cavity cross-sections (Figure 7.11), the temperatures are much warmer than were found for the studies done in Chapter 5. The structure of the water columns is similar. Each of the three sections is topped by a melt-water layer below which the water column is stratified with increasingly thick layers of warmer water, except near the bottom. Here, in the part of the cavity where circulation is weakest, there is an area with the warmest waters. The circulation processes which form the water column structure are similarly to those discussed in Chapter 5.

7.2.2 The effect of assimilation

The assimilation time scale (γ) affects the tracer distribution and the circulation. The general trend with the decrease in the assimilation time scale is for the gyres which are present in each model run to strengthen. This can be seen from the streamfunctions for the $\text{EXDOM}_{\gamma=100}$ and $\text{EXDOM}_{\gamma=50}$ runs, which are shown in Figures 7.12 and 7.13, respectively. The gyres effected by this are the Dominant Gyre and the Southern Gyre. The strengthening of the Dominant Gyre is uneven; the Prydz Bay Gyre increases by a larger amount.

In the $\text{EXDOM}_{\gamma=360}$ run the part of Dominant Gyre within the ocean cavity is almost separate from the Prydz Bay Gyre. In the $\text{EXDOM}_{\gamma=50}$ and $\text{EXDOM}_{\gamma=100}$ runs the two parts are closely connected. This closer connection can be seen by the increase in streamfunction contours which encircle both centres of the Dominant Gyre. The stronger connection between the two parts of the Dominant Gyre also increases the flow across the ice front. In the $\text{EXDOM}_{\gamma=360}$ run the inflow and outflow mass transport components were 0.93 Sv each, in the $\text{EXDOM}_{\gamma=100}$ and $\text{EXDOM}_{\gamma=50}$ runs these increase to 1.34 Sv and 1.77 Sv, respectively.

The change in the circulation inside the cavity moves the centre of the main gyre away from the ice front, where it was found in the $\text{EXDOM}_{\gamma=360}$ run, to nearer the Central Grounded Zone (Figure 7.13).

The most noticeable change in the domain between the different assimilation runs is the development of different gyre systems off the shelf break (north of ~67°S). The gyres which form are all most likely artifacts of the position of the boundary wall and the location of the shelf break.

The temperature and salinity both change with the reduction in the assimilation time scale from 360 days. The temperature and salinity structures are very similar for the $\text{EXDOM}_{\gamma=50}$ and $\text{EXDOM}_{\gamma=100}$ runs. The temperature fields for Sections A′, B′ and D for the $\text{EXDOM}_{\gamma=50}$ run are shown in Figure 7.14, and the temperature fields for Sections A, B and C are shown in Figure 7.15. The change in the open ocean part of the domain is related to the stronger forcing on the tracer evolution equation (Equation 7.1). This results in the waters north of the shelf break becoming slightly warmer ($\Delta T \sim 0.05$°C), and the deeper waters more saline ($\Delta S \sim 0.05$ PSU). On the shelf the upper

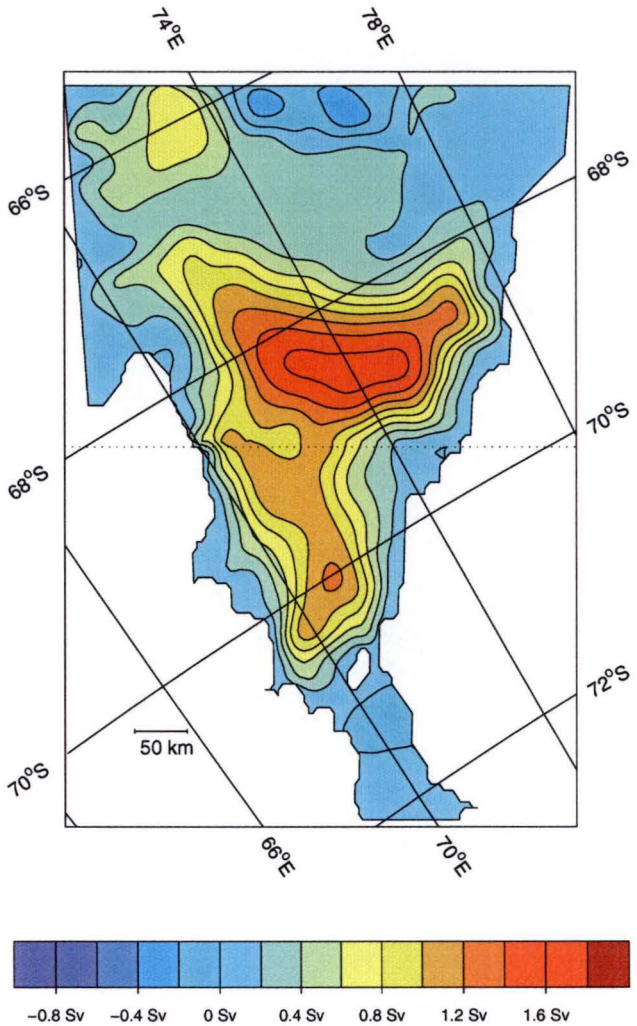

Figure 7.12: Vertically integrated streamfunctions for the EXDOM$_{\gamma=100}$ run. The circulation is clockwise about positive values. The dotted line indicates the position of the ice front.

waters, those shallower than the ice shelf draft, freshen and warm, in contrast the deeper waters cool slightly.

There is a notable exception to these generally small changes. This is at the western end of Section D, where for the EXDOM$_{\gamma=50}$ run (Figure 7.14c) the temperature increases by $\sim$0.7°C from the EXDOM$_{\gamma=360}$ run. This is a result of the increased strength of the assimilation, and that the area where this occurs is characterised by weak circulation. The circulation is weak in this part of the domain, because the deep part of the basin is constrained by Cape Darnley to the east, Fram Bank to the North, and the model's western boundary.

The other distinct feature in Section D is the appearance of an extensive core of cold water. The core is generated partly from cold water advected north in the Prydz Bay Gyre, and partly by the assimilation of ISW and similar water masses. It is these processes which place the coldest part of the core on the western side, the same location as it is found in the assimilation data set (Figure

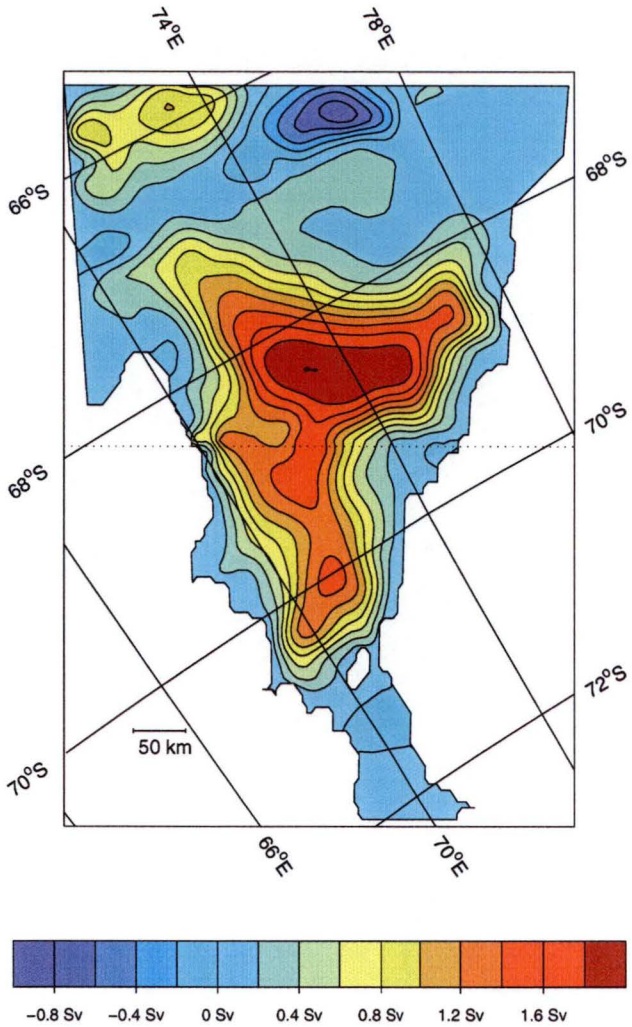

Figure 7.13: Vertically integrated streamfunctions for the EXDOM$_{\gamma=50}$ run. The circulation is clockwise about positive values. The dotted line indicates the position of the ice front.

7.5c). The east-west extent of this cold core is also the result of advection by the gyre, as this temperature cross-section bisects both the northerly flow along the east coast of Cape Darnley and part of the southeasterly flow along the side of Four Ladies Bank.

In the ocean cavity the temperature changes are about the same size as those seen in the open ocean part of the domain. The temperature structure changes markedly between the EXDOM$_{\gamma=360}$ run (Figure 7.11) and the other assimilation runs (Figure 7.15). The two most noticeable trends are a thickening of the intermediate layers and a general cooling of the water. These trends result in a generally homogeneous layer at intermediate depths. At the top there is a thin melt-water layer, and below there are the warmest waters that are separated by a sharp gradient from the intermediate waters. There are some exceptions to the general trend, in particular the appearance of temperature inversions in all three cross-sections. The temperature inversions are formed by

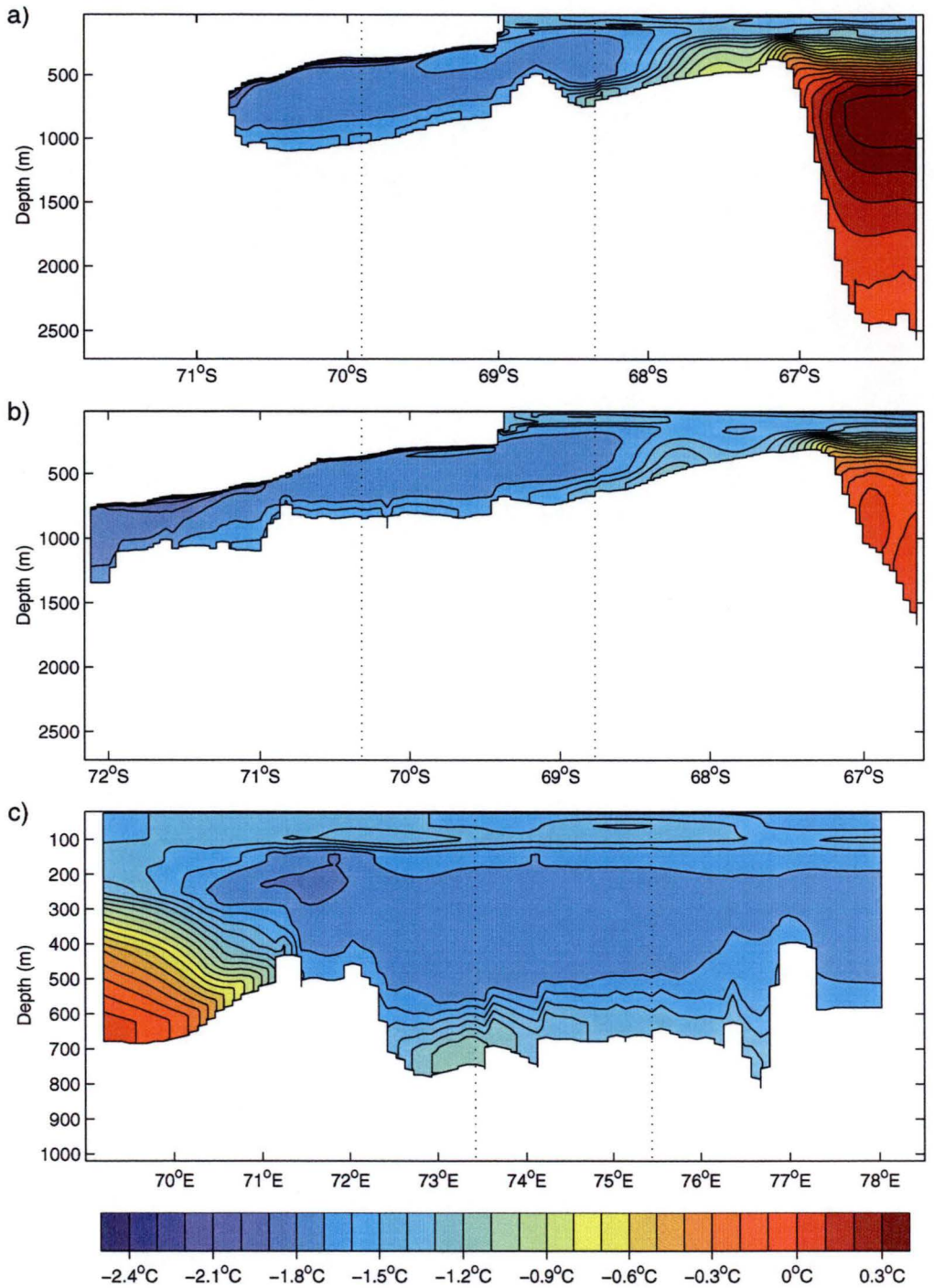

Figure 7.14: Temperature cross-sections for the EXDOM$_{\gamma=50}$ run. a) Section A′, b) Section B′, c) Section D. The locations of the cross-sections is shown in Figure 7.6. The dotted lines indicate where the cross-sections intersect.

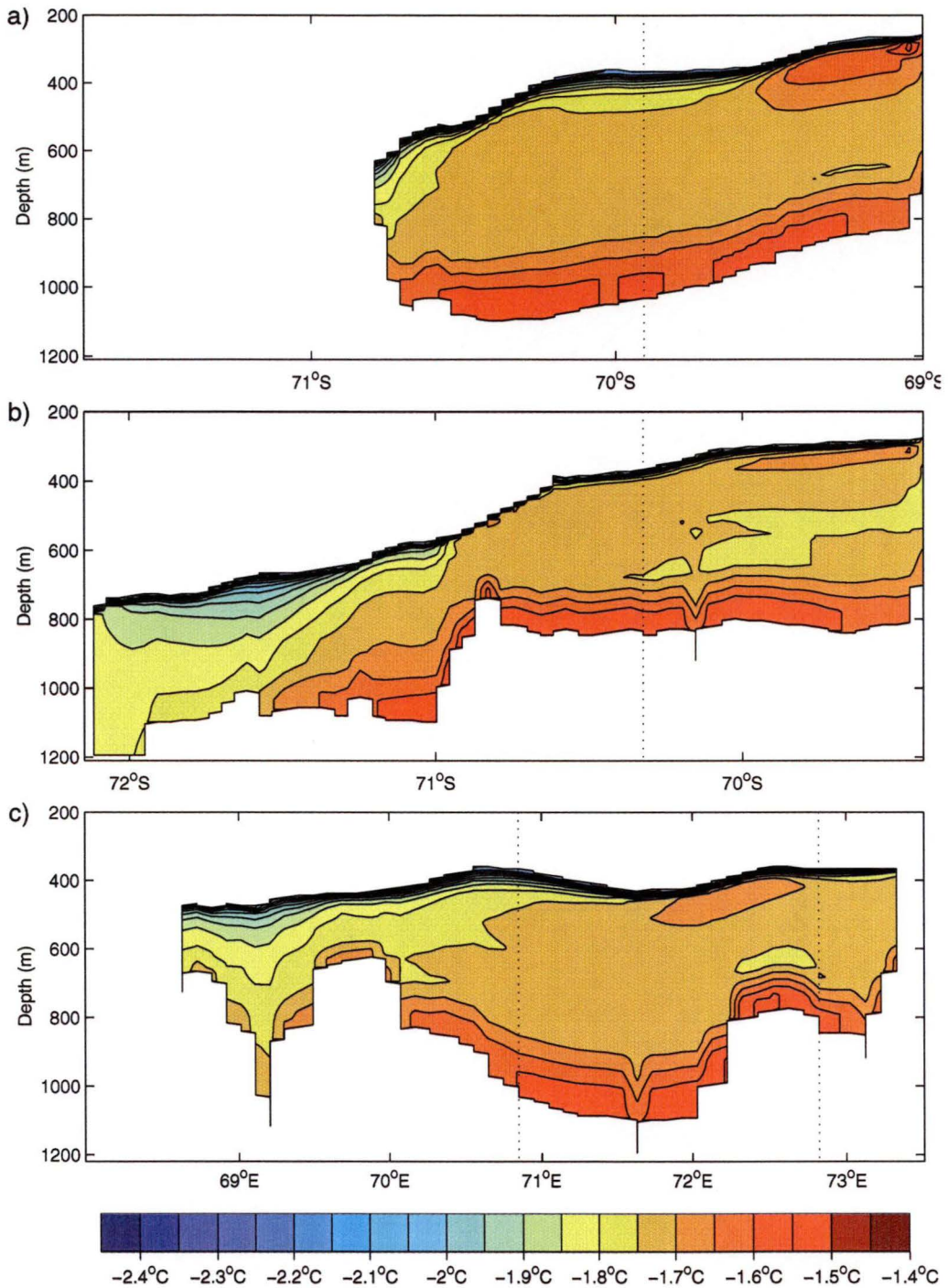

Figure 7.15: Temperature cross-sections in the ocean cavity for the EXDOM$_{\gamma=50}$ run. a) Section A in the ocean cavity, b) Section B in the c) Section C. The locations of the cross-sections is shown in Figure 7.6. The dotted lines indicate where the cross-sections intersect.

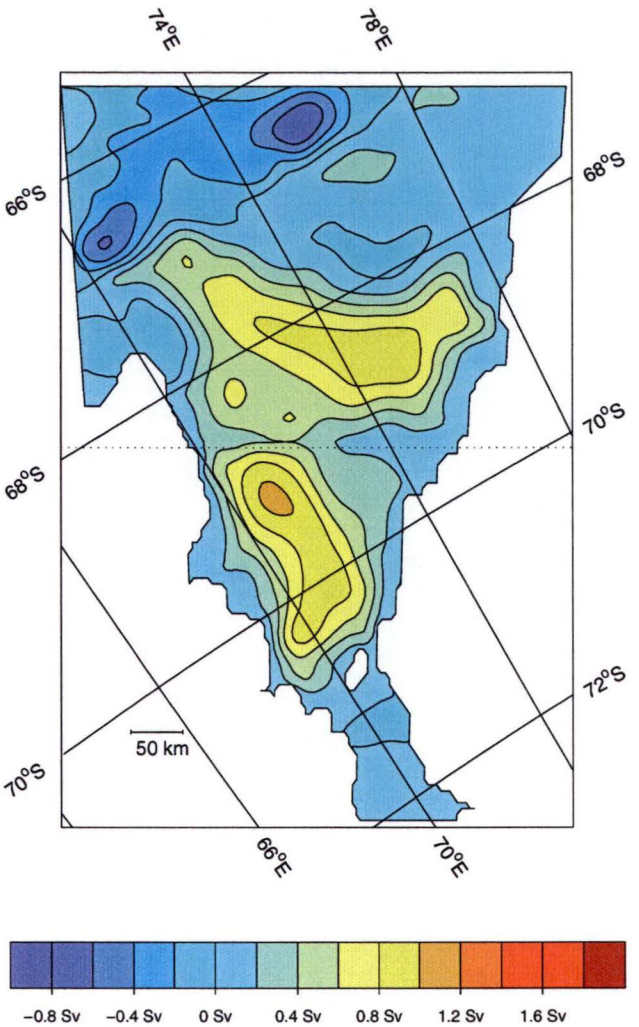

Figure 7.16: Vertically integrated streamfunctions for the $\text{EXDOM}_{\text{basic}}$ run. The circulation is clockwise about positive values. The dotted line indicates the position of the ice front.

water masses with similar densities but different temperatures, being advected from the open ocean into the cavity. The inversions come in on the eastern side with the inflow and are advected around the cavity. This is a process also seen in two of the cavity model runs ($\text{AIS}_{\text{P}\bar{v}}$ and $\text{AIS}_{\text{P}\partial\Psi}$).

In Section B (Figure 7.15b) the waters closest to the grounding line are substantially cooler and appear to extend further to the north. These same waters also appear on the western side of Section C (Figure 7.15c), indicating that the melt-water formed near the southern grounding line is following the horizontal circulation and flowing towards the ice front on the western side of the cavity.

To test the effectiveness of the assimilation scheme in the previous model runs, the model is run without the assimilation scheme. This changes Equation 7.1 by removing the final term, i.e., it reverts to its previous form (Equation 4.9). With no assimilation scheme only the surface boundary condition, and

the northern boundary condition influence the temperature and salinity. This model is labelled $\text{EXDOM}_{\text{basic}}$.

The horizontal circulation shown by the vertically integrated streamfunction in Figure 7.16, has noticeable differences from the circulation in the runs with assimilation. In this run the Prydz Bay and Main Gyres are largely separate gyres. This influences the mass transport across the ice front. It reduces from 0.93 Sv in the $\text{EXDOM}_{\gamma=360}$ run to 0.72 Sv, for each of the inflow and outflow components. The Main Gyre retains a shape similar to that seen in the other extended domain model runs, with the strongest part of the circulation again between the ice front and the Central Grounded Zone.

The temperature cross-sections for the $\text{EXDOM}_{\text{basic}}$ run are shown in Figures 7.17 and 7.18. Comparison of Sections A′ (Figure 7.17a) and B′ (Figure 7.17b) with the corresponding figures from the $\text{EXDOM}_{\gamma=360}$ run (Figure 7.10) or the $\text{EXDOM}_{\gamma=50}$ run (Figure 7.14) shows the differences in the temperature structure increase with distance north from the ice front. On the shelf the temperatures in Sections A′, B′ and D (Figure 7.10c) are similar to those found in the assimilation runs, with the exception of the western end of Section D. Here the bottom temperatures, which are markedly warmer in the assimilation runs, are close to the surface freezing point. This makes the whole of this part of the water column homogeneous.

The temperatures in the deep ocean part of the domain are different from those in any of the assimilation runs. The water here has properties close to those in the assimilation runs, because the northern boundary conditions are still restoring warm waters along this boundary. The warm core of water near the northern boundary in Section A′ found on all the assimilation runs is no longer present. It is replaced by a series of stratified layers with lower temperatures and steep isotherms separating the layers.

The temperatures within the ocean cavity, along Sections A (Figure 7.18a) and Section C (Figure 7.18c), in the $\text{EXDOM}_{\text{basic}}$ run are similar to those in the $\text{EXDOM}_{\gamma=360}$ run (Figure 7.11). There are some changes along Section B (Figure 7.18b), most noticeably in the south of the domain where warmer water fills most of the basin adjacent to the southern grounding line. This reduces the thickness of the melt-water layer adjacent to the ice shelf over most of the southern part of the section.

The use of the assimilation scheme clearly impacts on the temperature and salinity found in the open ocean part of the model domain. Shortening the assimilation time scale increases the similarity between the assimilation data set and the model results. However, it was found the assimilation time scale (γ) could not be shortened to less than 30 days, because the model then became unstable.

Even at short time scales, there are two areas of the water column where the assimilation scheme made little impact. These are on the shelf at the top and the bottom of the water column. At the top of the water column the warm water found in the assimilation data set (Figure 7.5) close to the ice front in Sections A′ and B′ and in Section D, does not appear in any of the assimilation model runs. At the bottom of the model water column the water is much warmer than

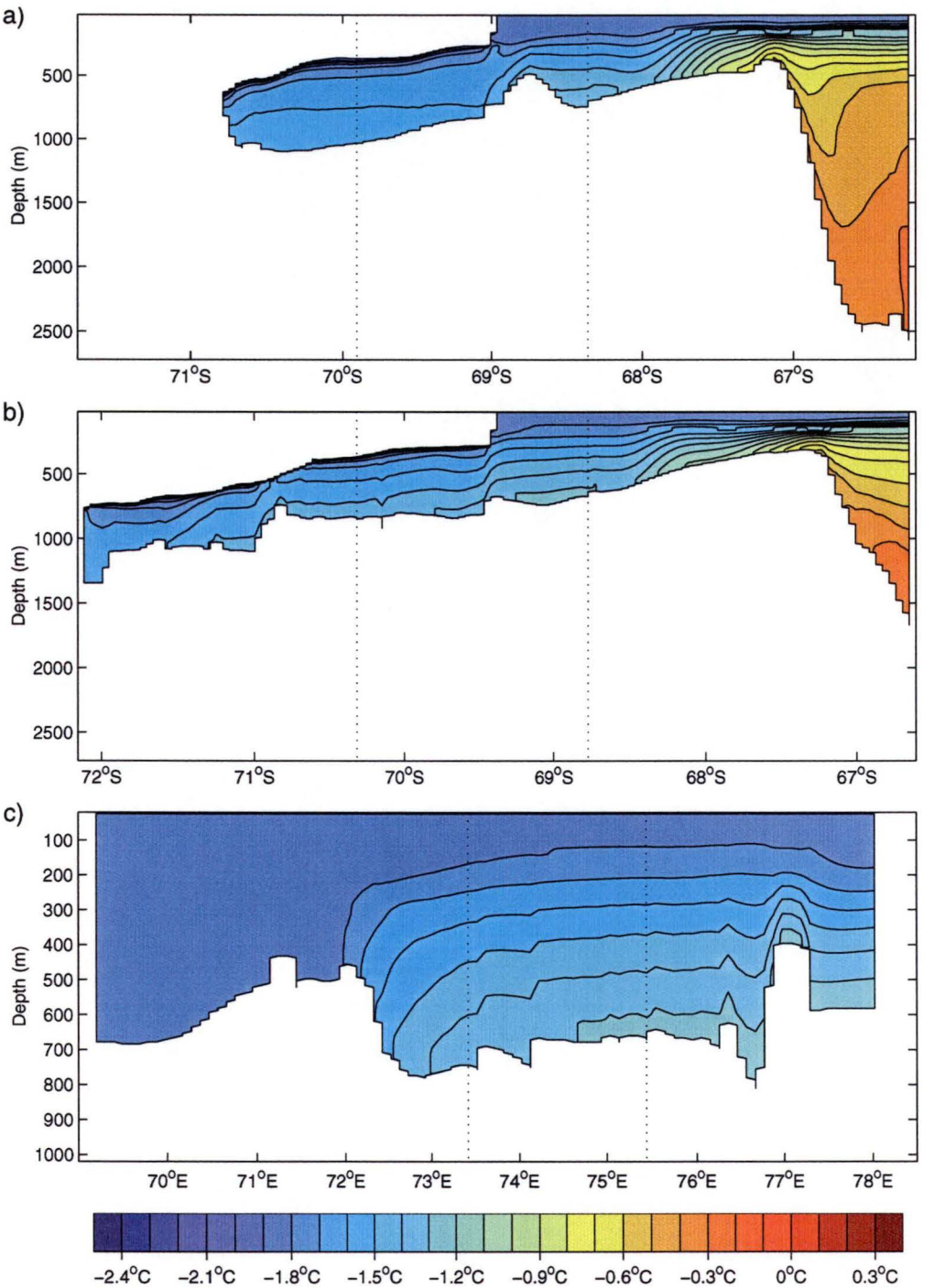

Figure 7.17: Temperature cross-sections for the $\text{EXDOM}_{\text{basic}}$ run. a) Section A′, b) Section B′, c) Section D. The locations of the cross-sections is shown in Figure 7.6. The dotted lines indicate where the cross-sections intersect.

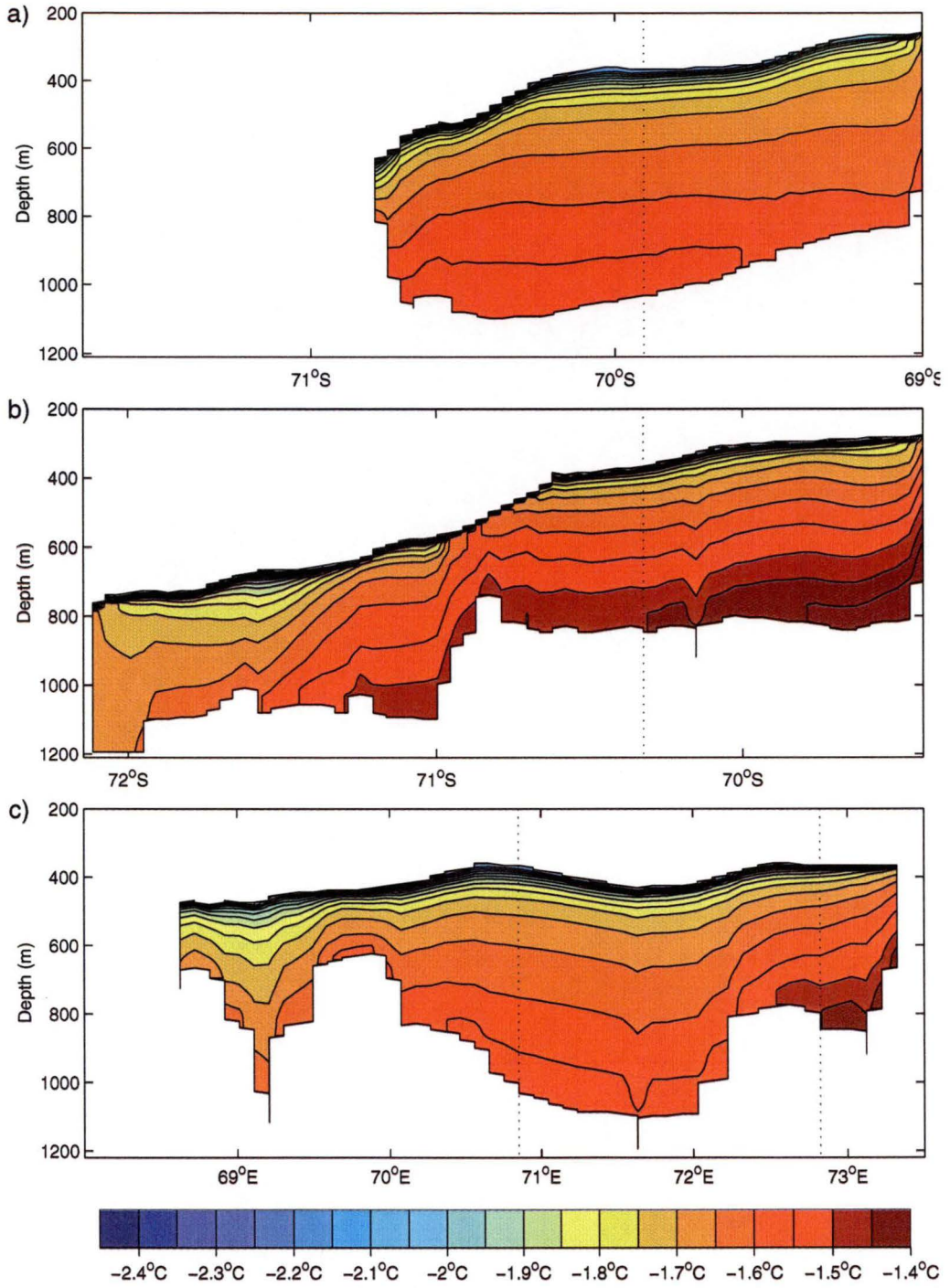

Figure 7.18: Temperature cross-sections in the ocean cavity for the $\text{EXDOM}_{\text{basic}}$ run. a) Section A in the ocean cavity, b) Section B in the c) Section C. The locations of the cross-sections is shown in Figure 7.6. The dotted lines indicate where the cross-sections intersect.

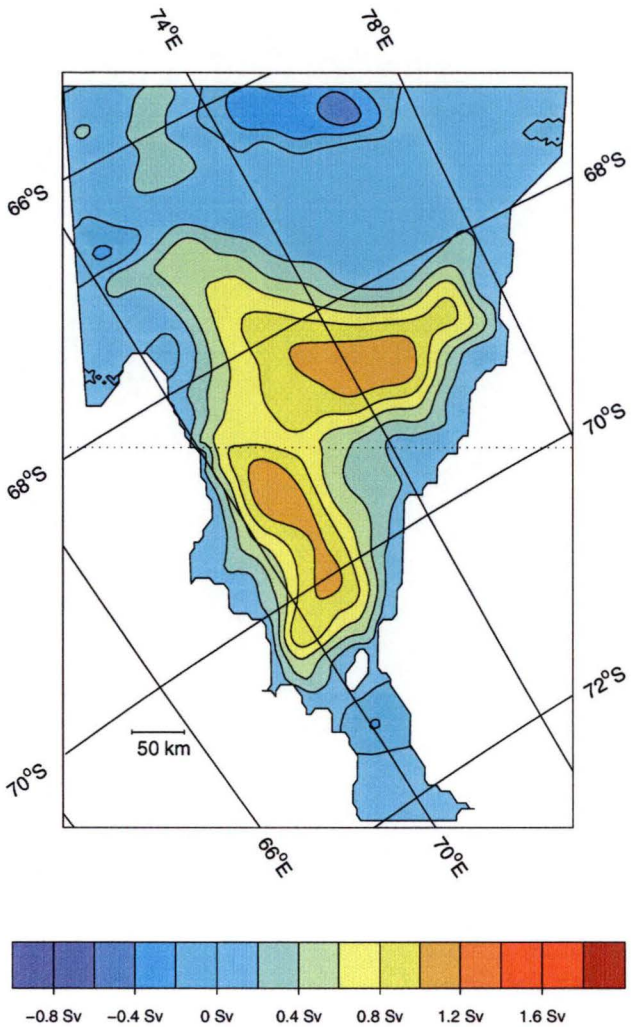

Figure 7.19: Vertically integrated streamfunction for the $\text{EXDOM}_{\tau=0}$ run. The circulation is clockwise about positive values. The dotted line indicates the position of the ice front.

in the assimilation data sets. In both of these areas the assimilation scheme has been less successful. A problem which appears to be inherent in the model. A possible explanation for the difference at the top of the water column is the choice of surface boundary condition. Currently, this will cool and freshen the top of the water column, if water warmer than surface freezing is present.

7.2.3 The effect of the wind stress field

The general structure of the circulation in Prydz Bay is similar in all the assimilation models and the $\text{EXDOM}_{\text{basic}}$ run. To investigate if this similarity is the result of the wind forcing regime used in all of these model runs, two experiments are presented with reduced wind stress fields. In the first experiment the wind stress is reduced by half ($\text{EXDOM}_{\frac{1}{2}\tau}$), and the second has no wind stress field ($\text{EXDOM}_{\tau=0}$). In both these experiments weak assimilation is used

($\gamma = 360$ days).

In both experiments the circulation does not change significantly. This can be seen by comparing the streamfunction for the $\text{EXDOM}_{\tau=0}$ run (Figure 7.19), with the streamfunction from the $\text{EXDOM}_{\gamma=360}$ run (Figure 7.7). There is a small decrease in the maximum circulation in the Prydz Bay Gyre in the $\text{EXDOM}_{\tau=0}$ run. The circulation north of the Prydz Bay Gyre also changes, but the extent of the change is similar to that seen between the different assimilation runs, as discussed earlier.

The temperature and salinity structure in the $\text{EXDOM}_{\frac{1}{2}\tau}$, $\text{EXDOM}_{\tau=0}$, and $\text{EXDOM}_{\gamma=360}$ runs is similar. There is a slight warming in the deepest waters within the ocean cavity ($\sim$0.1°C). The salinity fields do not show any change in the same location. In the open ocean the differences are similar between the model runs. This is not surprising since the temperature and salinity are being assimilated at the same rate as in the $\text{EXDOM}_{\gamma=360}$ run, and with a similar circulation the effects of the advection and diffusion terms in the tracer evolution equation will be similar.

The results from both experiments indicate the strength of the applied wind stress in the model does not significantly influence the circulation in Prydz Bay, although the assimilation of hydrographic data throughout the domain will give some consistency with the winds prevailing during the period of the FISHOG observations.

7.2.4 Modification of the assimilation data set

The warm cavity temperatures in all of the model runs presented so far suggests the assimilation data set may be biased by the constant summer forcing, from when the FISHOG observations were collected. The previously presented model runs also appear to be producing warm water near the bottom of the water column along the ice front.

To see if the effects of the overly warm water on the ice shelf cavity temperatures can be reduced, the assimilation is cooled. The temperature on all levels is reduced by 0.5°C, except where this would reduce the water below the salinity dependent surface freezing temperature, where instead the surface freezing temperature is used. This method of changing the temperature should have a minimal impact on the density structure as it mostly dependent on the salinity, which is kept constant. There are, however, some slight shifts in local density gradients.

In this experiment, labelled $\text{EXDOM}_{\text{cool}}$, the assimilation time scale is kept at $\gamma = 360$ days and the wind stress regime shown in Figure 7.3 is used.

In the horizontal circulation, shown by the vertically integrated streamfunction (Figure 7.20), there are two important changes in the circulation. The first is the weakening of the circulation in the open ocean on the shelf in comparison to that seen in the other models runs. The second is that the circulation to the north of the shelf break has formed a single gyre with a transport greater than the Dominant Gyre. This second change is not a major concern as it is unlikely the circulation in this part of the domain will be realistic, due to

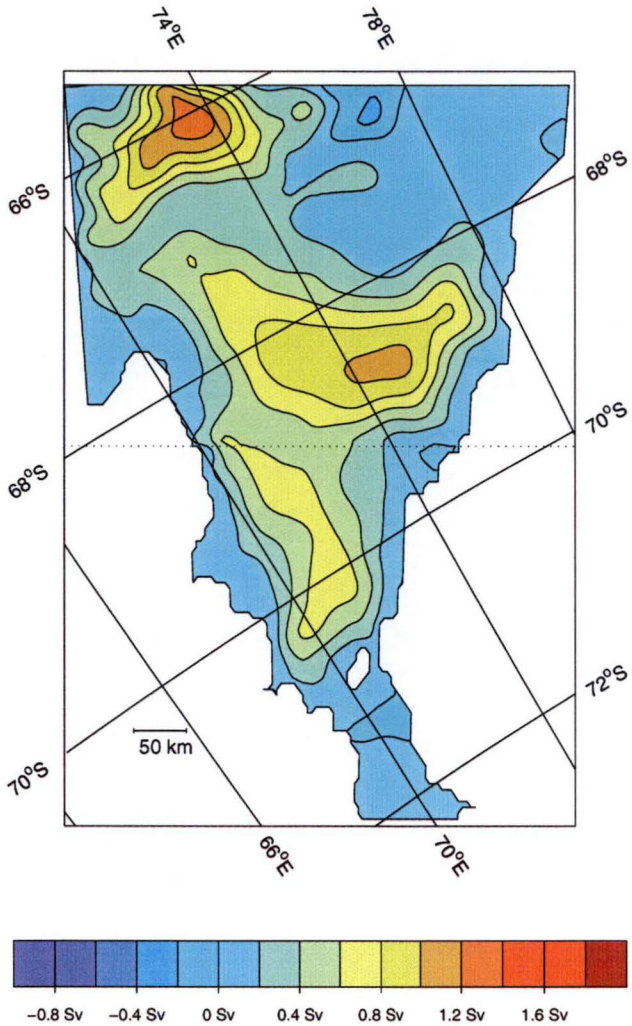

Figure 7.20: Vertically integrated streamfunction for the $\text{EXDOM}_{\text{cool}}$ run. The circulation is clockwise about positive features. The dotted line indicates the position of the ice front.

the topographic constraints imposed by the continental slope and the model boundaries.

In the $\text{EXDOM}_{\text{cool}}$ run both parts of the Dominant Gyre are weaker than in the $\text{EXDOM}_{\gamma=360}$ run. Despite the reduction in the strength of the streamfunction, the connection between the two parts of the gyre is still significant. This connection means the transport across the ice front is still stronger than in the $\text{EXDOM}_{\text{basic}}$ run. In the $\text{EXDOM}_{\text{cool}}$ run the respective transports for the inflow and outflow components are 0.78 Sv, less than in the other assimilation scenarios, but still greater than the $\text{EXDOM}_{\text{basic}}$ run.

In Figures 7.21 and 7.22 the temperature cross-sections for the $\text{EXDOM}_{\text{cool}}$ model run are shown. In all three of the sections shown in Figure 7.21 the surface waters have not changed significantly this suggests the temperature of the surface waters is strongly controlled by the surface boundary conditions. In the deeper water there are changes in the temperature found in the $\text{EXDOM}_{\text{cool}}$

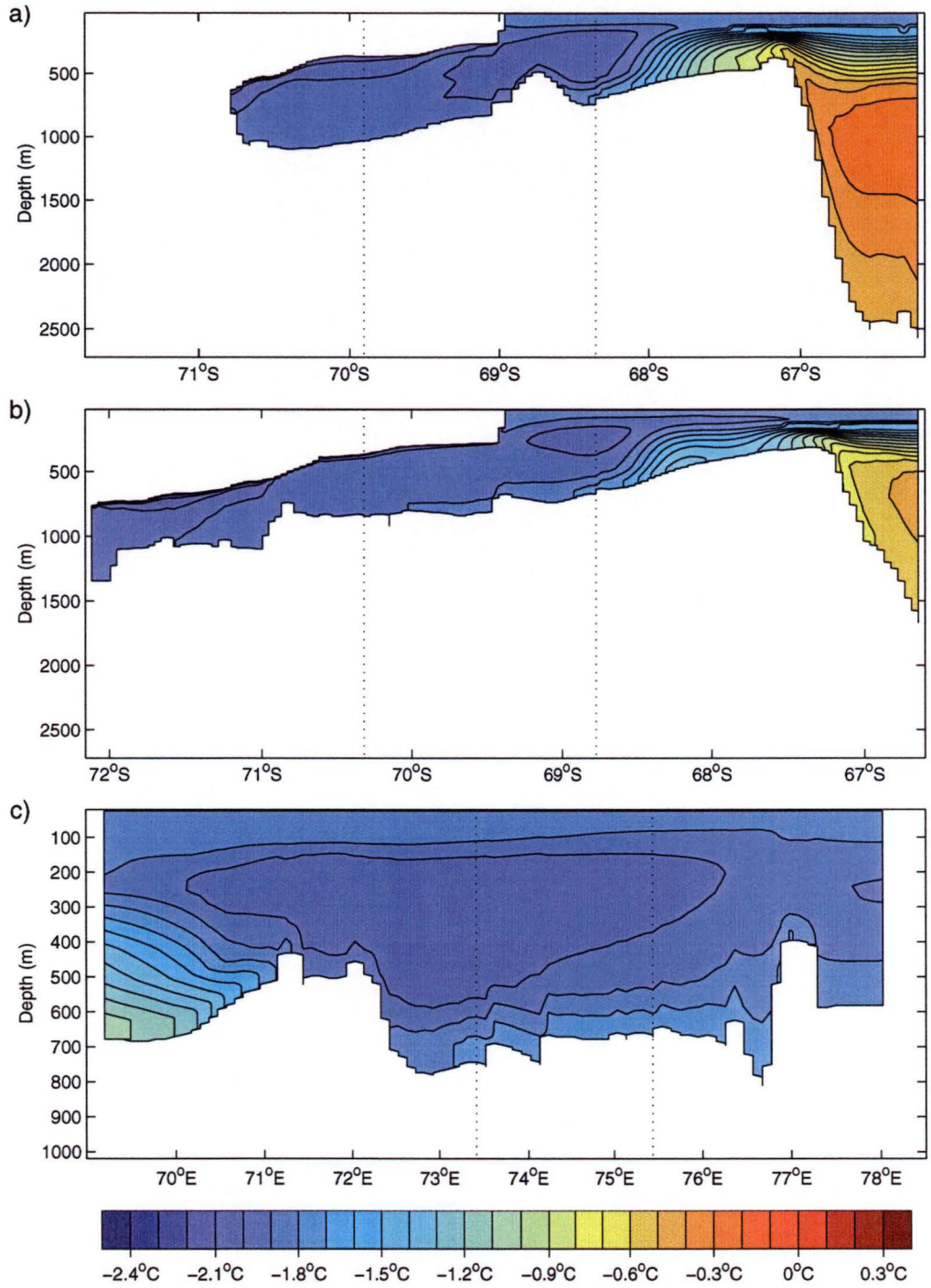

Figure 7.21: Temperature cross-sections for the $\text{EXDOM}_{\text{cool}}$ run. a) Section A′, b) Section B′, c) Section D. The locations of the cross-sections is shown in Figure 7.6. The dotted lines indicate where the cross-sections intersect.

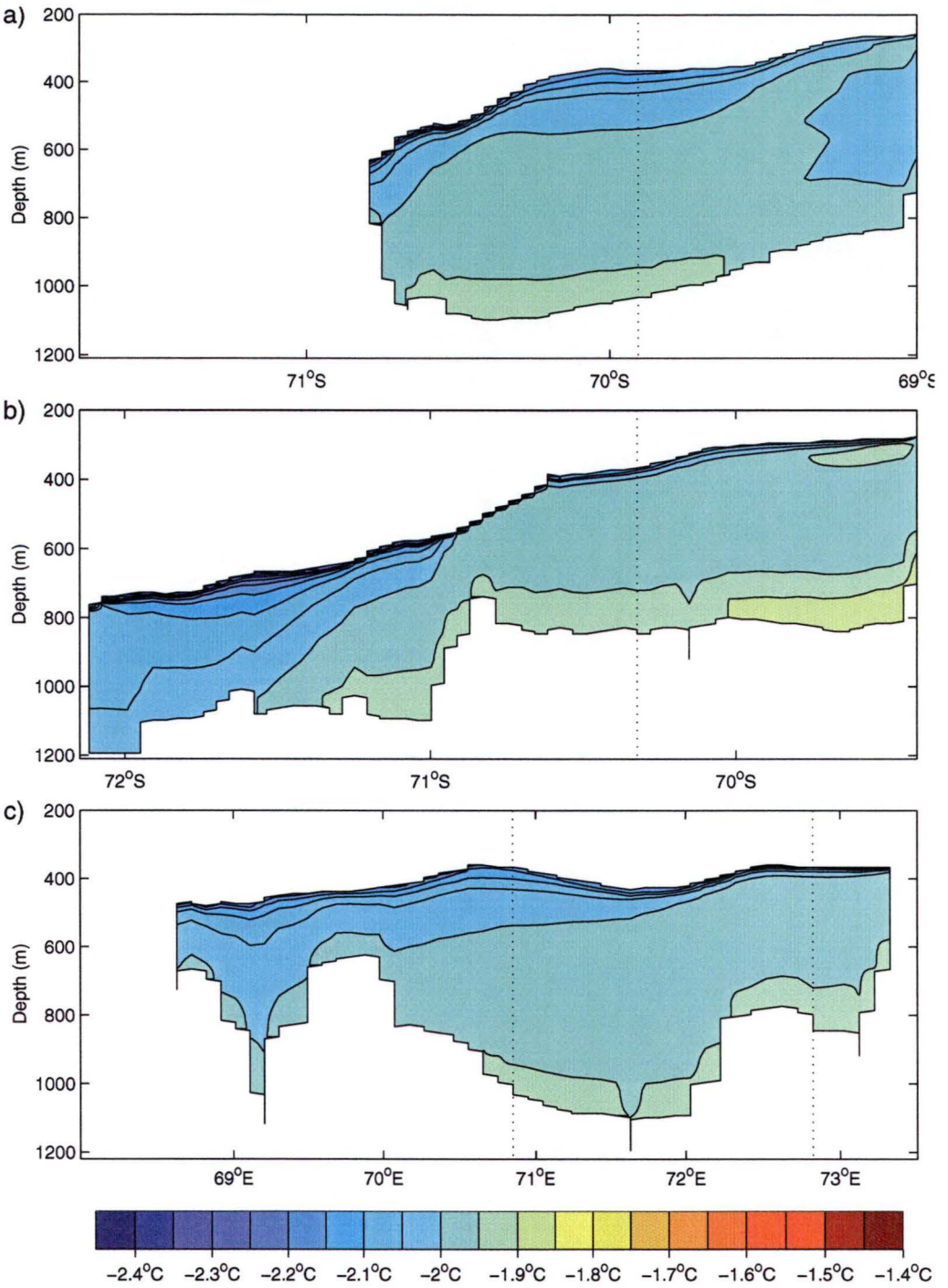

Figure 7.22: Temperature cross-sections in the ocean cavity for the $\text{EXDOM}_{\text{cool}}$ run. a) Section A in the ocean cavity, b) Section B in the c) Section C. The locations of the cross-sections is shown in Figure 7.6. The dotted lines indicate where the cross-sections intersect.

run from the $EXDOM_{\gamma=360}$ run. In Sections A′ (Figure 7.21a) and B′ (Figure 7.21b) the deep waters north of the shelf break have changed by approximately the same amount as the change in the assimilation data set (cooling of 0.5°C), for the same sections in the $EXDOM_{\gamma=360}$ run (Figure 7.10).

On the shelf the temperature changes at the bottom of the water column are also similar in magnitude to the change in the temperature in the assimilation data set. The exception to this trend is at the bottom on the western side of Section D (Figure 7.21c), here the temperature change is a cooling of ~0.2°C. The remainder of the water column is cooler by ~0.4°C. The most important feature on the temperature structure on the shelf can be seen in Section D. The intermediate waters in the shelf form a cold core, which appears biased towards the western or outflow side of the ice shelf. It is difficult to attribute the formation of all this cold water to outflow from the ice shelf, but given the weak assimilation used, it is probably the dominant contributer to the cold core.

In the cavity under the ice shelf, where no assimilation is applied, the changes in the temperature in the assimilation data have a marked impact. In all three sections in the cavity the water away from the ice shelf is cooler, with the warmest waters close to the ice front cooling by ~0.5°C. In the interior of the cavity the bottom of the water column cools by ~0.3°C.

The change in the temperature has a marked impact on the structure of the water column, as the temperature gradient between the ice shelf and the warmest inflow water decreases. In Section A (Figure 7.22a) the most significant change is the disappearance of the steep gradient in the isotherms near the ice front. This is characteristic of a change from a melting regime which was seen in the $EXDOM_{\gamma=360}$ run, to a freezing regime in the $EXDOM_{cool}$ run. In Section B (Figure 7.22b) the cooling changes the structure in the northern half of the section, where the temperature of the intermediate depths is generally homogeneous. In Section C (Figure 7.22c) the water column is also more homogeneous, although the east-west gradient in the isotherm remains. This is a product of the cooler waters from near the southern grounding line flowing out through the eastern side of the Main Gyre.

Cooling the assimilation data set by 0.5°C has a noticeable impact on the temperatures both in the cavity and in the open ocean. The changes in the ice shelf cavity are of particular importance, since the temperatures found in the $EXDOM_{cool}$ run are closer to those found in the cavity model runs, but they are still warmer by ~0.1°C.

7.3 Comparison of model results with observations

In the previous section the results from several model runs were discussed. In this section the model run results are compared with observations in Prydz Bay. The temperature and salinity are first compared over the open ocean domain. This is followed by a comparison between the mass transport in the model and

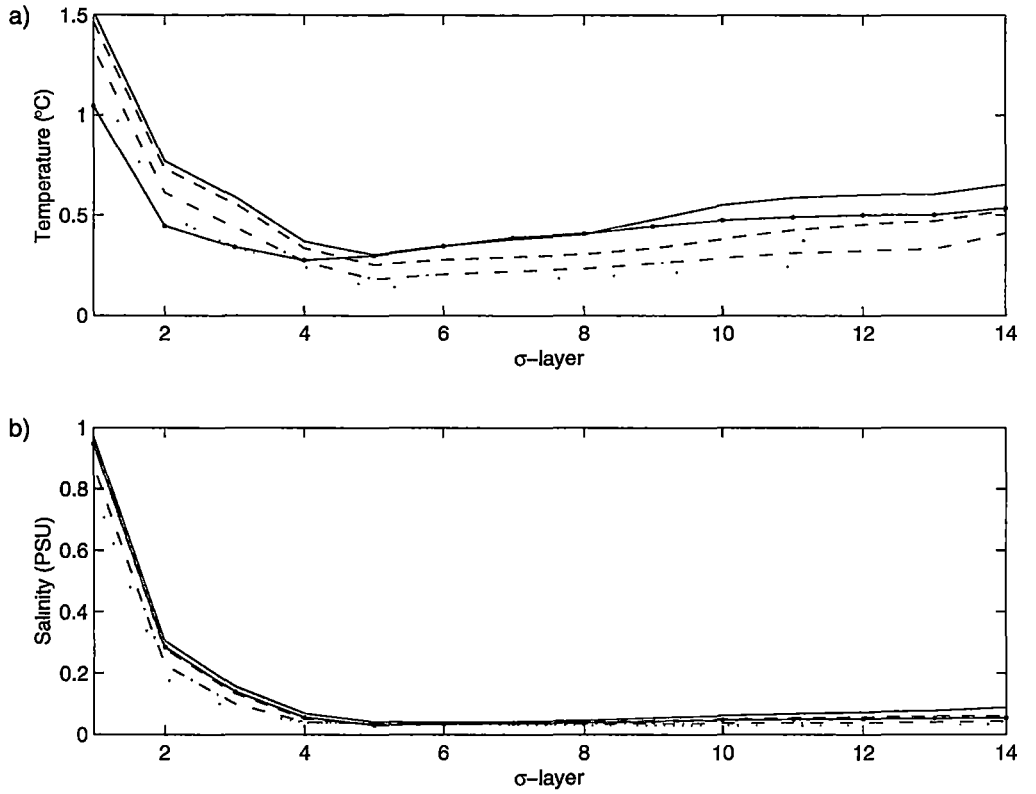

Figure 7.23: RMS differences between the model and the assimilation data set. a) temperature and (b) salinity. The solid line is from the $\text{EXDOM}_{\text{basic}}$ run, the dashed line is from the $\text{EXDOM}_{\gamma=360}$ run, the dash dot line is from the $\text{EXDOM}_{\gamma=100}$ run, the dotted line is from the $\text{EXDOM}_{\gamma=50}$ run, and the solid line with dots is the $\text{EXDOM}_{\text{cool}}$ run.

the transport through several CTD sections, and a comparison between the model velocities and current meter observations.

7.3.1 Temperature and salinity distribution

To compare the model results with ocean observations, the data set used in the assimilation scheme is utilised. This is used as a proxy for comparing the model results with the FISHOG data set, as it has the advantage of being able to be used in point by point comparisons over all of the open ocean domain. In addition, comparing the model with the assimilation data set allows the effectiveness of the assimilation scheme to be quantified.

To compare the model results and assimilation data the differences between the model results and observations were taken. The root-mean-square (RMS) differences and the mean differences were calculated for each of the model runs. The results for each model σ-level are presented in Figure 7.23 for the RMS differences and Figure 7.24 for the mean differences (model minus observations). The results for the $\text{EXDOM}_{\frac{1}{2}\tau}$ and $\text{EXDOM}_{\tau=0}$ runs have not been included, as the RMS and mean differences are similar to the $\text{EXDOM}_{\gamma=360}$ run. The difference between the assimilation data set and the model results

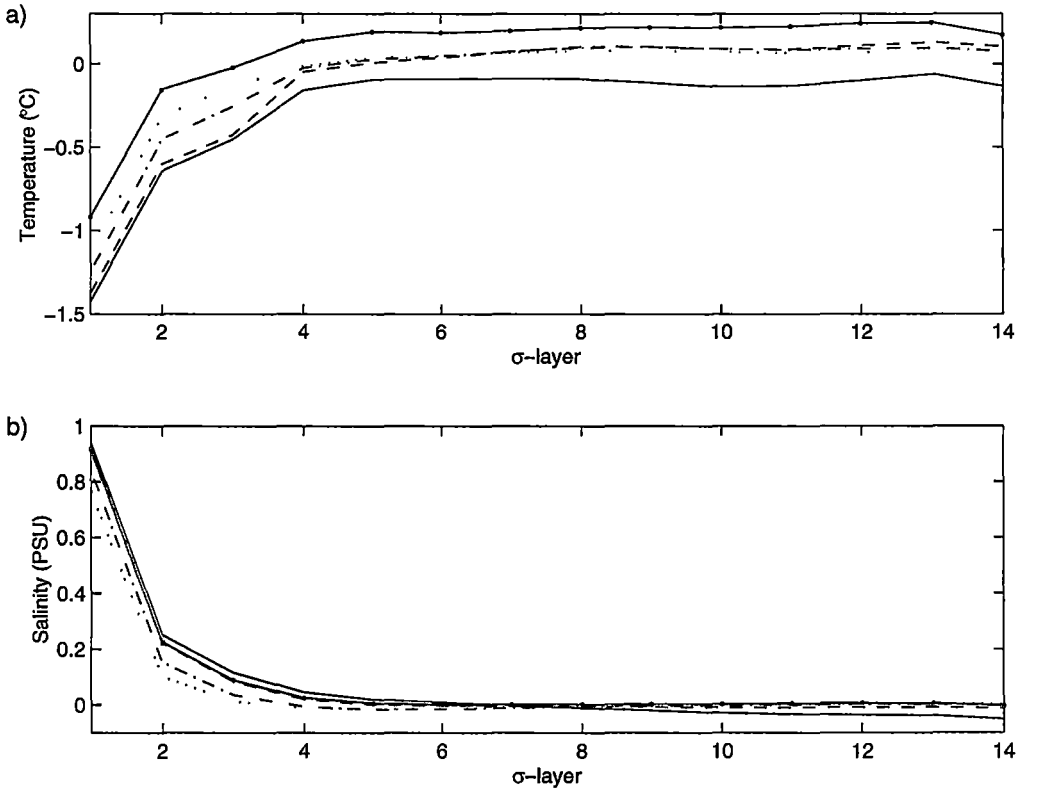

Figure 7.24: Mean differences between the model and the assimilation data set. a) temperature and (b) salinity. The solid line is from the $EXDOM_{basic}$ run, the dashed line is from the $EXDOM_{\gamma=360}$ run, the dash dot line is from the $EXDOM_{\gamma=100}$ run, the dotted line is from the $EXDOM_{\gamma=50}$ run, and the solid line with dots is the $EXDOM_{cool}$ run.

for the $EXDOM_{cool}$ run is found using the cool assimilation data set which was used in the $EXDOM_{cool}$ run.

In the assimilation runs and the $EXDOM_{basic}$ run the best agreement (minimum RMS difference) for both the salinity and temperature was found between σ-layers 4 to 8. Below this the salinity differences are much smaller than the temperature differences.

The mean differences for all the assimilation runs are very similar between σ-levels 4 and 14 (Figure 7.24). The model temperatures are warmer by $\sim$0.1°C. The difference in the salinity is much smaller with almost no variation. This contrasts with the $EXDOM_{basic}$ run where the mean model temperatures are cooler by $\sim$0.3°C.

In the $EXDOM_{cool}$ run there is little difference in both the RMS and mean difference in the assimilation of the salinity from the other model runs. The change in the temperature in the assimilation data set (cooling by 0.5°C) does change the effectiveness of the assimilation scheme. For the $EXDOM_{cool}$ run the assimilation of temperature into the model is worse in the lower layers than in the $EXDOM_{\gamma=360}$ run. The mean difference in each layer has the model warmer by $\sim$0.2°C in the lower layers.

The poor agreement in the upper layers of the model is most likely to be

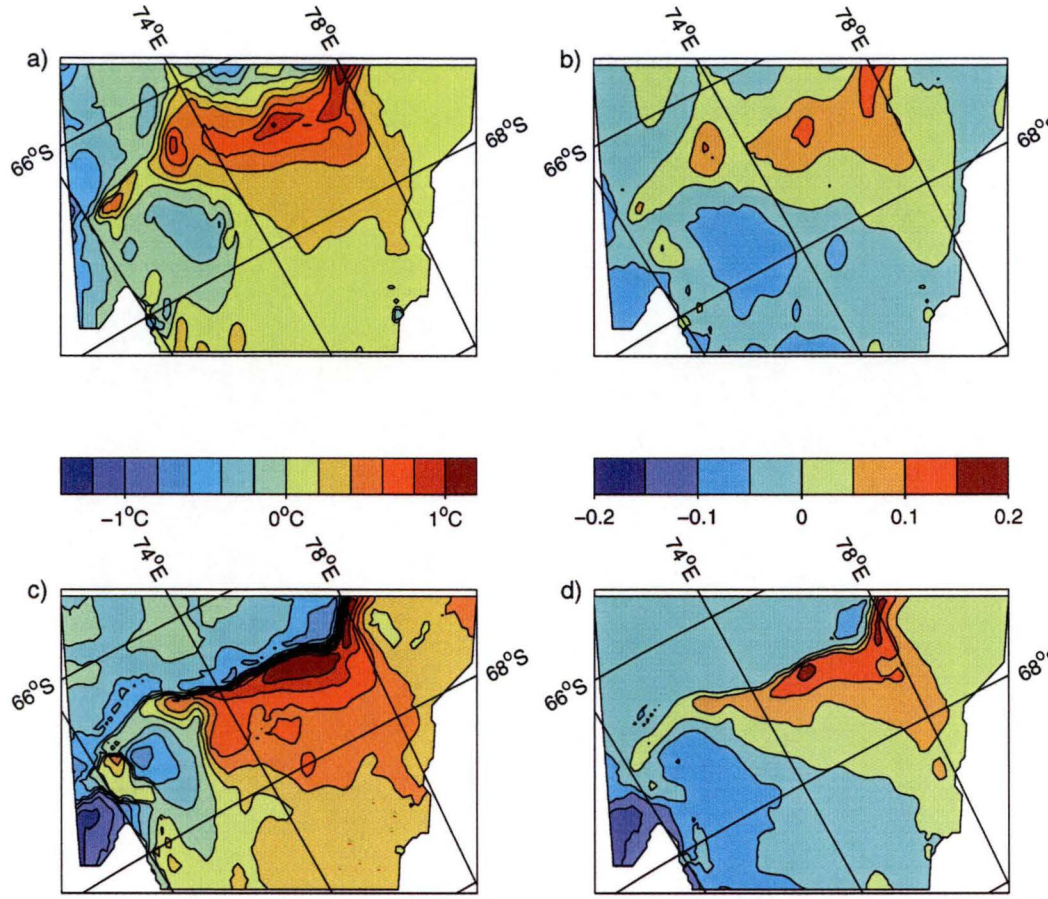

Figure 7.25: Temperature (°C) and salinity (PSU) difference fields between the $\text{EXDOM}_{\gamma=360}$ run results and the assimilation fields, for a) temperature on σ-level 8, b) salinity on σ-level 8, c) temperature on σ-level 12, and d) salinity on σ-level 12. For each figure only the open ocean part of the domain is shown.

from poor representation of processes occurring at the surface, in particular the simple parameterisation for heat and salt flux at the surface boundary between the atmosphere and the ocean. The mean differences shown in Figure 7.24 indicate the model temperatures in the upper layers are too cold and the model salinities are too saline. This suggests there is some conflict between the assimilation scheme and the model surface boundary conditions.

The results shown in Figures 7.23 and 7.24 do not indicate the spatial variation of the difference between the model results and the assimilation data set. In Figure 7.25 the differences between the model results and the assimilation field are shown for both temperature and salinity on σ-levels 8 and 12 for the $\text{EXDOM}_{\gamma=360}$ run. These levels are chosen as they lie in the range of σ-levels on which interaction with the ocean cavity is found.

On each σ-level the largest differences in both temperature and salinity occur in the same locations, suggesting the same processes are affecting the temperature and salinity differences. On σ-level 8 (Figures 7.25a and 7.25b) the largest positive difference, i.e., model results are warmer or saltier than observations, occurs over the Four Ladies Bank. The largest negative difference

in both the temperature and salinity occurs along the western boundary of the model. This is most likely related to the inability of westward flowing currents to leave the model domain. On σ-level 12 (Figures 7.25c and 7.25d) the largest negative difference is also on the western boundary, but it is instead constrained to the south of Fram Bank and west of Cape Darnley. The largest positive difference is on the Four Ladies Bank, although on the northern side the difference field has a sharp gradient in the same location as the continental slope.

The consistently large differences over the Four Ladies Bank appear to be related to the bathymetry. There are two likely reasons for the large differences, these are: the shallower bathymetry, as this could be more easily effected by the parameterisation of the surface boundary conditions; and the excessive mixing of shelf and off shelf waters in this region

Close to the ice front there are differences in the two levels. Both the temperature and salinity on σ-level 8 are homogeneous along the ice front. The model temperature is $\sim$0.1°C warmer than the assimilation data set; the salinity is fresher by $\sim$0.05 PSU. In contrast σ-level 12 has a distinct difference between the east and the west, with the division at approximately 72°E. This is about where the streamfunction (Figure 7.7) suggests the division between inflow and outflow lies. The temperature difference on the eastern side is $\sim$0.3°C. On the western side there is almost no difference between the model results and the assimilation data set. The salinity difference has the same trend along the ice front, on the eastern side it has a difference of $\sim$-0.025 PSU, and on the western side the difference is $\sim$-0.075 PSU.

The pattern of behaviour of the temperature and salinity differences between σ-level 8 and σ-level 12 along the ice front can be attributed to a greater production of ISW in the model than the observations would suggest. An increase in the production of ISW under the ice shelf could only be removed by an increase in velocities, an increase in the thickness of the ISW layer as it leaves the ice shelf, or a combination of both. A thicker ISW layer in the model would lead to negative differences between the model temperature and salinity and the assimilation data set on deep model layers. No difference would necessarily be found on the shallower layers as ISW outflow is anticipated there.

In Figure 7.26 the temperature and salinity on the σ-levels which interact with the ocean cavity are shown (σ-levels 5 to 14) for each of model runs, $\text{EXDOM}_{\gamma=360}$, $\text{EXDOM}_{\gamma=100}$, $\text{EXDOM}_{\gamma=50}$, and $\text{EXDOM}_{\text{cool}}$. In each TS-plot in the figure there are substantial differences between the model results and the observationally based assimilation data set. The $\text{EXDOM}_{\gamma=50}$ and $\text{EXDOM}_{\gamma=100}$ runs appear to have been more successful in reproducing the distribution of water masses close to the ice front. In the temperature and salinity plots for these runs (Figures 7.26b and 7.26c) the model results appear to be offset from the observations. In comparison the temperature and salinity distributions for the $\text{EXDOM}_{\gamma=360}$ run (Figure 7.26a) show no clear relation to the observation data set, nor do they contain the saltiest and coldest water in the observation data set.

In Figure 7.26d, where the comparison between the $\text{EXDOM}_{\text{cool}}$ results and

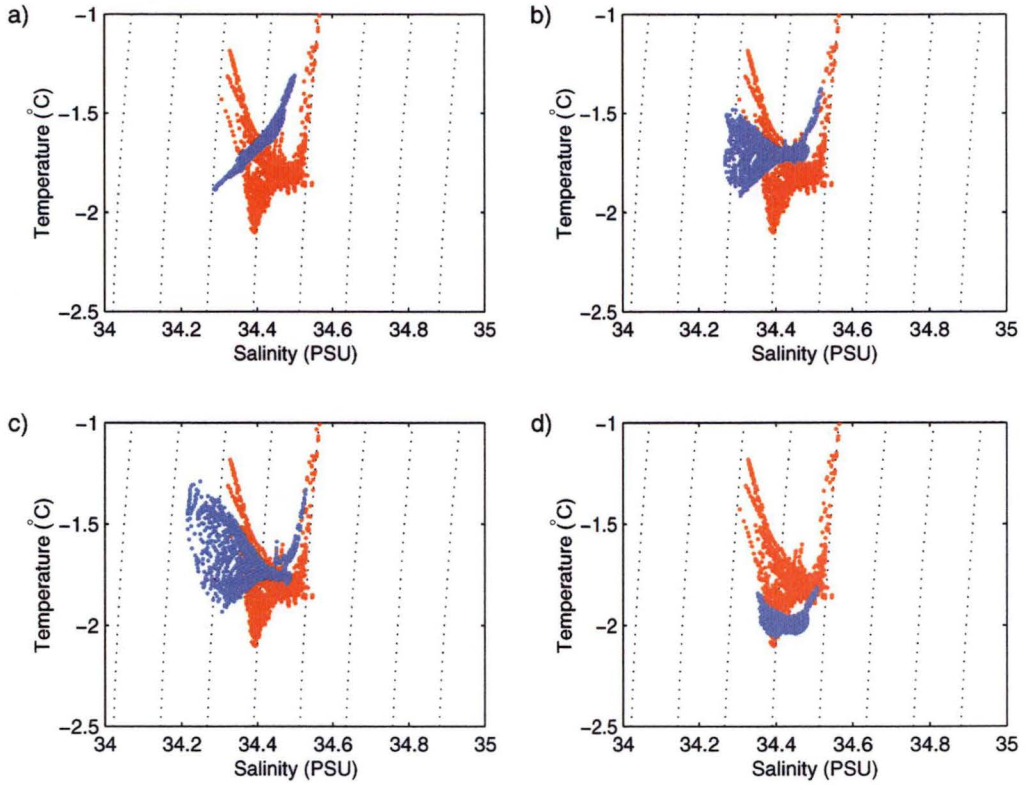

Figure 7.26: Temperature-salinity plots showing the assimilation (red) and model results (blue) for σ-levels 5 to 14 in the three model rows north of the ice front. a) EXDOM$_{\gamma=360}$, b)EXDOM$_{\gamma=100}$, c) EXDOM$_{\gamma=50}$, and d) EXDOM$_{\text{cool}}$. Note the original assimilation data set is shown in d) rather than the modified assimilation data set used in the model run.

the assimilation data is shown, the original assimilation data set is shown rather than the cooled assimilation data set used in the EXDOM$_{\text{cool}}$ run. One of the reasons for cooling the waters in the assimilation data set in the EXDOM$_{\text{cool}}$ run, was to try and produce waters along the ice front which were closer to those found in the observational data set. The comparison shown in Figure 7.26d shows the water along the ice front is both cooler and saltier than that found from decreasing the assimilation time scale. However, the range of temperatures along the ice front is less, with no water greater than surface freezing found in the EXDOM$_{\text{cool}}$ temperatures. The water masses found at the ice front may therefore be indicative of winter conditions.

7.3.2 Currents

In their analysis of the FISHOG data set, Wong et al. [1998] found three distinct east-west current systems in the region covered by the present model domain. These current systems were found by calculating the east-west transport through the north-south FISHOG CTD transects (Figure 3.1). Along the continental slope there is a westward flowing current with a transport of $\sim$0.23 Sv. On the continental shelf they found a westward flowing current between

Table 7.1: Transport estimates for the coastal current. The westward transport is in Sverdrups, where 1 Sv = 1×10^6 m^3s^{-1}.

Transect	B (78°E)	C (75.5°E)	D (73°E)	E (70.5°E)
Wong et al. [1998]	0.2	0.8	1.0	0.2
$EXDOM_{\gamma=360}$	0.4	1.2	0.5	-0.2
$EXDOM_{\gamma=100}$	0.6	1.7	0.5	-0.3
$EXDOM_{\gamma=50}$	0.6	2.0	0.4	-0.3
$EXDOM_{basic}$	0.3	0.9	0.5	-0.1
$EXDOM_{\tau=0}$	0.4	1.1	0.3	-0.2
$EXDOM_{cool}$	0.4	1.1	0.3	-0.1

the coast and 68°S. Also on the shelf, but between 66.5°S and 68°S they found an eastward flowing current, which with the coastal current formed the Prydz Bay Gyre. Wong et al. [1998] made no estimates of the transport in the Prydz Bay Gyre, or the transport of the eastward current on the shelf. They did make several estimates of the transport of the westward flowing coastal current. The transports through the four sections which lie in the model domain are shown in Table 7.1, along with the transports along the same sections from the model runs.

The transports from the model runs, which are shown in Table 7.1, are calculated by finding the maximum transport closest to the coast along the latitudes for each transect. In calculating the transport on Transects C, D, and E, it was assumed that the transport at the ice front was zero. This is the assumption made by Wong et al. [1998] in their calculations. On Transect B the transport at the coast is referenced to zero by the boundary conditions.

The two most noticeable discrepancies between the model results and the transport calculations of Wong et al., are the shift of the maximum transport from being on Transect D to Transect C, and the sign change in the transport on Transect E. The discrepancy in the transect with the maximum transport is most likely because the bulk of the flow under the ice shelf occurs between Transects C and D (see for example Figure 7.13). The calculation of the transport along Transect E, which lies between the ice front and Cape Darnley, is complicated by the proximity of the transect to the coast. Another factor likely to skew any calculation of the transport along Transect E is that most of the transport in the model in the region of the transect is north-south rather than east-west (see for example Figure 7.13).

To calculate the transport in the current along the continental slope, the difference in the streamfunction between the 800 m and 1600 m isobaths was calculated. These contours were chosen as they both occur only on the shelf slope and approximately define the top and bottom of the slope. In the different model runs a consistent slope current was not found. This is largely because of the variations in the gyres structure to the north of the shelf break. In two model runs ($EXDOM_{basic}$ and $EXDOM_{\gamma=100}$) there is a consistent current with

Table 7.2: Current meter monthly statistics for February and March 1985 [Hodgkinson et al., 1988]. The mean is shown with the standard deviation in parenthesis. Mooring A was situated at 66.77°S 72.95°E and Mooring B at 68.52°S 76.49°E (Figure 7.2).

	February		March	
Depth (m)	Speed (cms^{-1})	Direction (°)	Speed(cms^{-1})	Direction (°)
Mooring A				
117	17.3 (7.9)	210 (71)	14.2 (6.3)	215 (71)
263	16.8 (7.3)	219 (100)	14.6 (6.1)	217 (101)
472	17.0 (7.0)	226 (96)	14.3 (6.8)	215 (100)
Mooring B				
150	6.2 (3.8)	150 (85)	5.7 (3.3)	146 (85)
296	4.3 (2.3)	125 (72)	4.4 (2.7)	126 (59)
487	4.5 (2.9)	168 (98)	5.8 (3.4)	142 (94)
640	4.7 (3.1)	200 (77)	6.5 (4.0)	145 (77)

a similar magnitude (0.23 Sv) to that reported by Wong et al. [1998], however, it flows in the opposite direction. In the other model runs a westward transport between the western boundary and the sill between the Four Ladies and Fram Banks which peaks at ~0.2 Sv was found. To the east of the sill the transport was eastward at up to ~0.5 Sv.

Three sets of current meters have been successfully deployed and retrieved in Prydz Bay [Hodgkinson et al., 1988, 1991a, 1991b]. The current meters were deployed from January 1985 to January 1986 [Hodgkinson et al., 1988], from January 1986 to February 1987 [Hodgkinson et al., 1991a], and March 1987 to February 1988 [Hodgkinson et al., 1991b]. In most cases moorings were redeployed in approximately the same location as the previous deployment. This allows the current meter results from the successfully retrieved meters to be formed into two groups by their location. Within each location the current meters showed the same trend in speed and direction between the different deployments, so here only the results from February and March 1985 are considered. At this time Mooring A was situated at 66.77°S 72.95°E, and Mooring B was situated at 68.52°S 76.49°E. The locations of the moorings relative to the bathymetry are shown in Figure 7.2.

Summary statistics are shown in Table 7.2 for the current meters on each mooring for February and March 1985. At both moorings the current meters show reasonable agreement for speed and direction over all depths for both months. This suggests the velocity at each current meter site is essentially barotropic. Hence the barotropic velocities from the model can be easily compared with the mean speed and direction from the current meters. The barotropic velocity components in the model are found from the derivative of the streamfunction (Equations 4.23 and 4.24). The speeds and directions for several model runs are presented in Table 7.3. Also shown are the mean speed

Table 7.3: The barotropic velocity at the current meter sites A and B. The mean observations are derived from Table 7.2. Direction is found clockwise from true north.

	Mooring A		Mooring B	
	Speed (cms^{-1})	Direction (°)	Speed(cms^{-1})	Direction (°)
Mean Obs.	15.7	218	5.3	150
$EXDOM_{\gamma=360}$	0.1	28	3.1	81
$EXDOM_{\gamma=100}$	0.5	121	4.5	83
$EXDOM_{\gamma=50}$	0.1	242	5.0	81
$EXDOM_{basic}$	0.3	330	1.8	60
$EXDOM_{\tau=0}$	0.5	111	2.5	71
$EXDOM_{cool}$	0.8	119	2.7	78

and direction for each mooring calculated over both months.

The agreement between the model results and the observations at Mooring A is not favourable. The variation in the directions from the different model runs, and the low velocity suggests the mooring is located in an area of weak flow in the model domain. The observations, however, clearly indicate the current meter is situated in an area of strong consistent flow. Mooring A is located in the middle of the sill between Fram and Four Ladies Bank. This is in an area where the model is possibly giving unrealistic results because of the influence of the circulation off the continental shelf. The poor results from the comparison further support the concept that the results of the model north of the shelf break are unrealistic.

The comparison at Mooring B is more favourable. The directions are within one standard deviation of the mean direction at each current meter, and the model speeds are comparable to those recorded by the current meters. Given the mooring is a series of spot measurements and that the model grid box area is still relatively large in comparison, this may be considered as fair agreement between the model and the current meter observations at Mooring B.

7.4 Ice shelf basal mass balance

Several estimates of the basal component of the ice shelf mass balance for the extended model runs discussed in this chapter are presented in Table 7.4. The format of the table is the same as for similar tables presented in previous chapters. The majority of the ice mass loss rates from the ice shelf are much higher in the extended domain model, than for either previous modelling studies (excluding ocean warming scenarios), or from observationally based estimates. The exception to the results shown in Table 7.4 is the $EXDOM_{cool}$ run. It has values similar to those found for present conditions in other models. The net loss of ice in the $EXDOM_{cool}$ run also falls within the range of values found by Wong

Table 7.4: Mass balance estimates for the extended domain model runs.

Extended Model Run (EXDOM)	Mean Rates for Freezing Zone (ma^{-1})	Mean Rates for Melting Zone (ma^{-1})	Mean Rates for Whole (Loss) (ma^{-1})	Area of Melt (%)	Mass Change Rates Freezing (Gta^{-1})	Mass Change Rates Melting (Gta^{-1})	Mass Change Rates Net Loss (Gta^{-1})
γ=360	0.60	1.81	1.44	84.7	4.2	70.2	66.0
γ=100	0.60	1.76	1.40	84.8	4.2	69.3	65.1
γ=50	0.63	1.84	1.46	84.4	4.6	71.3	66.7
basic	0.56	1.79	1.41	83.8	4.2	68.9	64.7
τ=0	0.63	1.90	1.51	84.4	4.5	73.6	69.1
cool	0.33	0.56	0.38	77.8	3.3	20.9	17.6

Note: The total area of the ice shelf is 5.6 x 10^4 km^2.

et al. [1998].

There are two factors acting for the increases in net ice loss from the ice shelf found in all the models shown in Table 7.4 except the $EXDOM_{cool}$ run. These are an increase in melting rates, and an increase in the area where melting occurs. Of these the increase in melting rates is the dominant effect. In the assimilation model runs where the waters in the cavity are cooler, e.g., the $EXDOM_{\gamma=50}$ run, the increased strength of the circulation compensates for the cooler temperatures, leading to the overall heat flux being similar.

The impact of the increase in melting can be seen in Figure 7.27, which shows the melting and freezing rates in the ocean cavity for the $EXDOM_{\gamma=360}$ run. The melting and freezing rates shown in this figure are typical of those for all the extended domain studies except the $EXDOM_{cool}$ run. The melting and freezing rates for the $EXDOM_{cool}$ run are shown in Figure 7.28. In both Figure 7.27 and Figure 7.28 there are two noticeable changes in the melting and freezing rates. The first is the increase in the melting rates around the Central Grounding Zone and to the south along the eastern grounding line. The second is the patch of melting along the ice front. In the $EXDOM_{\gamma=50}$ run the melting along the ice front accounts for 19 Gta^{-1} of net loss. In the ocean cavity models discussed in Chapter 5, any melting in these areas was usually very low (see for example Figure 5.20).

The distinct difference in the melt rates between the $EXDOM_{cool}$ run and the other runs, shows that the melting rates at the ice shelf-ocean interface have been seriously impacted by the additional heat from the warmer water in the ocean cavity.

7.5 Discussion and conclusions

In the studies presented in this chapter the numerical model domain was expanded to include Prydz Bay, part of the continental slope, and the abyssal plane to the north of Prydz Bay, in addition to the ocean cavity under the

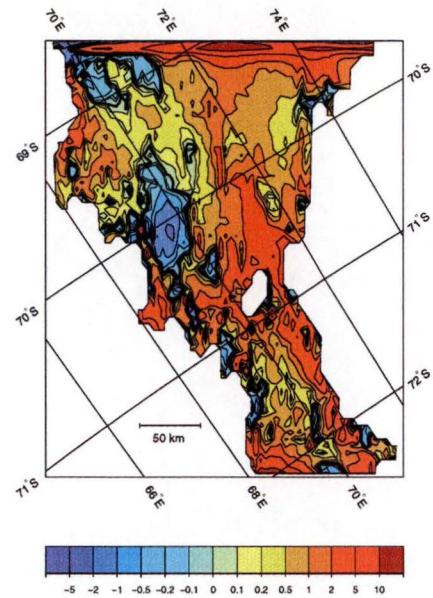

Figure 7.27: Melting (+) and freezing (-) rates for the $\text{EXDOM}_{\gamma=360}$ run in ma^{-1}. The bold contour denotes the boundary between melting and freezing.

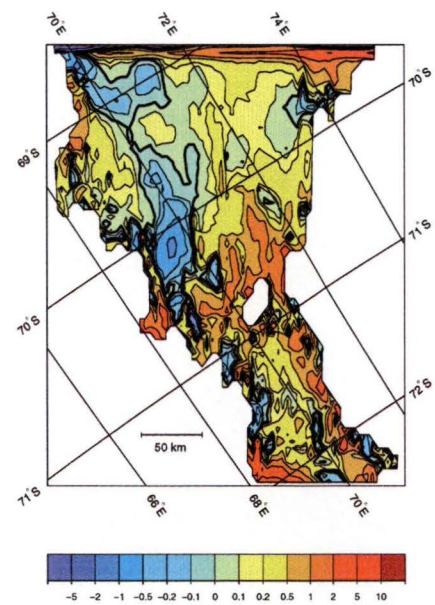

Figure 7.28: Melting (+) and freezing (-) rates for the $\text{EXDOM}_{\text{cool}}$ run in ma^{-1}. The bold contour denotes the boundary between melting and freezing.

Amery Ice Shelf. The main aim of extending the model domain was to remove the requirement of specifying the exchange of mass, heat and salt at the ice front through boundary conditions on the cavity model. For this aim to be achieved the flow across the ice front, and the temperature and salinity on the open ocean side of the ice front generated by the model have to be realistic.

The large scale circulation features in Prydz Bay appear to be reasonably well reproduced by the different models runs. The exception to this is the circulation to the north of the shelf break (~67.0°S). Here the strong influence of the bathymetry on the circulation, and the proximity of the model boundaries, led to topographically restricted gyres which were not consistent with the known circulation in this region. This was made clear by comparing the model results to the current meter mooring (Mooring A) situated near the continental slope, and by comparing the slope current in the model with that calculated by Wong et al. [1998]. None of the model results agree well enough with either set of observations.

On the shelf the circulation involved in the Prydz Bay Gyre appears realistic, although there is no observational data to confirm the circulation found on the outer part of the shelf. Close to the coast the model reproduced the westward flowing coastal current. The general strength and direction of the current in this part of the gyre had some consistency with current strength and direction observations from a mooring positioned at 68.52°S 76.49°E (Mooring B). In comparing the circulation with the analysis of Wong et al. [1998], it was noted the transect upon which the maximum transport was found was different in the model. Wong et al. found the maximum in the circulation along Transect D (73°E), however, in all the model runs the maximum transport was found along Transect C (75.5°E). Despite the discrepancy with the results of Wong et al., the circulation close to the ice front appears to be consistent with observations.

Comparison of the temperature and salinity between model results and observations at the ice front showed a marked difference. In Figure 7.26 the temperature and salinity in the $EXDOM_{\gamma=360}$, $EXDOM_{\gamma=100}$, and $EXDOM_{\gamma=50}$ runs, were shown to be warmer and fresher than the assimilation data set. The difference between the assimilation data set and the model results reduces with decreasing values of the assimilation time constant (γ). The change in the temperature and salinity characteristics along the ice front markedly impacted on the temperature and salinity found in the ocean cavity. This was confirmed in the $EXDOM_{cool}$ run, where cooling the temperature of the assimilation data set by 0.5°C, or to the surface freezing point, changed the characteristics of the water masses along the ice front (Figure 7.26d). This in turn reduced the temperatures found in the ocean cavity.

The warm waters at the bottom of the water column adjacent to the shelf are caused by the excessive mixing of the warm waters off the continental shelf into the waters circulating in the Prydz Bay Gyre. The movement of the warm Circumpolar Deep Water onto the shelf is driven by the anomalous circulation to the north of the continental shelf. The trapped gyres in this part of the domain cause the warm water to rise above the top of the continental slope (see for example Figure 7.14), where it is then able to mix more easily with the shelf

waters.

The impact of the warmer and fresher waters in the $EXDOM_{\gamma=360}$ run, the $EXDOM_{\gamma=100}$ run, and the $EXDOM_{\gamma=50}$ run were seen in the mass balance estimates for the Amery Ice Shelf (Table 7.4). The net ice loss from these runs is outside the range of the mass loss estimated by Wong et al. [1998] and it is equivalent to the mass lost in an ocean climate warming of between 2°C and 3°C, using the results found in Chapter 6. The net loss from the $EXDOM_{\gamma=360}$, $EXDOM_{\gamma=100}$, and $EXDOM_{\gamma=50}$ runs was significantly different from the mass lost from the $EXDOM_{cool}$ run, which was within the range of net basal mass loss estimated by Wong et al. [1998]. The mass loss in the $EXDOM_{\gamma=360}$, $EXDOM_{\gamma=100}$, and $EXDOM_{\gamma=50}$ runs was similar (Table 7.4), despite a cooling of the water in the cavity with stronger assimilation. This occurred as the transport tended to increase, keeping the heat flux across the ice front constant.

The results from the cooling of the assimilation data set in the $EXDOM_{cool}$ run have an effect on the water column similar to what might be expected to occur in winter. This is because in winter extensive sea ice formation would lead to the formation of large amounts of cold and salty water on the continental slope as found in the $EXDOM_{cool}$ run.

The lack of success of the assimilation scheme in generating the water masses observed in the FISHOG data set along the ice front, is the most likely reason for the inability of the model to realistically estimate the basal component of ice shelf mass balance. It appears it may be necessary to have sea ice and deep mixing for cooling the deeper water. To test this hypothesis three model runs with a simple sea ice model in place of the restoring boundary condition over the open ocean were later carried out. The results of these studies are presented in Appendix C. It was expected the introduction of a sea ice model would prevent the influx of warm Circumpolar Deep Water from off the shelf. This was not found to be the case, except when the extended domain model was run in a closed mode, with no heat or salt exchange across the northern boundary or assimilation of temperature or salinity.

In other applications of this model to extended domains, both Grosfeld et al. [1997] and Grosfeld and Gerdes [1998] found basal mass loss rates which were consistent with ice shelves remaining in a steady state. In Grosfeld and Gerdes [1998] model domain, no abyssal ocean was included and the water masses present were no warmer than -1.9°C. Hence, it is unlikely that the model would evolve with large amounts of ice being melted at the base of ice shelf. Grosfeld and Gerdes found the amount of ice lost from the base of the ice shelf increased in their warming scenario, where they increased the temperature of the waters accessing the domain by 0.6°C. The increase in temperature increased the mean amount of melting found by Grosfeld and Gerdes from 0.35 ma^{-1} to 0.71 ma^{-1}.

In Grosfeld et al. [1997] one of the theoretical domains they considered included an extensive abyssal ocean with a depth of 2000 m, which spanned a latitude range of 5°. In the abyssal ocean the water mass characteristics were similar to those found to the north of the shelf break in the model results presented here. However, instead of the warm water masses mixing on to the

continental shelf and warming the water interacting with the ocean cavity, two strong fronts on the continental shelf restricted the water masses which came into contact with the ocean cavity. These fronts appeared to be formed by strong vertical mixing, most likely convective adjustment, driven by salt rejection from the one-dimensional thermodynamic sea ice model used by Grosfeld et al. [1997] in that model scenario.

Oceanographic observations under other ice shelves [e.g., Jacobs et al., 1979; Nicholls et al., 1991] indicate that HSSW is the significant water mass found in ocean cavities. There is little to suggest the ocean cavity under the Amery Ice Shelf should be any different. Hence the failure of the assimilation scheme in the extended domain model runs to generate HSSW or a similarly cold water mass at the ice front is of concern. The most likely reason for the models inability to produce the needed water masses arises from running the model in a summer only scenario. The warm water at the surface in the assimilation data set, will stop freezing occurring at the sea surface. With no freezing, cold saline waters do not form. This is supported by the $\text{EXDOM}_{\text{cool}}$ run. In the $\text{EXDOM}_{\text{cool}}$ run changing the temperature cooled the waters at the ice front, and reduced the mass loss from the ice shelf.

Current meter deployments in the vicinity of Prydz Bay [Hodgkinson et al., 1988, 1991a, 1991b] show seasonal variation in the temperature, but the small number of locations for the current meters and the lack of salinity observations makes extrapolating their trends to all of Prydz Bay difficult. To change the assimilation scheme from its summer only configuration, ocean observations in winter would be required. Ideally, these would have spatial coverage similar to the FISHOG observations.

An alternative method of improving the model results is to modify the model boundary conditions. Two possible modifications are: changing the surface boundary condition, to reduce the production of cold and fresh water at the top of the water column, although something more than a simple sea ice model is needed (Appendix C); and removing the closed boundaries on the east and west sides of the open ocean domain, this could allow a more realistic flow to the shelf break to develop. The change to the model most likely to bring an immediate improvement is to move the northern boundary of the model on to the shelf. This could be done, so it does not impinge on the Prydz Bay Gyre. The benefits of this would be to remove the part of the domain where the warm waters to the north of the shelf are introduced. This should prevent warm water encroaching onto the shelf.

One of the potential uses of the results from the extended domain model runs is to generate velocity and tracer fields at the ice front, which might be used to drive the cavity only model. Although the results presented in this chapter are not an accurate representation of the circulation in Prydz Bay, it is still possible to compare the results in the cavity from extended domain models with cavity model results. A preliminary attempt at this is presented in Appendix D.

The results in this chapter provide some insight into the ocean circulation and interconnection between Prydz Bay and the ocean cavity under the Amery Ice Shelf. From the results it is clear further work is required to clarify the

movement of heat, salt, and mass between Prydz Bay and the ocean cavity. To improve the results of the extended domain model runs there are several possible options. These include changes to the model and modification of the assimilation data set by including additional observations.

Chapter 8

Summary, conclusions and outlook

Numerical models currently provide the principal approach for studying the ocean cavities under an ice shelf. In this study two models were used to simulate the ocean cavity under the Amery Ice Shelf, with the aim of describing the present ocean circulation and mass exchange with the ice shelf. In addition, a predictive study of the impact of ocean climate change on the ocean cavity and the basal mass balance of the Amery Ice Shelf has been presented.

In the early chapters background information to the thesis was provided. This included a discussion of previous modelling studies of ocean cavities under ice shelves (Chapter 2), a summary of the oceanography of Prydz Bay and the glaciology of the Amery Ice Shelf (Chapter 3), and a description of the model, the boundary conditions used and the model domain (Chapter 4).

The main results and analyses of the studies presented have been divided into three chapters. Two of the chapters (Chapters 5 and 7) focused on describing the present ocean circulation, the temperature and salinity distribution, and the mass exchange between the ice shelf and the ocean. The third chapter (Chapter 6) focused on assessing the impact of several different climate change scenarios on the mass balance of the Amery Ice Shelf, the distribution of temperature and salinity, and the ocean circulation within the ocean cavity under the Amery Ice Shelf.

The main chapters have been supplemented by five appendices. In the first of these (Appendix A) details are provided on the method used to calculate the marine ice layer thicknesses. The second appendix (Appendix B) examined an alternative choice of boundary condition at the ice-ocean interface, and assessed what affect a different parameterisation of ice-ocean boundary conditions has on the temperature and salinity distribution and the basal mass balance. In Appendix C a simple sea ice model was introduced in the extended domain model, with the aim of generating realistic water masses within Prydz Bay. Two attempts to use results from an extended domain model run to drive a cavity only model were made in Appendix D. In the last appendix (Appendix E) a simple attempt was made to quantify the possible affect that an expansion of the ocean cavity to the south, under the Lambert Glacier, would have on melting and freezing within the model domain.

Two different model domains were used in the studies. In Chapters 5 and 6, and Appendices B, D, and E the model domain was restricted to the ocean cavity under the Amery Ice Shelf. The flow in and out of the cavity was controlled by the parameterisation of the boundary conditions at the ice front. In Chapter 7 and Appendix C the model domain was expanded to include Prydz Bay. The primary aim of using the extended model domain was to allow the flow between the ocean cavity and the open ocean to evolve in a manner compatible with the hydrographic data over the whole Prydz Bay region, rather than to be prescribed by boundary conditions at the ice front.

8.1 Ocean Circulation

The general pattern of the ocean circulation found under the Amery Ice Shelf was reasonably consistent in all the studies, but with some variation in the structure and in the strength of the circulation. Differences arose from variations in the flow across the ice front, and from the temperature and salinity distributions at the ice front. The different conditions at the ice front arose, either from the specification of boundary conditions, or from flow evolving at the ice front in the extended domain model.

In the closed boundary, $AIS_{\bar{u},\bar{v}=0}$, $AIS_{P\bar{v}}$(Chapter 5), $AIS_{\gamma=50TS}$, $AIS_{\gamma=50}$ (Appendix D) and extended domain runs (Chapter 7 and Appendix C) the circulation under the ice shelf was dominated by a single large cyclonic circulating gyre, which was named the Main Gyre (see for example Figure 5.6 or 7.12). In contrast the horizontal circulation in the $AIS_{\Psi=0}$ and $AIS_{P\partial\Psi}$ runs (Chapter 5) had two smaller gyres in the same area. These were a cyclonic Central Gyre to the south and an anticyclonic Northern Gyre (see for example Figure 5.9).

The circulation in the remainder of the cavity was similar in both the cavity domain runs and the extended domain runs. The flow across the ice front influenced the gyres south of the Central Grounded Zone, but only with respect to the strengths of the gyres, not their direction or form. The similarity in the circulation was due to the strong influence which the topography had on the horizontal circulation. Both the Central and Main Gyres (depending on which boundary conditions were applied), and the Northeastern Gyre were topographically trapped on most sides, either by basins in the sea bed or ridges in the ice shelf draft.

In Chapter 6 it was shown that changes in the ocean temperature prescribed along the ice front affected the ocean circulation. The relative position and transport of some gyres shifted. The most important change was in the size of the gyres, which increased in area with increased warming. The limit of their extent was only reached in the $AIS_{CS+3.0°C}$ run. In this run the gyres were in some places restricted by the grounding line, rather than the internal topography of the ocean cavity.

For the cavity model it is difficult to decide which parameterisation of the boundary conditions most realistically represents the circulation under the Amery Ice Shelf. This is due largely to the lack of suitable observations for comparative purposes. In Chapter 5 it was argued that any of the $AIS_{\Psi=0}$,

$AIS_{P\bar{v}}$, or $AIS_{P\partial\Psi}$ runs were plausible. This was because they produced reasonable agreement with the available observations, in particular the estimate of the basal component of the ice shelf mass balance.

In the extended domain model runs, the simulated circulation in the open ocean part of the domain was compared with observationally based analyses. To the north of the shelf break (~67°S), where the model was artificially constrained by the boundaries, the model results could not be considered favourable, as here the model circulation consisted of topographically trapped gyres which were inconsistent with observations. The results from the comparison were, however, favourable in Prydz Bay where a relatively independent stationary gyre was found.

8.2 Temperature and salinity distribution

The temperature and salinity structure in the ocean cavity was found to be highly dependent on heat and salt exchange across the ice front. The inflow and outflow components of the heat and salt fluxes across the ice front were each larger than the heat and salt fluxes into or out of the ice shelf. The net flux integrals at the ice front, however, balanced with the net flux integrals at the ice shelf-ocean interface.

The size of the fluxes were dependent on two factors, the time restoring constant and the cross-boundary component of velocity. These two factors affect the exchange of heat and salt in different ways. The specification of the cross-boundary barotropic component of velocity had a greater effect; large velocities at the ice front allowed large amounts of melt-water to be advected out of the domain. This stopped outflowing waters recirculating or mixing with inflowing waters through diffusion. The large velocities also allowed water in inflow regions to move rapidly into the interior of the model, where it influenced the density gradient. The restoring time constant (α) had an effect, because the model was only quasi-stable and some areas of the boundary varied between inflow and outflow. The influence of the restoring time constant was smaller than that of the velocities on the boundary as its influence was restricted to the inflow on the tracer boundary row. However, reducing the restoring time constant increased the restoring of temperature and salinity, which in turn modified the temperature and salinity in the cavity.

The distribution of temperature and salinity may be influenced by the boundary conditions at the ice-ocean interface. This was investigated in Appendix B, where it was found the effect of the ice-ocean boundary conditions on the temperature and salinity distribution in the ocean cavity was limited and less significant than the influence of the various transport boundary conditions at the ice front.

In the climate change scenarios presented in Chapter 6 the temperature and salinity distributions differed within the ocean cavity in each scenario. The temperature in the ocean cavity increased as the temperature at the boundary was increased. The salinity tended to decrease, because the increased melting caused by the warmer waters in the cavity freshened the water column. The

temperature increase would have reduced the stability of the water column, if it was not accompanied by the decrease in salinity. The overall effect was an increase in stratification and a more stable water column (see for example Figure 6.18).

In Chapter 7, with the open ocean domain the water masses flowing into the ocean cavity from Prydz Bay were warmer, by between 0.3°C and 0.6°C, and fresher, by about 0.1 PSU, than for any of the cavity models presented in Chapter 5. The change in the cavity arose because the waters along the ice front were warmer and fresher than the observations. This was despite temperature and salinity observations being assimilated into the model. The inability of the assimilation scheme to reproduce appropriate water masses was attributed to the summer bias of the assimilation data set. The constant summer bias produced warm surface waters which precluded freezing at the ocean surface. With no freezing there was no production of cold and dense shelf waters, such as High Salinity Shelf Water (HSSW). Cold and dense shelf waters, such as HSSW are believed to dominate inflow to ocean cavities. This role is supported by observations in other ocean cavities [e.g., Jacobs et al., 1979; Nicholls et al., 1991] and it is conjectured that the cavity under the Amery Ice Shelf is unlikely to be different.

The absence of adequate deep mixing driven by sea ice formation also allows the entrainment of the warmer, more saline waters north of the shelf break onto the shelf. Attempts to rectify this by introducing a simple sea ice model to replace the previous surface boundary conditions in the extended domain model were not generally successful, primarily because not enough freezing and deep mixing occurred (Appendix C). In the model runs where warm water was able to enter the domain, either via the northern boundary or through assimilation, the ocean cavity temperatures were even warmer than in the corresponding non-sea ice model runs. Overall this suggests that even with a simple sea ice model the extended domain model runs tended to bring water of too high a temperature into the ice shelf cavity.

This was borne out by two different model runs: the $\text{EXDOM}_{\text{cool}}$ run, where the assimilation data set was cooled by up to 0.5°C (Chapter 7); and the $\text{EXDOM}_{\text{SI-closed}}$ run, where the sea ice model was run on a closed ocean domain (Appendix C). In both models the water masses along the ice front and in the ocean cavity were significantly cooler and closer to what is observed near the ice front in Prydz Bay. The cooler water reduced the basal mass loss from the ice shelf from unrealistically high rates to those within the range calculated by Wong et al. [1998]. This suggests that the generation of appropriate water masses in Prydz Bay is a necessary precursor to prevent the entrainment of warm water onto the shelf and for driving realistic circulation and water masses under the ice shelf in the extended domain model. Because of the questionable reliability of the model temperature and salinity results, no precise conclusions can be drawn about the heat and salt transport across the ice front. However, it appears that in the absence of adequate deep mixing from sea ice formation during winter, entrainment of warm water onto the continental shelf could lead to high melt rates under the ice shelf. The model results also show that differ-

ent combinations of circulation and temperature at the ice front can produce similar net melting.

8.3 Ice shelf mass balance

The melting and freezing at the ice shelf-ocean interface was found to be strongly linked to both the shape of the ice shelf draft and the ocean circulation. Of these two factors the horizontal ocean circulation was more important. The homogeneous vertical structure in the horizontal circulation meant the velocities adjacent to the ice shelf were not simply controlled by the combination of buoyancy and the ice shelf draft gradient, as occured in the two models based on the work of Jenkins [1991] (Plume Model, Section 2.3.2) or Hellmer and Olbers [1989] (HO Model, Section 2.3.4).

This control of the flow direction at the ice shelf-ocean interface by the horizontal circulation determined where melting and freezing could occur. For freezing to occur the ice shelf gradient still played an important role, since the direction of flow needed to be upslope. Thus water at the in situ freezing temperature which rose became supercooled because of the pressure change in the in situ freezing temperature. This lead to freezing. For melting the ice shelf draft had little effect. Melting occurred irrespective of the gradient, wherever the water adjacent to the ice shelf was warmer than the in situ freezing temperature.

The rates of melting and freezing also show some sensitivity to the design of the boundary conditions at the ice-ocean interface. In the alternative boundary condition implemented in Appendix B, the extremes of melting and freezing were typically reduced, however, the net basal mass balance of the ice shelf was not greatly effected by varying the parameterisation.

In Section 3.3 the components of the ice shelf mass balance were examined. There it was estimated the mass flux into the ice shelf was 46 Gta^{-1}. This consisted of 23 Gta^{-1} from the Lambert Glacier [Allison, 1979], 14 Gta^{-1} from glaciers feeding the sides of the Amery Ice Shelf [Budd et al., 1967], and 9 Gta^{-1} of snow accumulation on the ice shelf [Budd et al., 1967]. The two components of mass loss from the ice shelf are iceberg calving and basal melting. As discussed in Section 3.3 there are no reliable estimates of the iceberg calving rate at the front of the ice shelf.

In this thesis melting rates for the present were found. These ranged from 5.8 Gta^{-1}, for the $\text{AIS}_{\bar{u},\bar{v}=0}$ run in Chapter 5, to 66.7 Gta^{-1}, for the $\text{EXDOM}_{\gamma=50}$ run in Chapter 7. Most of the ice shelf mass balance rates were similar to the basal mass loss estimates of Wong et al. [1998] and lie between 10.6 Gta^{-1} for the $\text{AIS}_{\Psi=0}$ run and 20.2 Gta^{-1} for the $\text{AIS}_{\text{P}\partial\Psi}$ run.

With basal mass loss rates between $\sim$11 Gta^{-1} and $\sim$20 Gta^{-1} the amount of ice loss by iceberg calving for the ice shelf to remain in mass balance is between 26 Gta^{-1} and 35 Gta^{-1}. This amount of mass loss from the front of the ice shelf appears consistent with glaciological estimates of northward mass flux in the ice shelf based on the velocity and thickness profiles given in Budd et al. [1982] for a survey transect running through G1 (Figure 3.3). Although

this transect is a considerable distance south of the current and historical ice front positions, most of the cavity domain model results show the net amount of melting and freezing between G1 and the model ice front is close to zero.

In the climate change runs a linear rate of change for the net mass loss was estimated at $\sim$22 $Gta^{-1}{}^{\circ}C^{-1}$, with an accompanying change in the mean melt rate of $\sim$0.45 $ma^{-1}{}^{\circ}C^{-1}$. This would indicate significant changes in the mass balance of the ice shelf for relatively small amounts of warming. The uncertainties involved in estimating the components of the ice shelf mass balance make it premature to estimate how small this threshold is.

Recent analysis of the grounding line position of the Amery Ice Shelf, using satellite altimetery and new ice thickness data, suggests that it is further south than assumed in this study [Phillips, 1998]. This expansion of the ocean cavity domain has the potential to impact strongly on the implications of the results of this thesis, particulary on any assessments of the basal component of the ice shelf mass balance. In a simple attempt to quantify the possible effect that an expansion of the ocean cavity would have on melting and freezing, the model domain was expanded to the south (Appendix E). Two experiments on possible expanded cavity domains found that there is little change to the overall ice shelf net loss from melting. This is because the increase in the local mass loss from melting near the new grounding line is compensated by additional freezing further north in the cavity.

8.4 Conclusions and outlook

In any numerical modelling study there are uncertainties which arise from various sources. The largest uncertainties inherent in this study relate to the ice shelf draft and the bathymetry under the ice shelf. The errors in the ice shelf draft come from three sources. The first relates to the ice thickness observations. In these there are substantial gaps and possible observation errors related to poor radio echo-sounding returns in some portions of the ice shelf. The second error source is the interpolation of the ice thickness observations to give an ice thickness at each grid point. The third source of error lies in the assumptions made about the snow-ice density and the firn layer depth. These are used in calculating the draft from the buoyancy and ice thickness. The mean density and firn layer depth were both assumed constant over the ice shelf. The combination of errors over most of the ice shelf is generally less than 10%, but where observations are sparse near the ice front, the errors could be up to 30%. The errors in the bathymetry under the ice shelf could also be of the same magnitude, as the bathymetry was derived from interpolating map contours of bedrock depth which in turn were based on about 63 irregularly spaced spot seismic observations.

The water column thickness is derived from both the ice shelf draft and the bathymetry, and hence accumulates the errors associated with both data sets. Given the strong influence which the water column thickness has on the horizontal circulation, any error in the water column thickness can potentially affect the circulation and mass balance estimates. The overall impact should

be limited, as changes in the water column thickness would tend to shift the location of gyres within the ocean cavity. This would shift the distribution of melting and freezing at the ice shelf-ocean interface, but need not necessarily affect the overall mass balance of the ice shelf.

Some of the errors in the ice shelf thickness come from the radio echo-sounding returns finding the boundary between the meteoric and marine ice, rather than the marine ice ocean boundary. This could be potentially useful in identifying the extent of marine ice on the base of the ice shelf. A marine ice layer on the Amery Ice Shelf is also potentially observable using satellite altimetery [Phillips, 1998]. Both potential extra data sources could in the future be useful for model verification.

The assessment of the impact of climate change on the ice shelf highlighted one of the major limitations of the model. That is the fixed nature of the ice shelf including the restriction of the ice front being located along a constant line of model latitude. This restriction means expected changes in the ice shelf extent from climate change could not be readily incorporated into the modelling studies. This constraint on the ice shelf location also prevents other possible studies with this model, for example, estimating the impact of changes in the ice front location on the circulation and water mass properties. This would be particularly interesting in the case of the Amery Ice Shelf, as it is estimated that major calving events occur at intervals of 60-70 years. The last major calving event took place in 1963, and it reduced the ice shelf extent by approximately one-fifth [Budd, 1966].

The three stated aims of this work were: firstly, to describe the ocean circulation, temperature and salinity distribution and the ice shelf-ocean interaction beneath the Amery Ice Shelf; secondly, to estimate the interaction between the ocean cavity and Prydz Bay in terms of exchanges of heat, salt and momentum; and thirdly, to estimate the impact of climate change on the mass balance of the Amery Ice Shelf and the ocean circulation beneath the ice shelf. These aims, within the limitations of the model, have been achieved.

The different simulations have been able to reasonably successfully reproduce most of the observed oceanographic and glaciological features. Examples include, the estimation of marine ice layers of similar thickness to observations in the region of G1, the presence of Ice Shelf Water at the ice front and in Prydz Bay, and an estimate of the basal component of ice shelf mass balance, consistent with the other terms in the mass balance and the estimates of heat and salt fluxes at the cavity front [Wong et al., 1998].

Most of the cavity model runs produced similar results in comparison to observations. This made it difficult to establish which model gave the most realistic picture of the ocean circulation, and the distribution of temperature and salinity within the cavity. A more accurate determination of these features of the ocean cavity is difficult without a larger and more detailed set of observations. These should ideally include observations within the ocean cavity and high resolution observations along the ice front. Ideally observations along the ice front and extending into Prydz Bay should also include a full annual cycle of velocity, temperature and salinity. These would allow a better assessment

of mass exchange across the ice front, particularly in determining where inflow and outflow are occurring. In conjunction with observations of temperature and salinity, the improved mass exchange estimates would lead to better estimates of heat and salt exchange across the ice front, and by proxy at the ice shelf-ocean interface.

Observations within the ocean cavity would be useful for improving our understanding of oceanographic processes under the Amery Ice Shelf. They could potentially supplement the use of models for understanding the physical processes in the cavity and at the interface between the ice shelf and the ocean. The number of observations needed for a comprehensive analysis is substantial, but could potentially be obtained by a well planned field program. Despite this the benefits of even a small number of observations is still large. Observations within the cavity would allow a qualitative assessment of the oceanographic features found in modelling studies. They would also allow some tuning of model parameters, e.g., the diffusion parameters and boundary relaxation time scales. Establishing the appropriate values for such parameters is useful for predictive studies, e.g., climate change scenarios.

Although the desirability of temperature, salinity, and current observations in the ocean cavity and along the ice front is high, the minimisation of errors in the water column thickness is more important. This is because the water column thickness is important in determining the horizontal circulation which influences the transport of heat and salt and the interaction with the ice shelf. Earlier, it was highlighted that there may be large errors in the water column thickness due to the accumulation of errors in the bathymetry and the ice shelf draft. These errors could be substantially reduced by increasing the number of reliable observations of both the ice shelf and the bathymetry. An improved ice shelf draft alone is likely to allow the thickness of the marine ice layer to be more accurately determined through reducing uncertainties in the slopes of the ice base.

It is not possible, given the predictive nature of the study, to compare the climate change results with observations. However, the estimate of change in the ice shelf mass balance appears to be consistent in general terms with a number of other numerical studies of other ice shelves [Jenkins, 1991; Hellmer and Jacobs, 1995; Grosfeld and Gerdes, 1998]. All of the studies found the mass loss from the base of the ice shelf increases as a function of ocean temperature. This consistency suggests the climate change response from this study can be generalised to the other large Antarctic ice shelves. Thus the substantial increase in mass loss from the Amery Ice Shelf with warmer ocean temperatures may have wider implications, not just for the Lambert Glacier and Amery Ice Shelf system, but for the mass balance of the Antarctic Ice Sheet.

The results from this study provide, at a minimum, initial answers to questions about the ocean circulation, and heat and salt transport under the Amery Ice Shelf. For further progress the observations on which the model geometry and boundary conditions are based need to be improved. The results of this thesis hopefully provide motivation and guidance for future observational programs. In addition these results raise questions for future study. Some

questions, however, cannot be answered without the development of more sophisticated modelling tools. For example, a coupled ice shelf and ocean model would remove the need for specifying the draft and extent of the ice shelf. This would be desirable for assessing the affect of different ice front positions or the impact of climate change on the ice shelf and the ocean cavity.

The results for the present day, and the prediction of significant long term alteration in the ice shelf in response to possible climate changes, highlights that this part of the ocean domain merits continuing investigation.

References

Allison, I. 1979. The mass budget of the Lambert Glacier drainage basin, Antarctica. *J. Glaciol.*, 22, 223-235.

Bombosch, A., and A. Jenkins. 1995. Modeling the formation and deposition of frazil ice beneath Filchner-Ronne Ice Shelf. *J. Geophys. Res.*, 100, 6983-6992.

Bryan, K. 1969. A numerical method for the study of the circulation of the world ocean. *J. Comput. Phys.*, 4, 347-376.

Budd, W. 1966. The dynamics of the Amery Ice Shelf. *J. Glaciol.*, 6, 335-357.

Budd, W., I. Landon Smith, and E. Wishart. 1967. The Amery Ice Shelf. *In* Oura H. *ed. Physics of snow and ice: International conference on low temperature science. 1966. Proceedings 1(2).* Sapporo, Hokkaido University. Institute of Low Temperature Science, 447-467.

Budd, W. F., M. J. Corry and T. H. Jacka. 1982. Results from the Amery Ice Shelf Project. *Ann. Glaciol.*, 3, 36-41.

Budd, W. F., D. Jenssen, E. Mavrakis, and B. Coutts. 1994. Modelling the Antarctic ice-sheet changes through time. *Ann. Glaciol.*, 20, 291-297.

Cox, M.D. 1984. A primitive equation, 3-dimensional model of the ocean. GFDL Ocean Group Technical Report 1. Princeton University, Princeton, New Jersey.

Crabtree, R. D., and C. S. M. Doake. 1982. Pine Island Glacier and its drainage basin: results from radio echo-sounding. *Ann. Glaciol.*, 3, 65-70.

Determann, J. 1991. Numerical modelling of ice shelf dynamics. *Antarct. Sci.*, 3, 187-195.

Determann, J., and R. Gerdes. 1994. Melting and freezing beneath ice shelves: implications from a three-dimensional ocean-circulation model. *Ann. Glaciol.*, 20, 413-419.

Determann, J., K. Grosfeld, R. Gerdes, and H. Hinze. 1994. Melting and freezing rates beneath Filchner-Ronne Ice Shelf from a 3D-ocean circulation model. *In* Oerter, H., *ed. Filchner-Ronne Ice Shelf Programme. Report 8.* Bremerhaven, Alfred-Wegener-Institute for Polar and Marine Research, 12-19.

Doake, C. S. M. 1976. Thermodynamics of the interaction between ice shelves and the sea. *Polar Rec.*, 18, 37-41.

Engelhardt, H., and J. Determann. 1987. Borehole evidence for a thick layer of basal ice in the central Ronne Ice Shelf. *Nature*, 327, 318-319.

Foldvik, A., and T. Kvinge. 1974. Conditional instability of sea water at the freezing point. *Deep Sea Res.*, 21, 169-174.

Foldvik, A., and T. Gammelsrød. 1988. Notes on Southern Ocean hydrography, sea-ice and bottom water formation. *Palaeogeogr. Palaeoclimatol. Palaeoecol.*,

67, 3-17.
Foster, T., and E. Carmack. 1976. Frontal zone mixing and Antarctic Bottom Water formation in the southern Weddell Sea. *Deep Sea Res.*, 23, 301-317.
Gammelsrød, T. 1994. Water mass distribution and tides along the Filchner-Ronne ice shelf. Preliminary results from the Norwegian Antarctic Expedition 1992-93. *In* Oerter, H., *ed. Filchner-Ronne Ice Shelf Programme. Report 7.* Bremerhaven, Alfred-Wegener-Institute for Polar and Marine Research, 42-46.
Gerdes, R. 1993. A primitive equation ocean circulation model using a general vertical coordinate transformation. Part 1: description and testing of the model. *J. Geophys. Res.*, 98, 14,683-14,701.
Gordon, H. B., and S. P. O'Farrell. 1997. Transient climate change in the CSIRO coupled model with dynamical sea ice. *Mon. Weather Rev.*, 125, 875-907.
Grosfeld, K., and R. Gerdes. 1998. Circulation beneath the Filchner Ice Shelf and its sensitivity to changes in the oceanic environment: a case study. *Ann. Glaciol.*, 27, 99-104.
Grosfeld, K., J. Determann, and R. Gerdes. 1995. Interaction between ice-shelf cavities and the open ocean. *In* Oerter, H., *ed. Filchner-Ronne Ice Shelf Programme. Report 9.* Bremerhaven, Alfred-Wegener-Institute for Polar and Marine Research, 23-30.
Grosfeld, K., R. Gerdes, and J. Determann. 1997. Thermohaline circulation and interaction between ice shelf cavities and the adjacent open ocean. *J. Geophys. Res.*, 102, 15,595-15,610.
Grosfeld, K., H. H. Hellmer, M. Jonas, H. Sandhäger, M. Schulte, and D. G. Vaughan. 1998. Marine ice beneath Filchner Ice Shelf: Evidence from a multi-disciplinary approach. *In* Jacobs, S. S. and R. F. Weiss, *ed. Ocean, ice, and atmosphere: Interactions at the Antarctic continental margin*, Washington DC, American Geophysical Union, Antarctic Research Series, 75, 319-339.
Hamley, T. C., and W. F. Budd. 1986. Antarctic iceberg distribution and dissolution. *J. Glaciol..*, 32, 242-251.
Haney, R. L. 1991. On the pressure gradient force over steep topography in sigma coordinate ocean models. *J. Phys. Oceanogr.*, 21, 610-619.
Hansen, J., A. Lacis, D. Rind, G. Russell, P.Stone, I. Fung, R. Ruedy and J. Lerner. 1984. Climate sensitivity: analysis of feedback mechanisms. *In* Hansen, J.E. and T. Takahashi, *ed. Climate Processes and Climate Sensitivity*, Washington DC, American Geophysical Union, Geophysical Monography Series 29, 130-163.
Hellmer, H. H., and D. J. Olbers. 1989. A two-dimensional model for the themohaline circulation under an ice shelf. *Antarct. Sci.*, 1, 325-336.
Hellmer, H. H., and D. J. Olbers. 1991. On the thermohaline circulation beneath the Filchner-Ronne Ice Shelves. *Antarct. Sci.*, 3, 433-442.
Hellmer, H. H., and S. S. Jacobs. 1992. Ocean interactions with the base of Amery Ice Shelf, Antarctica, *J. Geophys. Res.*, 97, 20,305-20,317.
Hellmer, H. H., and S. S. Jacobs. 1995. Seasonal circulation under the eastern Ross Ice Shelf, Antarctica. *J. Geophys. Res.*, 100, 10,873-10,885.
Hellmer, H. H., S. S. Jacobs, and A. Jenkins. 1998. Oceanic erosion of a floating Antarctic glacier in the Amundsen Sea. *In* Jacobs, S. S. and R. F. Weiss, *ed.*

Ocean, ice, and atmosphere: Interactions at the Antarctic continental margin, Washington DC, American Geophysical Union, Antarctic Research Series, 75, 83-99.

Hodgkinson, R. P., R. S. Colman, K. R. Kerry, and M. S. Robb. 1988. Water currents in Prydz Bay, Antarctica, during 1985. Australian National Antarctic Research Expedition Research Notes 59. Antarctic Division, Kingston, Tasmania, Australia.

Hodgkinson, R. P., R. S. Colman, M. S. Robb, and R. Williams. 1991a. Current meter moorings in the region of Prydz Bay, Antarctica, 1986. Australian National Antarctic Research Expedition Research Notes 81. Antarctic Division, Kingston, Tasmania, Australia.

Hodgkinson, R. P., R. S. Colman, M. S. Robb, and R. Williams. 1991b. Current meter moorings in the region of Prydz Bay, Antarctica, 1987. Australian National Antarctic Research Expedition Research Notes 82. Antarctic Division, Kingston, Tasmania, Australia.

Jacobs, S. S., A. F. Amos, and P. M. Bruchhausen. 1970. Ross Sea oceanography and Antarctic Bottom Water formation. *Deep Sea Res.*, 17, 935-962.

Jacobs, S. S., A. L. Gordon, and J. L. Ardai. 1979. Circulation and melting beneath the Ross Ice Shelf, *Science*, 203, 439-443.

Jacobs, S. S., H. H. Hellmer, C. S. M. Doake, A. Jenkins and R. M. Frolich. 1992. Melting of ice shelves and the mass balance of Antarctica, *J. Glaciol.*, 38, 375-387.

Jenkins, A. 1991. A one-dimensional model of ice shelf-ocean interaction. *J. Geophys. Res.*, 96, 20,671-20,677.

Jenkins, A., and C. S. M. Doake. 1991. Ice-ocean interaction on Ronne Ice Shelf, Antarctica. *J. Geophys. Res.*, 96, 791-813.

Jenkins, A., and A. Bombosch. 1995. Modeling the effects of frazil ice crystals on the dynamics and thermodynamics of ice shelf water plumes. *J. Geophys. Res.*, 100, 6967-6981.

Kader, B. A., and A. M. Yaglom. 1972. Heat and mass transfer laws for fully turbulent wall flows. *Int. J. Heat Mass Transfer*, 15, 2329-2351.

Kader, B. A., and A. M. Yaglom. 1977. Turbulent heat and mass transfer from a wall with parallel roughness ridges. *Int. J. Heat Mass Transfer*, 20, 345-357.

Killworth, P. D. 1977. Mixing on the Weddell Sea continental slope. *Deep Sea Res.*, 24, 427-448.

Kurinin, R.G. and N.D. Aleshkova. 1987. Bedrock relief of Enderby Land, Mc-Robertson Land and Princess Elizabeth Land, East Antarctica (In Russian). *Antarktika* 26, 62-65.

Lane-Serff, G. F., 1993. On drag-limited gravity currents. *Deep Sea Res.*, 40, 1699-1702.

Lane-Serff, G. F., 1995. On meltwater under ice shelves. *J. Geophys. Res.*, 100, 6961-6965.

Lewis, E. L., and R. G. Perkin. 1986. Ice pumps and their rates. *J. Geophys. Res.*, 91, 11,756-11,762.

Loewe, F. 1961. On melting of fresh-water ice in sea-water. *J. Glaciol..*, 3, 1051-1052.

MacAyeal, D. R. 1984a. Numerical simulations of the Ross Sea tides. *J. Geophys. Res.*, 89, 607-615.

MacAyeal, D. R. 1984b. Thermohaline circulation below the Ross Ice Shelf: a consequence of tidally induced vertical mixing and basal melting. *J. Geophys. Res.*, 89, 597-606.

MacAyeal, D. R. 1985a. Tidal rectification below the Ross Ice Shelf, Antarctica. *In* S. S. Jacobs. *ed. Oceanology of the Antarctic continental shelf*, Washington DC, American Geophysical Union, Antarctic Research Series, 43, 109-132.

MacAyeal, D. R. 1985b. Evolution of tidally triggered meltwater plumes below ice shelves. *In* S. S. Jacobs. *ed. Oceanology of the Antarctic continental shelf*, Washington DC, American Geophysical Union, Antarctic Research Series, 43, 133-143.

Manabe, S. and R. Stouffer. 1994. Multiple-century response of a coupled ocean-atmosphere model to an increase of atmospheric carbon dioxide. *J. Climate*, 7, 5-23.

McCave, I. N., and S. A. Swift. 1976. A physical model for the rate of deposition of fine-grained sediments in the deep sea. *Geol. Soc. Am. Bull.*, 87, 541-546.

Melling, H., and E. L. Lewis. 1982. Shelf drainage flows in the Beaufort Sea and their effect on the Arctic Ocean pycnocline. *Deep Sea Res.*, 29, 967-985.

Mellor, G. L. 1991. An equation of state for numerical models of oceans and estuaries. *J. of Atmos. Oceanic. Technol.*, 8, 609-611.

Mesinger, F., and A. Arakawa. 1976. Numerical methods used in atmospheric models. GARP Publ. Ser., 17, vol 1.

Michel, R. L., T. W. Linick and P. M. Williams. 1979. Tritium and carbon-14 distributions in sea water from under the Ross Ice Shelf Project ice hole. *Science*, 203, 445-446.

Middleton, J. H., and S. E. Humpries. 1989. Thermohaline structure and mixing in the region of Prydz Bay, Antarctica. *Deep Sea Res.*, 36, 1255-1266.

Mikolajewicz, U., B. D. Santer, and E. Maier-Reimer. 1990. Ocean response to greenhouse warming. *Nature*, 345, 589-593.

Morgan, V. I. 1972. Oxygen isotope evidence for bottom freezing on the Amery Ice Shelf. *Nature*, 238, 393-394.

Morgan, V. I. and W. F. Budd. 1975. Radio-echo sounding of the Lambert Glacier Basin. *J. Glaciol.*, 15, 103-111.

Nicholls, K. W. 1997. Predicted reduction in basal melt rates of an Antarctic ice shelf in a warmer climate. *Nature*, 388, 460-462.

Nicholls, K. W. and A. Jenkins. 1993. Temperature and salinity beneath Ronne Ice Shelf, Antarctica. *J. Geophys. Res.*, 98, 22,553-22,568.

Nicholls, K. W., K. Makinson, and A. V. Robinson. 1991. Ocean circulation beneath the Ronne Ice Shelf. *Nature*, 354, 221-223.

Nicholls, K. W., K. Makinson, and M. R. Johnson. 1997. New oceanographic data from beneath Ronne Ice Shelf, Antarctica. *Geophys. Res. Lett.*, 24, 167-170.

Nunes Vaz, R., and G. Lennon. 1996. Physical oceanography of the Prydz Bay region of Antarctic waters. *Deep Sea Res.*, 43, 603-641.

Nøst, O. A., and A. Foldvik. 1994. A model of ice shelf-ocean interaction with application to the Filcher-Ronne and Ross Ice Shelves. *J. Geophys. Res.*, 99,

14,243-14,254.

Oerter, H., J. Kipfstuhl, J. Determann, H. Miller, D. Wagenbach, A. Minikin and W. Graf. 1992. Evidence for basal marine ice in the Filchner-Ronne Ice Shelf. *Nature*, 358, 399-401.

O'Farrell, S. P., J. L. McGregor, L. D. Rotstayn, W. F. Budd, C. Zweck, and R. Warner. 1997. Impact of transient increases in atmospheric CO_2 on the accumulation and mass balance of the Antarctic Ice Sheet. *Ann Glaciol.* 25, 137-144.

Orlanski, I. 1976. A simple boundary condition for unbounded hyperbolic flows. *J. Comput. Phys.*, 21, 251-269.

Penrose, J. D., M. Conde, and T. J. Pauly. 1994. Acoustic detection of ice crystals in Antarctic waters. *J. Geophys. Res.*, 99, 12,573-12,580.

Phillips, H. A. 1998. Digital mapping of the glaciological characteristics in the Lambert-Amery System, East Antarctica. Doctor of Philosphy thesis, University of Tasmania, Hobart, Australia.

Pozdeyev, V. S., and R. G. Kurinin. 1987. New data on the morphology of the ice cover and relief of the subglacial bed and sea bottom in the southern part of the Weddell Sea basin, West Antarctica (in Russian). *Antarktika*, 26, 66-71.

Robin, G. de Q. 1979. Formation, flow, and disintegration of ice shelves. *J. Glaciol.*, 24, 259-271.

Russell-Head, D. S. 1980. The melting of free-drifting icebergs. *Ann. Glaciol.*, 1, 119-122.

Sanderson, T. J. O., and C. S. M. Doake. 1979. Is vertical shear in an ice shelf negligible? *J. Glaciol.*, 22, 285-292.

Scheduikat M., and D. J. Olbers. 1990. A one-dimensional mixed layer model beneath the Ross Ice Shelf with tidally induced vertical mixing. *Antarct. Sci.*, 2, 29-42.

Schlesinger, M.E., and Z.-C. Zhao. 1989. Seaonal climatic changes induced by doubled CO_2 as simulated by the OSU atmospheric GCM/mixed-layer ocean model. *J. Climate*, 2, 459-495.

Smith, N., and P. Treguer. 1994. Physical and chemical oceanography in the vicinity of Prydz Bay, Antarctica. *In* Z. El-Sayed. *ed. Southern ocean ecology: The BIOMASS perspective*, Cambridge, Cambridge University Press, 25-43.

Smith, N. R., D. Zhaoqian, K. R. Kerry and S. Wright. 1984. Water masses and circulation in the region of Prydz Bay, Antarctica. *Deep Sea Res.*, 31, 1121-1147.

Stevens, D. P. 1990. On open boundary conditions for three dimensional primitive equation ocean circulation models. *Geophys. Astrophys. Fluid Dyn.*, 51, 103-133.

Stevens, D. P. 1991. The open boundary condition in the United Kingdom Fine-Resolution Antarctic model, *J. Phys. Oceanogr.*, 21, 1494-1499.

The FRAM Group. 1991. An Eddy-Resolving Model of the Southern Ocean. *EOS Transactions*, American Geophysical Union, 72, 169, 174-175.

Thyssen, F., A. Bombosch, and H. Sandhäger. 1993. Elevation, ice thickness and structure mark maps of the central part of Filchner-Roone Ice Shelf, Antarctica. *Polarforschung*, 62, 17-26.

Trenberth, K. E., J. G. Olson, and W. G. Large. 1989. A global ocean wind stress climatology based on ECMWF analyses. NCAR Technical Note, NCAR/TN-338 +STR. National Center for Atmospheric Research, Boulder, Colorado, 93pp.

Warren, S. G., C. S. Roesler, V. I. Morgan, R. E. Brandt, I. D. Goodwin, and Allison, I. 1993. Green icebergs formed by freezing of organic-rich seawater to the base of Antarctic ice shelves. *J. Geophys. Res.*, 98, 6921-6928

Wetherald, R.T. and S. Manabe. 1986. An investigation of cloud cover change in response to thermal forcing. *Clim. Change*, 8, 5-23.

Wexler, H. 1960. Heating and melting of floating ice shelves, *J. Glaciol.*, 3, 626-645.

Williams, M. J. M., A. Jenkins, and J. Determann. 1998a. Physical controls on ocean circulation beneath ice shelves revealed by numerical models. *In* Jacobs, S. S. and R. F. Weiss, *ed. Ocean, ice, and atmosphere: Interactions at the Antarctic continental margin*, Washington DC, American Geophysical Union, Antarctic Research Series, 75, 285-299.

Williams, M. J. M., R. C. Warner, and W. F. Budd. 1998b. The effects of ocean warming on melting and ocean circulation under the Amery Ice Shelf, East Antarctica. *Ann. Glaciol.*, 28, 75-80.

Wilson, C.A., and J.F.B. Mitchell. 1987. A double CO_2 climate sensitivity experiment with a global climate model including a simple ocean. *J. Geophys. Res.*, Vol 92, 13,315-13,343.

Wong, A. P. S. 1994. Structure and dynamics of Prydz Bay, Antarctica, as inferred from a summer hydrographic data set. Master of Polar and Oceanic Science thesis, University of Tasmania, Australia, 104pp.

Wong, A. P. S., N. L. Bindoff, and A. Forbes. 1998. Ocean-ice shelf interaction and possible bottom water formation in Prydz Bay, Antarctica. *In* Jacobs, S. S. and R. F. Weiss, *ed. Ocean, ice, and atmosphere: Interactions at the Antarctic continental margin*, Washington DC, American Geophysical Union, Antarctic Research Series, 75, 173-187.

Appendix A

Calculation of marine ice layer thicknesses along flowlines

Marine ice layer thicknesses derived from drilling programs in ice shelves [e.g., Morgan, 1972] provide potential points of comparison between numerical model results and observations. In models of the ocean cavity under the ice shelf only the rate of melting or freezing of ice along the base of the ice shelf is estimated. Unfortunately this melt rate cannot be integrated over time in the model to estimate the thickness of the marine ice layer, as integrating over time fails to account for the physics of the ice shelf.

In the ocean model the ice shelf is assumed to be in a steady state. Effectively this assumption means the ice shelf draft does not change with time. Thus the flow of ice within the ice shelf and the fluxes in and out of the ice shelf are in balance.

With the assumption that the ice shelf is flowing, the physics of the ice shelf needs to be considered in calculating the marine ice layer thickness. In the simplest case an ice shelf can be considered as several ice flowlines flowing adjacent to one another, but with little or no interaction between the individual flowlines. Furthermore, an individual flowline can be separated into two layers. A top layer of meteoric ice which has flowed off the continent and any snow accumulation which falls on the top of the ice shelf, and the bottom layer which consists of marine ice formed from frozen sea water.

Using this view of the ice shelf a simple steady state flowline model based on the principle of conservation of mass can be developed [e.g., Budd et al., 1982]. Because of the negligible vertical shear in the ice shelf [Sanderson and Doake, 1979] each layer of the ice shelf can be considered independently of the other layer. As no flux between the two layers is expected, the top layer in the ice shelf can be ignored. This has the advantage that knowledge of the accumulation on the top of the ice shelf is not needed.

The continuity equation for the marine ice layer thickness, z, is

$$\frac{\partial z}{\partial t} + \frac{uz}{y}\frac{\partial y}{\partial x} + u\frac{\partial z}{\partial x} + z\frac{\partial u}{\partial x} = -m, \tag{A.1}$$

where u is the along flowline velocity, x is the along flowline coordinate, with its origin at the grounding line, y is the across flowline coordinate, and m is the

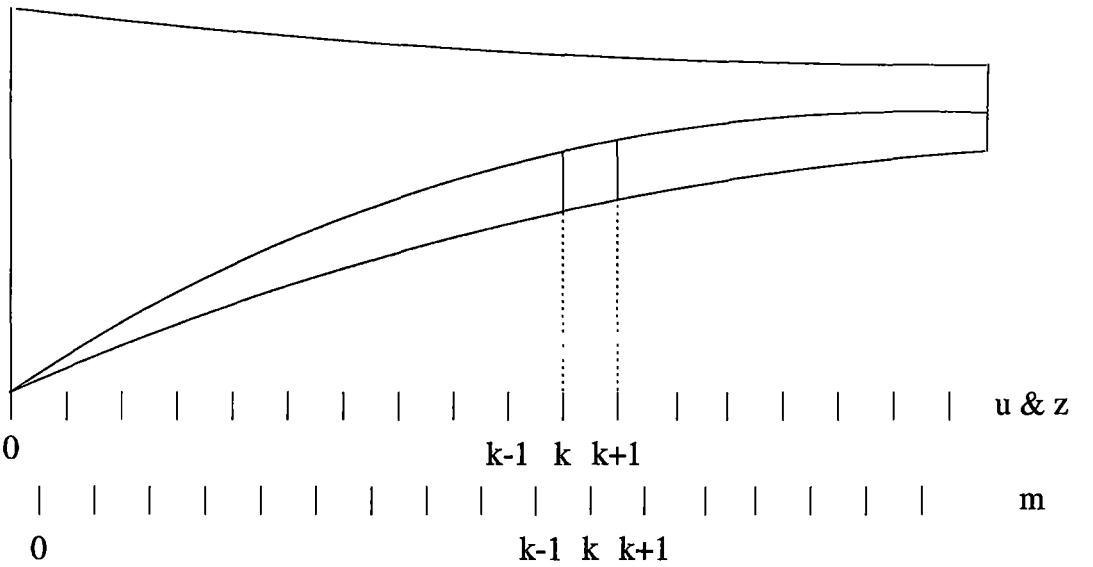

Figure A.1: Schematic of the location of finite difference calculation points in the marine ice layer.

rate of melting. By assuming the flowline is a constant width, and ignoring this width in the calculations, the transverse strain term can be ignored. As the ice shelf is already assumed to be in a steady state, the time evolution term is also ignored. Excluding these terms reduces the equation of interest to

$$u\frac{\partial z}{\partial x} + z\frac{\partial u}{\partial x} = -m. \tag{A.2}$$

Equation A.2 is solved using a finite difference scheme. The grid positions for the velocity, marine ice thickness and melt rates are shown in Figure A.1. In finite difference form, using forward differences, it becomes

$$u_{k+\frac{1}{2}}\frac{(z_{k+1} - z_k)}{\Delta x_k} + z_{k+\frac{1}{2}}\frac{(u_{k+1} - u_k)}{\Delta x_k} = -m_k, \tag{A.3}$$

where u_k and z_k are the finite difference representations of the velocity and marine ice thickness at grid point k, m_k is the finite difference representation of the melt rate, and Δx_k is the distance between grid points. The terms $u_{k+\frac{1}{2}}$ and $z_{k+\frac{1}{2}}$ are defined in terms of their neighbours as

$$u_{k+\frac{1}{2}} = \frac{u_{k+1} + u_k}{2}, \tag{A.4}$$

$$z_{k+\frac{1}{2}} = \frac{z_{k+1} + z_k}{2}. \tag{A.5}$$

Substituting these terms into Equation A.3 and simplifying produces the equation,

$$u_{k+1}z_{k+1} - u_k z_k = -m_k \Delta x_k. \tag{A.6}$$

This equation upon rearrangement gives,

$$z_{k+1} = \frac{1}{u_{k+1}}(u_k z_k - m_k \Delta x_k). \tag{A.7}$$

This allows the marine ice thickness at any point $k+1$ to be found in terms of the marine ice thickness at point k and the ice shelf velocities at points k and $k+1$.

At the grounding line it is assumed the marine ice layer has zero thickness. Hence the marine ice layer thickness can be solved iteratively from the grounding line. Equation A.6 must be solved with care as the marine ice layer may thin and in high melt areas lead to negative marine ice thickness solutions of Equation A.6. This occurs because the melt rates in the ocean model do not differentiate between meteoric and marine ice, so when no marine ice is present it is assumed the melt is coming from the meteoric ice layer. To avoid unrealistic negative thicknesses the marine ice thickness is reset to zero wherever this occurs, and remains zero until accretion recommences. This is important as it is only the accreted thickness which is able to be observationally measured.

Appendix B

Alternative ice shelf-ocean boundary conditions

As part of the review of previous work in Chapter 2 the boundary conditions utilised at the interface between the ice shelf and the ocean were discussed. The main boundary condition formulations used in ocean cavity modelling differ on two key aspects: the inclusion of the heat flux into the ice shelf, and the inclusion of a salt flux balance at the ice shelf-ocean interface.

The effect of the heat flux into the ice shelf on the ocean model is highly dependent on the parameterisation used to calculate the flux. In earlier studies [e.g. Hellmer and Olbers, 1989; Jenkins, 1991] the heat flux through the ice shelf was assumed to follow a linear temperature gradient through the ice shelf. This estimated the heat flux through the ice shelf at approximately two orders of magnitude smaller than the other two heat flux components. This appears to have motivated Determann and Gerdes [1994] to neglect this term in their parameterisation of the ice-ocean boundary condition for the three-dimensional ocean model. Recently, since this current study began, Hellmer et al. [1998] has proposed a new parameterisation of the heat flux into the ice shelf based on the work of Wexler [1960] (See Section 2.3.4). Here the effect of melting at the base of the ice shelf and the consequent change in the temperature gradient within the ice shelf is included. This parameterisation gives a significantly larger estimate of the heat flux into the ice shelf than is obtained by assuming a linear temperature gradient through the ice shelf.

The parameterisation implemented by Hellmer et al. [1998] is only applicable in areas of melting. In areas where freezing occurs it remains unclear how the heat flux through the ice shelf should be included. The work of Wexler [1960] suggests that where there is freezing there will be little or no gradient in temperature at the base of the ice shelf. Hence, at least in areas of freezing, ignoring the heat flux into the ice shelf is a valid assumption.

In the studies presented in the main part of this thesis a passive role for salinity has been assumed in determining the melting and freezing rates and hence the heat and salt fluxes at the ice shelf-ocean interface. The decision to assume a passive role for salinity was made to allow the results from this study to be comparable to those of other studies using this three-dimensional model [Determann and Gerdes, 1994; Determann et al., 1995; Grosfeld et al., 1997;

Grosfeld and Gerdes, 1998].

It is unclear what ramifications ignoring the salinity flux boundary condition (Equation 2.3) may have on the model results. In this appendix an alternative boundary condition at the ice shelf-ocean boundary which includes a parameterisation for the salt flux balance is used. This allows the impact of ignoring the salt flux in other model runs in this thesis to be explicitly assessed. The results from this model run are compared with the results from the $\text{AIS}_{\Psi=0}$ run.

B.1 Model setup

The set up of the model with the altered boundary conditions, labelled $\text{AIS}_{\text{altbc}}$, is as for the $\text{AIS}_{\Psi=0}$ model run presented in Chapter 5 except for the ice shelf-ocean boundary conditions. Here the modifications to the boundary condition shown in Section 4.3.3 are presented.

The changes are the introduction of a boundary salinity, S_{ice}, and a salt flux balance equation at the ice shelf-ocean interface, i.e. $Q_S = Q_S^B$. The two salt flux terms are defined following Hellmer and Olbers [1989] as

$$Q_S = \rho_0 \gamma_s (S_{ice} - S_w), \tag{B.1}$$

and

$$Q_S^B = -\rho_{ice} m \, S_{ice}, \tag{B.2}$$

where ρ_0 is a typical water density (1028 kgm^{-3}), γ_s is the turbulent heat exchange coefficient (5.05×10^{-7} ms^{-1}) [Hellmer and Olbers, 1989], S_w is the water salinity adjacent to the ice shelf-ocean interface, ρ_{ice} is a typical density of ice (915 kgm^{-3}), and m is the melt rate of the ice.

With the changes in calculating the salt flux at the ice shelf-ocean interface, the salt flux into the ocean model is no longer calculated by turning the freshwater flux from the melt rate into a salt flux by assuming a constant salinity. Instead the salt flux is calculated directly.

The introduction of a boundary salinity also changes the calculation of the in situ freezing temperature at the ice shelf-ocean interface, it is now

$$T_{ice} = a - bP_{ice} - cS_{ice}, \tag{B.3}$$

where P_{ice} is the pressure at the ice shelf-ocean interface and the coefficients a, b, and c are, respectively, 0.094°C, 7.53×10^{-8}°CPa^{-1}, and 0.057°C.

Except for the change in calculating the in situ freezing temperature, the heat flux balance remains unchanged.

B.2 Model results

There is little difference in the circulation between the two model runs with different ice shelf boundary conditions. This can be seen by comparing the vertically integrated streamfunction for the $\text{AIS}_{\text{altbc}}$ run (Figure B.1) with the streamfunction for the $\text{AIS}_{\Psi=0}$ run (Figure 5.9). There are changes in the

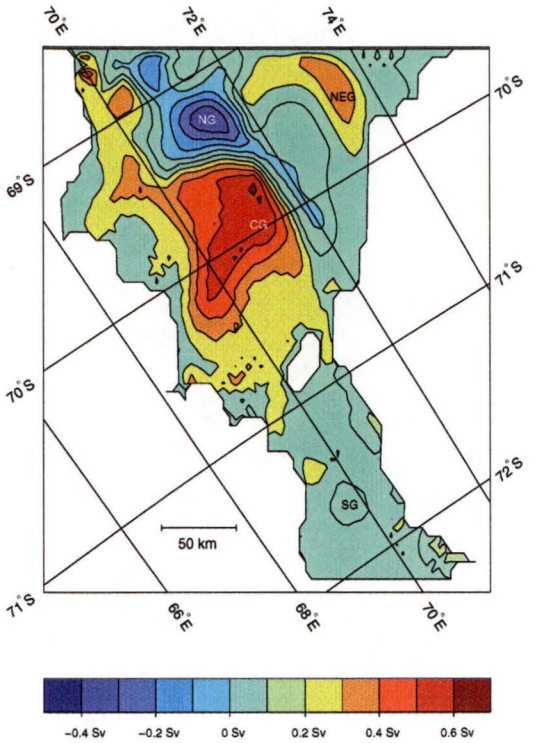

Figure B.1: Vertically integrated streamfunction for the AIS_{altbc} run. The circulation is clockwise about positive features.

strengths of the gyres between the two model runs, but the general gyre structure is similar. In the AIS_{altbc} run the strength of the central gyre is ~0.52 Sv, and in the Northern Gyre the peak circulation is ~-0.48 Sv.

The change in the ice shelf-ocean boundary conditions does affect the temperature and salinity in the ocean domain. This can be seen in Figure B.2, which shows temperature-salinity plots for model runs $AIS_{\Psi=0}$ and AIS_{altbc}, for both the whole model domain and the ocean layer adjacent to the ice shelf.

The range of temperature and salinity in both ocean domains is similar. The main difference between the two model runs is a small change in the slope of the 'freezing' line, which defines the relationship between temperature and salinity at the ice shelf-ocean interface. In the AIS_{altbc} model run the gradient of this line is ~2.35°C/PSU and in the $AIS_{\Psi=0}$ model the slope is ~2.41°C/PSU. Both of these slopes are similar to the ~2.5°C/PSU slope derived by Nøst and Foldvik [1994] from their simple model (See Section 2.3.1). The change in slope of the 'freezing' line is a consequence of using different boundary conditions. The different parameterisations of the heat and salt flux exchange at the ice shelf will lead to different heat and salt fluxes into the upper ocean model layer. Consequently this gives different temperatures and salinities adjacent to the ice shelf in the two models.

The variation in the circulation between the two model runs is also reflected in the temperature and salinity plots. The variation in the circulation along the open ocean boundary leads to slightly different water mass characteristics entering the model domain. The effect of this variation on the temperature and

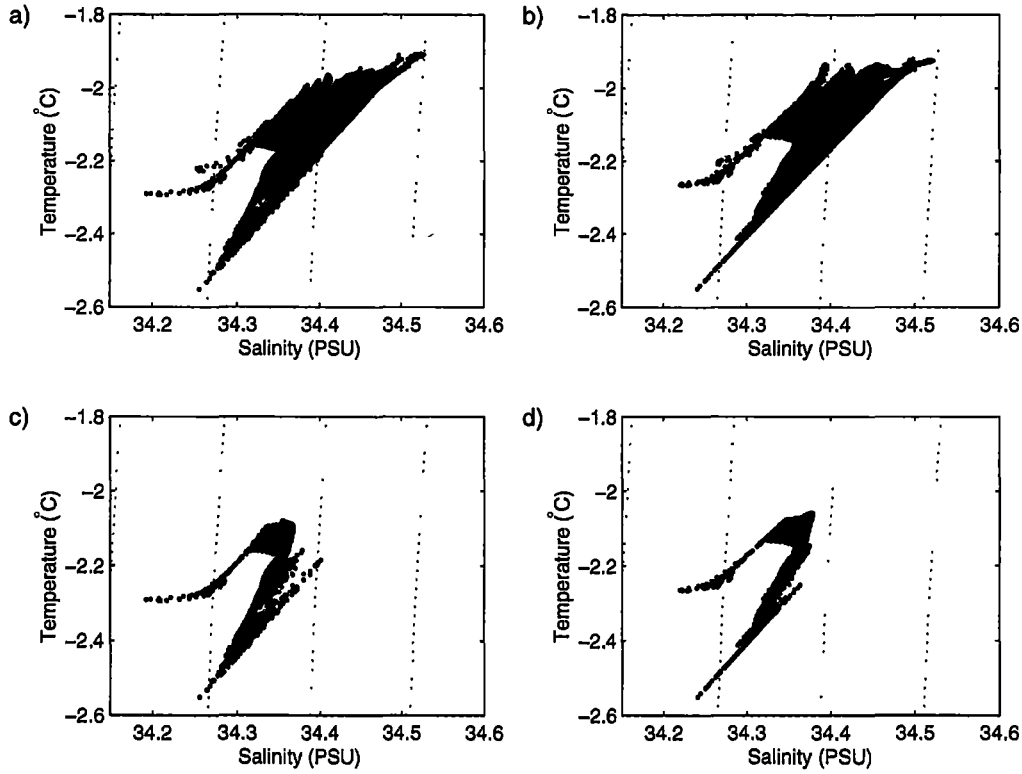

Figure B.2: Temperature-salinity plots for a) the whole domain in the AIS_{altbc} run, b) the whole domain in the $AIS_{\Psi=0}$ run, c) the ocean layer adjacent to the ice shelf in the AIS_{altbc} run, and d)the ocean layer adjacent to the ice shelf in the $AIS_{\Psi=0}$ run.

salinity structure can be seen in some of the water masses, particularly those warmer than -2°C (see Figures B.2a and B.2b).

The change in the boundary condition parameterisation has an impact on the rates of melting and freezing in the model domain. In the AIS_{altbc} run the melting and freezing rates, shown in Figure B.3, have a smaller magnitude than the melting and freezing rates for the $AIS_{\Psi=0}$ run (Figure 5.12). In the AIS_{altbc} run the melt rates are less than $\sim$5.0 ma^{-1}, and the freezing rates are smaller than $\sim$0.5 ma^{-1}. In contrast, the maximum melt rate in the $AIS_{\Psi=0}$ run is $\sim$12.5 ma^{-1}, and the maximum freezing rate is $\sim$1.0 ma^{-1}. Along with the general reduction in the magnitude of the rates of melting and freezing, the area where freezing occurs reduces substantially. This is particularly noticeable in the south of the domain where the localised areas of freezing reduce to a few grid points near the eastern and western grounding lines.

In the northern part of the domain the melting and freezing pattern is fairly similar in the two model runs, with peak areas of freezing occurring in similar locations in both model runs. This similarity leads to similar marine ice layer thicknesses in the two model runs along Flowline 1. This can be seen in Figure B.4, which shows the marine ice thicknesses along Flowlines 1, 2, and 3, for both the AIS_{altbc} run and the $AIS_{\Psi=0}$ run. The marine ice thickness along Flowlines 2 and 3 differ. In the AIS_{altbc} run no marine ice layer forms along Flowline 2

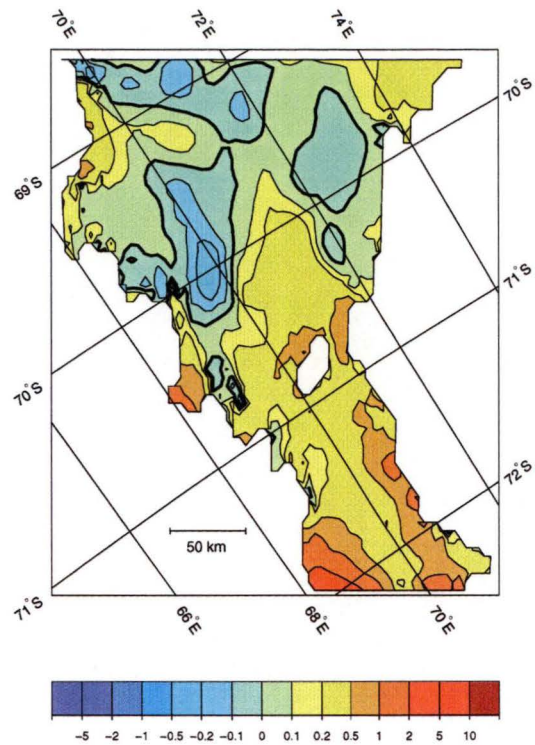

Figure B.3: Rates of melting (+) and freezing (-) from the $\text{AIS}_{\text{altbc}}$ run. The bold contour denotes the boundary between melting and freezing.

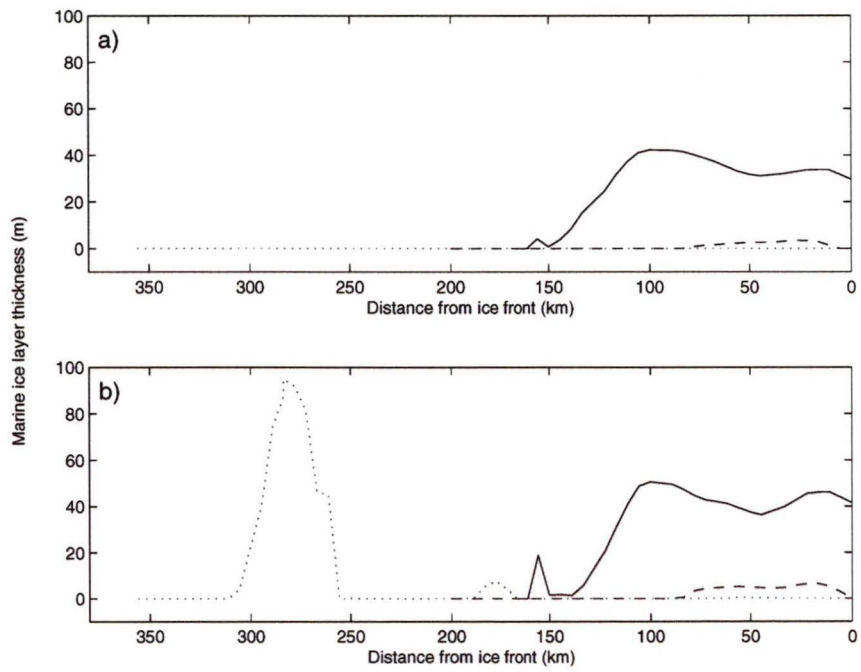

Figure B.4: Marine ice layer thickness for a) the $\text{AIS}_{\text{altbc}}$ run and b) the $\text{AIS}_{\Psi=0}$ run. The solid line is Flowline 1, the dotted line is Flowline 2 and the dashed line is Flowline 3. The locations of the flowlines is shown in Figure 5.24.

Table B.1: Estimates of the mass balance rates at the base of the Amery Ice Shelf, for different boundary conditions.

Amery Model Run (AIS)	Mean Rates for Freezing Zone (ma^{-1})	Mean Rates for Melting Zone (ma^{-1})	Mean Rates for Whole (Loss) (ma^{-1})	Area of Melt (%)	Mass Change Rates Freezing (Gta^{-1})	Mass Change Rates Melting (Gta^{-1})	Mass Change Rates Net Loss (Gta^{-1})
Ψ=0	0.16	0.40	0.21	66.6	2.8	13.4	10.6
altbc	0.06	0.32	0.23	76.3	0.8	12.5	11.7

Note: The total area of the ice shelf is 5.6 x 10^4 km^2.

and on Flowline 3 the marine ice layer thickness reduces significantly. These changes occur because the area of freezing in the AIS_{altbc} run has in comparison to the $AIS_{\Psi=0}$ run both shifted and reduced in area.

The similarity in thicknesses along Flowline 1 in the two models is most likely linked to a combination of two effects. The first is that the reduction in freezing rates in the AIS_{altbc} model run is coupled with a reduction in the melting rates, hence less of the accreted ice later melts off. The second is the change around 69.5°S 71.0°E from weak melting to weak freezing which will help reinforce the marine ice layer.

In Table B.1 a comparison is presented between the AIS_{altbc} run and $AIS_{\Psi=0}$ run mass balance rates. The mean melt rate and the net ice shelf mass balance for the AIS_{altbc} run are similar to those found in the $AIS_{\Psi=0}$ run. The similarity in the results is a combination of two effects. The first is the increase in the area where melting occurs. This helps compensate for the reduced melt rates within this area. The second is a decrease in the net amount of freezing. This arises from a reduction in both the mean rate of freezing and the area where freezing occurs.

The net amount of melting in the AIS_{altbc} run is consistent with the estimates of basal mass loss calculated by Wong et al. [1998] (see Section 3.3).

B.3 Discussion and conclusions

The results presented in the previous section suggest that modifying the parameterisation of the boundary condition at the ice-ocean interface does affect the results of the ocean cavity models. Within the ocean this effect appears to be limited as only small changes in the temperature and salinity in the cavity were found. The effects of the boundary condition parameterisation on the basal mass balance of the ice shelf is potentially significant.

Comparison between the ocean circulation in the AIS_{altbc} run and the $AIS_{\Psi=0}$ run shows a consistent circulation. There was some variation in the strengths of some gyres, but this variation was less than was found in model runs where the boundary conditions at the ice front were modified (see Chapter 5). This adds further weight to the conclusion that the ocean dynamics is strongly determined by the topography of the ocean cavity under the ice shelf.

Although there was some variation in the patterns of melting and freezing and the strength of melting and freezing; the net amount of melting from the ice shelf into the ocean cavity was similar in the AIS_{altbc} and $AIS_{\Psi=0}$ runs. This similarity in net melting gives similar net heat and salt fluxes into the ocean cavity in the two model runs, and leads to the similar temperature-salinity distributions in the model layer adjacent to the ice shelf (Figure B.2). The variation in the gradient of the 'freezing' line is small and is likely to be caused by the differences in the parameterisation of the boundary conditions.

The effects of the change of boundary conditions on the ice shelf appear to be larger than the effect of the change on the ocean. Although there is substantially less freezing in the AIS_{altbc} run, this does not lead to as noticeable a reduction in the thickness of the marine ice layers (Figure B.4) as might be expected. The thickness of the marine ice along Flowline 1 for the AIS_{altbc} run was found to be very similar to that for the $AIS_{\Psi=0}$ run. In contrast, along Flowlines 2 and 3 there is a reduction in the marine ice layer thickness.

The changes in the boundary conditions between the AIS_{altbc} and the $AIS_{\Psi=0}$ run, have in general, had little effect on the ocean circulation or the distribution of temperature and salinity under the Amery Ice Shelf, in comparison to changes of the boundary conditions at the ice front (see Chapter 5). The variation in the melting and freezing rates between the two model runs, however, does suggest that there may be significant local variations in the ice shelf basal mass balance from different ice-ocean boundary parameterisations.

There remain some important differences between the model runs, despite the broadly similar results. These differences highlight that the choice of parameterisation for the heat and salt flux balances at the ice-ocean interface are more complicated than was anticipated. They also show that this is an important part of the ice shelf and ocean system and care is needed in prescribing the processes across this boundary.

Appendix C

Application of a simple sea ice model in the open ocean

In Chapter 7 several studies using a model which included the ocean cavity under the Amery Ice Shelf and Prydz Bay were presented. In all of those studies the effect of sea ice in Prydz Bay was parameterised by keeping the surface temperature fixed at the surface freezing point (-1.9°C). Although this is unrealistic it was thought this boundary condition would be of minor importance, because temperature and salinity data were assimilated into the open ocean part of the domain, and this would include the effects of ice formation and transport in Prydz Bay.

Given the excessive amount of melting found in the ice shelf cavity in all of the extended domain runs, except the $\text{EXDOM}_{\text{cool}}$ run (Chapter 7), the assumption that this open ocean surface boundary condition is unimportant needs to be examined. The likely problem is that the surface boundary is not allowing the formation of saline water masses, such as High Salinity Shelf Water, through freezing at the open ocean surface. Saline water masses are needed to drive deep convection which would transport the cold water to the bottom and stop the flow of warmer waters from off the shelf into the cavity under the ice shelf.

In this appendix three model runs are presented where a simple sea ice model is used as the surface boundary condition in the open ocean. Two of the model runs are modifications of model runs which were presented in Chapter 7; the $\text{EXDOM}_{\gamma=360}$ and $\text{EXDOM}_{\text{basic}}$ model runs. These were chosen since the sea ice model attempts to reproduce the annual sea ice cycle and aggressive restoration of the summer hydrographic conditions through the assimilation scheme could significantly impact on the annual cycle. In addition a third model run, with no assimilation of observations and a closed northern boundary is presented. In this run there is no temperature or salinity forcing except through interaction with the ice shelf or sea ice.

C.1 Sea ice model

The sea ice model used in this study is the one-dimensional thermodynamic sea ice model described by Grosfeld et al. [1997]. The successful results from their study using this sea ice model are described in Section 2.3.6.

In the sea ice model the boundary condition for the heat flux, Q_T^A, at the sea ice surface is

$$Q_T^A = \alpha(T_{is} - T_a) = -k_i \frac{T_{is} - T_{ib}}{h_i} = -Q_T^C, \tag{C.1}$$

where Q_T^C is the conductive heat flux through the sea ice, T_{is} and T_{ib} are, respectively, the temperatures of the sea ice surface and base, T_a is a prescribed atmospheric temperature function, and h_i is the thickness of the sea ice, which evolves through time from the melt rate. Following Grosfeld et al. [1997], the constant α is chosen as 16 $\mathrm{Wm^{-2}K^{-1}}$, and k_i the thermal conductivity for sea ice is set to 2.04 $\mathrm{Wm^{-1}K^{-1}}$. Thus from the above equation the surface temperature for sea ice can be calculated from a given atmospheric temperature by assuming that the temperature at the bottom of the sea ice is at the in situ freezing temperature for water.

The atmospheric temperature, T_a, in the model is prescribed to vary sinusoidally with an annual cycle from -26°C in winter to -6°C in summer.

The heat balance at the sea ice base is given by

$$Q_T = Q_T^C + Q_T^B, \tag{C.2}$$

where Q_T is the total heat flux from the ocean, and Q_T^B is the heat flux due to melting or freezing of the sea ice. Both Q_T and Q_T^B follow the formulations used at the ice shelf-ocean interface (their parameterisations are shown in Equations 4.60 and 4.62, respectively).

The salt flux accompanying the thermodynamic sea ice model is parameterised from the melting or freezing rate calculated from the heat flux balance. This gives the equation

$$Q_S = -\rho_{ice} m S_D, \tag{C.3}$$

where ρ_{ice} is the density of the ice, m is the melt rate and S_D is the salinity difference between the water and the sea ice. For simplicity S_D is assumed to be 30 PSU [Grosfeld et al., 1997].

Where there is no sea ice cover the temperature of the upper ocean layer is restored to -1.9°C. Thus when the water temperature falls below the surface freezing point sea ice production starts.

This model does not reproduce horizontal ice movement, and no attempt has been made to parameterise this.

C.2 Incorporation of the sea ice model in previous runs

The first experiment using the sea ice model is based on the $\mathrm{EXDOM_{basic}}$ run, which is described in Section 7.2.2. The only change in the model setup from

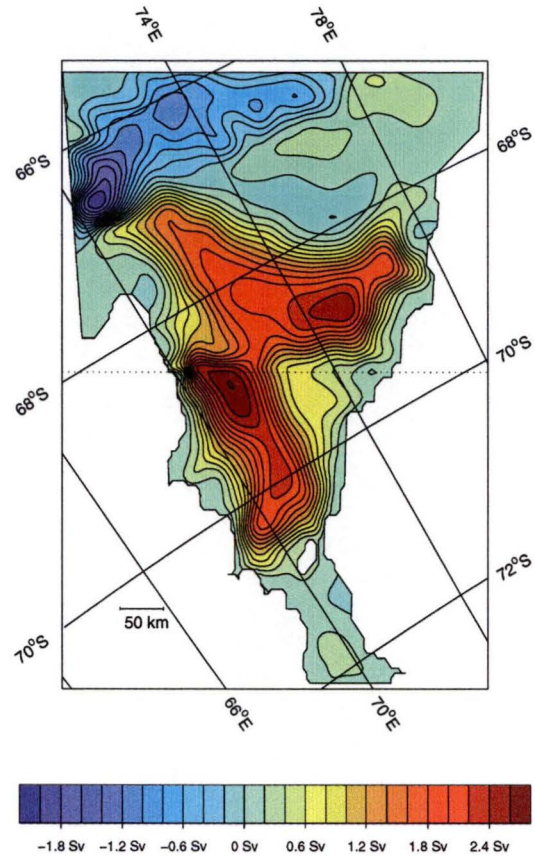

Figure C.1: Vertically integrated streamfunction for the $\text{EXDOM}_{\text{SI-basic}}$ run. The circulation is clockwise about positive features.

that used in Chapter 7 is to implement the sea ice model described in the preceding section. This model is labelled $\text{EXDOM}_{\text{SI-basic}}$. The second experiment involves implementing the sea ice model in the $\text{EXDOM}_{\gamma=360}$ run. Again implementing the sea ice model is the only change. This model is labelled $\text{EXDOM}_{\text{SI-}\gamma=360}$.

Both the $\text{EXDOM}_{\text{SI-basic}}$ and $\text{EXDOM}_{\text{SI-}\gamma=360}$ models were started with a constant temperature of -1.9°C in the open ocean domain, and the temperature in the ice shelf cavity set using the formula in Section 4.4. The initial salinity was varied over the model layers from 34.60 PSU at the surface to 34.67 PSU at the lowest model layer. These are the same initial conditions as used in the other extended domain model runs. The model was then run for approximately 12.7 years, and the last annual cycle was studied.

The changed thermohaline structure introduced by the addition of the sea ice model strongly affects the circulation in the model domain. The general structure of the circulation is similar, in both the $\text{EXDOM}_{\text{SI-basic}}$ and $\text{EXDOM}_{\text{SI-}\gamma=360}$ runs, to that seen in the other extended domain runs, but with a noticeable change in the strength of the circulation. This can be clearly seen in both Figures C.1 and C.2, which show the vertically integrated streamfunction for the $\text{EXDOM}_{\text{SI-basic}}$ and the $\text{EXDOM}_{\text{SI-}\gamma=360}$ runs, respectively. In the $\text{EXDOM}_{\text{SI-}\gamma=360}$ run the maximum transport in Prydz Bay is $\sim$4.0 Sv. This

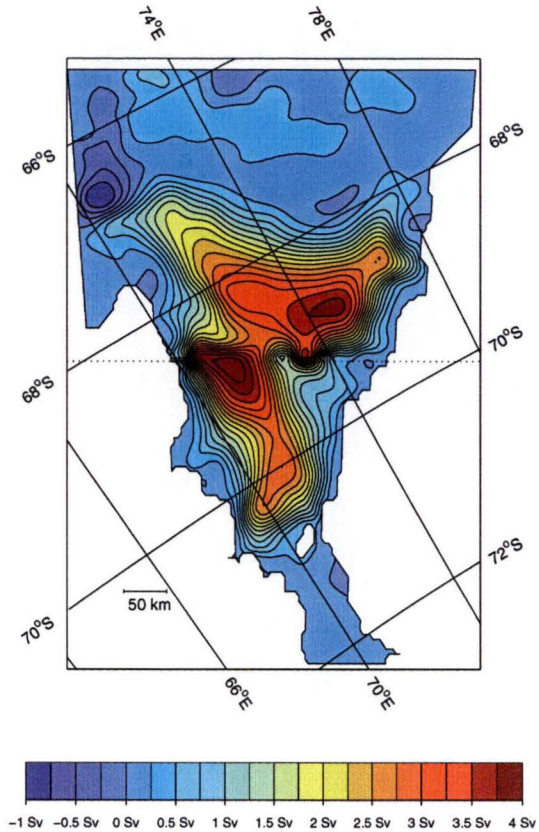

Figure C.2: Vertically integrated streamfunction for the $\text{EXDOM}_{\text{SI-}\gamma=360}$ run. The circulation is clockwise about positive features.

contrasts greatly with the other extended domain runs where the maximum transport was not more than 2.0 Sv. The $\text{EXDOM}_{\text{SI-basic}}$ run does not show the same increase in the strength of the circulation, although both the maximum clockwise and anticlockwise transports are larger than found in the other extended domain model runs.

The change over the open ocean part of the domain from the previous boundary condition to a sea ice model also modifies the temperature in the model domain. Although the temperature structure is expected to vary because of the annual cycle in the atmospheric temperature forcing on the sea ice model. This variation is not significant in contrast to the changes to the water column from changing the sea surface boundary conditions, so only a single temperature section typical of spring atmospheric temperature conditions is presented for each model run. The temperature sections are shown in Figures C.3 and C.4, for the $\text{EXDOM}_{\text{SI-basic}}$ and $\text{EXDOM}_{\text{SI-}\gamma=360}$ runs respectively.

In both the sea ice model runs the temperature in the model domain is warmer than in the corresponding run without sea ice (Figures 7.10 and 7.17). This increase in temperature is particularly noticeable with regard to the ocean cavity where the temperature is of order half a degree warmer in the sea ice model runs than in the other runs.

The effect of the warmer ocean cavity is to increase the basal mass loss. As the basal mass loss rates for the coupled open ocean and cavity model runs

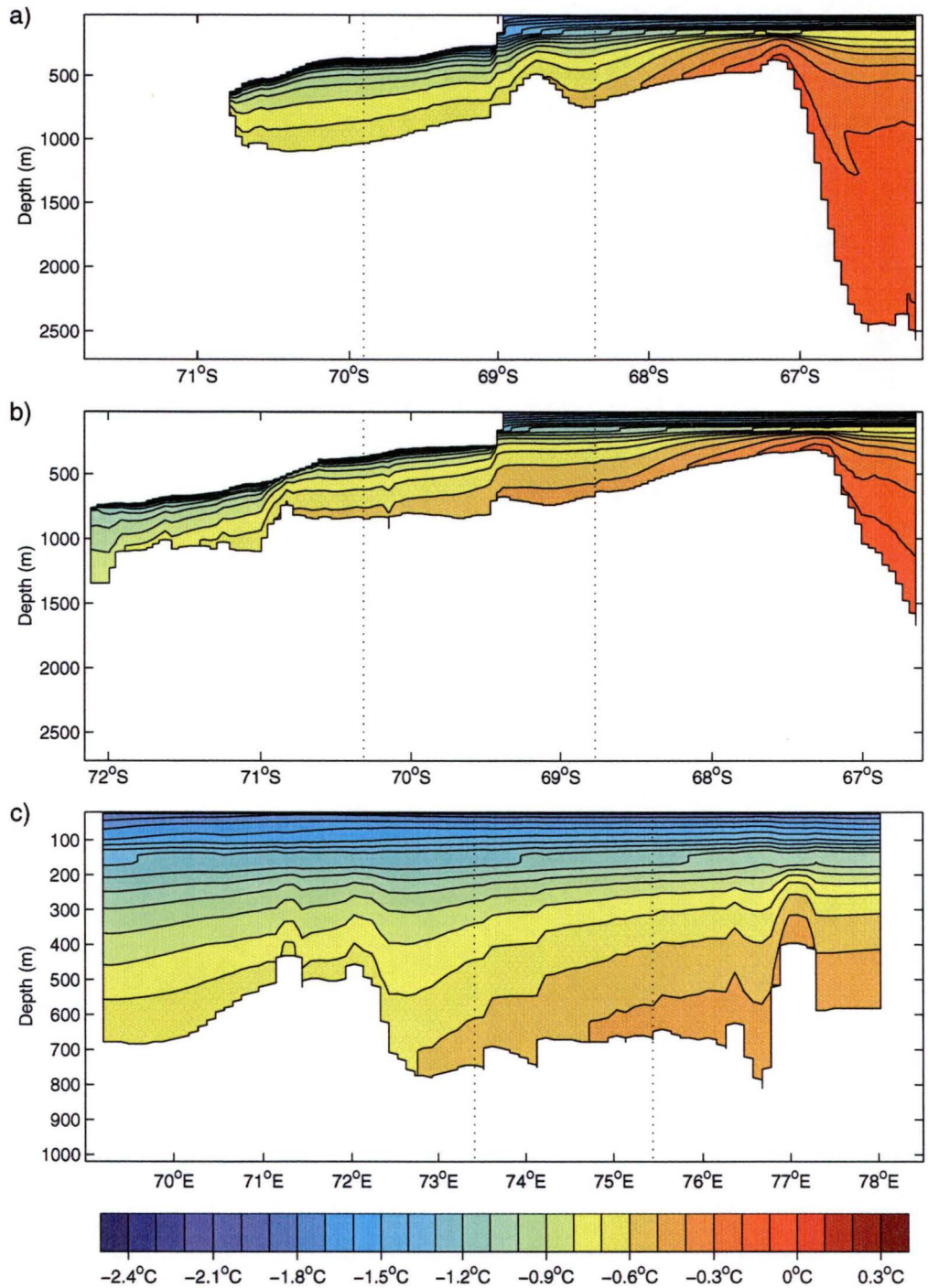

Figure C.3: Temperature cross-sections for the $\text{EXDOM}_{\text{SI-basic}}$ run. a) Section A′, b) Section B′, c) Section D. The locations of the cross-sections is shown in Figure 7.6. The dotted lines indicate where the cross-sections intersect.

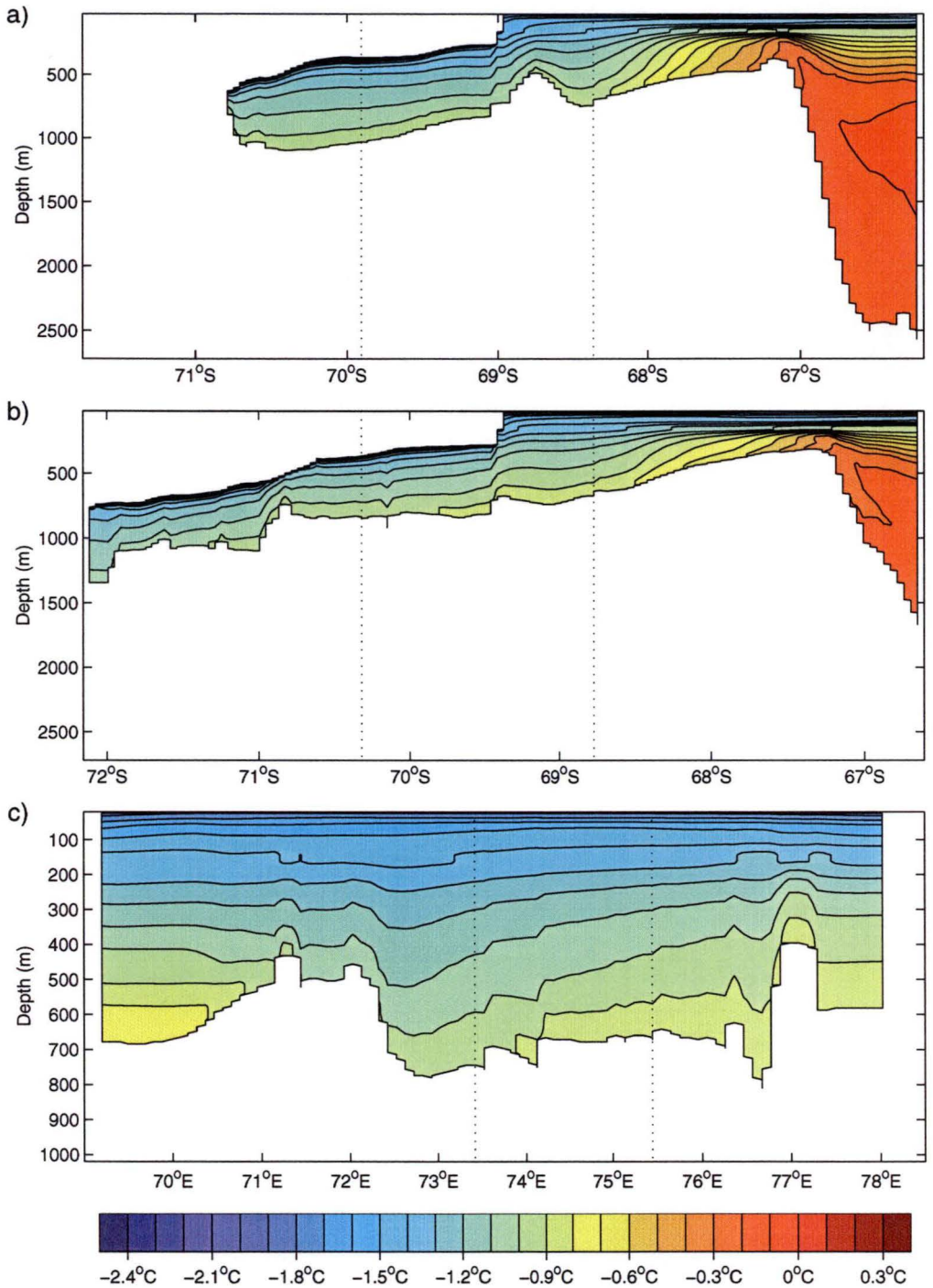

Figure C.4: Temperature cross-sections for the $\text{EXDOM}_{\text{SI-}\gamma=360}$ run. a) Section A′, b) Section B′, c) Section D. The locations of the cross-sections is shown in Figure 7.6. The dotted lines indicate where the cross-sections intersect.

Table C.1: Annual mean mass balance estimates for the extended domain model runs, where a sea ice model is used. The non-sea ice model runs corresponding to $EXDOM_{SI\text{-}basic}$ and $EXDOM_{SI\text{-}\gamma=360}$ and the $EXDOM_{cool}$ run are also shown.

Extended Domain Run (EXDOM)	Mean Rates for Freezing Zone (ma^{-1})	Mean Rates for Melting Zone (ma^{-1})	Mean Rates for Whole (Loss) (ma^{-1})	Area of Melt (%)	Mass Change Rates Freezing (Gta^{-1})	Mass Change Rates Melting (Gta^{-1})	Mass Change Rates Net Loss (Gta^{-1})
basic	0.56	1.79	1.41	83.8	4.2	68.9	64.7
SI-basic	1.13	5.43	4.80	90.3	5.9	264.1	258.2
γ=360	0.60	1.81	1.44	84.7	4.2	70.2	66.0
SI-γ=360	1.02	4.10	3.54	89.1	6.0	196.5	190.5
SI-closed	0.35	0.52	0.32	76.4	3.8	18.4	14.6
cool	0.33	0.56	0.38	77.8	3.3	20.9	17.6

Note: The total area of the ice shelf is 5.6 x 10^4 km^2.

are already higher than comparisons with observations would consider realistic, this additional warming further increases the mass loss from the ice shelf. This increase is clearly shown in Table C.1, which contains the annual mean mass balance estimates for the sea ice model runs and the non-sea ice model runs. The mass balance estimates do not vary widely over the annual cycle of the model hence only the annual mean is shown.

C.3 Closed boundary sea ice model

The lack of success in reducing the high mass loss from the ice shelf in both the $EXDOM_{SI\text{-}basic}$ and $EXDOM_{SI\text{-}\gamma=360}$ model runs, prompted a study of a simpler extended domain model configuration which includes a sea ice model. This model, labelled $EXDOM_{SI\text{-}closed}$, has a closed northern boundary and no assimilation within the domain, otherwise its configuration is similar to the other extended domain models.

Closing the northern boundary has noticeable affects on the temperature distribution, the circulation in the model domain and the mass balance of the ice shelf.

The change in the horizontal circulation is mainly in terms of the strength of the circulation. The vertically averaged streamfunction, presented in Figure C.5, shows a circulation similar to the other extended domain runs in Chapter 7 and in this appendix. The strength of the circulation, however, is much reduced with a peak circulation of 0.96 Sv in the dominant gyre in Prydz Bay. The circulation is expected to be weaker than in the other extended domain runs, because the horizontal density gradients are weaker than in other model runs.

The sea ice model produces a well stratified water column in all of the domain, with the salinity ranging from 34.60 PSU, in the deep ocean to the

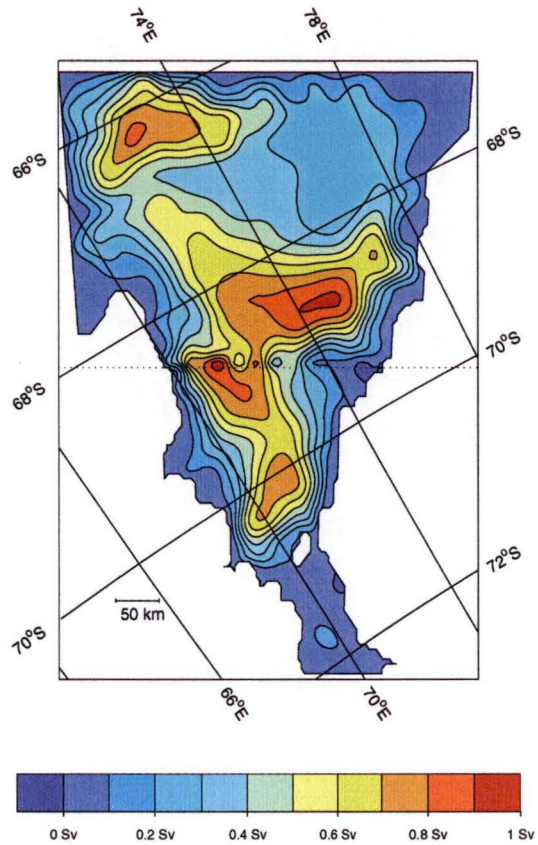

Figure C.5: Vertically integrated streamfunction for the $\text{EXDOM}_{\text{SI-closed}}$ run. The circulation is clockwise about positive features.

north of the domain, to 34.30 PSU, in areas of melting in the ice shelf cavity. Within the cavity the maximum salinity is 34.55 PSU in the inflowing water on the eastern side of the cavity.

The changes in the temperature distribution within the domain can be clearly seen in Figures C.6 and C.7. The temperature over all the domain is significantly cooler than was found in any of the other extended domain model runs. The temperatures within the ocean cavity are similar to those found in the $\text{EXDOM}_{\text{cool}}$ model run (Figures 7.21 and 7.22).

The most significant feature in the temperature distribution is the lack of warm water in the domain. The maximum temperature in the domain is the surface freezing temperature. This is caused by the sea ice model and it clearly leads to the formation of sufficiently cold and saline water on the continental shelf. This relatively cold and saline water is flowing into the cavity under the ice shelf as part of the Prydz Bay Gyre, it is also flowing off the shelf in the direction of the northern boundary.

In Section A′ (Figure C.6a) the water is generally colder, than in Section B′ (Figure C.6b). This is because the warmer water is flowing in on the eastern side of the ocean cavity and out on the western side. However, both sections are relatively homogeneous.

The generally homogeneous nature of the water column on the two north-

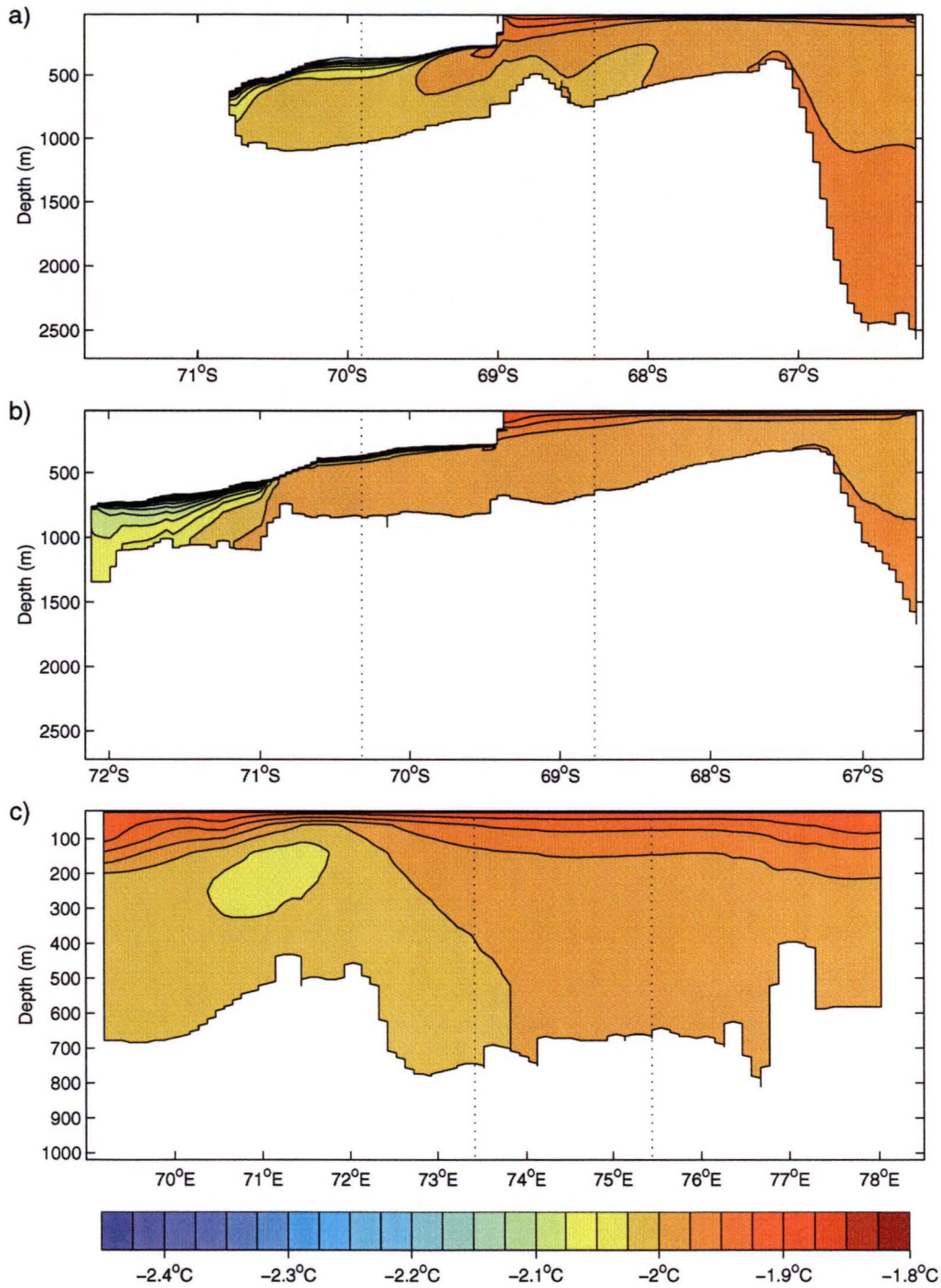

Figure C.6: Temperature cross-sections for the $\text{EXDOM}_{\text{SI-closed}}$ run. a) Section A′, b) Section B′, c) Section D. The locations of the cross-sections is shown in Figure 7.6. The dotted lines indicate where the cross-sections intersect. Note: Temperature scale is modified.

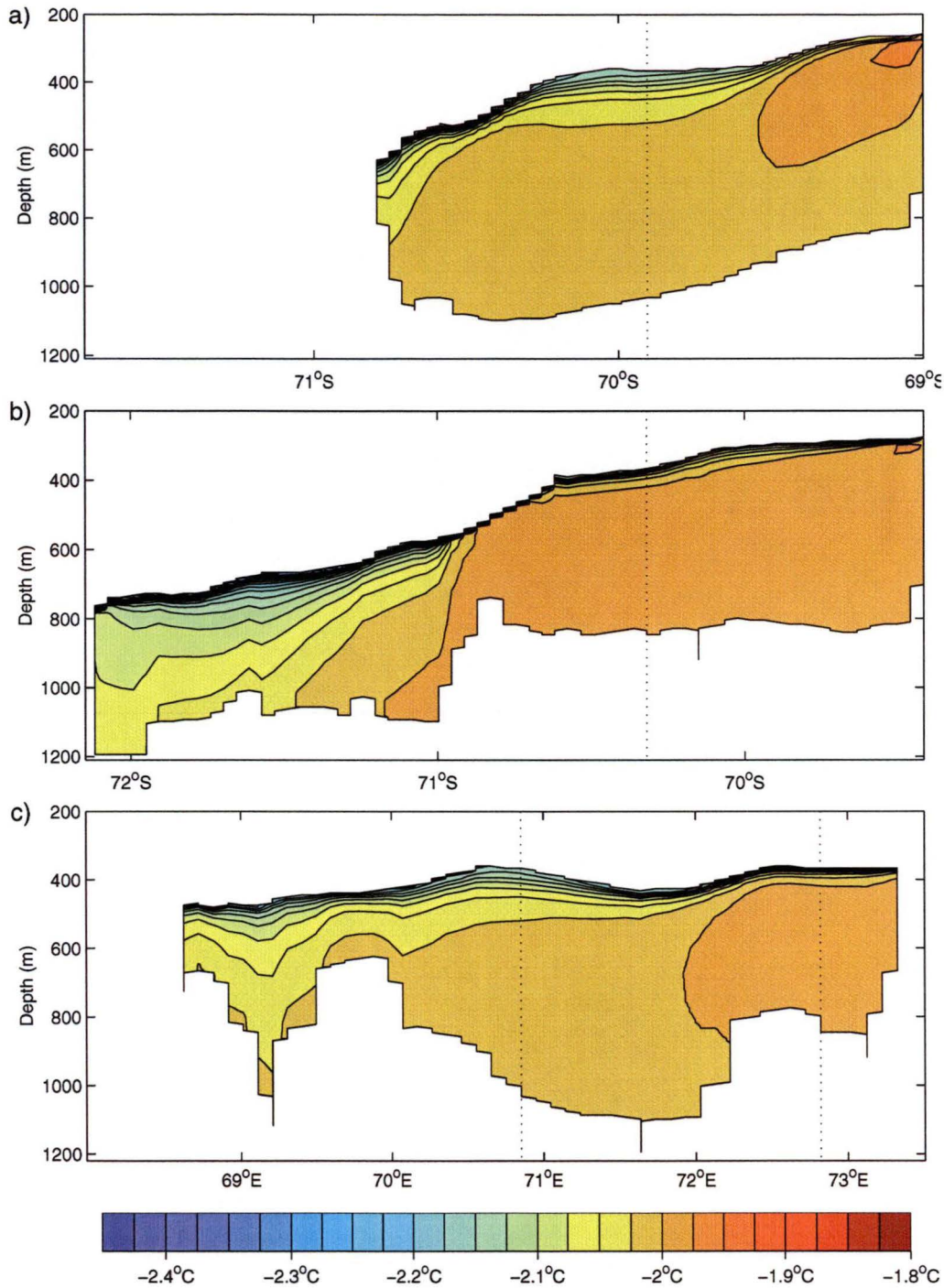

Figure C.7: Temperature cross-sections for the $\text{EXDOM}_{\text{SI-closed}}$ run. a) Section A, b) Section B, c) Section C. The locations of the cross-sections is shown in Figure 7.6. The dotted lines indicate where the cross-sections intersect.

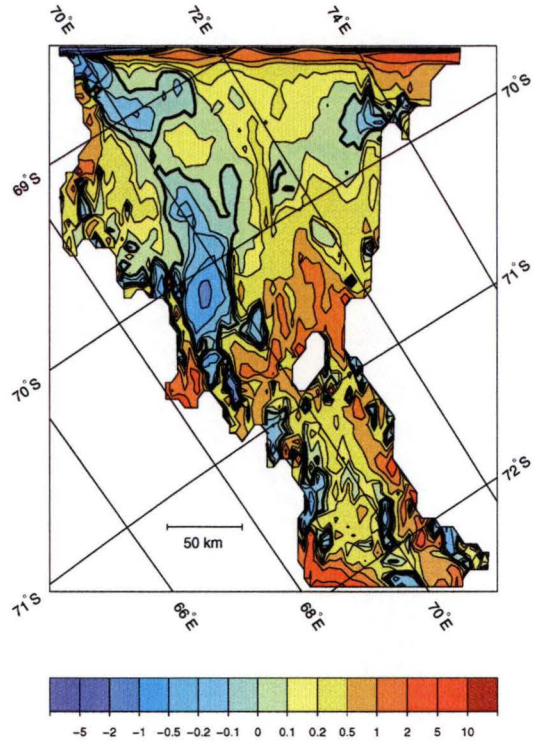

Figure C.8: Rates of melting (+) and freezing (-) from the $\text{EXDOM}_{\text{SI-closed}}$ run. The bold contour denotes the boundary between melting and freezing.

south sections in the ocean cavity is a reflection of the small range of temperatures which can occur within the closed model domain. There are two noticeable deviations from the generally homogeneous water column. In Section A (Figure C.7a) around 69.0°S there is a layer of warm water overlying the water cooled within the ice shelf cavity. This comes from the small amount of recirculation, centred at about 68.8°S 71.0°E, within the dominant gyre. In Section B (Figure C.7b) the southern part of the section is clearly stratified. This stratification appears to follow the same pattern as seen in the model runs, though with less temperature stratification.

The temperature structure in Section D (Figure C.6c) clearly shows the effect of the circulation under the Amery Ice Shelf. There is a clear east-west temperature gradient with warmer water on the eastern side of the section. On the western side, below the stratified layer adjacent to the sea ice, there is a cold core in the water flowing out from under the ice shelf. Within the ice shelf cavity itself the temperature gradient on Section C (Figure C.7c) also clearly shows the inflow of warm water on the eastern side of the domain and the outflow of cold water adjacent to the ice shelf on the western side of the domain.

The colder temperatures in the domain have a significant affect on the melting and freezing rates at the ice shelf-ocean interface. These are shown in Figure C.8. The melting and freezing rates are noticeably reduced compared with those for other extended domain runs, see for example Figure 7.27, and are similar to those found in the cavity only model runs (Chapter 5).

The impact of the reduced melt rates on the basal mass balance of the ice shelf is shown in Table C.1. The mean melting and freezing rates are similar to those found in the cavity only model runs and in the $EXDOM_{cool}$ run. The overall net mass balance of the ice shelf, which in the $EXDOM_{SI\text{-}closed}$ model run has a loss of 14.6 Gta^{-1}, is within the range of mass loss estimates of Wong et al. [1998] and is consistent with the other mass balance terms for the Amery Ice Shelf (Section 3.3).

It is unclear what effect using the same initial conditions for this model run as used for the other sea ice model runs might have on the water column structure. With all the boundaries closed there is no possibility of water warmer than the initial conditions entering the model domain, hence the results from this model run, may be more a reflection of not allowing water warmer than -1.9°C into the model domain, rather than the success of the sea ice model.

C.4 Discussion and conclusions

It was hoped the introduction of a sea ice model to the extended domain model would lead to the formation of cold and saline waters, similar in characteristics to High Salinity Shelf Water, on the continental shelf. It was assumed that if these waters could be formed then the warm water off the continental shelf would be blocked from entering the cavity under the ice shelf, and instead the cold and saline water would enter the cavity. The presence of such water in the cavity was expected to reduce the excessive amount of basal melting.

To a limited extent this has occurred, however, to achieve this all exchange between the model domain and the Southern Ocean had to be blocked. In the $EXDOM_{SI\text{-}closed}$ model run cold and saline waters were able to form, and when this water circulated under the Amery Ice Shelf the excessive quantities of melting found in the majority of the extended domain runs disappeared. The interaction in the model between the ice shelf and the ocean appeared consistent both with the results of the cavity only model runs and with observational estimates of basal mass loss from the ice shelf.

In both model runs, where there was interaction with the Southern Ocean, either through assimilation of observations into the model or through interaction along the northern boundary, the introduction of a simple thermodynamic sea ice model reversed the expected results. In both the $EXDOM_{SI\text{-}basic}$ and $EXDOM_{SI\text{-}\gamma=360}$ runs the temperatures in the model domain and the basal mass balance rates increased to highly unrealistic levels. The increase in warming in the ocean cavity is most likely linked to the increase in the strength of the horizontal circulation, which is significantly larger than in the previous model runs. This increase would be expected to transport more heat from Prydz Bay into the cavity under the ice shelf.

The increase of heat into the ocean cavity led to a reduction in the potential effectiveness of the sea ice model. The warmer water in the cavity greatly increased melting and generated a larger amount of relatively fresh water in the top layers of the ocean cavity. This water then flowed out of the cavity and rose to lie under the sea ice. Although the outflowing water from the cavity

was cold, it did not drive sufficient freezing to overcome the low salinity of the outflowing waters. Because of this the outflow water formed an insulating layer at the top of the water column that effectively cut off salinity driven vertical mixing on the continental shelf.

The main aim of the first two experiments was to see if the production of cold and saline water via sea ice formation would block the intrusion of warm water onto the continental shelf and its subsequent flow into the ocean cavity under the ice shelf. In this regard introducing a sea ice model was unsuccessful. The third experiment ($\text{EXDOM}_{\text{SI-closed}}$) showed that the introduction of a relatively simple sea ice model could produce the cold and saline waters that are likely to presently circulate under the Amery Ice Shelf. However to achieve this it was necessary to artificially restrict the circulation of warm water within the model.

In some respects the results from the $\text{EXDOM}_{\text{SI-closed}}$ model run are similar to those of the $\text{EXDOM}_{\text{cool}}$ model run (Section 7.2.4). The aim of both model runs was the production of cold and saline water on the continental shelf. The success of both model runs in producing ice shelf basal mass balance estimates similar to observationally based estimates suggests that this is a key process missing from other model runs. The problem remains, that to get cold and saline water in the model it was necessary to either use unrealistic boundary conditions or modify the observations being assimilated into the domain.

That these modifications are necessary indicates there still remain problems with the extended domain model. It remains unclear if this is because the sea ice model does not include the processes necessary to produce the deep convection which would block the intrusion of warm water onto the shelf, or if the problems are related to other defects in the model design. Absent processes which might be important in a sea ice model include ice export from the domain and strong freezing in ice leads. However, before considering these possibilities there are other approaches or changes to the model design which are probably more profitable to investigate, some of these were outlined in Section 7.5.

Appendix D

Cavity domain model driven with extended domain forcing

The main objective of utilising the extended domain model in Chapter 7 was to realistically represent the heat, salt and mass transport across the ice front. A secondary aim of using the extended domain model was to see if suitable boundary conditions could be found for use with the cavity model. The motivation for this is that the extended domain model is 3.5 times more computationally expensive, and for some questions the cavity model, with appropriate boundary conditions, would provide suitable answers. An example is climate change scenarios where finding suitable forcing for the open ocean in the extended domain model could be problematic.

The results of Chapter 7 were inconclusive as to which expanded domain model run best represented the circulation and water mass properties near the ice front. For the exploratory study in this appendix the $\text{EXDOM}_{\gamma=50}$ run (Section 7.2.2) was chosen.

The data sets needed from the extended domain model to drive the cavity model are the temperature, salinity, and streamfunction along the ice front. The temperature and salinity are needed for restoring inflow tracer points as detailed in Section 4.3.4. The streamfunction is used to provide a boundary condition for the barotropic component of velocity.

In addition to the data sets from the extended domain models, the temperature and salinity data sets utilised in the experiments in Chapter 5 are also used. These data sets are used because comparisons between the observations and model results in Chapter 7 show the extended domain model temperatures near the ice front are warmer than is realistic.

Two model runs are presented here. The first experiment, labelled $\text{AIS}_{\gamma=50\text{TS}}$, uses the streamfunction, temperature and salinity from the $\text{EXDOM}_{\gamma=50}$ run. In the second model run, labelled $\text{AIS}_{\gamma=50}$, the temperature and salinity from the $\text{EXDOM}_{\gamma=50}$ run are replaced with the temperature and salinity used in Chapter 5.

The two methods of applying the $\frac{\partial \Psi}{\partial \lambda}$ boundary condition to the streamfunction, as discussed in Section 4.3.5, were trialled. Of the two methods, only the specification of both the streamfunction boundary row and the first row inside the domain would spin up. To set the cross-boundary transport via

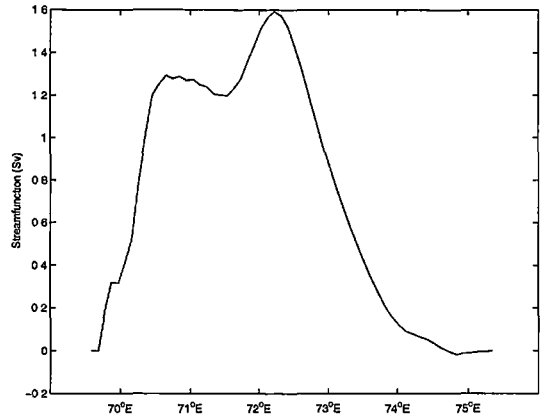

Figure D.1: The streamfunction along the ice front from which the barotropic velocity components are derived for model runs $AIS_{\gamma=50TS}$ and $AIS_{\gamma=50}$.

these two streamfunction rows the streamfunction gradient along the ice front is needed. This was found by averaging Ψ on the two streamfunction grid point rows closest to the ice front in the $EXDOM_{\gamma=50}$ run. From the average of Ψ the streamfunction gradient along the ice front was found and applied to the boundary row and the first row inside the cavity in the $AIS_{\gamma=50TS}$ and $AIS_{\gamma=50}$ model runs. The streamfunction from which the gradient is found is shown in Figure D.1.

Setting the streamfunction boundary conditions in this way generates a cross ice front barotropic velocity component which is the same in the $AIS_{\gamma=50TS}$ and $AIS_{\gamma=50}$ runs as in the $EXDOM_{\gamma=50}$ run. It does, however, change the along ice front barotropic velocity component to zero.

The other boundary conditions on the cavity model are identical to those used in the cavity models presented in Chapters 5 and 6. As in most of the model runs in these chapters the restoring time constant on the tracer boundary conditions is set to 80 days.

D.1 Extended domain streamfunction and tracer forcing

For the $AIS_{\gamma=50TS}$ run the temperature and salinity restoring fields along the ice front are also extracted from the $EXDOM_{\gamma=50}$ run. They are taken from the first tracer grid row under the ice shelf and are shown in Figure D.2.

The vertically integrated streamfunction for the $AIS_{\gamma=50TS}$ run is shown in Figure D.3. The circulation has few similarities with the circulation in the cavity for the $EXDOM_{\gamma=50}$ run from which the forcing was extracted. Instead, the streamfunction structure is similar to the streamfunction in the $AIS_{P\bar{v}}$ run (Figure 5.15).

In the $EXDOM_{\gamma=50}$ run the circulation in the northern part of the cavity is dominated by a single gyre with two centres which occupies all of the northern part of the cavity. In the $AIS_{\gamma=50TS}$ run the northern half of the circulation

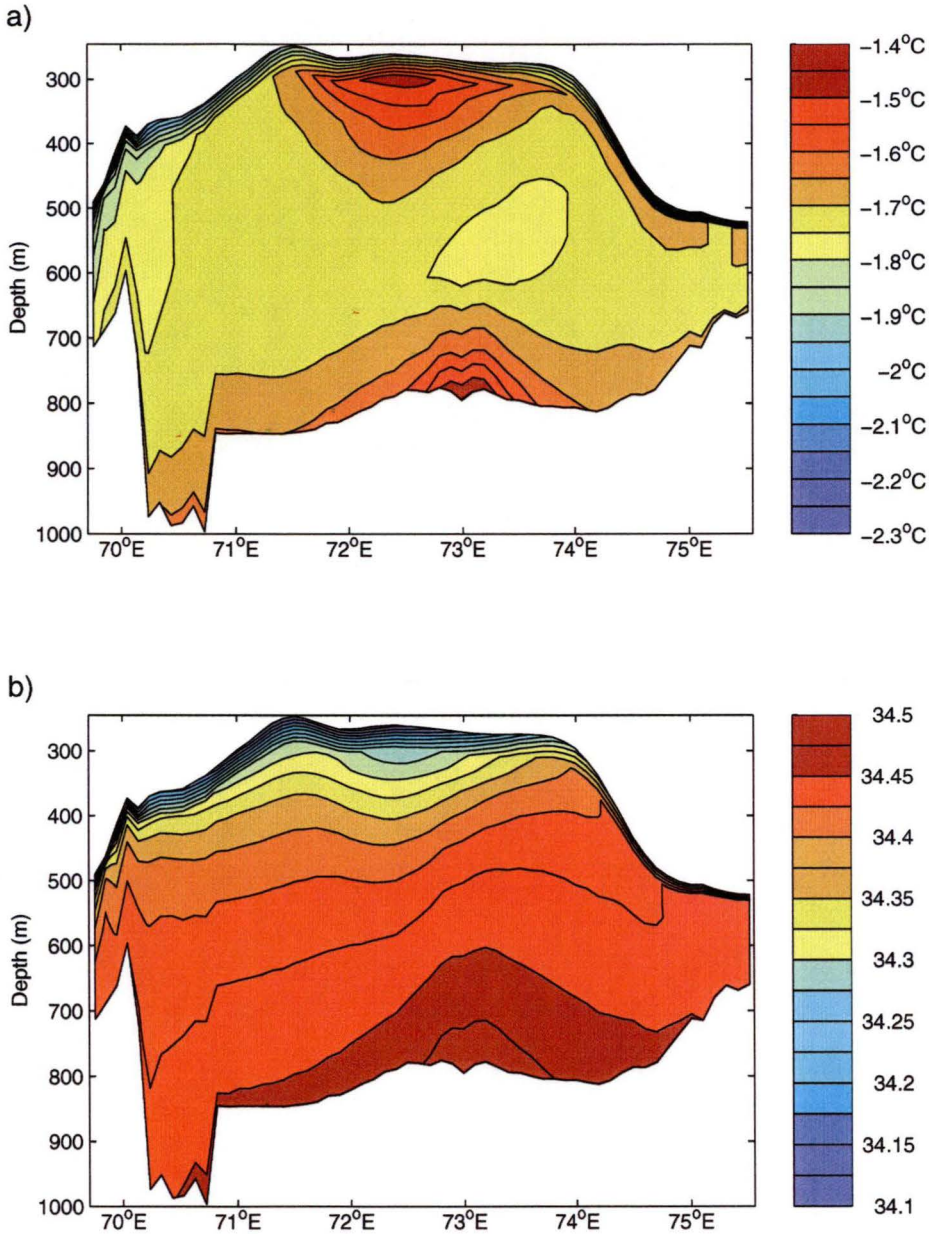

Figure D.2: The temperature and salinity along the ice front used for forcing in the $\text{AIS}_{\gamma=50\text{TS}}$ experiment. They are extracted from the first row under the ice shelf for the $\text{EXDOM}_{\gamma=50}$ run.

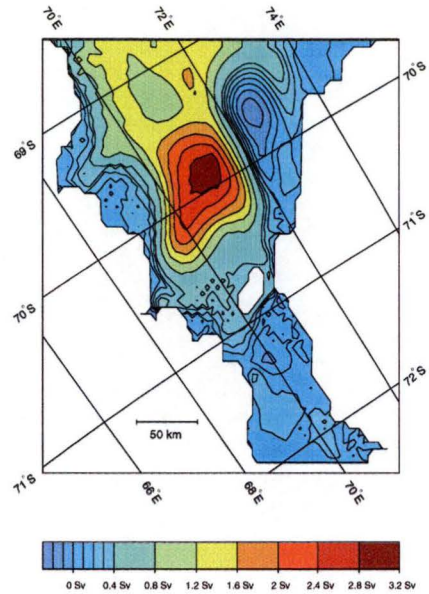

Figure D.3: The vertically integrated streamfunction for the $AIS_{\gamma=50TS}$ run. The circulation is clockwise about positive features.

changes. The circulation now contains features similar to those seen in the $AIS_{P\bar{v}}$ and $AIS_{P\partial\Psi}$ model runs in Chapter 5. The main changes are in the north-east of the domain and between the Central Gyre and the ice front.

The dominant feature of the circulation in the $AIS_{\gamma=50TS}$ run has similarities with both the Central and Main Gyres found in the cavity model runs in Chapter 5. In the southern part of the gyre, where the gyre is strongest, its transport is ~3.11 Sv; about the same magnitude as the $AIS_{P\bar{v}}$ run. To the north of this is a local minimum in the streamfunction in the same position as the Northern Gyre.

The broad inflow region in the north-east corner of the domain which forms part of the Dominant Gyre in the extended domain assimilation runs is not present. Instead the inflow circulation from the boundary is steered around a region of shallow water column thickness.

The temperature on Sections A, B, and C is shown in Figure D.4. There are several differences in the temperature structure in the $AIS_{\gamma=50TS}$ run, compared with the same cross-sections in the $EXDOM_{\gamma=50}$ model run (Figure 7.15). In all three sections the temperature of the warmest waters decreases by ~0.15°C, and the temperature in the intermediate waters increases. In Sections A (Figure D.4a) and B (Figure D.4b) the temperature of the water adjacent to the ice shelf near the ice front is cooler than in the $EXDOM_{\gamma=50}$ run. There is also an increase in the thickness of the melt-water layer near the ice front. The change in the temperature and thickness of the melt-water layer is caused by the change in the patterns of melting and freezing at the ice shelf-ocean interface.

Figure D.5 shows the melting and freezing rates. In the $EXDOM_{\gamma=50}$ model run the northern part of Sections A and B were in areas of high melting. In contrast, in the $AIS_{\gamma=50TS}$ run the northern parts of these sections are in areas of freezing. This leads to the decrease of temperature and the increase in the

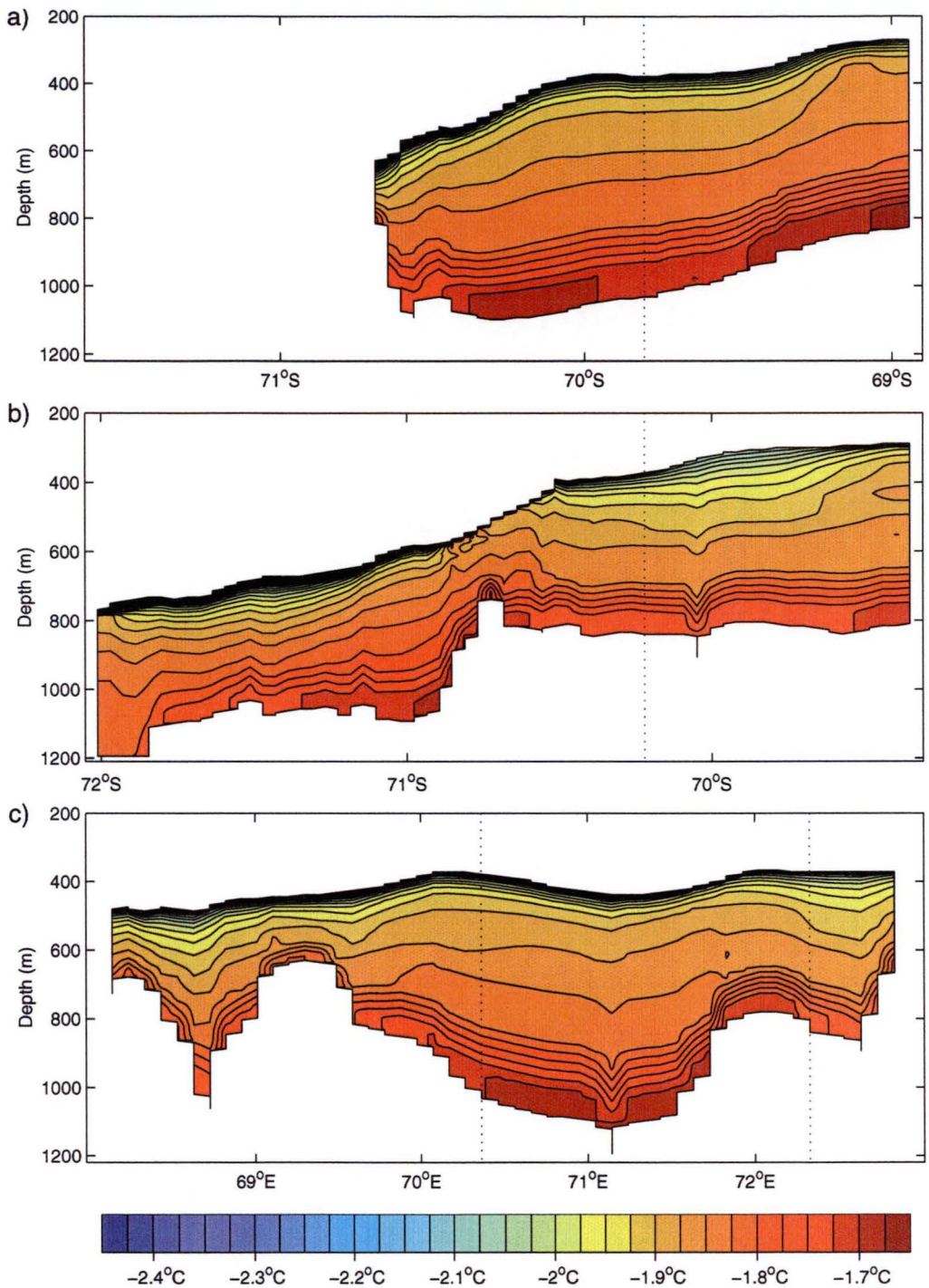

Figure D.4: Temperature cross-sections of the model domain for the $\text{AIS}_{\gamma=50\text{TS}}$ run. a) Section A, b) Section B, and c) Section C. The locations of the cross-sections are shown in Figure 5.4.

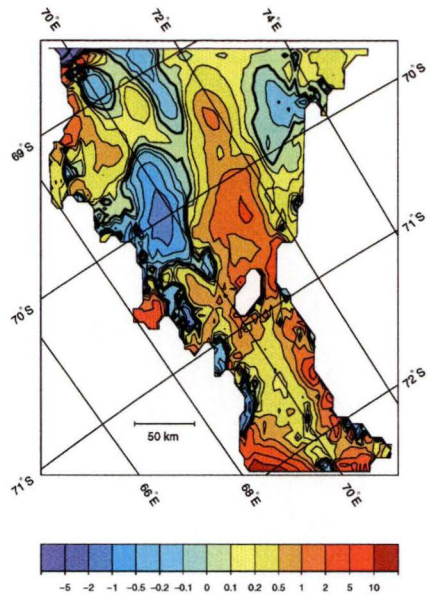

Figure D.5: Melting (+) and freezing (-) rates for the $AIS_{\gamma=50TS}$ run in ma^{-1}. The bold contour denotes the boundary between melting and freezing.

Table D.1: Mass balance estimates for the $AIS_{\gamma=50TS}$ and $AIS_{\gamma=50}$ runs.

Amery Model Run (AIS)	Mean Rates for Freezing Zone (ma^{-1})	Mean Rates for Melting Zone (ma^{-1})	Mean Rates for Whole (Loss) (ma^{-1})	Area of Melt (%)	Mass Change Rates Freezing (Gta^{-1})	Mass Change Rates Melting (Gta^{-1})	Mass Change Rates Net Loss (Gta^{-1})
γ=50TS	1.17	0.85	0.34	75.1	14.8	32.4	17.6
γ=50	1.33	0.73	0.28	78.0	14.9	29.1	14.2

Note: The total area of the ice shelf is 5.6 x 10^4 km^2.

melt-water layer thickness.

The melting and freezing rates for the $AIS_{\gamma=50TS}$ run show several noticeable changes from the $EXDOM_{\gamma=50}$ run. The first is the general reduction in melting within the domain. The second is the general absence of melting along the ice front. The third is the area of accumulation in the north-west corner of the domain.

The changes in the melting and freezing distribution impact on the mass balance of the ice shelf. This can be seen in the mass balance measures presented in Table D.1. The net loss from the ice shelf reduces from 66.8 Gta^{-1} to 17.6 Gta^{-1}. This is within the range of the estimates by Wong et al. [1998], and agrees with estimates from other cavity model runs in this thesis. The mass change components are, however, relatively large, with 32.4 Gta^{-1} of loss from melting and 14.8 Gta^{-1} of accretion. The large amount of accretion occurs mainly in the north west corner of the model domain.

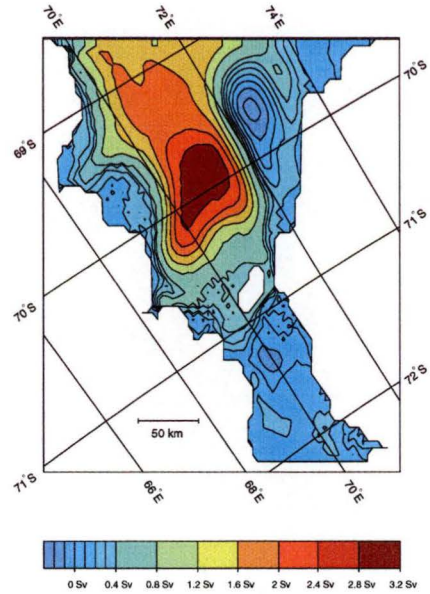

Figure D.6: The vertically integrated streamfunction for the $AIS_{\gamma=50}$ run. The circulation is clockwise about positive features.

D.2 Extended domain streamfunction forcing only

In the $AIS_{\gamma=50}$ model run the temperature and salinity fields calculated for the cavity models (Figure 4.6) are used in place of temperature and salinity from the extended domain runs. This is done as the extended domain model runs appear to be advecting water which is warmer than observations suggest is realistic into the cavity. It is anticipated this could be avoided by the use of different temperature and salinity fields. The temperature and salinity fields used in Chapter 5, which are cooler than those shown in Figure D.2, are used.

The streamfunction used to derive the barotropic velocity terms in the $AIS_{\gamma=50}$ run is the same as that used in the $AIS_{\gamma=50TS}$ run (Figure D.1).

The horizontal circulation, as shown by the streamfunction, for the $AIS_{\gamma=50}$ run is shown in Figure D.6. The circulation is similar to that found for the $AIS_{\gamma=50TS}$ run. There are some differences, particularly in the Main Gyre where the structure and transport changes and the maximum transport reduces from ~3.11 Sv to ~2.78 Sv. Also the local minimum in the streamfunction, which is seen in the $AIS_{\gamma=50TS}$ run in the same position as the Northern Gyre, is no longer present.

The three temperature cross-sections for the $AIS_{\gamma=50}$ run are shown in Figure D.7.

At the northern end of Section A (Figure D.7a) is an anomalous patch of warm water. It is present here due to diffusion from a region of unrealistic model behaviour localised to a few grid points in the north-west corner of the model domain. The behaviour of the model in the north-western corner of the domain is verging on the unstable. In this area of the domain there are

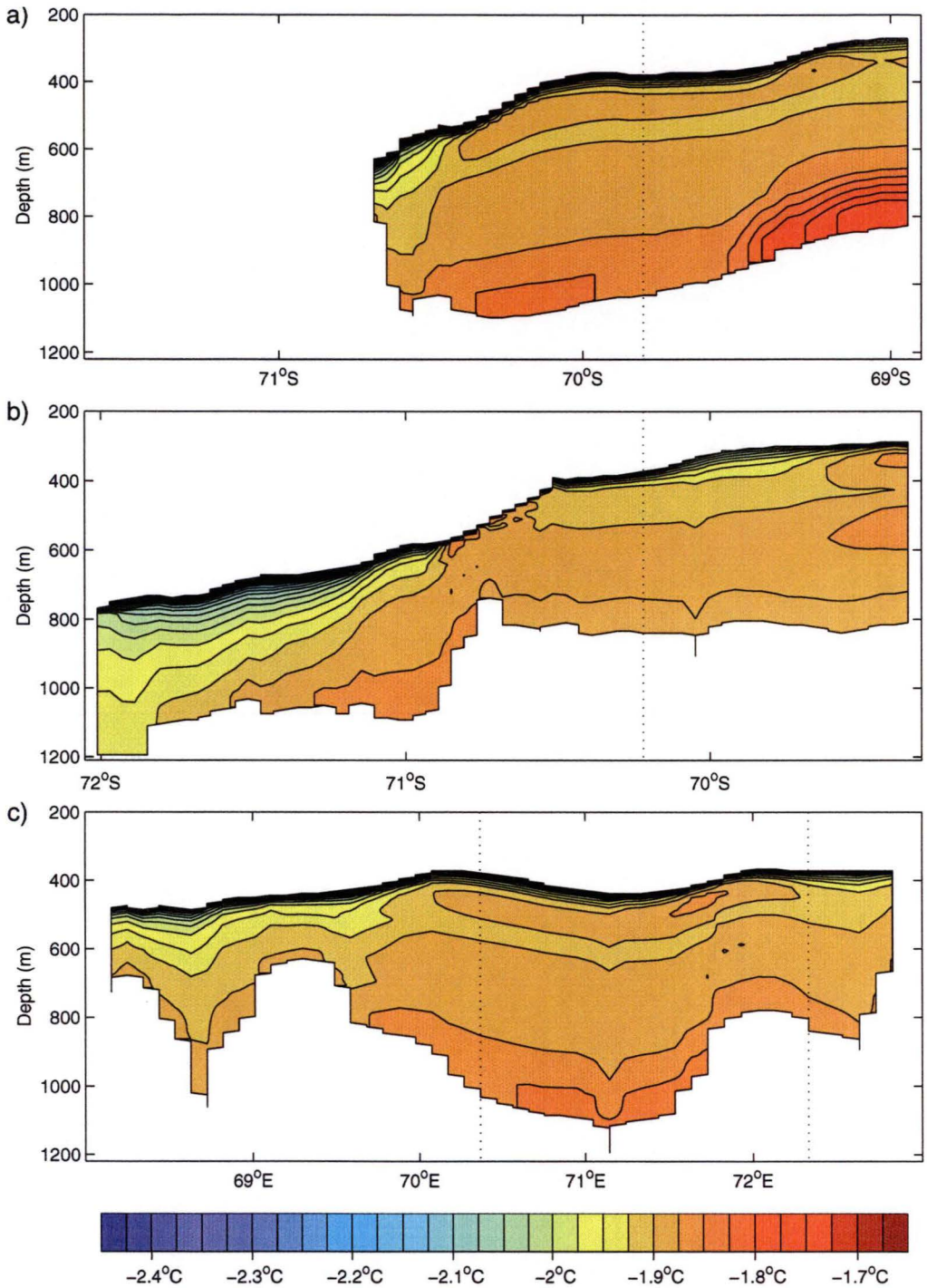

Figure D.7: Temperature cross-sections of the model domain for the $AIS_{\gamma=50}$ run. a) Section A, b) Section B, and c) Section C. The locations of the cross-sections are shown in Figure 5.4.

high velocities (50 to 100 cms^{-1}), high freezing rates and both overly warm and overly cold water. It is unclear what mechanism creates these unrealistic results in this part of the model domain. However, it is likely to be a product of the restricted extent of the domain, and the application of a geostrophic boundary condition. The boundary condition expects a net outflow from this area, but by also setting the along front barotropic velocities to be zero it restricts flow into this small part of the domain.

In all three of the temperature cross-sections there are inversions in the temperature. These inversions are formed by the advection of warm water from the boundary forcing. The inversions in Section A and in the upper part of Section C are formed from the warmest parcel of water in the boundary forcing, which is situated between 73°E and 74°E at the ice front (Figure 4.6a). This water flows in the eastern side of the Main Gyre where advection and diffusion spread the warm layer along the base of the ice shelf. The water which forms inversions in Section B, and the bottom part of Section C comes from the water parcel on the eastern side of the ice front at about 600 m. This water has a maximum temperature of -1.82°C (Figure 4.6a) as it flows into the domain. It is then diverted westward, to the north of the shallow region on the east side of the Main Gyre. Here it joins the gyre and flows south. It has not been seen in other model runs, with the observationally derived temperature and salinity at the ice front, as it is only with the current velocity boundary conditions that there is inflow in this region.

The temperature structure in the southern part of Section A is correlated with the strength of the horizontal circulation in the western side of the Main Gyre, which it bisects. At the southern end of the cross-section the gyre has its strongest velocities and flow lies along the cross-section (Figure D.6). Here, the temperature structure in the bottom part of the water column is homogeneous. Further north (around 69.5°S) where the flow broadens out and no longer flows along the cross-section the temperature structure is stratified, with warmer waters trapped close to the ice front.

Apart from the temperature inversion, the temperature structure in both Section B (Figure D.7b) and Section C (Figure D.7c) is very similar to that seen for the same sections in the $AIS_{P\bar{v}}$ run (Figure 5.17).

The distribution of melting and freezing in the $AIS_{\gamma=50}$ run does not vary greatly from that found in the $AIS_{\gamma=50TS}$ run (Figure D.5). This is seen in the mass balance estimates presented in Table D.1.

The large amount of accumulation in both the $AIS_{\gamma=50TS}$ run and $AIS_{\gamma=50}$ run on the western side of the ice front is partly an artifact of the ice front boundary conditions. The area in which it occurs is close to the ice front and the barotropic velocity components in this area are controlled by the boundary conditions, this restricts the ability of the model to mix water from this part of the domain into the interior. The high freezing rates are responsible for approximately 9.7 Gta^{-1} and 10.1 Gta^{-1} of mass gain in the $AIS_{\gamma=50TS}$ and $AIS_{\gamma=50}$ runs, respectively.

D.3 Discussion and Conclusions

In this appendix an attempt has been made to use the results of the $\text{EXDOM}_{\gamma=50}$ extended domain model run to prescribe the boundary conditions at the ice front for the cavity domain model ($\text{AIS}_{\gamma=50\text{TS}}$). In addition, a further run of the cavity domain model with only the streamfunction from the $\text{EXDOM}_{\gamma=50}$ run was completed. In this run the temperature and salinity fields used in Chapter 5 were used at the ice front. In these two model runs the mass exchange across the ice front was prescribed in terms of the across ice front barotropic velocity component.

There were some changes to the circulation in the ice shelf cavity between the cavity domain models and that seen in the $\text{EXDOM}_{\gamma=50}$ run. The most significant difference was in the strength of the circulation. In both the $\text{AIS}_{\gamma=50\text{TS}}$ and $\text{AIS}_{\gamma=50}$ runs the Main Gyre was significantly stronger. The mass exchange across the ice front was also greater. In the $\text{EXDOM}_{\gamma=50}$ run the inflow and outflow components were $\sim$1.77 Sv, in the $\text{AIS}_{\gamma=50\text{TS}}$ and $\text{AIS}_{\gamma=50}$ runs they were $\sim$3.02 Sv and $\sim$1.96 Sv, respectively.

In the $\text{AIS}_{\gamma=50\text{TS}}$ run the temperature in the ocean cavity was reduced compared with that seen in the $\text{EXDOM}_{\gamma=50}$ run. This significantly changed the mass lost by the ice shelf from the 66.7 Gta^{-1} lost in the $\text{EXDOM}_{\gamma=50}$ run to 17.6 Gta^{-1}. Changing the temperature and salinity forcing along the ice front to that used in Chapter 5, did not further significantly change the amount of ice lost. In the $\text{AIS}_{\gamma=50}$ run 14.2 Gta^{-1} of ice was lost.

The success of the $\text{AIS}_{\gamma=50\text{TS}}$ and $\text{AIS}_{\gamma=50}$ runs is only partial; there are some discrepancies between these model runs and the $\text{EXDOM}_{\gamma=50}$ run. For example in the strength of the transport in the Main Gyre and across the ice front. There are also some features in the model results which are unlikely to be realistic. The most significant of these is the abnormally large amount of freezing in the north-west corner of the domain adjacent to the ice front. This is unrealistic as the amount of supercooled water needed to drive this amount of freezing is unlikely to stay inside the ocean cavity, as any buoyant melt-water would flow out across the ice front, which it is not able to do in the cavity only model. This problem in the northwest corner is localised and does not affect the results in the rest of the model domain.

The discrepancies between the model results for the $\text{EXDOM}_{\gamma=50}$ run and the $\text{AIS}_{\gamma=50\text{TS}}$ and $\text{AIS}_{\gamma=50}$ runs, suggests extracting suitable forcing data from the results of the $\text{EXDOM}_{\gamma=50}$ run may not be as simple as assumed. The most likely reason for this is that the streamfunction and tracer restoring fields are applied to an at rest ocean. During the model spin up period the ocean conditions in the cavity would not necessary evolve to the same state as was found in the $\text{EXDOM}_{\gamma=50}$. The other factor which is likely to impact on the results is the freedom in the baroclinic velocity components. Unlike the barotropic components of velocity these are not prescribed. This allows the transport across the ice front in the cavity models to be different from that found in the $\text{EXDOM}_{\gamma=50}$ model. This effect occurs as there are substantial differences in the mass transport components across the ice front in the $\text{EXDOM}_{\gamma=50}$, $\text{AIS}_{\gamma=50\text{TS}}$, and $\text{AIS}_{\gamma=50}$ model runs.

It is clear changes are required to enable the results of the extended domain model to be used in driving the cavity model to reproduce similar ocean cavity results between the two models. Two possible changes which could resolve this problem are: modifying the boundary conditions, so mass, heat and salt transport across the ice front are similar in both the extended domain and cavity models; and utilising the extended domain model results in the cavity as initial conditions for the cavity model. However, before attempting to achieve better agreement progress is needed in the quality of the extended domain model results.

Appendix E

Southern expansion of the ocean cavity under the Amery Ice Shelf

Recent analysis by Phillips [1998] of the Amery Ice Shelf using satellite altimetry and newly available ice thickness data suggests the southern grounding line of the ice shelf is further south than was found from the comparison of bedrock depth and ice shelf thickness in this thesis (Section 4.5). If so, this could impact greatly on the results found in this thesis. However, the extent and dimensions of the ocean cavity under the ice shelf in the southern part of the domain are still unclear.

In this appendix the preliminary results from two exploratory model runs where the cavity under the Amery Ice Shelf is expanded are presented.

In Section 4.5 the extent of the ice shelf cavity and the location of the southern grounding line was found by calculating the water column thickness from the ice shelf draft and bathymetry. Outside the current ice shelf cavity the bathymetry and ice thickness data used in defining the current ocean cavity provide little assistance in describing the possible dimensions of any southward expansion. It is however known that the general trend of the ice shelf is to thicken with further distance south [Morgan and Budd, 1975; Phillips, 1998].

The maximum possible zonal and meridional extent of the ice shelf cavity can be inferred from the positions of the mountain ranges which border the Lambert Glacier. For the two exploratory expansions it has been assumed that, the ice shelf grounding line is near Mt Stinear (73.0°S 66.3°E), the eastern side of the cavity is bounded by the Mawson Escarpment, and the western side is bounded by the Southern Prince Charles Mountains.

In the first experiment, labelled EC_A, the north-south variation in the ice shelf draft is found by extrapolating the trend in the maximum draft in the current cavity. This is chosen as it leads to a thick ice shelf over a deep bed rock depression near the confluence in the Lambert Glacier. The existence of such a bed rock depression was reported by Morgan and Budd [1975] in their radio echo sounding study of the Lambert Glacier. The east-west variation in the ice shelf draft for the cavity extension propagates from the east-west variation at the current grounding line into the extension. The ice shelf draft for the EC_A run is shown in Figure E.1.

The north-south variation in the second experiment, labelled EC_B, is found

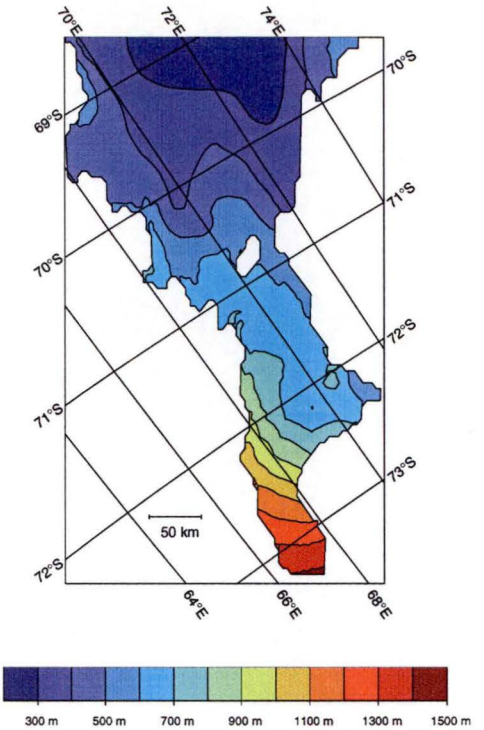

Figure E.1: The ice shelf draft used in the EC_A run.

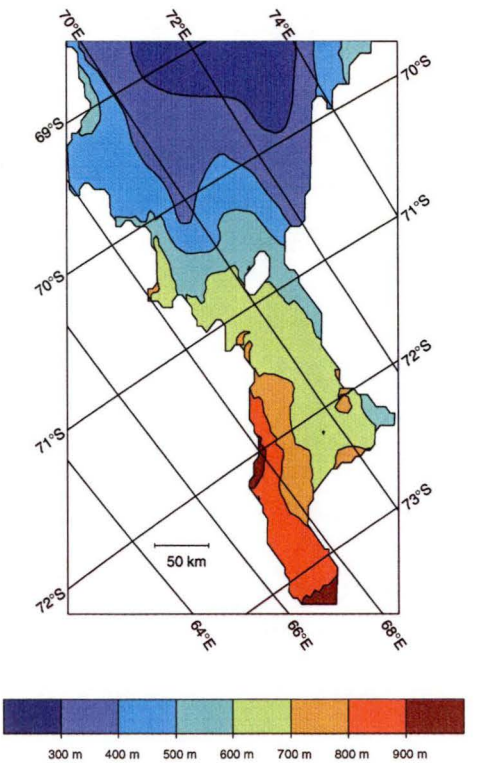

Figure E.2: The ice shelf draft used in the EC_B run.

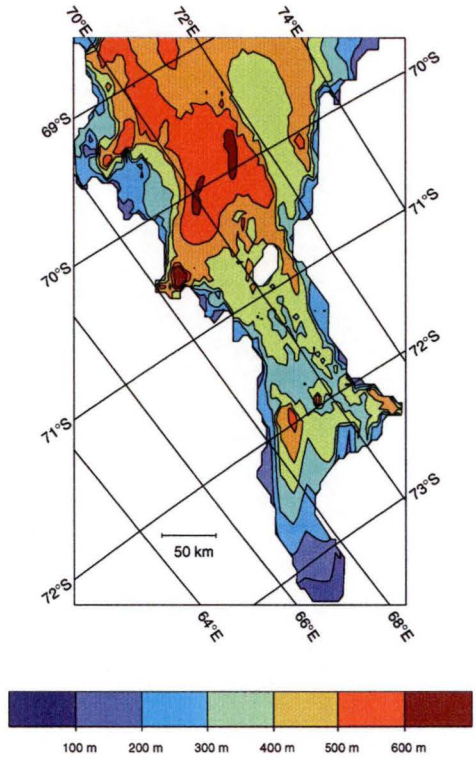

Figure E.3: The water column thickness used in both the EC_A and EC_B runs.

by extrapolating the ice shelf draft from the current grounding line, using the gradient of the mean ice shelf draft in the current domain. Again the east-west variation in the cavity extension comes from the propagation of the east-west variation at the current grounding line into the extension. The ice shelf draft for the EC_B run is shown in Figure E.2.

There is no useful information on which to base the expansion of the bathymetry under the cavity. Instead it has been assumed that the water column thickness would taper to a thickness of 50 m at the grounding line. This is the minimum depth able to be resolved by the model. The same water column thickness is used in both of the EC_A and EC_B runs, and is shown in Figure E.3

Apart from the changes related to expanding the ice shelf cavity to the south, the model implementation is otherwise identical to that used in the $AIS_{\Psi=0}$ model run (Section 5.2.2).

E.1 Expanded cavity experiment A

The horizontal circulation in the expanded ocean cavity for the EC_A run is shown by the vertically integrated streamfunction in Figure E.4. The Central, Northeastern and Northern Gyres are largely unchanged from those found in the $AIS_{\Psi=0}$ run (Figure 5.9). South of the Central Gyre and north of the domain extension there are substantial changes in the horizontal circulation compared with the $AIS_{\Psi=0}$ run. This part of the cavity is dominated by a series of interconnected anticlockwise gyres. The northern part of this circulation is similar

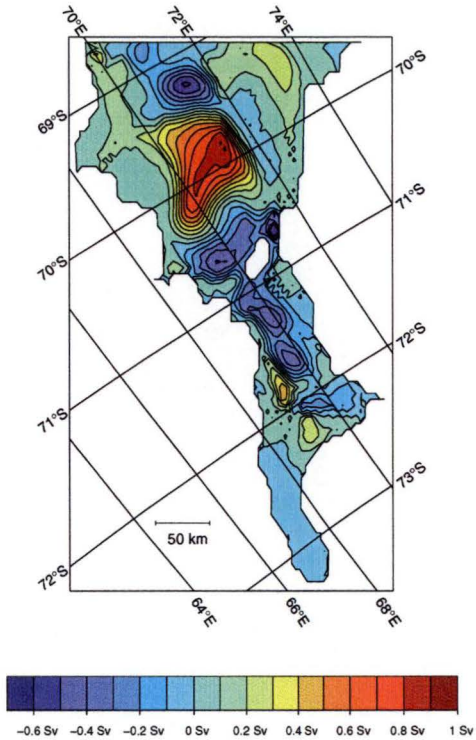

Figure E.4: Vertically integrated streamfunction for the EC_A run. The circulation is clockwise about positive features.

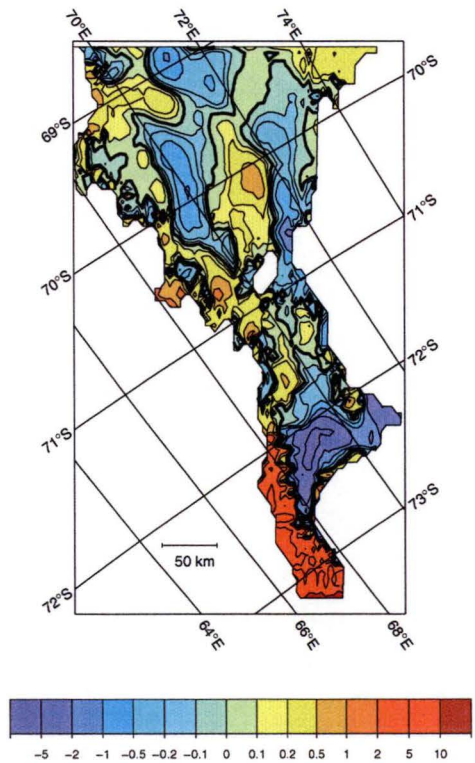

Figure E.5: Rates of melting (+) and freezing (-) from the EC_A run. The bold contour denotes the boundary between melting and freezing.

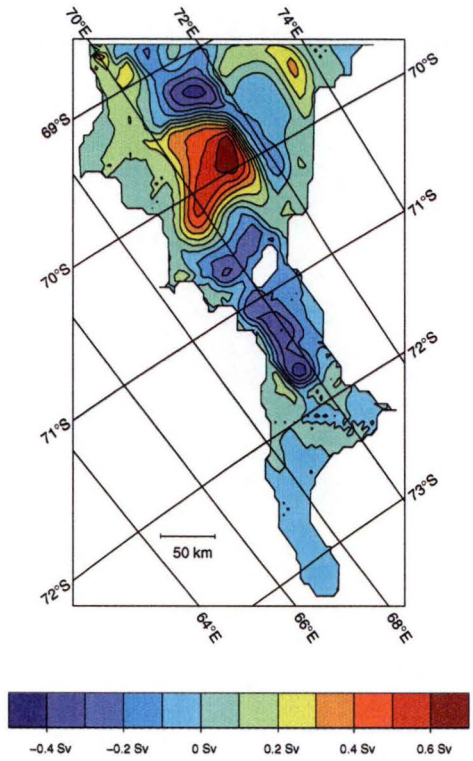

Figure E.6: Vertically integrated streamfunction for the EC_B run. The circulation is clockwise about positive features.

to that seen in the closed boundary run (Figure 5.2), with the South-Central and Southern Gyres controlling circulation around the Central Grounded Zone. In the cavity extension the horizontal circulation is relatively weak and the circulation appears to be dominated by the overturning circulation.

The overturning circulation is driven by the step north-south ice shelf gradient and the intensive areas of melting and freezing in the domain extension. The areas of intense melting and freezing can be seen in Figure E.5. North of the domain expansion and south of the Central Gyre the pattern of melting and freezing is different from that seen in the $AIS_{\Psi=0}$ run. This change reflects the modified horizontal circulation. In the areas of the Central, Northeastern, and Northern Gyres there is a slight increase in the rate of melting and a doubling of the rate of freezing. The increase in the amount of freezing occurs because of the increased availability of melt-water adjacent to the ice shelf-ocean interface. There is also a change from melting to freezing in the channel to the east of the Central Grounded Zone.

E.2 Expanded cavity experiment B

The streamfunction in the EC_B run is shown in Figure E.6. It shows a horizontal circulation which is similar in most of the cavity to that seen in the EC_A run (Figure E.4), but with a reduced transport. The transport in all the gyres is reduced from that seen in run EC_A. The transport in the Central, Northern,

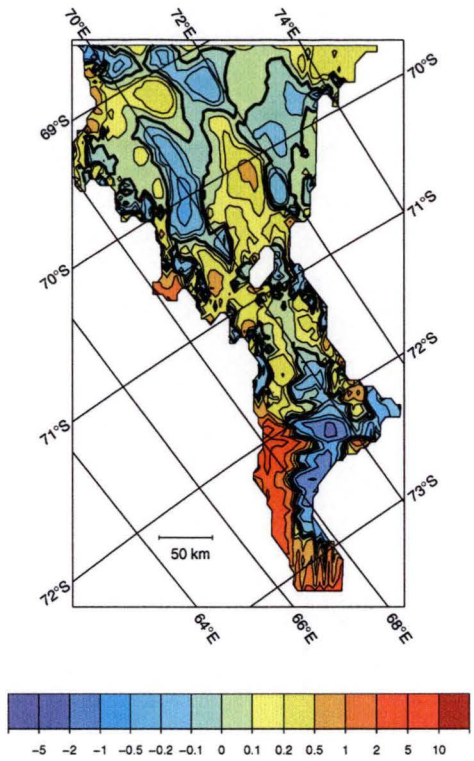

Figure E.7: Rates of melting (+) and freezing (-) from the EC_B run. The bold contour denotes the boundary between melting and freezing.

and Northeastern Gyres is similar in strength to that seen in the $AIS_{\Psi=0}$ run (Figure 5.9).

The different model domain expansion in the EC_B run leads to a change in the pattern of melting and freezing at the ice shelf-ocean interface from the EC_A run. The melting and freezing rates for the EC_B run are shown in Figure E.7. In the south of the domain the melting and freezing rates are less than those seen in the EC_A run, but they still have a strong gradient in the melting and freezing pattern.

E.3 Discussion and conclusions

The main aim of these expanded cavity runs is to determine if a more southerly grounding line, as suggested by Phillips [1998], will impact on the circulation in the ocean cavity and the basal component of the ice shelf mass balance.

The extension of the domain and the change in the ocean circulation leads to substantial changes in the ice shelf in the pattern of melting and freezing. The effect of these changes on the basal component of ice shelf mass balance is shown in Table E.1. Also shown are the mass balance estimates for the $AIS_{\Psi=0}$ run. The $AIS_{\Psi=0}$ run is presented as it has the same ice front boundary conditions as the EC_A and EC_B runs. The format of the table is the same as those presented in other chapters (e.g., Table 5.1).

In both the EC_A and EC_B runs the expansion of the domain and the ac-

Table E.1: Estimates of the mass balance rates for the expanded cavity runs.

	Mean Rates for			Area of	Mass Change Rates		
	Freezing Zone (ma^{-1})	Melting Zone (ma^{-1})	Whole (Loss) (ma^{-1})	Melt (%)	Freezing (Gta^{-1})	Melting (Gta^{-1})	Net Loss (Gta^{-1})
$AIS_{\Psi=0}$	0.16	0.40	0.21	66.6	2.8	13.4	10.6
EC_A	0.71	1.01	0.19	52.2	21.3	32.9	11.6
EC_B	0.36	0.52	0.18	61.3	8.6	19.9	11.3

Note: The total area of the ice shelf is 6.8 x 10^4 km^2, in the EC_A and EC_B runs, and 5.6 x 10^4 km^2 for the $AIS_{\Psi=0}$ run.

companying change in the melting and freezing has not substantially changed the overall ice shelf mass balance. The mass change components of melting and freezing have changed — by a large amount in the EC_A run and a lesser amount in the EC_B run. The net loss from the ice shelf has increased, but not in proportion to the expansion of the ocean cavity. In both the EC_A and EC_B runs the net mass loss from the ice shelf changes by less than 10% in comparison with the $AIS_{\Psi=0}$ run. The increased area of the cavity leads to a drop in the net melt rate.

In Chapter 5 the thickness of the marine ice layer along several ice shelf flowlines was calculated using the method outlined in Appendix A. In some of these calculations it was found a marine ice layer could form and subsequently melt away. With the change in the melting and freezing patterns in the two expanded cavity domain runs, it might be possible for the extensive freezing in the southern part of the domain to generate a substantial marine ice layer that could survive subsequent movement through areas of melting. If this did occur it might provide a possible explanation for the marine ice layer observed at the G1 drill site [Morgan, 1972]. Of the three flowlines discussed in Section 5.6.1, the western and eastern flowlines (Flowlines 1 and 3, Figure 5.24) do not reach into the south of the domain, so are not affected by the cavity expansion. The central flowline (Flowline 2) does reach into the south of the domain, but does not flow through the region of high accumulation in either of the EC_A or EC_B runs.

The effect of expanding the ocean cavity is different in the north and south of the domain. In the north of the domain the effects are minimal, the structure of the horizontal circulation is very similar to that seen in the $AIS_{\Psi=0}$ runs for both the EC_A and EC_B model runs. There is also little change in the pattern of melting and freezing in the areas of the Central, Northern and Northeastern Gyres. The similarity of the melting and freezing, and the horizontal circulation, with that seen in the $AIS_{\Psi=0}$ run, leads to the temperature and salinity structure in the northern part of the domain being similar in the EC_A, EC_B, and $AIS_{\Psi=0}$ runs.

In the south of the domain the changes in the model results are significantly effected by the expansion of the model domain. The most notable change is in

the domain extension where there is weak horizontal circulation. This raises the possibility that vertical circulation may be more important for the transport of heat and salt in this part of the domain. This is borne out by the large exchange of heat with the ice shelf which is shown by the high melting and freezing rates in the southernmost part of the domain (Figure E.5). The high melting and freezing rates impact on the whole water column, and have the net affect of cooling the domain more than was seen in other model runs.

The similarity of the results in both the EC_A and EC_B runs to those for the $AIS_{\Psi=0}$ run in the north of the domain indicates the results in the north of the domain are largely unaffected by the extent of the southern part of the domain. Thus the results of this thesis in the northern part of the domain appear to be largely independent of the southern grounding line position.

If the grounding line is as far south as suggested by Phillips [1998], then the larger ocean cavity will affect the results described in this thesis. The effect that the larger cavity will have on the results is difficult to determine from the two preliminary experiments presented here. However, these two experiments suggest that the changes in the model results due to the expansion of the ocean cavity are localised to the southern part of the cavity, and that the northern part of the domain is largely uneffected. It is unlikely that either of the cavity expansion studies in this appendix are completely realistic, given the simple assumptions used in extending the ice shelf draft and the lack of information about the possible bathymetry. Hence, a definitive description awaits the availability of accurate observations on the extent of the cavity under the Amery Ice Shelf. Nevertheless, it is reassuring that changes in the far southern boundary of the domain, where the data are sparse, appear to have relatively little impact on the general conclusions derived from the earlier model simulations.